The Structure and Behavior of Plate Boundary Regions Through the Wilson Cycle

by

Zachary Molitor

B.S. in Geology and Geophysics, Purdue University, 2018

Submitted to the Department of Earth, Atmospheric, and Planetary Sciences in partial fulfillment of the requirements for the degree of

Doctor of Philosophy in Geology

at the

Massachusetts Institute of Technology

May 2024

Authored by: Zachary Molitor

Department of Earth, Atmospheric, and Planetary Sciences

March 7, 2024

Certified by: Prof. Oliver Jagoutz

Department of Earth, Atmospheric, and Planetary Sciences, Thesis supervisor

Accepted by: Prof. Rob van der Hilst

Chair, Department of Earth, Atmospheric, and Planetary Sciences

The Structure and Behavior of Plate Boundary Regions Through the Wilson Cycle

By
Zachary Molitor

Submitted to the Department of Earth, Atmospheric, and Planetary Sciences in March 2024
in Partial Fulfillment of the Requirements for the Degree of
Doctor of Philosophy in Geology

Abstract

This thesis explores the geochemical and geophysical properties of plate boundary regions in the Atlantic, East Africa, the New England Appalachians, and subduction zones around the Pacific Ocean. Chapter One presents geochemical constraints on the extent of enriched mantle from upwelling mantle plumes relative to the observed extent of topographic swells related to mantle flow. It builds on this data by presenting a new geophysical model of mantle flow around mantle plumes that constrains the viscosity structure of the upper mantle and emphasizes the role of dynamic pressure from flowing mantle in the generation and maintenance of plume swell topography. Chapter 2 presents new experimental constraints on subduction zone melts at 2.4 GPa and temperatures representative of conditions near the top of the subduction slab in the mantle wedge. Our experimental constraints support existing hypotheses that proposed erupted primitive high magnesian andesites are produced through mantle melting and mixing of melts in the mantle wedge, while also presenting novel constraints on the concentration of water that can be maintained in glass during quenching. Chapter 3 presents a field-based study of low melt fraction migmatites in central New Hampshire. In it, we utilize a unique approach, based on the compaction lengthscale, to calculate the shear viscosity of the migmatite during deformation associated with the Acadian-Neoacadian orogeny and the presence of an orogenic plateau. Chapter 4 presents a detailed macro- and microscale analysis of structures and deformation in southern New England related to contemporaneous strike-slip conjugate faulting in the upper crust. In it we present new electron backscatter diffraction (EBSD) data and *in situ* trace element and U-Pb isotopic compositions for monazite and titanite. These datasets provide quantitative constraints on the style and conditions of deformation in the weak middle crust beneath an orogenic strike-slip conjugate shear system (in the upper crust). Furthermore, this data constrains the late Paleozoic stress field in New England and the kinematics of collision between Gondwana and Laurasia.

Thesis Supervisor: Dr. Oliver E. Jagoutz
Title: Full Professor in Earth, Atmospheric, and Planetary Sciences Massachusetts Institute of Technology

Acknowledgements

I would like to thank all of my colleagues, friends, family, and mentors who have supported me during my Ph.D. study and encouraged my interest in Geology throughout my life.

Firstly, I would like to thank my advisor, Dr. Oliver Jagoutz. Oli has continually kept me on track during my study and pushed me to develop clear-cut, testable, and interesting scientific hypotheses. He has encouraged me to seek out a variety of means to test my hypotheses further and motivated me to always think critically at every step of the way. Oli has also encouraged me to speak my mind and not be afraid to ask questions, building skills which have dramatically improved my ability to collaborate and communicate my ideas to other scientists and the general public. I owe my sincere thanks to Oli for pointing me towards the New England Appalachians for my research. As I have worked throughout New England, I have realized its incredible potential for testing a number of process-oriented hypotheses and I hope to build my career and reputation in the region over the coming decades.

I would also like to express my gratitude to the other members of my thesis committee: Dr. Andy Cross, Dr. Leigh (Wiki) Royden, and Dr. Tim Grove. Andy, thank you for introducing me to the wonderful world of EBSD. I look forward to collaborating with you in the future on all of my microstructural and rheology related questions. Wiki, you have been like a second advisor throughout my research. Your ability to translate geologic systems into simple quantitative models is unmatched. I look forward to using what I have learned during my study to create simple quantitative models to test my field-based hypotheses. Tim, thank you for giving me a solid foundation in petrology and geochemistry and patiently working alongside me as I learned the ins and outs of experimental petrology and interpreting major element geochemical data.

Outside of my committee, there are a number of people who have aided me during my thesis and introduced me to new quantitative and laboratory methods: Dr. Alicia (Cici) Cruz-Uribe, Dr. Amy Moser, Dr. Nilanjan Chatterjee, Dr. Stephanie Krein, and Dr. Tushar Mittal. Cici, thank you for aiding in my *in situ* laser mass spectroscopy analysis and helping me get started on monazite and titanite geochronology. Amy, I am grateful to you for introducing me to titanite geochronology and answering all my questions about titanite analysis and data interpretation. Neel, thank you for teaching me how to operate the microprobe and ensuring that I collected the highest quality data possible. Steph, thank you for working with me on learning your reverse fractionation model and providing me with countless insightful discussions on mid-ocean ridge geochemistry and petrology. Tushar, thank you for being a dedicated and insightful collaborator and field partner, and working diligently to ensure the quality and appeal of our manuscript.

I would like to express my gratitude to my undergraduate research advisors Prof. Chris Andronicos, Prof. Julie Elliott, and Prof. Ken Ridgway. Chris, thank you for introducing me to geologic research and encouraging me along the way as I learned more and more about structural geology and petrology. Julie, thank you for introducing me to geodetic modelling and providing me with an amazing summer research experience. Ken, thank you for being an incredible teacher and introducing me to the fundamentals of geologic field work and geochronologic analysis.

To all my lab mates and fellow G-cubed graduate students, I would like to express my thanks for your support over the years. Thank you to all the graduate students and postdocs in the Jagoutz group for supporting me over the years: Josh Murray, Craig Martin, Billy Shinevar, Hongze Bo, Ze Liu, Cameron Murphy, Tushar Mittal, Herve Rezeau, Emilie Bowman, Ben Klein, and Liang Guo. Additional thanks to Craig, Josh, Tushar, and Ze who provided me with needed support during my initial field work in New Hampshire. Special shoutout to Josh, thank you for the fun final years in our mutual office, checking my figures were up to snuff, and helping sketch outcrops in the field. Additionally, I would like to thank all of the graduate students and postdocs who I've encountered throughout my study in the field or lab: Cailey Condit, Daniel Ortega-Arroyo, Ekaterina Bolotskaya, Eli Mansback, Joanna Millstein, Lucy Sandhoe, Maia Cohen, Max Collinet, Susanna Hoyos, and Patrick Beaudry.

Thank you to all of the administrative and HQ staff including Ann Greaney-Williams, Heather Hubbard, Jamu White, Kayla Bauer, Megan Jordan, and Roberta Allard. I would also like to thank all my fellow members of LINK12: Eric Roy, Jodie Ream, John Biersteker, and Suyash Bire.

Finally, I would like to thank my family and friends back home for their support during my long university study. To Mom and Dad, thank you for supporting me as a scientist from the beginning and harboring my rock collection over the years. Our annual trips to national parks and interesting new places continually stoked my interest in the natural world, and the countless books and science themed gifts kept me engaged and set on a career in science.

Table of Contents

List of Figures

List of Tables

Chapter 1: Introduction

The Earth is composed of three major layers on the basis of increasing density with depth below the surface: the crust, mantle, and core. The crust and uppermost mantle comprise a rigid, and largely elastic layer, termed the lithosphere. Most field-based geologic studies address the structure, behavior, and composition of the lithosphere and the interplay between the lithosphere and adjacent asthenosphere, atmosphere, cryosphere, and hydrosphere. The lithosphere and underlying ductile and convective asthenosphere are of utmost importance to geologists as these layers participate in plate tectonics. The theory of plate tectonics states that the lithosphere is fragmented into a series of plates, each of which move semi-independently on top of the underlying ductile asthenosphere (i.e., Wilson, 1963; 1966; 1968a). The "Wilson Cycle," or the cycle of continental breakup and supercontinent formation (e.g., Wilson, 1968; Burke and Dewey, 1973; Burke, 2007), is commonly used to reference the variety of observed structures in the lithosphere corresponding to the repeated creation and destruction of ocean basins and the occasional production of a singular "supercontinent" in Earth's lithosphere.

We have a relatively detailed understanding of the structure, behavior, and composition of the upper crust as this is the most accessible and continuously exposed section of the Earth's interior. Since the conception of modern plate tectonics in the 1960s, there is a large body of field-based work that has mapped out the structure of the upper crust in detail with associated discussions and interpretations regarding the behavior and composition of the upper crust (e.g., Crider and Peacock, 2004; Gratier et al., 2013). The deep lithosphere, composed of the lower crust and uppermost mantle, is not nearly as well studied as the upper crust (e.g., Burgmann and Dresen, 2008; Hacker et al., 2015). Much of our understanding of the deep lithosphere is derived from geophysical and remote sensing data as well as increasingly complex geodynamic models (Shinevar et al., 2015). Much of the recent work in solid earth geoscience over the last couple decades has focused on identifying and characterizing lower crustal exposures around the globe (Jagoutz and Schmidt, 2012; Getsinger et al., 2013; Jagoutz and Keleman, 2015; Dumond et al., 2018; Tassara et al., 2021), with the aim to improve our understanding of the composition and rheology of lower crustal rocks. The identification and detailed study of bedrock exposures, formerly held at extreme depth in the Earth, is of utmost importance to studying the structure of the deep lithosphere in detail and directly testing hypotheses born out of remote sensing data, geodynamic models of the lithosphere, and experimental work on lower crustal petrology and rheology.

In this thesis, we discuss the structure and behavior of the lithosphere, in particular the mid-lower crust and upper mantle in plate boundary regions. Plate boundary regions are the sub-linear zones between lithospheric plates which accommodate deformation due to their relative movement (Stein and Stella, 2013). The first chapter focuses on the behavior of the upper mantle surrounding upwelling mantle plumes in proximity to oceanic spreading centers (mid-ocean ridges). The second chapter presents the results of an experimental investigation on the composition of hydrous lherzolite melts in the deep mantle wedge (2.4 GPa). The last two chapters present field-based studies of the mid-lower crust in the late Paleozoic Appalachian orogen, produced during multistage continental collision and the formation of the supercontinent Pangea.

In Chapter 1, we present geochemical constraints on the extent of plume material in the upper mantle relative to the extent of topographic swells related to uplift around the plume. Previous studies highlight a discrepancy between the extent of geochemical anomalies away from the center of upwelling mantle plumes and the extent of topographic uplift around the plumes. Geochemical anomalies are typically limited to within ~400-700 km of the center of the mantle plume, while topographic swells extend for ~1500-2000 km from the plume center. Many past geophysical models have hypothesized that the majority of topographic uplift around mantle plumes is due to a combination of i) crustal thickness (Darbyshire et al., 1998; Ito et al., 1999; Canales et al., 2002), ii) thermal erosion of the lithosphere (Davies, 1994), iii) isostatic compensation of the relatively low-density plume (Zhoe and Dick, 2013), and iv) dynamic pressure and uplift related to mantle flow (Sleep, 1990; Yamamoto et al., 2007). Of these four hypotheses, the first three are much more prevalent in the literature with only a handful of studies arguing for significant dynamic compensation of mantle plume swells. As part of our work, we calculated the mantle potential temperature beneath spreading ridges that transect the Iceland, Afar, and Azores mantle plumes following the method of Krein et al. (2021). The results of this analysis are in rough agreement with previously published studies on the extent of plume material from geochemical anomalies. Together with available crustal thickness data around Iceland and the Azores (i.e., Weir et al., 2001; Ferreira et al., 2020), we find that elevated crustal thickness, thermal erosion, and isostatic compensation of low-density plume material are insufficient to explain the majority of dynamic topography, principally beyond the extent of geochemical anomalies associated with hot, enriched plume material in the upper mantle. In this chapter, we present a new model of dynamic topography and mantle flow around upwelling mantle plumes, with the modelled plume extent (and plume viscosity) constrained by the extent of geochemical anomalies and the majority of model topography is constrained by a combination of plume volume flux and upper mantle viscosity. Our model strongly supports the hypothesis that plume swells are primarily supported by dynamic pressure due to mantle flow away from the upwelling plume center. Moreover, the dependence of the model on dynamic pressure, viscosity, and shear stress terms, allows us to provide new constraints regarding the viscosity structure of the upper mantle beneath the oceanic lithosphere. We find that a thin (~30 km), low viscosity (~10^{19} Pa·s) channel beneath the lithosphere is required for consistency with previous constraints on the shear stress at the base of the lithosphere.

In Chapter 2, we present the results of experiments on hydrous lherzolite melting at 2.4 GPa corresponding to the deep mantle wedge in subduction zones. There is a long standing debate regarding whether primitive high magnesian andesites (HMAs) such as those found the Cascade range in the Northwest United States are the product of primary mantle melting or crustal assimilation and differentiation (Strek et al., 2007; Keleman and Yogodzinski, 2007;Barr et al., 2007; Streck and Leeman, 2018; Phillips and Till, 2022). As we cannot directly observe the structure and composition of the upper mantle wedge in subduction zones, we can constrain the composition of primary mantle melts through high temperature, high pressure experimentation. Previous experimental results (i.e., Mitchell and Grove, 2015; Grove and Till, 2019) support an interpretation where primitive HMAs are produced through hydrous mantle melting and mixing between deep mantle melts close to the slab (~3 GPa) and shallow (~1-1.2 GPa), harzburgite melts. However, we still do not have detailed constraints on the composition of melts intermediate between the deep and shallow mantle wedge and observed alkali compositional systematics (Na and K) remain elusive. Our results provide further support for the hypothesis of Grove and Till (2019) suggesting that primitive HMAs are produced via mixing of mantle melts between the dehydrating oceanic slab and shallow mantle wedge. The compositions of experiments at 2.4 GPa are either intermediate between shallow and deep experiments, or further bracket the range of erupted compositions in conjunction with past experiments. In particular, deep melts (this chapter, Grove and Till, 2019) are better able to explain the observed low Ca and relatively high Na and K concentrations of erupted HMAs in comparison to past experiments. Additionally, our experiments were terminated through pressure quenching as opposed to quenching by turning off the thermocouple (as in previous experiments). Pressure quenching, while also turning off the thermocouple, prevents quench crystal growth and preserves more of the primary glass textures in the experiment. By utilizing this quenching method, we preserved a range of glass textures between the high and low temperature experiments in our study. Related to the glass textures, the inferred water contents of the glass from major element compositional totals range from ~6-10 % depending on the experimental temperature. Higher temperature experiments typically result in glass with lower concentrations of water and a mix of smooth, continuous glass and vesiculated glass. Lower temperature experiments result in glass with relatively high, but consistent concentrations of water at ~9 wt.% associated with strongly vesiculated glass or isolated, small glass spheres. These findings are consistent with the recent study of Gavrilenko et al. (2019) which suggests that during quenching, and the associated melt to glass transition, only <10 wt.% water can be 'locked' into the structure of the glass while the remaining fluid must be released. These results suggest that existing constraints on magmatic water content from melt inclusions or erupted glass are biased toward upper crustal water solubilities and may inaccurately reflect the water solubilities and concentrations of melts in the deep crust and upper mantle.

In Chapter 3, I present new structural observations and simple geophysical modelling of a late Devonian (~360 Ma) migmatite in Central New Hampshire. Studies of major collisional orogens such as the Tibetan-Himalaya in Asia or the Andes in South America commonly suggest a weak ($<10^{18}$ Pa·s) and flowing mid-crustal layer (e.g., Clark and Royden, 2000). Geophysical models of the Tibetan plateau require this weak layer to explain the elevated, broad, and flat topography of the plateau. Isolated field investigations as well as seismic and magnetotelluric data for the Tibetan and Andean plateaus suggest that the weak middle crust is produced due to extensive partial melting and associated melt-induced weakening (Schmitz et al., 1997; Schilling and Partzsch, 2001; Li et al., 2003; Schilling et al., 2006; Jamieson et al., 2011; Hacker et al., 2014; Xie et al., 2021). In Central New Hampshire, we identified an exposure of low melt fraction (<~9 %) discordant migmatite which formed in the middle crust of the late Devonian Acadian orogen contemporaneous with an Acadian-Neoacadian orogenic plateau (Hillenbrand et al., 2021). As the original structure of the pre-migmatitic schist is preserved due to the low degrees of melting, this exposure provides an unprecedented opportunity to study the effect of partial melting on mid-crustal structure and weakening. We utilize the compaction lengthscale of McKenzie (1984) to estimate the shear viscosity of the migmatite contemporaneous with late Devonian deformation. The compaction lengthscale can be directly related to the spacing of discordant leucosomes, or bodies of partial melt, in the lithology. Therefore, by measuring the spacing of leucosomes and placing field-based and geochemical constraints on permeability and melt viscosity, we are able to calculate a shear viscosity for the migmatite during late Devonian deformation. We find that the migmatite deformed with a shear viscosity of $10^{17\text{-}18}$ Pa·s in the middle crust of the Acadian-Neoacadian plateau, corresponding to a 2-3 order of magnitude reduction in viscosity relative to a completely solid-state assemblage with no melt. This finding is in exact agreement with geophysical estimates of mid-lower crustal viscosity in Tibet and the Andes. Furthermore, our estimates of partial melt volume both in the field area and throughout Central New Hampshire are remarkably consistent with seismic and magnetelluric estimates of partial melt volume beneath the Tibetan and Andean plateaus. Ultimately, we find that high volumes of partial melt are not required to significantly affect the rheology of the mid-crust (~20-60 % melt) and that low volumes of melt and increasing melt connectivity are sufficient to reduce mid-crustal viscosity in accordance with mid-lower crustal ductile flow.

In Chapter 4, we present the results of a detailed structural and deformation analysis of Alleghenian deformation in southern New England. In this chapter, we seek to test whether conjugate strike slip shear zones, active in the Carboniferous during the early Alleghenian orogeny (~330-300 Ma), crosscut the entire crust or lithosphere (e.g., Tapponnier, 2001) or sole out in a mid-crustal weak zone (e.g., Van Buer et al., 2015). Furthermore, we investigate dynamic mechanism driving conjugate shear relative to the convergence direction of Gondwana and Laurasia, plate boundary orientation, and the presence or absence of orogen parallel flow in the mid-lower crust. We first present a regional compilation of macrostructural data (foliation, mineral lineation, and fold axis lineations) from Connecticut and Central Massachusetts bedrock geologic maps. The regional macrostructural data demarcates a significant transition between the medial Central Maine Terrane (CMT) in central and northern New England and the underlying Merrimack Terrane in eastern Connecticut. While the CMT consists of moderately to steeply dipping foliations both in its interior and on bounding strike-slip shear zones, the Merrimack Terrane is almost entirely subhorizontal and shallowly dipping. Subvertical conjugate strike slip shear zones, well documented in northern New England (dextral

Norumbega fault zone, West and Lux, 1993; sinistral Western Bronson Hill Shear Zone (WBHSZ), Massey and Moecher, 2013; McWilliams et al., 2013), transition to moderately and shallowly dipping flattening and dip-slip shear zones in eastern Connecticut. To further quantify the style and grade of deformation related to Alleghenian deformation in New England, we collected new EBSD data for ~10 thin sections of Alleghenian shear zones and high grade metamorphic rocks. The results of microstructural analysis and interpretation of the EBSD data suggest that the macro-structural transition identified above also corresponds to a transition in deformation style from rigid behavior and mylonitic strike-slip deformation in the upper crust (on the margins of the CMT) to ductile flattening and dip-slip deformation in the middle crust, exposed in eastern Connecticut. To ensure that the studied deformation is associated with upper crustal conjugate shear and Alleghenian deformation, we dated late-post kinematic monazite in the CMT and synkinematic titanite in the Merrimack Terrane. Monazite growth primarily reflects Acadian-Neoacadian metamorphism and deformation in the CMT; however, at the southern terminus along the Eastford fault, young monazite rims date top-to-southeast dip-slip deformation at ~330-300 Ma, contemporaneous with upper crustal conjugate shear. U-Pb titanite ages constrain the age of subhorizontal, dip-slip deformation in the middle crust to ~320-290 Ma, and late subhorizontal flattening to ~280 Ma. Altogether, these datasets suggest that strike-slip conjugate shear was confined to the upper crust and transitions to subhorizontal flattening and dip-slip shear along a weak mid-crustal decollement during Alleghenian orogenesis. Furthermore, estimates of paleostress direction from EBSD data provide new constraints on the Carboniferous stress field associated with Alleghenian deformation in New England, and suggest that deformation related to convergence is strongly partitioned into mylonitic strike-slip shear zones in the upper crust and distributed ductile shear in the mid-lower crust. The regional convergence direction and stress field suggest that the conjugate shear system is accommodating lateral escape of the CMT away from the zone of head-on collision in the central and southern Appalachians.

In summary, the chapters within this thesis present new geochemical and field-based constraints on the physical behavior and structure of plate boundary regions as well as the rheology and composition of the upper mantle. Each chapter is intended to represent a separate manuscript. Chapter 2 is in preparation but will be resubmitted to Geology, Geochemistry, and Geosystems following reviews received in 2023. Chapter 2 is currently in preparation and will be submitted to Contributions to Mineralogy and Petrology. Chapter 4 has been submitted to Earth, Planetary, and Science Letters as of January, 2024 and is currently under review. Chapter 5 is currently in preparation and will be submitted to the American Journal of Science.

References

Barr, J., Grove, T. L., & Elkins-Tanton, L. (2007). High-magnesian andesite from Mount Shasta: A product of magma mixing and contamination, not a primitive melt: COMMENT AND REPLY: COMMENT. *Geology*, *35*(1), e147–e147. https://doi.org/10.1130/G24058C.1

Bürgmann, R., & Dresen, G. (2008). Rheology of the Lower Crust and Upper Mantle: Evidence from Rock Mechanics, Geodesy, and Field Observations. *Annual Review of Earth and Planetary Sciences*, *36*(1), 531–567. https://doi.org/10.1146/annurev.earth.36.031207.124326

Burke, K. (2011). Plate Tectonics, the Wilson Cycle, and Mantle Plumes: Geodynamics from the Top. *Annual Review of Earth and Planetary Sciences*, *39*(1), 1–29. https://doi.org/10.1146/annurev-earth-040809-152521

Burke, K., & Dewey, J. F. (1973). Plume-Generated Triple Junctions: Key Indicators in Applying Plate Tectonics to Old Rocks. *The Journal of Geology*, *81*(4), 406–433. JSTOR.

Canales, J. P., Ito, G., Detrick, R. S., & Sinton, J. (2002). Crustal thickness along the western Galápagos Spreading Center and the compensation of the Galápagos hotspot swell. *Earth and Planetary Science Letters*, *203*(1), 311–327. https://doi.org/10.1016/S0012-821X(02)00843-9

Clark, M. K., & Royden, L. H. (2000). Topographic ooze: Building the eastern margin of Tibet by lower crustal flow. *Geology*, *28*(8), 703–706. https://doi.org/10.1130/0091-7613(2000)28<703:TOBTEM>2.0.CO;2

Crider, J. G., & Peacock, D. C. P. (2004). Initiation of brittle faults in the upper crust: A review of field observations. *Journal of Structural Geology*, *26*(4), 691–707. https://doi.org/10.1016/j.jsg.2003.07.007

Darbyshire, F. A., Bjarnason, I. Th., White, R. S., & Flóvenz, Ó. G. (1998). Crustal structure above the Iceland mantle plume imaged by the ICEMELT refraction profile. *Geophysical Journal International*, *135*(3), 1131–1149. https://doi.org/10.1046/j.1365-246X.1998.00701.x

Davies, G. F. (1994). Thermomechanical erosion of the lithosphere by mantle plumes. *Journal of Geophysical Research: Solid Earth*, *99*(B8), 15709–15722.

Dumond, G., Williams, M. L., & Regan, S. P. (2018). The Athabasca Granulite Terrane and Evidence for Dynamic Behavior of Lower Continental Crust. *Annual Review of Earth and Planetary Sciences*, *46*(1), 353–386. https://doi.org/10.1146/annurev-earth-063016-020625

Ferreira, A. M. G., Marignier, A., Attanayake, J., Frietsch, M., & Berbellini, A. (2020). Crustal structure of the Azores Archipelago from Rayleigh wave ellipticity data. *Geophysical Journal International*, *221*(2), 1232–1247. https://doi.org/10.1093/gji/ggaa076

Gavrilenko, M., Krawczynski, M., Ruprecht, P., Li, W., & Catalano, J. G. (2019). The quench control of water estimates in convergent margin magmas. *American Mineralogist*, *104*(7), 936–948. https://doi.org/10.2138/am-2019-6735

Getsinger, A. J., Hirth, G., Stünitz, H., & Goergen, E. T. (2013). Influence of water on rheology and strain localization in the lower continental crust. *Geochemistry, Geophysics, Geosystems*, *14*(7), 2247–2264. https://doi.org/10.1002/ggge.20148
Gratier, J.-P., Dysthe, D. K., & Renard, F. (2013). The Role of Pressure Solution Creep in the Ductility of the Earth's Upper Crust. In *Advances in Geophysics* (Vol. 54, pp. 47–179). Elsevier. https://doi.org/10.1016/B978-0-12-380940-7.00002-0
Grove, T. L., & Till, C. B. (2019). H2O-rich mantle melting near the slab–wedge interface. *Contributions to Mineralogy and Petrology*, *174*(10), 80. https://doi.org/10.1007/s00410-019-1615-1
Hacker, B. R., Kelemen, P. B., & Behn, M. D. (2015). Continental Lower Crust. *Annual Review of Earth and Planetary Sciences*, *43*(1), 167–205. https://doi.org/10.1146/annurev-earth-050212-124117
Hacker, B. R., Ritzwoller, M. H., & Xie, J. (2014). Partially melted, mica-bearing crust in Central Tibet. *Tectonics*, *33*(7), 1408–1424. https://doi.org/10.1002/2014TC003545
Hillenbrand, I. W., Williams, M. L., Li, C., & Gao, H. (2021). Rise and fall of the Acadian altiplano: Evidence for a Paleozoic orogenic plateau in New England. *Earth and Planetary Science Letters*, *560*, 116797. https://doi.org/10.1016/j.epsl.2021.116797
Ito, G., Shen, Y., Hirth, G., & Wolfe, C. J. (1999). Mantle flow, melting, and dehydration of the Iceland mantle plume. *Earth and Planetary Science Letters*, *165*(1), 81–96. https://doi.org/10.1016/S0012-821X(98)00216-7
Jagoutz, O., & Kelemen, P. B. (2015). Role of Arc Processes in the Formation of Continental Crust. *Annual Review of Earth and Planetary Sciences*, *43*(1), 363–404. https://doi.org/10.1146/annurev-earth-040809-152345
Jagoutz, O., & Schmidt, M. W. (2012). The formation and bulk composition of modern juvenile continental crust: The Kohistan arc. *Chemical Geology*, *298–299*, 79–96. https://doi.org/10.1016/j.chemgeo.2011.10.022
Jamieson, R. A., Unsworth, M. J., Harris, N. B. W., Rosenberg, C. L., & Schulmann, K. (2011). Crustal Melting and the Flow of Mountains. *Elements*, *7*(4), 253–260. https://doi.org/10.2113/gselements.7.4.253
Kelemen, P. B., & Yogodzinski, G. (2007). High-magnesian andesite from Mount Shasta: A product of magma mixing and contamination, not a primitive melt: COMMENT AND REPLY: COMMENT. *Geology*, *35*(1), e149–e150. https://doi.org/10.1130/G24099C.1
Krein, S. B., Molitor, Z. J., & Grove, T. L. (2021). ReversePetrogen: A Multiphase Dry Reverse Fractional Crystallization-Mantle Melting Thermobarometer applied to 13,589 Mid-Ocean Ridge Basalt Glasses. *Journal of Geophysical Research - Solid Earth*.
Li, S., Unsworth, M. J., Booker, J. R., Wei, W., Tan, H., & Jones, A. G. (2003). Partial melt or aqueous fluid in the mid-crust of Southern Tibet? Constraints from INDEPTH magnetotelluric data. *Geophysical Journal International*, *153*(2), 289–304. https://doi.org/10.1046/j.1365-246X.2003.01850.x
Massey, M. A., Moecher, D. P., Walker, T. B., O'Brien, T. M., & Rohrer, L. P. (2017). The role and extent of dextral transpression and lateral escape on the post-Acadian tectonic evolution of south-central New England. *American Journal of Science*, *317*(1), 34–94. https://doi.org/10.2475/01.2017.02
McKenzie, D. (1984). The Generation and Compaction of Partially Molten Rock. *Journal of Petrology*, *25*(3), 713–765. https://doi.org/10.1093/petrology/25.3.713
McWilliams, C. K., Kunk, M. J., Wintsch, R. P., & Bish, D. L. (2013). Determining ages of multiple muscovite-bearing foliations in phyllonites using the 40Ar/39Ar step heating method: Applications to the Alleghanian orogeny in central New England. *American Journal of Science*, *313*(10), 996–1016. https://doi.org/10.2475/10.2013.02
Mitchell, A. L., & Grove, T. L. (2015). Melting the hydrous, subarc mantle: The origin of primitive andesites. *Contributions to Mineralogy and Petrology*, *170*(2), 13. https://doi.org/10.1007/s00410-015-1161-4
Phillips, M., & Till, C. B. (2022). Crustal storage and ascent history of the Mt. Shasta primitive magnesian andesite: Implications for arc magma crustal flux rates. *Contributions to Mineralogy and Petrology*, *177*(1), 9. https://doi.org/10.1007/s00410-021-01853-x
Schilling, F. R., & Partzsch, G. M. (2001). Quantifying partial melt fraction in the crust beneath the central andes and the Tibetan plateau. *Physics and Chemistry of the Earth, Part A: Solid Earth and Geodesy*, *26*(4–5), 239–246. https://doi.org/10.1016/S1464-1895(01)00051-5
Schilling, F. R., Trumbull, R. B., Brasse, H., Haberland, C., Asch, G., Bruhn, D., Mai, K., Haak, V., Giese, P., Muñoz, M., Ramelow, J., Rietbrock, A., Ricaldi, E., & Vietor, T. (2006). Partial Melting in the

Central Andean Crust: A Review of Geophysical, Petrophysical, and Petrologic Evidence. In O. Oncken, G. Chong, G. Franz, P. Giese, H.-J. Götze, V. A. Ramos, M. R. Strecker, & P. Wigger (Eds.), *The Andes* (pp. 459–474). Springer Berlin Heidelberg. https://doi.org/10.1007/978-3-540-48684-8_22

Schmitz, M., Heinsohn, W.-D., & Schilling, F. R. (1997). Seismic, gravity and petrological evidence for partial melt beneath the thickened Central Andean crust (21–23°S). *Tectonophysics*, *270*(3–4), 313–326. https://doi.org/10.1016/S0040-1951(96)00217-X

Shinevar, W. J., Behn, M. D., & Hirth, G. (2015). Compositional dependence of lower crustal viscosity. *Geophysical Research Letters*, *42*(20), 8333–8340. https://doi.org/10.1002/2015GL065459

Sleep, N. H. (1990). Hotspots and mantle plumes: Some phenomenology. *Journal of Geophysical Research: Solid Earth*, *95*(B5), 6715–6736.

Stein, S., & Sella, G. F. (2013). Plate Boundary Zones: Concepts and Approaches. In S. Stein & J. T. Freymueller (Eds.), *Geodynamics Series* (pp. 1–26). American Geophysical Union. https://doi.org/10.1029/GD030p0001

Streck, M. J., & Leeman, W. P. (2018). Petrology of "Mt. Shasta" high-magnesian andesite (HMA): A product of multi-stage crustal assembly. *American Mineralogist*, *103*(2), 216–240. https://doi.org/10.2138/am-2018-6151

Streck, M. J., Leeman, W. P., & Chesley, J. (2007). High-magnesian andesite from Mount Shasta: A product of magma mixing and contamination, not a primitive mantle melt. *Geology*, *35*(4), 351. https://doi.org/10.1130/G23286A.1

Tapponnier, P., Zhiqin, X., Roger, F., Meyer, B., Arnaud, N., Wittlinger, G., & Jingsui, Y. (2001). Oblique Stepwise Rise and Growth of the Tibet Plateau. *Science*, *294*(5547), 1671–1677. https://doi.org/10.1126/science.105978

Tassara, S., Ague, J. J., & Valencia, V. (2021). The deep magmatic cumulate roots of the Acadian orogen, eastern North America. *Geology*, *49*(2), 168–173. https://doi.org/10.1130/G47887.1

Van Buer, N. J., Jagoutz, O., Upadhyay, R., & Guillong, M. (2015). Mid-crustal detachment beneath western Tibet exhumed where conjugate Karakoram and Longmu–Gozha Co faults intersect. *Earth and Planetary Science Letters*, *413*, 144–157. https://doi.org/10.1016/j.epsl.2014.12.053

Weir, N. R. W., White, R. S., Brandsdóttir, B., Einarsson, P., Shimamura, H., & Shiobara, H. (2001). Crustal structure of the northern Reykjanes Ridge and Reykjanes Peninsula, southwest Iceland. *Journal of Geophysical Research: Solid Earth*, *106*(B4), 6347–6368. https://doi.org/10.1029/2000JB900358

West, D. P., & Lux, D. R. (1993). Dating mylonitic deformation by the 40Ar-39Ar method: An example from the Norumbega Fault Zone, Maine. *Earth and Planetary Science Letters*, *120*(3–4), 221–237. https://doi.org/10.1016/0012-821X(93)90241-Z

Wilson, J. T. (1963). Hypothesis of Earth's Behaviour. *Nature*, *198*(4884), 925–929. https://doi.org/10.1038/198925a0

Wilson, J. T. (1966). Did the Atlantic Close and then Re-Open? *Nature*, *211*(5050), 676–681. https://doi.org/10.1038/211676a0

Wilson, J. T. (1968). Static or Mobile Earth: The Current Scientific Revolution. *Proceedings of the American Philosophical Society*, *112*(5), 309–320. JSTOR.

Xie, C., Jin, S., Wei, W., Ye, G., Jing, J., Zhang, L., Dong, H., & Yin, Y. (2021). Middle Crustal Partial Melting Triggered Since the Mid-Miocene in Southern Tibet: Insights From Magnetotelluric Data. *Journal of Geophysical Research: Solid Earth*, *126*(9), e2021JB022435. https://doi.org/10.1029/2021JB022435

Yamamoto, M., Morgan, J. P., & Morgan, W. J. (2007). Global plume-fed asthenosphere flow-I: motivation and model development. *Special Papers-Geological Society of America*, *430*, 165.

Zhou, H., & Dick, H. J. B. (2013). Thin crust as evidence for depleted mantle supporting the Marion Rise. *Nature*, *494*(7436), 195–200. https://doi.org/10.1038/nature11842

Chapter 2: Dynamic Pressure as the Primary Compensation Mechanism around Mantle Plume Swells

Abstract

Mantle plumes are associated with diapiric upwelling in the mantle and are commonly overlain by a region of surface uplift. We present new geochemical data from the Iceland, Afar and Azores plumes, consisting of mantle potential temperature, and Sr and Pb isotopic measurements, indicate that 'plume-mantle' material is restricted to a region within ~700 km from the plume center. In contrast, the attendant topographic swells extend for ~2000 km from the plume center. These data indicate that compensation for the uplifted regions, beyond a radius of 500-700 km, is not due to the presence of hot, low-density material or crustal thickness. We use a simple model for viscous flow in a two-layer upper mantle, to model the injection of hot, low viscosity plume material into the upper mantle and the development of swell topography due to dynamic pressure in the upper mantle. The dynamic pressure is developed as plume material and "normal" asthenosphere flow away from the plume center. Model results show good correspondence with the geochemical data and observed topography around the Afar, Azores, and Iceland plume centers, and suggest that most of the swell topography beyond the plume radius is compensated by elevated dynamic pressure within the upper mantle. Our results suggest a volume flux of plume material into the upper mantle of 10^5 - 10^6 km^3/m.y. Our model has important implications for the viscosity structure of the upper mantle, supporting the existence of a thin (~30 km) oceanic low viscosity (~10^{19} Pa·s) layer below the lithosphere.

2.1 Introduction

Mantle plumes are buoyant upwellings in the Earth's mantle that source oceanic and continental hot spots, including those observed at Iceland, the Azores, Afar, Kerguelen, Hawaii, and the Galapagos (Morgan, 1972; Wilson, 1973). Plumes are hypothesized to be composed of hot, low-density mantle that rises to the base of the lithosphere and are associated with topographic swells that surround the plume center (e.g., Almond, 1986). Only a small fraction of plume-sourced magma erupts onto or intrudes the shallow crust while the remainder is underplated or intrudes the lower crust (Duncan and Richards, 1991).

The total volume of plume material, flux of plume material into the upper mantle, and mode of compensation of the associated swells are hotly debated (Courtney and White, 1986; Monnereau and Cazenave, 1990; Sleep, 1990; Marks and Sandwell, 1991; Canales et al., 2002). Geochemical proxies, including isotopic ratios and whole rock composition, suggest that the lateral extent of Icelandic plume material is limited to a distance of less than ~700 km from its plume center (Hart et al., 1973; Schilling, 1973; Unni and Schilling, 1978; Fitton et al., 1997; Murton et al., 2002, Shorttle et al., 2015). In contrast, many geophysical and geodynamic studies of mantle plumes conclude that the topographic swells, which typically have a radius much greater than 700 km (typically 1000-2000 km, e.g., Jones and White, 2003; Hoggard et al., 2017), are largely supported by low density plume material in the upper mantle and by crustal thickness variations (Sleep, 1990; Ito et al., 1999; Canales et al., 2002).

In this paper, we better constrain the radial extent of plume material and the mode of swell compensation at three plumes transected by oceanic spreading ridges: Iceland, Afar, and the Azores. We present a new dataset of the mantle potential temperatures that constrain the hot plume material in all three plumes to distances less than ~700 km from each plume center.

This new dataset places strong constraints on the mode of swell compensation at distances greater than ~700 km from the plume centers and on the viscosity structure of the upper mantle. Using a quantitative model for upper mantle flow above and adjacent to plume sources, we demonstrate that the swell topography at radial distances greater than ~700 km from the plume sources can be readily explained by the dynamic pressure of fluid flow within the upper mantle. The results of this study have significant implications for estimates of upper mantle viscosity structure and support the existence of a thin low viscosity layer directly beneath the (young) oceanic lithosphere (i.e., Scoppola et al., 2006; Barnhoorn et al., 2011).

2.2 Geochemistry and Topography of Mantle Plumes

Plume-derived volcanic rocks are more abundant where oceanic spreading ridges intersect the plume (Schilling, 1973). In this setting, basaltic rocks erupted along the ridge can be sampled for the presence of plume-derived material as a function of distance from the plume center. Furthermore, the excess topography associated with the plume can be determined directly from ridge bathymetry without corrections for pre-existing variations in topography, such as age-depth relations in the oceanic lithosphere. Thus, plumes intersected by spreading ridges provide an excellent opportunity to constrain the lateral extent of plume material and the compensation mechanism for swell topography.

2.2.1 Geochemistry

A wide range of isotopic and whole rock analyses of erupted rocks have been published for the Reykjanes ridge, including Hart et al. (1973), Schilling (1973), Unni and Schilling (1978), Fitton et al. (1997), Murton et al. (2002), Shorttle et al. (2015). These studies, taken together, suggest that depleted MORB geochemical properties are representative of the erupted basalts at distances greater than ~700 km from the Iceland plume center, while basalts in close proximity to the plume are relatively enriched in trace elements and isotopes. In order to test and refine this result, we compute the mantle potential temperatures of magmatic rocks sampled on spreading ridges that intersect the Iceland, Afar, and Azores mantle plumes.

We use the major element geochemical model of Krein et al. (2021) to calculate mantle potential temperature (T_p) as a function of distance from the mantle plume center. This method 'reverse fractionates' the major element geochemical data by incrementally correcting the erupted composition for multiphase fractionation of olivine, clinopyroxene, and/or plagioclase.

By calculating the primary melt compositions from numerous multiphase fractionation paths and comparing them to a regression of dry mantle melting experiments, the composition, melting temperature, and melting pressure of the primary melt can be constrained (see Section 2 in Krein et al., 2021 for a detailed methodology). The average global T_p, as constrained by Krein et al. (2021), for mid-ocean ridge basalts not affected by mantle plumes, is 1322 ± 56°C. (A list of references for samples used in this paper can be found in Appendix 1 (A1.4), along with the EarthChem search criteria for each plume.)

We also use two isotopic systems, $^{87}Sr/^{86}Sr$ and $^{206}Pb/^{204}Pb$, to constrain the lateral extent of plume-derived melts (Schilling et al., 1992; Tayler et al., 1997; Harpp and White, 2001). Because Sr and Pb isotopes are thought to reflect the composition of the melt source, values of $^{87}Sr/^{86}Sr$ and $^{206}Pb/^{204}Pb$ close to that of average MORB are generally interpreted to have little to no plume component in the melting region. Basalts with enriched Pb and Sr isotopes relative to MORB are expected where some fraction of the melts are derived from the deep mantle (Hofmann and White, 1982). The isotopic ratios and the mantle potential temperatures can then be used to constrain the lateral extent of plume material as a function of distance from the plume center, as is described in Section 2.2.3.

2.2.2 Swell Topography

The topographic swells above and surrounding mantle plumes have been variously attributed to: (i) elevated asthenospheric temperatures above and around the plume (Montelli et al., 2004); (ii) low density of plume material caused by non-thermal compositional differences relative to the ambient mantle (Zhou and Dick, 2013); (iii) thermal erosion and/or heating of the lithosphere (Davies, 1994); (iv) thickening of oceanic crust due to partial melting of plume material (Darbyshire et al., 1998; Ito et al., 1999; Canales et al., 2002). It is likely that some or all these processes play some role in elevating the topography above plumes, especially near the plume center. Several authors have also suggested that the longer-wavelength component of swell topography may be due to the pressure of fluid flow in the asthenosphere, with increased mantle pressure leading to topographic uplift above the plume (Sleep, 1990; Yamamoto et al., 2007; see also Parsons and Daly, 1983 and McNutt, 1988)

2.2.3 Iceland, Afar and Azores Plumes

The Iceland, Afar and Azores plumes intersect actively spreading mid-ocean ridges bordered by plates with slow relative and absolute velocities (<10-20 mm/yr) in an Indo-Atlantic hot spot frame (DeMets et al., 2010; Koivisto et al., 2014; Barnett-Moore et al., 2017). This is in contrast with plumes located in the Pacific and Indian oceans, where the over-riding plates move at rates > 50 mm/yr in most hot spot frames of reference (i.e., Morgan and Morgan, 2007; Kovisto et al., 2014; Wang et al., 2018). By studying plumes overlain by slowly moving plates, we can, to first order, ignore the velocity of the plates, simplifying analysis of the plumes and the associated swells.

2.2.3.1 Iceland Plume

The Iceland plume underlies the North Atlantic spreading ridge, which rises above sea level over the plume center (Figure 2.1A). Here, full spreading rates across the North Atlantic ridge (from 50-70°N) are between 15 and 20 mm/yr (Muller et al., 2008). The Iceland plume appears to have been located near its present position along the north Atlantic ridge for ~20-30 Ma and to have become active no earlier than 130 Ma (Lawver and Muller, 1994).

We define the location of the Iceland plume conduit as the region having S-wave speed perturbations ($\delta V_S/V_S$ %) less than -2% at a depth of 135 km (Montelli et al., 2004), placing the Iceland plume conduit directly beneath the North Atlantic ridge (Figure 2.1A). Topography (bathymetry) profiles along the spreading ridges (Kolbeinsey and Reykjanes ridges, Figures 2.1A and 2A) were computed along the ridges using data from Ryan et al. (2009) and a centered moving average from a 100 km window (the same moving window was applied to the Afar and Azores topography along each profile; Figure 2.2). The topographic profiles display a swell with a radius of ~1500-2000 km and a maximum height of ~3000 m (Figure 2.2A).

The T_p for basalts collected from the Iceland ridge system are binned by radius, with bin increments of 100 km for the innermost bins and 200 km at greater distances from the plume center (Figure 2.2; the same binning procedure is used for the Afar and Azores plumes and for the isotopic data). For samples erupted > 500 km from the plume center, computed T_p is consistent with the global average of 1300-1350°C for ridges without underlying plumes (Krein et al., 2021) and there is little correlation with distance from the plume center. At radial distances < 400 km from the plume center, the average value of T_p is ~1450°C, significantly above the global average (Krein et al., 2021). In this domain, T_p is also largely independent of distance from the plume center. An abrupt change in T_p of basalts is present at a radial distance of 400-500 km from the plume center.

$^{87}Sr/^{86}Sr$ measurements from basalts show a nearly identical spatial pattern (Figure 2.2A). $^{87}Sr/^{86}Sr$ values are ~0.7028 for samples located > 500 km from the plume center, consistent with the depleted MORB (DMM) mantle reference value of 0.7026 ± 0.0004 (Workman and Hart, 2005). In contrast, $^{87}Sr/^{86}Sr$ ratios for samples located < 500 km from the plume center range from 0.7030 to 0.7032, indicating a more radiogenic mantle source than DMM. The transition from enriched $^{87}Sr/^{86}Sr$ ratios to depleted ratios occurs fairly abruptly at ~500 km from the plume source. $^{206}Pb/^{204}Pb$ measurements show a similar spatial pattern, although the transition from enriched values to those consistent with typical DMM (18.275 ± 0.702 Workman and Hart, 2005), occurs somewhat gradually, between ~400 and ~750 km from the plume center.

Taken together, geochemical data from the Iceland region suggests that anomalously hot mantle, with isotopic ratios indicating derivation from an enriched mantle source, extends radially for no more than ~700 km from the plume center. This contrasts with the ~2000 km radius of the swell topography.

To estimate the contribution of excess crustal thickness to the ridge topography we use crustal thickness data from Weir et al. (2001) (see also Smallwood et al., 1995, and Ito, 1999) and crustal thicknesses under Iceland from Kumar et al. (2007) and Jenkins et al. (2018). (This was computed as water-loaded topography using a crustal density of 3000 kg/m^3 and a density of the uppermost asthenosphere of 3200 kg/m^3.) Although topography due to excess crustal thickness reaches ~1500 m near Iceland, it is less than 500 m outside of the ~700 km radius that defines the limit of anomalously hot and enriched mantle.

2.2.3.2 Afar Plume

The Afar plume underlies oceanic and continental lithosphere and is overlain by the young Red Sea and Gulf of Aden oceanic spreading systems (Figure 2.1B) (Ghebreab, 1998; Almalki et al., 2015). The plume is thought to have originated at ~30 Ma (Hofmann et al., 1997), with the initiation of oceanic spreading in the Gulf of Aden at 20 Ma (Leroy et al., 2012) and in the Red Sea at around 13 Ma (Augustin, 2021). Spreading rates around the Afar triple junction are slow to ultra-slow, with the Red Sea opening at rates between 7 mm/yr (north) to 15 mm/yr (south) (ArRajehi et al., 2010) and the Gulf of Aden opening at rates between 16 mm/yr (west) to 24 mm/yr (east) (Jestin et al., 1994). The East African rift, in continental crust, extends at a rate of 6.5 mm/yr in the north to ~2.7 mm/yr at its far southern extent (Stamps et al., 2008).

The location of the plume center (Figure 2.1B) was determined from anomalies in V_S perturbation, using the -2% contour at 135 km depth (Montelli et al., 2004). Because the old continental lithosphere is in proximity to the rift zone, it is significantly thicker than 135 km (Wolbern et al., 2012). Therefore, we also examined S-wave velocity anomalies at 225 km, which yielded essentially the same results.

Bathymetry profiles along the Red Sea and Afar spreading ridges suggest a plume-related swell ~2000 km in radius and 3000 m in maximum elevation (Ryan et al., 2009; Figure 2.2B). Continental regions surrounding the Afar plume appear to have been beveled to near sea level prior to the arrival of the plume, as indicated by the presence of Cretaceous-Paleogene shallow marine sediments on the Arabia-Nubia Shield (Beydoun, 1989; Bojar et al., 2002). This implies that plume-related uplift did not begin until the latest Paleogene (Oligocene) and that the topography on these continental profiles can also be used to estimate swell topography (although some effects of short wavelength rift flank uplift are evident near the plume center,

Figure 2.2B). To permit direct comparison of subaerial profiles with the submarine profiles, we adjusted this "air-loaded topography" to water-loaded topography, multiplying elevations by a factor equal to $\frac{\rho_{mantle}}{\rho_{mantle}-\rho_{water}}$ (see Table 2.1 for values).

Figure 2.2B shows these topographic data plotted relative to an "unperturbed" baseline of sea level for the continental regions and 3500 m depth for the spreading ridges (Le Douaran and Francheteau, 1981). (3000-3500 m depth is approximately the depth of typical segments of slow-spreading ridges.) The oceanic and continental profiles show a similar swell radius and (water-loaded) amplitude and suggest approximately circular symmetry for the swell. Although, a slight radial asymmetry in the swell morphology has been suggested along the eastern Red Sea margin (Chang and Van der Lee, 2011), the swell appears to be generally symmetrical around the plume center. Although, the swell is arguably narrower in an east-west direction than in a north-south direction.

Residual topography for the Afar plume places interesting constraints on the compensation of swell topography at distances greater than 500-700 km from the plume center. With the sub-aerial topography profiles converted to isostatically equivalent water-loaded profiles, similar patterns and magnitudes of residual topography exist on profiles along the mid-ocean spreading ridges and on profiles through old continental lithosphere (Figure 2.2B). This suggests a common mechanism for swell formation lies below the lithosphere, and that this mechanism is largely independent of lithospheric structure, age, and composition. It would be fortuitous that, where the plume underlies the thick continental lithosphere, basal erosion of the lithosphere generates residual topography that is nearly the same as that generated by excess crustal thickness beneath the spreading ridges.

Basalts located within 500 km of the plume center yield average values of T_p equal to ~1450°C (Figure 2.2B). An abrupt transition in T_p occurs at a radial distance of ~500 km from the plume center; beyond this distance the average values of T_p are less than 1350 °C, consistent with average MORB. Likewise, enriched values of $^{87}Sr/^{86}Sr$, relative to DMM, are observed only at distances < 500 km from the plume center. Radiogenic values of $^{206}Pb/^{204}Pb$ are found up to a 700 km radial distance from the plume center.

The geochemical data and topographic observations from the Afar swell present a pattern nearly identical to that observed for Iceland: anomalously hot mantle and more radiogenic $^{87}Sr/^{86}Sr$ and $^{206}Pb/^{204}Pb$ compositions extend for no more than 500-700 km from the plume center. This contrasts with the swell topography, which extends for ~1500 km from the plume center.

2.2.3.3 Azores Plume

The Azores plume is adjacent to the North Atlantic spreading ridge (Figure 2.1C), where the full spreading rate is approximately 30 mm/yr (Muller et al., 2008). Gente et al. (2003) estimate that the Azores plume was initiated by at least 85 Ma and has underlain the Mid-Atlantic ridge for ~30-50 m.y. In Section 2.7, we assume an age of 30 m.y. to place a maximum constraint on the plume flux for the Azores. We determined the component of topography related to plume activity as equivalent to the residual topography of Muller et al. (2008). These data indicate a topographic swell around the plume center with moderate circular symmetry and a radius of ~2000 km. Although the swell radius is similar to that of the Iceland and Afar plumes, the swell amplitude is less than half that of those swells, being at most ~2500 m (Figure 2.1C).

The location of the Azores plume center was determined from the perturbation in V_S at 135 km depth (Montelli et al., 2004), but using a -1% perturbation in S-wave speeds (in comparison to the -2% perturbation used to define the plume center for Iceland and Afar, Figure 2.1C). The smaller magnitude of perturbations in S-wave speed observed over the Azores plume, relative to Iceland and Afar, seem consistent with the smaller amplitude of swell topography and perhaps a smaller flux of plume material into the upper mantle.

The spreading ridge does not pass directly over the plume center, so zero-age basalt compositions for the Azores plume are sparse (Figure 2.1C). To mitigate this lack of data, we analyzed young basalts erupted subaerially on the ocean islands in the Azores. The data show an average T_p of 1450 - 1500 °C at distances < 300 km from the plume center, and an apparently abrupt transition to values of 1300 to 1350 °C beyond 300 km. However, the data is sparser than for the Iceland and Afar plumes, making spatial patterns more difficult to identify with certainty. Virtually all of the samples near the plume center come from the oceanic islands while samples far from the plume center (> 250 km) are derived from sea floor basalts. There are few samples located in between.

Radiogenic $^{87}Sr/^{86}Sr$ compositions, between 0.7035 and 0.7042, are found up to ~350 km from the plume center, with a transition to depleted MORB values at ~500 km from the plume center. Highly elevated $^{206}Pb/^{204}Pb$ ratios above 19.5 are also found on the oceanic islands within 250 km of the plume center. There is a gap in the $^{206}Pb/^{204}Pb$ coverage between 250 and 500 km from the plume center, beyond which $^{206}Pb/^{204}Pb$ values are consistent with typical NMORB (Figure 2.2C). Despite the smaller swell amplitude and limitations in determining the details of the spatial distribution of geochemically anomalous basalts, the Azores plume shows the same basic features as the Iceland and Afar plumes, with a topographic swell extending significantly beyond the much smaller radial extent of the geochemically anomalous basalts.

2.2.4 Common Features for the Iceland, Azores, and Afar Plumes

The Iceland, Afar and Azores plume regions exhibit many of the same characteristics. They have spatially focused regions of slow S-wave speed in the uppermost mantle, which most probably defines a plume conduit and the "plume center." Mantle potential temperatures in basaltic rocks are elevated, by 150°-200°C, only within a radial distance of 300-500 km of the plume centers. Magmas with an enriched signature in both Pb and Sr isotopic systems, interpreted as the involvement of a radiogenic lower mantle source component, are also restricted to a radial distance of approximately 400-700 km from the plume center. These data strongly suggest that anomalously hot, low-density plume material is limited to radial distances less than 400-700 km from the plume center.

If this interpretation is correct, swell topography outside of a 400-700 km radius cannot be supported by low-density plume material. Crustal thickness data for Iceland indicate that, beyond the limit of the plume material, only a small fraction of the swell topography is compensated by excess crustal thicknesses. Although we do not have similar crustal thickness data for the other two plumes, excess crustal thickness along spreading ridges is thought to be correlated with excess melting of anomalously high temperature mantle (White and McKenzie, 1989). Initial estimates of crustal thickness for the Azores archipelago suggest values in the range of 13-16 km (Ferreira et al., 2020). The spreading ridge adjacent to the Azores yields comparable crustal thicknesses to the rest of the Mid-Atlantic ridge (6-7 km, Gente et al., 2003). Based on the data for Iceland and the Azores, crustal thicknesses beneath the oceanic lithosphere outside the region of elevated mantle temperature are unlikely to be anomalously thick.

Taking all of these data together, for all three plumes, we propose that plume material in the upper mantle is limited to a radius of 400-700 km around the plume centers. Outside of this region, we propose that swell topography is dynamically supported. In particular, we propose that the dynamic pressure surrounding the plumes is related to radial flow of upper mantle material away from the plume centers, as is investigated in the following sections.

2.3 Viscous Flow in the Upper Mantle Surrounding Plumes

We investigate whether dynamic pressure related flow can plausibly explain the apparently dynamic topography that exists outside of the region where plume material is present. If this interpretation is correct, then the topography surrounding each plume should be a direct measure of the dynamic pressure needed to drive mantle flow away from the plume centers (at least outside of the region containing plume material). The viability of this hypothesis is examined in the remainder of this paper, where we test if a quantitative model of fluid flow around plumes is consistent with the observations.

Lateral flow within the upper mantle near plumes is assumed to be driven by the upward flux of plume material from the lower mantle into the upper mantle through a localized plume conduit (Sleep, 2006). Plume material, being hotter and less dense than the surrounding asthenosphere (Schilling, 1973), is expected to rise to the base of the overlying lithosphere, forming a "plume pillow" in the upper part of the asthenosphere (Figure 2.3). As the volume of plume-derived material increases, outward radial flow occurs within the plume pillow, beyond the plume pillow within the "normal" depleted asthenosphere, and beneath the plume pillow. Because flow occurs from regions of high pressure to regions of low pressure, high dynamic pressure and high swell topography is expected to develop near the plume center and to decrease with radial distance in a way that is consistent with outward radial flow. Simply defined, the dynamic pressure of a fluid is the component of total pressure due to the movement (or kinetic energy) of the fluid.

Where plume material is present, we expect that a variety of phenomena may contribute to the residual topography, including the low density of the plume material and an anomalously thick oceanic crust. Thus, the best test of our hypothesis lies in examining the swell topography outside of the plume radius, which should reflect the rate of outward flow of mantle material, the thickness of the conduit – or channel – within which mantle flow occurs, and the viscosity structure within the upper mantle.

2.4 A Quantitative Plume Flux Model

To investigate the swell topography resulting from lateral flow of asthenosphere away from the plume center, we construct a radially symmetric flow model using a two-layer Hele-Shaw approximation. Hele-Shaw flow neglects shear stresses and differential normal stresses on vertical planes and assumes a dynamic (viscous) pressure that is invariant with depth (e.g., see Royden and Holt, 2020, for a detailed derivation and application of Hele-Shaw flow to the upper mantle). Hele-Shaw flow provides a good to excellent approximation to the flow of fluid in a thin channel when the horizontal length scales of interest are greater than one-third to one-half of the thickness of the viscous layer and are appropriate for investigating lateral flow in the upper mantle surrounding plumes.

The assumption of radial symmetry is an acceptable approximation for the plumes investigated in this paper because the overriding plates move relatively slowly (~20 mm/yr, Iceland; < 15 mm/yr, Afar, ~20 mm/yr, Azores, ~30 mm/yr) with respect to the plume source so that, as a first approximation, we can set their velocities to zero to maintain the simplicity of radial symmetry. We neglect the sphericity of the Earth, which should have a negligible effect on upper mantle processes over length scales examined here and use cylindrical coordinates with r=0 at the center of the plume source.

We model the sub-lithospheric part of the upper mantle as two channels of infinite horizontal extent. The upper channel, with thickness $c_u(r)$, contains the plume material and initially has zero thickness. The lower channel, with thickness $c_\ell(r)$, consists of "normal" asthenosphere and initially comprises a portion of the sub-lithospheric upper mantle (see Section 2.6 for discussion of initial channel thickness). The channels are assigned different densities and viscosities reflecting the higher temperature of the plume material. The "plume" is initiated and maintained by a radially symmetric flux of low density, low viscosity material from a 100 km wide gaussian source region around the plume center (e.g., Montelli et al., 2004). The plume material is assumed to rise buoyantly through the asthenosphere and is added to the upper (plume) channel through the vertical surface of the cylindrical source region.

A force balance gives the relationship between the dynamic pressure, P, the shear stress on horizontal planes (τ_{rz}), which can then be related to the horizontal flow velocity, v, and channel viscosity, μ:

$$\frac{\partial P}{\partial r} = \frac{\partial \tau_{rz}}{\partial z} \qquad \tau_{rz} = \mu \frac{\partial v}{\partial z} \qquad (2)$$

(For the remainder of this paper, we will use the term "pressure" in the asthenosphere to mean the viscous, or equivalently dynamic, pressure of the fluid flow. This is equivalent to the total pressure minus the lithostatic pressure of a column of “normal”- depleted asthenosphere beneath a spreading oceanic ridge. See Table 2.1 in the main text for a list of variable names.)

If we explicitly include the excess thickness of the crust, c_{ex}, in the calculation, then the pressure within the upper channel, P_u, is related to the swell topography, T, and the excess crustal thickness by:

$$P_u(r) = (\rho_u - \rho_w)gT(r) - c_{ex}g(\rho_u - \rho_{ex}) \tag{3}$$

(If the excess crustal thickness is not included explicitly in the calculation, then c_{ex} is set to zero.)

The pressure within the lower channel, P_ℓ, depends on P_u and on the of the upper (plume) channel:

$$P_\ell(r) = P_u(r) + (\rho_u - \rho_\ell)gc_u(r) \tag{4}$$

Substituting for pressure in eq. (2) and integrating twice, gives an expression for the horizontal velocity of flow in the upper (v_u) and lower (v_ℓ) viscous channels:

$$v_u(z) = \frac{1}{\mu_u}\frac{\partial P_u}{\partial r}\left(\frac{z^2}{2}\right) + A_u z \tag{5a}$$

$$v_\ell(z) = \frac{1}{\mu_\ell}\frac{\partial P_\ell}{\partial r}\left[\frac{(z - c_\ell)^2}{2}\right] + A_\ell(z - c_\ell) \tag{5b}$$

where z is measured downwards from the upper surface of each layer, the horizontal velocity is set to zero at the top of the upper layer and the bottom of the lower layer and A_u and A_ℓ are constants that are derived by setting the horizontal velocity and shear stress equal at the interface between the upper and lower channels (see Appendix A1.1).

We assume that all of the plume material remains in the upper channel and that the volume of plume material in the upper channel increases at the rate at which it enters from the cylindrical plume source. Similarly, all the mantle material in the lower channel remains in the channel and the volume of the lower channel remains constant through time. We further assume that the mantle beneath the channel is of sufficiently high viscosity that its horizontal velocity at the base of the channel is small relative to the average channel velocity and can be treated as zero (see Figure A1.2).

The time derivatives of the channel thicknesses are found by integrating the velocity from top to bottom of each channel to obtain the horizontal flux of material in the channel, and taking the divergence of the horizontal flux:

$$\frac{\partial c_u}{\partial t} = -\frac{1}{r}\frac{\partial}{\partial r}\left(\int_0^{c_u} v(z)\,dz\right) \qquad \frac{\partial c_\ell}{\partial t} = -\frac{1}{r}\frac{\partial}{\partial r}\left(\int_0^{c_\ell} v(z)\,dz\right) \tag{6}$$

Finally, we need a relationship between channel thickening and topography. For example, if the rate at which the base of the lower channel moves downward is zero, the rate at which topography is created will be equal to the rate of channel thickening. Stream function analysis (Appendix A1.2) shows that the rate at which the base of the channel moves downward is wavelength (and viscosity) dependent and, at a set wavelength, is proportional to the dynamic pressure at the base of the channel. In the Appendix (A1.2) we show that, at wavelengths comparable to that of the swell topography, the ratio between dynamic pressure and the (downward) vertical velocity at the base of the channel is expected to be in the vicinity of 10^{-18} m s^{-1} Pa^{-1}. We denote this ratio as $f = v_z/P_\ell$, where v_z is the vertical velocity of the interface between the lower channel and the underlying mantle and f is a parameter with units of m $Pa^{-1}s^{-1}$. The vertical velocity at the base of the channel is equal to the rate of thickening of the channels minus the rate of change of the topography, or:

$$fP_\ell = \frac{\partial c_u}{\partial t} + \frac{\partial c_\ell}{\partial t} - \frac{\partial T}{\partial t} \tag{7}$$

Because the value of f depends on a number of somewhat poorly determined factors, including the viscosity structure of the lower mantle, in fitting our observed topography profiles we make no assumptions about the value of f *a priori*, but instead test a range of values. (In the results section, we find that values of f between 0 and 10^{-18} m s^{-1} Pa^{-1} yield acceptable fits to the observed topography around, in reasonable agreement with the results of the stream function analysis.)

Details of the mathematical derivation and code for implementation in MATLAB are included in the Appendix (A1.1).

2.5 Fundamental Behavior of Plume Model

In this section we illustrate how model swell topography varies depending on the parameters assumed to govern mantle flow. This is intended to give the reader an understanding of how each parameter may affect the results for individual plumes (Section 2.7). We illustrate this by varying key parameters relative to those that we found produce a good fit for the Iceland swell. All results are shown for a lower channel with an initial thickness of 30 km and a normal upper mantle viscosity of $7 \cdot 10^{19}$ Pa s. (In the next section we demonstrate why a only very thin, low viscosity zone provides for stresses that are consistent with a wide range of constraints on upper mantle viscosity.) We use a cylindrical plume conduit with a 100 km radius.

Figure 2.4 demonstrates how model topography changes with increasing time and constant plume flux, using parameters that correspond to one of the fits to observed topography in Iceland, with $f = 0$ (see Table 2.2). After initiation of the plume, the swell topography attains close to its maximum amplitude adjacent to the plume pillow by 5 m.y., with only minor changes in maximum swell height thereafter. With time, the radius of the plume pillow and the topographic swell beyond the plume pillow grow. The thickness of the plume pillow also achieves near maximum thickness very quickly, thereafter accomodating the increase in volume mainly by an increase in radius.

Figure 2.5 illustrates how results at 30 m.y. depend on various individual parameters. Varying the viscosity of the plume material (upper channel) while holding the other variables constant has little effect on the swell topography beyond the plume pillow (Figure 2.5A). Instead, varying the plume viscosity primarily affects the radial extent and thickness of the plume material (Figure 2.5A). Therefore, in fitting observations around the plumes examined in this study, the plume viscosity is largely constrained by radial extent of plume material (at ~400-700 km) as indicated by the geochemical data.

The viscosity of the upper mantle (within the lower channel) is critical to the size and topographic gradient of the plume swell, having a relatively minor impact on the radial extent of the plume material (Figure 2.5B). Reducing the viscosity of the material in the lower channel allows it to flow faster at lower pressure gradients, producing a flatter wider swell. (Because the plume flux is the same in all cases in Figure 2.5B, the integrals of the topographic elevation over the area of the swell must be the same for all cases. But, because we show radial profiles, this is not readily apparent over the line of the section.)

Varying the plume flux has a significant effect on the maximum height and radius of the topographic swell (Figure 2.5C). It not only changes the volume of the plume pillow but, because the pressure gradients associated with flow in the upper mantle change linearly with horizontal flux of material in the mantle, it also changes the topographic gradients beyond the plume pillow.

Figure 2.5D shows the effect on topography when the vertical velocity at the base of the channel is linearly dependent on dynamic pressure (as defined by the parameter f in eq. 7) with all other parameters held constant. As the ratio between (downward) vertical velocity and dynamic pressure increases from zero, the radius and amplitude of the swell topography are reduced. This occurs because the base of the channel increases in depth and the overlying topography decreases. This reduces the radial pressure gradient that drives outward flow in the channel, so that the radius of the swell is also reduced. In contrast, the radius and thickness of the plume pillow are not greatly affected.

2.6 Constraints on the Viscosity and Thickness of the Lower Channel

Quantitative modeling of mantle flux away from upwelling plumes has the potential to better constrain upper mantle viscosity structure beneath young oceanic lithosphere. This opportunity exists because the scaling relations between thickness and viscosity differ between pressure-driven flow in a channel (as in this paper) and shear stress across a layer undergoing predominantly simple shear.

From eqn. (2), simple channel flow within a layer of thickness c and uniform viscosity μ (and zero velocity at the top and base of the layer, with f=0) provides a net lateral flux that scales with the channel thickness cubed (additional background in Appendix A1.3):

$$\int_0^h v(z)\ dz = -\frac{1}{12}\frac{\partial P}{\partial r}\left(\frac{c^3}{\mu}\right) \tag{8}$$

Although the viscosity model that we employ is more complex, having upper and lower viscous layers and thicknesses that change laterally and with time, the scaling relations are similar. Figure 2.6 shows sample results for model configurations that provide a "best" fit to the observed swell topography after 30 m.y. and that are consistent with the observed radius of Iceland plume material (400-700 km). (A more complete discussion and analysis of results is given in the next section with results.)

With all parameters held fixed except for the initial thickness and viscosity of the lower layer (Table 2.2), the resulting swell topography and plume radii are virtually identical for all three configurations despite more than an order of magnitude change in the initial thickness of the lower channel (from 30 to 400 km) and more than three orders of magnitude change in the lower channel viscosity (from $7 \cdot 10^{19}$ to $1.5 \cdot 10^{23}$ Pa s). However, Table 2.2 shows that the ratio of viscosity to initial channel thickness cubed is virtually identical for all three configurations, consistent with the scaling in eq. (8). Thus, equivalent results for swell topography and plume radius can be obtained for nearly any initial thickness of the lower channel provided that this scaling relation remains constant.

In contrast, the ratio of viscosity to the initial thickness of the lower channel changes by approximately two orders of magnitude, from ~2×10^{15} to ~3.8×10^{17} Pa s m^{-1}. This ratio is important because the primary published constraints on upper mantle viscosity are based, directly or indirectly, on estimates of the shear stresses acting on the base of the plates and are largely determined from plate velocities incorporated into models of plate motion, subduction, and mantle convection (Hager and O'Connell, 1979; Richards et al., 2001; Podolefsky et al., 2004; Becker, 2006; Conrad and Behn, 2010). If one considers that the layer over which most of the shear takes place between the plates and the deeper mantle to be of thickness c and viscosity μ, then the scaling relation for shear stress across this layer is:

$$\tau_{rz} = \Delta v \left(\frac{\mu}{c}\right) \qquad (9)$$

where τ_{rz} is shear stress and Δv is the difference in velocity across the layer.

Many studies, over a wide range of disciplines (e.g. Mitrovica and Forte, 2004: Conrad and Lithgow-Bertelloni; 2006; Holt and Becker, 2016; Behr et al., 2022), have concluded that the upper mantle has a viscosity structure consistent with (μ/c) in the vicinity of 10^{15} Pa s m $^{-1}$ (for example a viscosity of $5 \cdot 10^{20}$ Pa s over a layer thickness of 400 km yields a ratio of $1.2 \cdot 10^{15}$ Pa s m $^{-1}$). Therefore, deformation accommodated largely within a thin (tens of kilometers) low viscosity (10^{19}-10^{20} Pa s) layer is the mechanism that satisfies the shear stress constraints on the base of the plates and the observed swell topography due to lateral flux of mantle material. The implications of this are explored further in the discussion section. And, for the remainder of this paper, we consider only flux in a thin (30 km) channel located beneath the (young) oceanic lithosphere.

2.7 Results

The model described in Sections 2.3 and 2.4 was applied to the Iceland, Afar, and Azores plumes using an initial lower channel thickness of 30 km as per Section 2.6. We are mainly interested in fitting swell topography outside of the plume radius (> 400-700 km from the plume center), and simultaneously satisfying the geochemical constraints on the radius of the plume material. We focus on topography beyond the plume pillow because, above the plume pillow, a variety of factors may affect the swell topography, most notably elevated melting temperatures within the plume mantle producing anomalously thick and/or exhibit highly variable crustal thickness (Allen et al., 2002; Kumar et al., 2007). In addition, other processes related to localized buoyant upwelling of plume material may affect the topography over the plume itself.

For the Iceland plume we are able to test the influence of excess crustal thickness on the swell topography because there exist comprehensive measurements of crustal thickness along the Reykjanes ridge (e.g., Weir et al., 2001) that can be incorporated explicitly into eq. 3, showing that there is little qualitative difference in the results (Figure 2.7A). For the other plumes we lack comprehensive crustal thickness measurements and ignore the effects of excess crustal thickness on topography.

We use the ages of plume initiation from Section 2.2 (Table 2.1) but note that identical results to those shown can be obtained by trade-offs in time, viscosity, and plume flux (as is readily shown by non-dimensionalizing all variables). For example, doubling the age of onset of plume activity, increasing the viscosity of plume and "normal" mantle by a factor of two, and halving the plume flux, while leaving all other parameters the same, result in no change to the model results.

Model results that provide acceptable fits to the topographic and geochemical data around Iceland are shown in Figure 2.7A, and the associated flux and viscosities for each model are given in Table 2.3. When the ratio between vertical velocity at the base of the lower channel and dynamic pressure within the channel is zero (f = 0 in eq.7), corresponding to zero velocity at the base of the lower channel, a low plume flux is needed to match the swell topography, severely limiting the volume of plume material entering the channel system. And, in order to reach the minimum plume radius of 400-500 km as required by the geochemical data, the model plume viscosity must be extremely low ($<10^{18}$ Pa·s) resulting in a very thin plume pillow ~20 km thick.

Through trial-and-error, we explore various values of f, finding that values of f up to $\sim 10^{-18}$ m·(Pa^{-1}·s^{-1}) can produce reasonable fits to the observed topography and to the observed radius of the plume pillow. This upper bound on f is broadly consistent with the results of the stream function analysis for whole mantle flow as derived in the Appendix 1 (A1.2). For values of f larger than this, the radius of the plume pillow becomes significantly larger than the observational limit. This occurs because downward motion at the base of the lower channel reduces the model topography, therefore a correspondingly larger plume flux is needed to match the observed swell topography. In turn, greater plume flux produces a thicker, more laterally extensive plume pillow, even when the plume viscosity is increased to be the same as the underlying normal mantle. A value of $f = 5\cdot10^{-19}$ m·(Pa^{-1}·s^{-1}) provides our preferred model results for the Iceland plume. This can result in a plume pillow that is over a hundred kilometers thick with a lower (normal mantle) channel viscosity of $4\cdot10^{-19}$ Pa·s and a plume viscosity of $1\cdot10^{-19}$ Pa·s.

When we account for observed crustal thickness variations along the Reykjanes ridge in our quantitative model, we obtain nearly identical results to the model in which crustal thickness is not included (Figure 2.7A, Table 2.3), the main difference being a better fit to the observed swell topography above the plume pillow. With or without inclusion of the excess crustal thickness, the model plume fluxes are similar although the viscosity of the plume material increases by a factor of three. Ultimately, the similarity of the Iceland models including and lacking crustal thickness in the computation leads us to conclude that crustal thickness does not significantly affect the model topography beyond the plume pillow.

The results between Iceland and Afar and the Azores are relatively consistent both in terms of the extent of the geochemical data presented in Figure 2 and in the results of our quantitative modelling of upper mantle flow (Figure 2.7, Table 2.3). The plume material viscosity is exactly the same in the $f = 0$ case for Iceland and Afar (10^{17} Pa·s). This reflects the need for extremely low viscosities to ensure consistency with the plume pillow extent as determined by the geochemical data (Figure 2.2).

For Afar, we find that $f = 5\cdot10^{-19}$ or 10^{-18} m·(Pa^{-1}·s^{-1}) is consistent with the observed swell topography (Figure 2.7B). These values of f result in ambient upper mantle viscosities ~$3\cdot10^{19}$ Pa·s. The Azores is also best fit by a model with $f = 5\cdot10^{-19}$ m·(Pa^{-1}·s^{-1}) (Figure 2.7c), yielding an ambient upper mantle viscosity of $2\cdot10^{19}$ Pa·s, which is in line with the Iceland and Afar mantle viscosity estimates.

Given the best fit values of f discussed for the three plumes above, we note the Iceland is characterized by the highest plume flux ($3\cdot10^{6}$ km^3/m.y.) and an upper mantle viscosity of $4\cdot10^{19}$ Pa·s. The volume flux for Afar is equal to slightly less than that of Iceland (2-3 10^{6} km^3/m.y.) with an upper mantle viscosity slightly less than Iceland (2-$3\cdot10^{19}$ Pa·s). The Azores plume has a volume flux that is slightly lower than the other two plumes (1.8 10^{6} km^3/m.y.).

2.8 Discussion and Implications

The model for upper mantle plume flow developed in this paper provides a conceptual and quantitative framework that can explain the apparent mismatch between the lateral extent of topographic swells and the geochemical anomalies associated with plume material in the upper mantle. Our results suggest an answer to long standing controversy over thermal versus dynamic compensation within the upper mantle (Courtney and White, 1986; Monnereau and Cazenave, 1990; Sleep, 1990; Marks and Sandwell, 1991; Canales et al., 2002), hinging on new constraints provided by geochemical data. Moreover, we present new constraints on the shallow viscosity structure of the upper mantle in support of a thin tens of kilometers), low-viscosity (~10^{19} Pa·s) zone directly beneath the oceanic lithosphere, underlain by a thick, relatively strong (>10^{22} Pa·s) upper mantle.

2.8.1 Compensation Mechanism of Swell Topography

The absence of geochemical indicators of plume material at distances greater than 400-700 km necessitates an alternative mechanism for swell compensation beyond this point. We find that models of the dynamic pressure associated with the outward flowing plume material are able to reproduce the magnitude, extent, and topographic gradient of the outer plume swell (Figure 2.7). Our new constraints on the extent of hot, buoyant plume material from major element geochemical modelling suggest that thermal compensation of the Iceland, Afar, and Azores mantle plumes should be limited to within 400-700 km of the plume center (Figure 2.2). Our model results further suggest that above the plume pillow, excess crustal thickness in the young oceanic lithosphere accounts for additional swell topography (i.e., Ito et al., 1999; Canales et al., 2002) with relatively little contribution from the relatively low-density plume material.

Although we generally neglected the contribution of excess oceanic crustal thickness in our models, inclusion of crustal thickness in models of the Iceland swell yields similar model values of volume flux, ambient upper mantle viscosity, and plume viscosity. It also produced a nearly identical fit to the swell topography outside of the plume radius and a better fit to the swell topography inside the plume radius (Figure 2.7A). This suggests that while crustal thickness variations support some of the swell topography variations above the plume pillow, they exert a negligible effect on the swell topography beyond the plume pillow, at > 400-700 km.

Our estimates of plume flux are in broad agreement with previous estimates. Previous studies have inferred plume fluxes ranging from 10^5 to 10^7 km^3/m.y. (Griffiths and Campbell, 1990; Sleep, 1990; Schilling, 1991; Albers and Christensen, 2001). For a direct comparison to past literature, we convert our modelled volume fluxes to buoyancy flux using the well-established formula, $B = \Delta\rho V_{flux}$ (Sleep, 1990; King and Adam, 2014; Hoggard et al., 2020). For the best fit models of the three plumes, we obtain buoyancy fluxes of ~800-1500 kg s^{-1} . These are somewhat less, but in the same general range, as previous literature estimates. For example, Sleep (1990) estimated 1400, 1200, and 1100 kg s^{-1} (for Iceland, Afar, and the Azores, respectively). The more recent study of King and Adam (2014) estimated fluxes for these three plumes of 1500, 2100, and 400 Mg s^{-1} while Hoggard et al. (2020) estimate fluxes of 4100, 3300, and 800 Mg s^{-1}.

2.8.2 Upper Mantle Viscosity Structure

A variety of interdisciplinary studies have produced evidence favoring the presence of a thin low viscosity layer immediately underlying oceanic lithosphere (e.g., Hager and O'Connell, 1979; Podolefsky et al., 2004; Bagley and Revenaugh, 2008; Stein and Hansen, 2008; Barnhoorn et al., 2011; Schmerr, 2012; Naif et al., 2013; Becker, 2017; Rychert et al., 2020; Selway et al., 2020; Hua et al., 2023). Our study has the potential to further constrain the thickness and viscosity of this layer because lateral flux of material within a channel has a different scaling of viscosity to thickness than do the shear stress constraints normally used to determine the viscosity of the upper mantle.

In particular, the lateral pressure gradient that drives flux in a channel scales as viscosity divided by layer thickness cubed (Figure 2.6 and Table 2.2). In contrast, the shear stress across a layer undergoing primarily simple shear scales as viscosity divided by layer thickness. In order to satisfy the constraints on upper mantle viscosity from studies of plate motion and mantle convection (i.e., Hager and O'Connell, 1979; Stein and Hansen, 2012), and to satisfy the constraints on upper mantle viscosity from this study of swell topography, we suggest that this thin, low viscosity layer should be several tens of kilometers in thickness and have a viscosity as low as 10^{19} Pa·s. This provides a new constraint on the viscosity and thickness of a low viscosity layer directly beneath the oceanic lithosphere as has been suggested by previous studies (\ Bagley and Revenaugh, 2008; Schmerr, 2012; Naif et al., 2013; Becker, 2017; Rychert et al., 2020; Selway et al., 2020). In addition, our study suggests viscosities in the range of $5 \cdot 10^{18}$-10^{19} Pa·s the for hot plume material. This is within the expected range for dry to damp enriched mantle (Hirth and Kohlstedt, 2003; Dixon et al., 2004).

The work outlined here provides a first test of lateral flow in the asthenospheric as a dominant compensation mechanism for swell topography but neglects a number of other factors, including the motion of the overlying plates. Future work that applies a similar approach to plumes located beneath intermediate to fast moving oceanic lithosphere will help to better constrain plume dynamics and the compensation of swell topography on a global basis.

2.9 Conclusion

We have presented a comprehensive exploration of upper mantle plume flow with implications for the mode of swell compensation and the viscosity structure of the uppermost mantle asthenosphere. Through new geochemical constraints on mantle potential temperature, in concert with existing topographic and geochemical data around plume swells we have constrained the limit of plume material to ~500-700 km radial distance from the plume centers of Iceland, Afar, and the Azores. While thermal compensation and crustal thickness variations play a role in determining topographic variations directly above the plume pillow, they cannot explain the high magnitudes of residual topography beyond the extent of the hot, buoyant plume material. We present a quantitative model for upper mantle flow around a cylindrical plume conduit, which suggests dynamic pressure from fluid flow in the upper mantle is the primary mechanism responsible for excess residual topography at distances exceeding ~700 km from the plume centers. Our new model supports the existence of a thin (<50 km) low viscosity (~10^{19} Pa·s) layer directly beneath the oceanic lithosphere, ruling out thicker (100-400 km) higher viscosity channels on the basis of existing shear stress constraints on the lithosphere-asthenosphere boundary. In summary, our new model explains the observed discrepancy between the extent of geochemical anomalies versus topographic/bathymetric swells around mantle plumes. We suggest that dynamic pressure from asthenospheric flow away from the upwelling plume conduit is the dominant compensation mechanism for plume swell topography, with a thin, low viscosity channel required directly below the lithosphere.

Figures and Captions

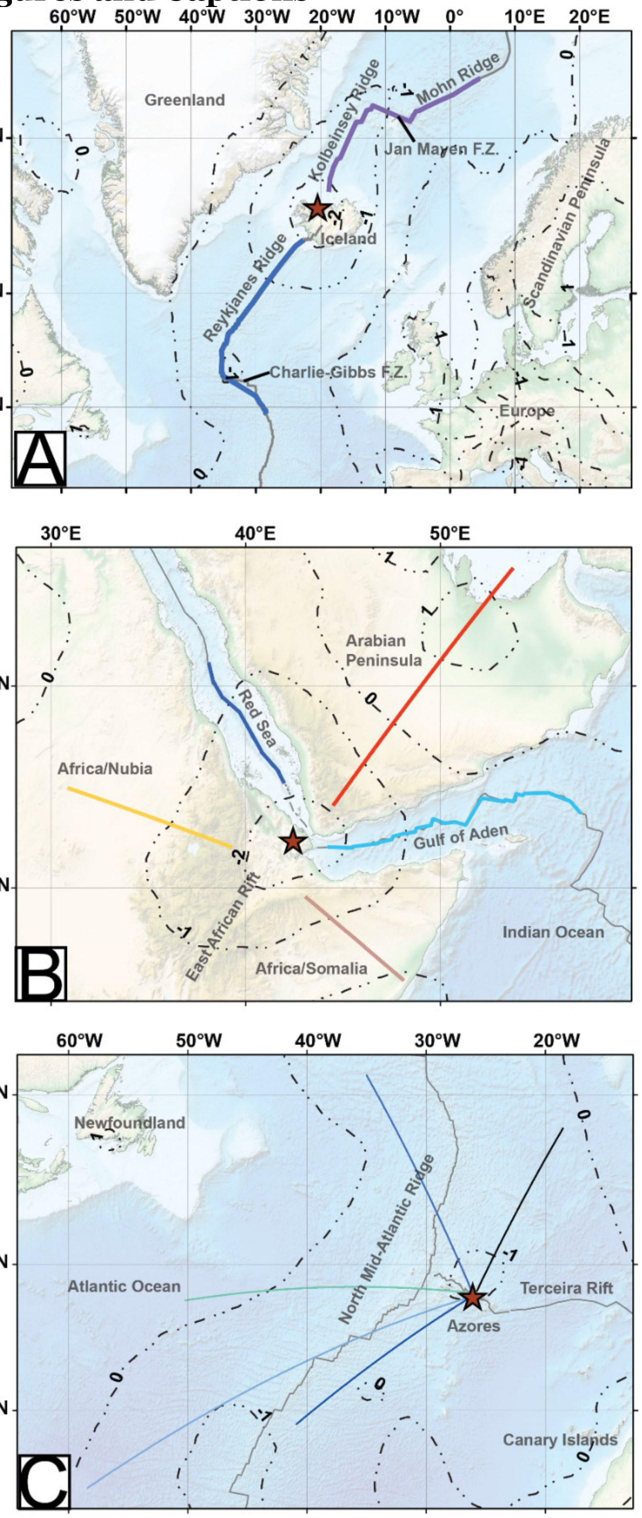

Figure 2.1: Regional maps of bathymetry and topography for Iceland (A), Afar (B), and the Azores (C) with contours of seismic s-wave perturbations ($\delta V_S/V_S$%) at 135 km depth (Montelli et al., 2004). The estimated plume center is shown as a red star and the locations of topographic profiles are

shown as colored lines corresponding to the profiles shown in Figures 2 and 6. Thick gray lines represent plate boundaries.

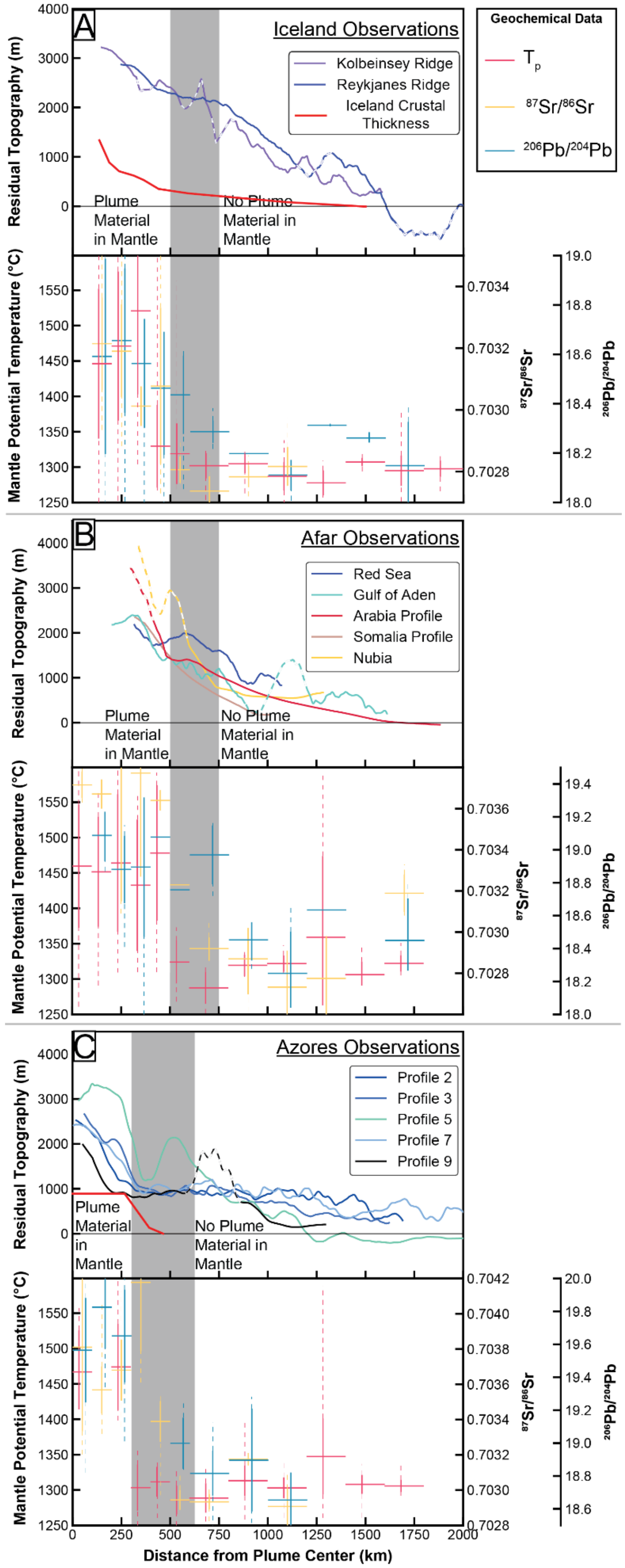
A
Iceland Observations
Kolbeinsey Ridge
Reykjanes Ridge
Iceland Crustal Thickness
Plume Material in Mantle
No Plume Material in Mantle
Geochemical Data
T_p
87Sr/86Sr
206Pb/204Pb
B
Afar Observations
Red Sea
Gulf of Aden
Arabia Profile
Somalia Profile
Nubia
C
Azores Observations
Profile 2
Profile 3
Profile 5
Profile 7
Profile 9
Residual Topography (m)
Mantle Potential Temperature (°C)
87Sr/86Sr
206Pb/204Pb
Distance from Plume Center (km)

Figure 2.2: Residual topography profiles (top), and mantle potential temperature, Pb and Sr isotope data (bottom) plotted as a function of distance from the plume center for (A) Iceland, (B) Afar, and (C) Azores. Panel A also shows contribution to residual topography from observations of crustal thickness south of Iceland (data from Smallwood et al.,1995 and Weir et al., 2001). Topographic profiles (colors corresponding to profile locations in Figure 1) are dashed across fracture zones and continental. Geochemical data (mantle potential temperature, T_p, Sr isotopes, and Pb isotopes show average value (horizontal bars), standard deviation (solid vertical bars) and total range of data (dashed vertical bars) within bins; with the radial extent of each bin shown by the width of the horizontal bars.

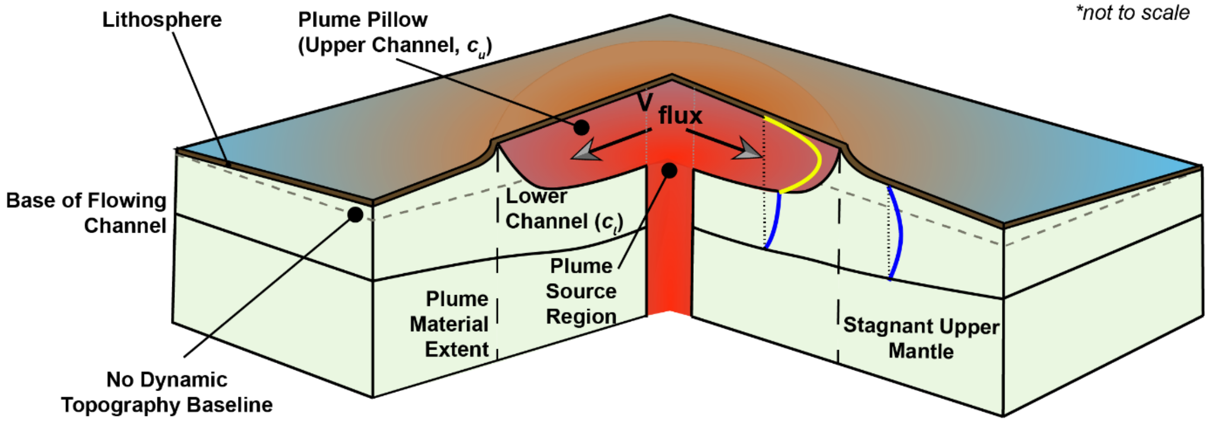

Figure 2.3: Schematic figure of plume flow as used in modeling. Blue lines display the velocity profile of non-plume upper mantle; yellow line displays the velocity of the plume material. Vertical displacement of the lithosphere and base asthenosphere is shown relative to the case of no dynamic topography baseline.

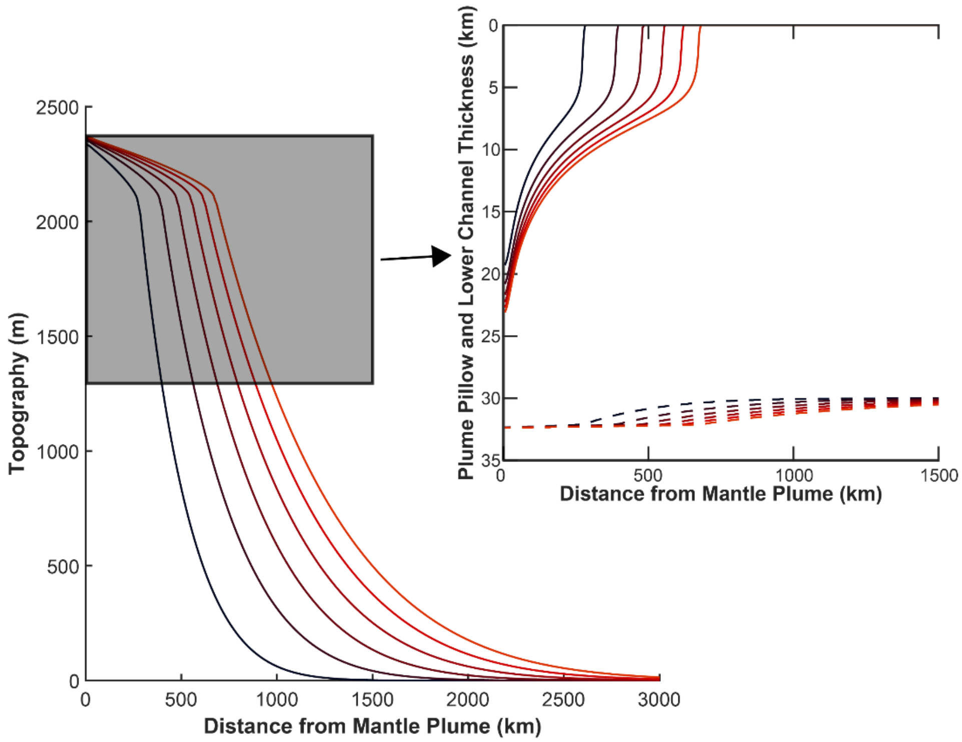

Figure 2.4: Evolution of model topography and channel thickness (upper channel/plume pillow (solid) and total channel thickness, c_u+c_ℓ (dashed)) through time, from 5 to 30 m.y., where each line represents a 5 m.y. interval. Parameters used are for Iceland with zero vertical velocity at the base of the lower channel, or f = 0 (see Table 2.3 for parameters).

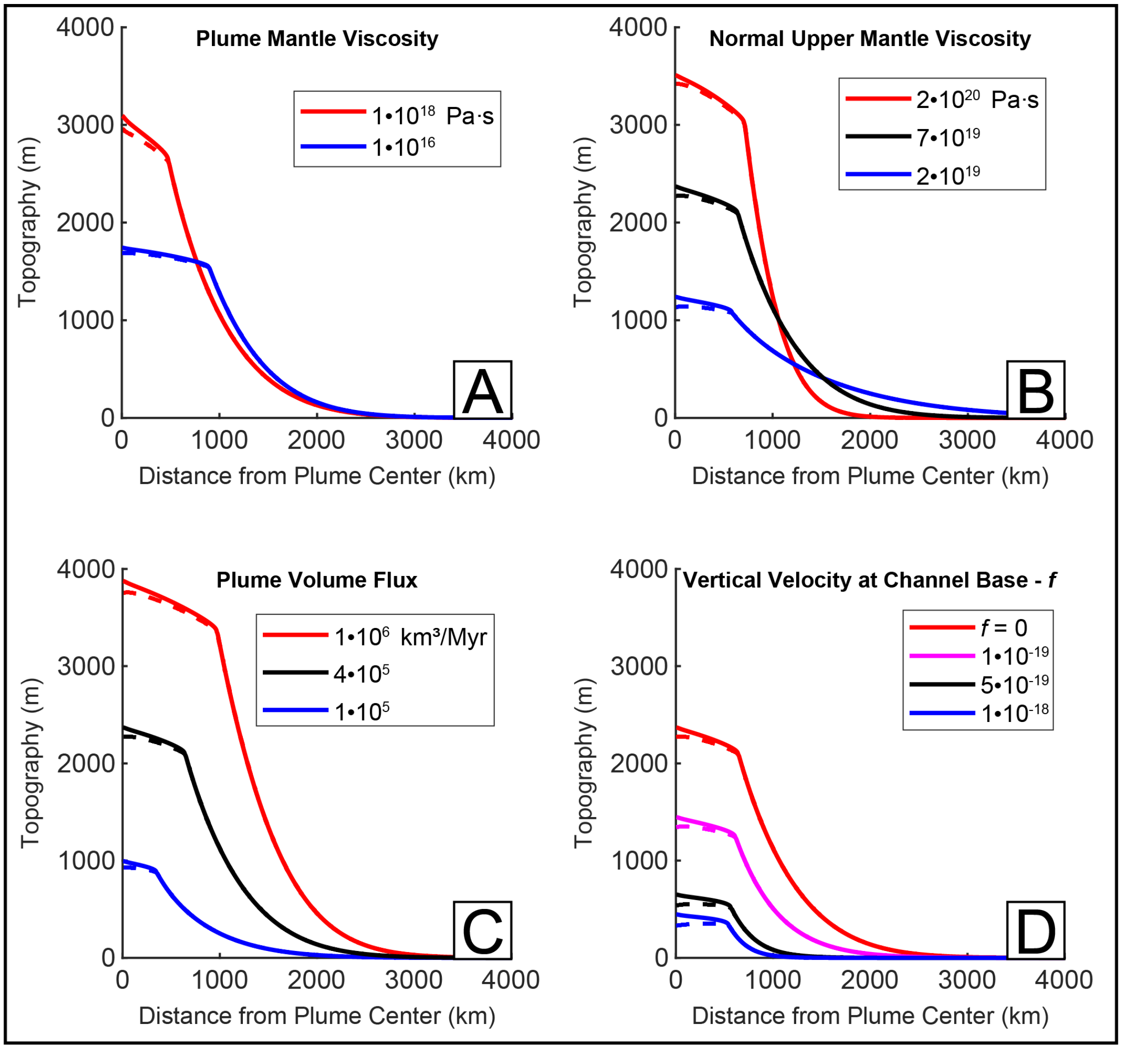

Figure 2.5: Plots showing the sensitivity of model results to chosen parameters for an initial lower channel thickness of 30 km. Solid lines show total topography. Above the plume the dashed line shows the component of topography due to the increased pressure of mantle flow with the difference being due to the low density of the plume material. (A) plume (upper channel) viscosity, (B) normal upper mantle (lower channel) viscosity, (C) plume volume flux, (D) vertical velocity at base of the lower channel (f = vertical velocity divided by dynamic pressure in the lower layer, in units of $m\ s^{-1}\ Pa^{-1}$).

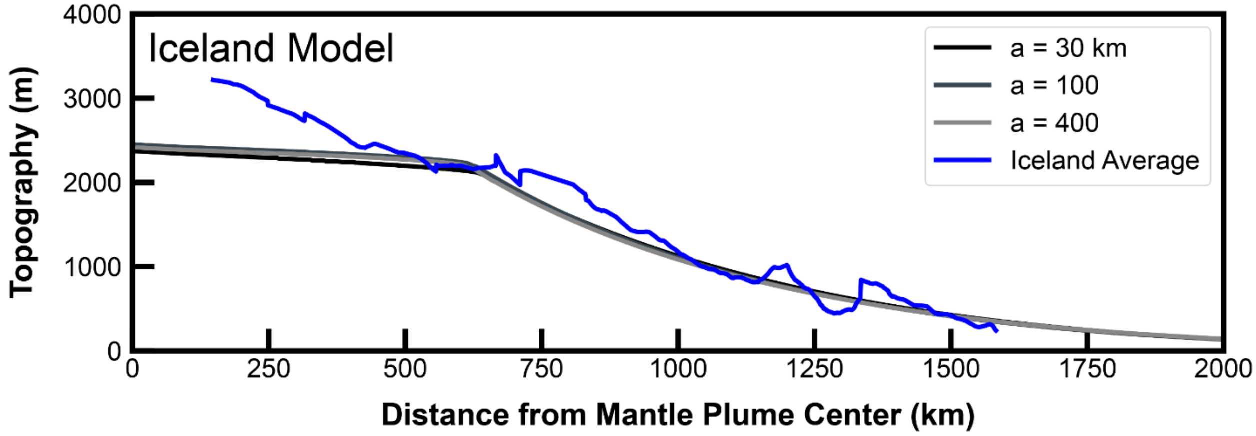

Figure 2.6: Model results for variable channel thicknesses a = 30 (μ_ℓ =$7{\cdot}10^{19}$ Pa·s), 100 ($2.5{\cdot}10^{21}$ Pa·s), and 400 km ($1.5{\cdot}10^{23}$ Pa·s) compared to the averaged mid-ocean ridge topography at Iceland. Corresponding parameters for these models are given in Table 2.2. For all runs, V_{flux}=$4{\cdot}10^5$ km^3/m.y., μ_u=10^{17} Pa s, and f=0, c_{ex}=0.

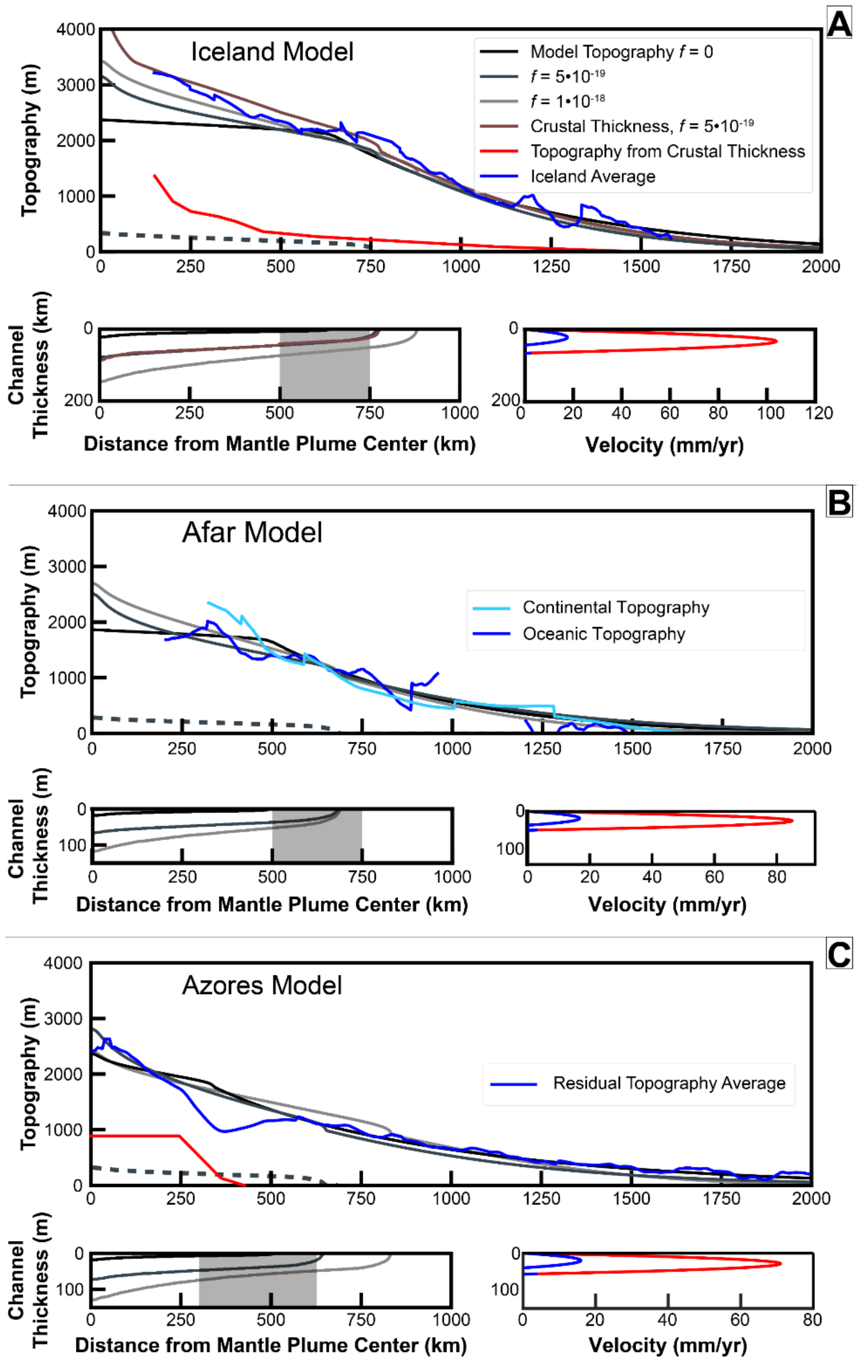

Figure 2.7: Model results for residual topography (gray scale) and observed topographic profiles for Iceland (A), Afar (B), and the Azores (C). Solid lines on the top panel of A, B, and C show the total model topography. The dashed line displays the contribution to topography from the isostatic compensation of low density plume material in the plume pillow for the $f = 5{\cdot}10^{-19}$ m·(Pa^{-1}·s^{-1}). Colored lines show observed topography around the plume swell as described in Section 2.2. Solid grayscale lines on the bottom panels represent channel thicknesses corresponding to the model topography in the top panel. The bottom right panels display the velocity-depth structure of the model at 100 km radius and at the outer limit of the model plume pillow for $f = 5{\cdot}10^{-19}$ m·(Pa^{-1}·s^{-1}).

Tables

Variable	Definition	Value	Units
P	Dynamic (viscous) pressure		Pa
T	Topography		m
$\Delta Temp$	Difference in temperature between channel and upper mantle	200	K
r	Radial distance from plume center		m
Δr	Lateral grid spacing for model	1-10	km
g	Gravitational acceleration	9.81	m/s^2
z	Depth from top of each layer		m
a	Initial channel thickness	30, 100, or 400	km
c_{ex}	Excess crustal thickness		m
c_u	Thickness of upper channel (plume pillow)		m
c_ℓ	Thickness of lower channel ("normal" mantle)		m
μ_u	Viscosity of mantle plume material		Pa·s
μ_ℓ	Viscosity of normal upper mantle		Pa·s
ρ_{ex}	Crustal density		kg/m^3
ρ_u	Density of upper channel material		kg/m^3
ρ_ℓ	Density of the asthenosphere	3200	kg/m^3
$\Delta\rho$	Density contrast between plume channel and upper mantle	$\Delta Temp{*}\rho_\ell{*}\alpha$	kg/m^3
ρ_w	Density of water	1000	kg/m^3
t_f	Duration of model	27 (Iceland) 28 (Afar) 30 (Azores)	m.y. m.y. m.y.
α	Coefficient of thermal expansion	$2 \cdot 10^{-5}$	K^{-1}
V_{flux}	Volume flux of plume material		km^3/Myr
f	Vertical velocity at the base of channel		$m\ s^{-1}\ Pa^{-1}$

Table 2.1: Variables used in quantitative mantle flow model.

Initial c_ℓ km	μ_ℓ (Pa·s)	μ_ℓ / c_ℓ^3 (Pa·s·m^{-3})	μ_ℓ / c_ℓ (Pa·s·m^{-1})
400	$1.5 \cdot 10^{23}$	2.3×10^6	3.8×10^{17}
100	$2.5 \cdot 10^{21}$	2.5×10^6	2.5×10^{16}
30	$7.00 \cdot 10^{19}$	2.6×10^6	2.3×10^{15}

Table 2.2: Initial thickness and viscosity of lower channel for sample Iceland results shown in Figure 6. For all runs, $V_{flux}=4 \cdot 10^5$ km³/m.y., $\mu_u=10^{17}$ Pa s, and $f=0$, $c_{ex}=0$.

	f (m·(Pa^{-1}·s^{-1}))	V_{flux} (km^3/m.y.)	μ_u (Pa·s)	μ_l (Pa·s)
Iceland	0.0	$4 \cdot 10^5$	$1 \cdot 10^{17}$	$7 \cdot 10^{19}$
	$5 \cdot 10^{-19}$	$3 \cdot 10^6$	$1 \cdot 10^{19}$	$4 \cdot 10^{19}$
	$1 \cdot 10^{-18}$	$6 \cdot 10^6$	$3 \cdot 10^{19}$	$3 \cdot 10^{19}$
Crustal	$5 \cdot 10^{-19}$	$3 \cdot 10^6$	$3 \cdot 10^{19}$	$3 \cdot 10^{19}$

Thickness Included				
Afar	0.0 $5 \cdot 10^{-19}$ $1 \cdot 10^{-18}$	$2 \cdot 10^{5}$ $2 \cdot 10^{6}$ $3 \cdot 10^{6}$	$1 \cdot 10^{17}$ $1 \cdot 10^{19}$ $3 \cdot 10^{19}$	$1 \cdot 10^{20}$ $2 \cdot 10^{19}$ $3 \cdot 10^{19}$
Azores	0.0 $5 \cdot 10^{-19}$ $1 \cdot 10^{-18}$	$2.5 \cdot 10^{5}$ $1.8 \cdot 10^{6}$ $4 \cdot 10^{6}$	$5 \cdot 10^{18}$ $1.8 \cdot 10^{19}$ $1.8 \cdot 10^{19}$	$5 \cdot 10^{19}$ $2 \cdot 10^{19}$ $2 \cdot 10^{19}$

Table 2.3: Parameter values for model results shown in Figure 7.

Open Research

The geochemical and topographic data for Figures 2.2 and 2.6 and discussed in the text are available at the Harvard Dataverse via https://doi.org/10.7910/DVN/HPYYYO. The repository also contains a MATLAB function and script for the quantitative plume model described in the text.

(Agranier et al., 2005)(Al Kwatli et al., 2012)(Andres et al., 2004)(Antonini et al., 1998)(Arevalo et al., 2008)(Arevalo et al., 2009)(Ashchepkov et al., 2010)(Aumento, 1968)(Aumento et al., 1977)(Ayalew et al., 2016)(Baragar et al., 1968)(Barberi et al., 1971)(Barberi et al., 1980)(Barberi et al., 1975)(Barberi et al., 1974)(Barrat et al., 1998)(Barrat et al., 1993)(Barrat et al., 2003)(Barry et al., 2014)(Beier et al., 2008)(Beier et al., 2006)(Beier et al., 2012)(Beier et al., 2007)(Bézos et al., 2005)(Bizouard et al., 1980)(Blichert-Toft et al., 2005)(Bougault et al., 1979)(Bougault et al., 1988)(Bourdon et al., 2000)(Bourdon et al., 1996)(Brandl et al., 2015)(Brandl et al., 2013)(Brandon et al., 2007)(Breddam et al., 2000)(Bryan et al., 1979)(Bryan et al., 1981)(Bryan et al., 1979)(Burnard, 1999)(Burnard et al., 2003)(Cann, 1970)(Carlson et al., 1978)(Cartigny et al., 2008)(Charlier et al., 2013)(Chase, 1969)(Chaussidon and Jambon, 1994)(Chaussidon and Marty, 1995)(Cheminee, 1970)(Chesner and Luhr, 2010)(Christie et al., 1986)(Chu et al., 2009)(Cohen et al., 1980)(Cohen and O'Nions, 1982)(Colin et al., 2015)(Condomines et al., 1983)(Condomines et al., 1981)(Corazzato et al., 2008)(Costa et al., 2015)(Cottrell and Kelley, 2011)(Cottrell and Kelley, 2013)(Craig and Lupton, 1976)(Crovisier et al., 1992)(Czamanske and Moore, 1977)(Danyushevsky et al., 2008)(Daoud et al., 2010)(Daux et al., 1994)(Daux et al., 1990)(David et al., 2000)(Debaille et al., 2006)(Delaney et al., 1978)(Deniel et al., 1994)(Déruelle et al., 1992)(Des Marais and Moore, 1984)(Detrick et al., 1990)(Devey et al., 1990)(Dixon et al., 2000)(Dixon et al., 2017)(Dixon et al., 2002)(Dmitriev et al., 1979)(Don Hermes and Schilling, 1976)(Donnelly et al., 2004)(Dosso et al., 1993)(Dosso et al., 1999)(Dosso et al., 1991)(Draut et al., 2009)(Duncan et al., 1997)(Dungan et al., 1978)(Dymond and Hogan, 1973)(Eason et al., 2015)(Eiler et al., 1996)(Eiler et al., 2000)(Eissen et al., 1989)(Elkins et al., 2016)(Elkins et al., 2011)(Ferguson et al., 2010)(Field et al., 2012)(Field et al., 2013)(Fine et al., 1986)(Fino et al., 1973)(Fino et al., 1978)(Flude et al., 2010)(Frey et al., 1977)(Frey et al., 1993)(Fryer et al., 1992)(Füri et al., 2010)(Furman et al., 2006)(Gale et al., 2011)(Gale et al., 2014)(Gamble et al., 1993)(Gannoun et al., 2007)(Gannoun et al., 2004)(Gass et al., 1973)(Gibson et al., 1995)(Giordano et al., 2014)(Gurenko et al., 1995)(Gurenko and Chaussidon, 1997)(Gurenko and Chaussidon, 2002)(Gurenko and Sobolev, 2006)(Haase et al., 2003)(Haase et al., 2000)(Hagos et al., 2016)(Hall et al., 1984)(Halldórsson et al., 2016)(Halldórsson et al., 2016)(Hamelin and Allègre, 1985)(Hamelin et al., 1984)(Hanan et al., 2000)(Hanyu et al., 2011)(Hart et al., 1983)(Hart and Ravizza, 2013)(Hekinian et al., 1976)(Hekinian et al., 2000)(Helgason, 1989)(Hémond et al., 2006)(Hertogen et al., 1980)(Hildenbrand et al., 2008)(Hildenbrand et al., 2012)(Hildenbrand et al., 2014)(Hilton et al., 2000)(Hiyagon et al., 1992)(Hofmann et al., 1986)(Ito et al., 1987)(Jambon et al., 1995)(Jambon and Zimmermann, 1987)(Jambon and Zimmermann, 1990)(Jancin et al., 1985)(Jaques et al., 1980)(Jeffery et al., 2016)(Jeffries et al., 1995)(Jenner et al., 2012)(Jenner et al., 2010)(Jochum and Hofmann, 1997)(Jochum et al., 1983)(Kamenetsky, 1996)(Kamenetsky and Crawford, 1998)(Kamenetsky et al., 1998)(Kelley et al., 2013)(Kendrick et al., 2017)(Kent and Fitton, 2000)(Khalaf, 2010)(Kingsley and Schilling, 1995)(Kobussen et al., 2008)(Kurz et al., 1982)(Kurz et al., 1985)(Kyser and O'Neil, 1984)(Kyser and Rison, 1982)(Labidi et al., 2012)(Langmuir et al., 1977)(Lucic et al., 2016)(Lukács et al., 2015)(Luyendyk et al., 1979)(Machado et al., 1982)(Maclennan, 2008a)(Maclennan, 2008b)(Madureira et al., 2014)(Maeno and Taniguchi, 2007)(Marschall et al., 2017)(Marty and Humbert, 1997)(Marty and Jambon, 1987)(Marty and Ozima, 1986)(Marty and Tolstikhin, 1998)(Marty et al., 1983)(Mathez, 1976)(Mattey et al., 1984)(McGarvie et al., 2007)(Melson et al., 1979)(Mercer et al., 2015)(Mertz et al., 1991)(Mertz and Haase, 1997)(Meurer et al., 2001)(Meyer and Bryan, 1996)(Meyer et al., 1985)(Michael, 1995)(Michael and Cornell, 1998)(Michael and Graham, 2015)(Michael and Schilling, 1989)(Miyashiro et al., 1969)(Moorbath and Walker, 1965)(Moreira and Allègre, 2002)(Moreira et al., 2000)(Moreira et al., 2011)(Mungall and Martin, 1994)(Murton, 2002)(Neave et al., 2015)(Nichols et al., 2002)(Nichols and Wysoczanski, 2007)(Nielsen et al., 2020)(Nielsen et al., 2014)(Nishio et al., 1990)(Nishio et al., 2007)(Nishio et al., 1998)(Niu et al., 2001)(Nohara et al., 1994)(Ohba et al., 2009)(O'Reilly et al., 1993)(Ottonello et al., 1978)(Peate et al., 2009)(Peate et al., 2001)(Perkins and Nash, 2002)(Pik et al., 1998)(Pimentel et al., 2016)(Pineau et al., 2004)(Poreda and Brozolo, 1984)(Poreda et al., 1986)(Pracht and Kinnaird, 1997)(Ragnarsdóttir et al., 1994)(Raquin and Moreira, 2009)(Rea et al., 1995)(Reekie et al., 2019)(Révillon, 1999)(Reynolds and Langmuir, 1997)(Ripley and Al-Jassar, 1987)(Roeder et al., 2006)(Rogers, 1993)(Rooney et al., 2007)(Rooney et al., 2012)(Rowe and Schilling, 1979)(Roy-Barman and Allègre, 1994)(Roy-Barman et al., 1998)(Ryan and Langmuir, 1987)(Ryan and Langmuir, 1993)(Sakai et al., 1984)(Salters, 1996)(Sarda et al., 1998)(Sarda et al., 1985)(Schiano et al., 1997)(Schiano and Bourdon, 1999)(Schiellerup, 1995)(Schilling, 1973)(Schilling and Kingsley, 2017)(Schilling et al., 1999)(Schlanger et al., 1976)(Schneider and Wachendorf, 1973)(Shibata et al., 1979)(Shido et al., 1974)(Shirey et al., 1987)(Shorttle et al., 2015)(Sigurdsson, 1981)(Smith et al., 2008)(Smith et al., 1998)(Snyder, 2004)(Snyder et al., 2007)(Stakes et al., 1984)(Staudacher et al., 1989)(Stolper et al., 2004)(Sturm et al., 2000)(Sun et al., 2003)(Tang et al., 2017)(Teklay et al., 2010)(Thomson and Maclennan, 2013)(Thorarinsson and Tegner, 2009)(Thordarson et al., 1996)(Thorseth et al., 1991)(Thy, 1983)(Timm et al., 2010)(Tomlinson et al., 2012)(Trønnes, 1990)(Tuller-Ross et al., 2019)(Ulrich et al., 2012)(Uto et al., 2004)(Vigier et al., 1999)(Volker et al., 1997)(Wallace, P., & Carmichael, 1992)(Walraven et al., 1992)(Welke et al., 1968)(White, 1993)(Yalçın et al., 1998)(Yang et al., 2011)(Yang et al., 2018)(Yi et al., 2000)(Zanon and Pimentel, 2015)

References

Albers, M., & Christensen, U. R. (2001). Channeling of plume flow beneath mid-ocean ridges. Earth and Planetary Science Letters, 187(1–2), 207–220. https://doi.org/10.1016/S0012-821X(01)00276-X

Allen, R. M., Nolet, G., Morgan, W. J., Vogfjörd, K., Nettles, M., Ekström, G., & Julian, B. R. (2002). Plume-driven plumbing and crustal formation in Iceland. Journal of Geophysical Research: Solid Earth, 107(B8), 4.

Almalki, K. A., Betts, P. G., & Ailleres, L. (2015). The Red Sea – 50 years of geological and geophysical research. Earth-Science Reviews, 147, 109–140. https://doi.org/10.1016/j.earscirev.2015.05.002

Almond, D. C. (1986). Geological evolution of the Afro-Arabian dome. Tectonophysics, 131(3–4), 301–332.

ArRajehi, A., McClusky, S., Reilinger, R., Daoud, M., Alchalbi, A., Ergintav, S., & Kogan, L. (2010). Geodetic constraints on present-day motion of the Arabian Plate: Implications for Red Sea and Gulf of Aden rifting. Tectonics, 29(3).

Augustin, N., van der Zwan, F. M., Devey, C. W., & Brandsdóttir, B. (2021). 13 million years of seafloor spreading throughout the Red Sea Basin. Nature Communications, 12(1), 2427. https://doi.org/10.1038/s41467-021-22586-2

Bagley, B., & Revenaugh, J. (2008). Upper mantle seismic shear discontinuities of the Pacific. Journal of Geophysical Research: Solid Earth, 113(B12), 2008JB005692. https://doi.org/10.1029/2008JB005692

Barnett-Moore, N., Hassan, R., Flament, N., & Müller, D. (2017). The deep Earth origin of the Iceland plume and its effects on regional surface uplift and subsidence. Solid Earth, 8(1), 235–254. https://doi.org/10.5194/se-8-235-2017

Barnhoorn, A., Van Der Wal, W., & Drury, M. R. (2011). Upper mantle viscosity and lithospheric thickness under Iceland. Journal of Geodynamics, 52(3–4), 260–270. https://doi.org/10.1016/j.jog.2011.01.002

Becker, T. W. (2006). On the effect of temperature and strain-rate dependent viscosity on global mantle flow, net rotation, and plate-driving forces. Geophysical Journal International, 167(2), 943–957. https://doi.org/10.1111/j.1365-246X.2006.03172.x

Becker, T. W. (2017). Superweak asthenosphere in light of upper mantle seismic anisotropy. Geochemistry, Geophysics, Geosystems, 18(5), 1986–2003. https://doi.org/10.1002/2017GC006886

Behr, W. M., Holt, A. F., Becker, T. W., & Faccenna, C. (2022). The effects of plate interface rheology on subduction kinematics and dynamics. Geophysical Journal International, 230(2), 796–812. https://doi.org/10.1093/gji/ggac075

Beydoun, Z. R. (1989). THE HYDROCARBON PROSPECTS OF THE RED SEA-GULF OF ADEN: A REVIEW. Journal of Petroleum Geology, 12(2), 125–144. https://doi.org/10.1111/j.1747-5457.1989.tb00229.x

Bojar, A.-V., Fritz, H., Kargl, S., & Unzog, W. (2002). Phanerozoic tectonothermal history of the Arabian–Nubian shield in the Eastern Desert of Egypt: Evidence from fission track and paleostress data. Journal of African Earth Sciences, 34(3–4), 191–202. https://doi.org/10.1016/S0899-5362(02)00018-0

Canales, J. P., Ito, G., Detrick, R. S., & Sinton, J. (2002). Crustal thickness along the western Galápagos Spreading Center and the compensation of the Galápagos hotspot swell. Earth and Planetary Science Letters, 203(1), 311–327. https://doi.org/10.1016/S0012-821X(02)00843-9

Chang, S. J., & Van der Lee, S. (2011). Mantle plumes and associated flow beneath Arabia and East Africa. Earth and Planetary Science Letters, 302(3–4), 448–454.

Conrad, C. P., & Behn, M. D. (2010). Constraints on lithosphere net rotation and asthenospheric viscosity from global mantle flow models and seismic anisotropy. Geochemistry, Geophysics, Geosystems, 11(5), 2009GC002970. https://doi.org/10.1029/2009GC002970

Conrad, C. P., & Lithgow-Bertelloni, C. (2006). Influence of continental roots and asthenosphere on plate-mantle coupling. Geophysical Research Letters, 33(5), 2005GL025621. https://doi.org/10.1029/2005GL025621

Courtney, R. C., & White, R. S. (1986). Anomalous heat flow and geoid across the Cape Verde Rise: Evidence for dynamic support from a thermal plume in the mantle. Geophysical Journal International, 87(3), 815–867. https://doi.org/10.1111/j.1365-246X.1986.tb01973.x

Darbyshire, F. A., Bjarnason, I. Th., White, R. S., & Flóvenz, Ó. G. (1998). Crustal structure above the Iceland mantle plume imaged by the ICEMELT refraction profile. Geophysical Journal International, 135(3), 1131–1149. https://doi.org/10.1046/j.1365-246X.1998.00701.x
Davies, G. F. (1994). Thermomechanical erosion of the lithosphere by mantle plumes. Journal of Geophysical Research: Solid Earth, 99(B8), 15709–15722.
DeMets, C., Gordon, R. G., & Argus, D. F. (2010). Geologically current plate motions. Geophysical Journal International, 181(1), 1–80. https://doi.org/10.1111/j.1365-246X.2009.04491.x
Dixon, J. E., Dixon, T. H., Bell, D. R., & Malservisi, R. (2004). Lateral variation in upper mantle viscosity: Role of water. Earth and Planetary Science Letters, 222(2), 451–467. https://doi.org/10.1016/j.epsl.2004.03.022
Duncan, R. A., & Richards, M. A. (1991). Hotspots, mantle plumes, flood basalts, and true polar wander. Reviews of Geophysics, 29(1), 31–50.
Ferreira, A. M. G., Marignier, A., Attanayake, J., Frietsch, M., & Berbellini, A. (2020). Crustal structure of the Azores Archipelago from Rayleigh wave ellipticity data. Geophysical Journal International, 221(2), 1232–1247. https://doi.org/10.1093/gji/ggaa076
Fitton, J. G., Saunders, A. D., Norry, M. J., Hardarson, B. S., & Taylor, R. N. (1997). Thermal and chemical structure of the Iceland plume. Earth and Planetary Science Letters, 153(3–4), 197–208. https://doi.org/10.1016/S0012-821X(97)00170-2
Gente, P., Dyment, J., Maia, M., & Goslin, J. (2003). Interaction between the Mid-Atlantic Ridge and the Azores hot spot during the last 85 Myr: Emplacement and rifting of the hot spot-derived plateaus. Geochemistry, Geophysics, Geosystems, 4(10).
Ghebreab, W. (1998). Tectonics of the Red Sea region reassessed. Earth-Science Reviews, 45(1–2), 1–44. https://doi.org/10.1016/S0012-8252(98)00036-1
Griffiths, R. W., & Campbell, I. H. (1990). Stirring and structure in mantle starting plumes. Earth and Planetary Science Letters, 99(1–2), 66–78.
Hager, B. H., & O'Connell, R. J. (1979). Kinematic models of large-scale flow in the Earth's mantle. Journal of Geophysical Research: Solid Earth, 84(B3), 1031–1048. https://doi.org/10.1029/JB084iB03p01031
Hanan, B. B., Blichert-Toft, J., Kingsley, R., & Schilling, J.-G. (2000). Depleted Iceland mantle plume geochemical signature: Artifact of multicomponent mixing?: ICELAND PLUME GEOCHEMICAL SIGNATURE. Geochemistry, Geophysics, Geosystems, 1(4), n/a-n/a. https://doi.org/10.1029/1999GC000009
Harpp, K. S., & White, W. M. (2001). Tracing a mantle plume: Isotopic and trace element variations of Galápagos seamounts. Geochemistry, Geophysics, Geosystems, 2(6).
Hart, S. R., Schilling, J.-G., & Powell, J. L. (1973). Basalts from Iceland and Along the Reykjanes Ridge: Sr Isotope Geochemistry. Nature Physical Science, 246(155), 104–107. https://doi.org/10.1038/physci246104a0
Hirth, G., & Kohlstedt, D. (2003). Rheology of the upper mantle and the mantle wedge: A view from the experimentalists. In J. Eiler (Ed.), Geophysical Monograph Series (Vol. 138, pp. 83–105). American Geophysical Union. https://doi.org/10.1029/138GM06
Hofmann, A. W., & White, W. M. (1982). Mantle plumes from ancient oceanic crust. Earth and Planetary Science Letters, 57(2), 421–436. https://doi.org/10.1016/0012-821X(82)90161-3
Hofmann, C., Courtillot, V., Feraud, G., Rochette, P., Yirgu, G., Ketefo, E., & Pik, R. (1997). Timing of the Ethiopian flood basalt event and implications for plume birth and global change. Nature, 389(6653), 838–841.
Hoggard, M. J., Parnell-Turner, R., & White, N. (2020). Hotspots and mantle plumes revisited: Towards reconciling the mantle heat transfer discrepancy. Earth and Planetary Science Letters, 542, 116317. https://doi.org/10.1016/j.epsl.2020.116317
Hoggard, M. J., Winterbourne, J., Czarnota, K., & White, N. (2017). Oceanic residual depth measurements, the plate cooling model, and global dynamic topography. Journal of Geophysical Research: Solid Earth, 122(3), 2328–2372.
Holt, A. F., & Becker, T. W. (2017). The effect of a power-law mantle viscosity on trench retreat rate. Geophysical Journal International, 208(1), 491–507. https://doi.org/10.1093/gji/ggw392
Holt, A. F., & Royden, L. H. (2020). Subduction Dynamics and Mantle Pressure: 2. Towards a Global Understanding of Slab Dip and Upper Mantle Circulation. Geochemistry, Geophysics, Geosystems, 21(7), e2019GC008771. https://doi.org/10.1029/2019GC008771

Hua, J., Fischer, K. M., Becker, T. W., Gazel, E., & Hirth, G. (2023). Asthenospheric low-velocity zone consistent with globally prevalent partial melting. Nature Geoscience, 16(2), 175–181. https://doi.org/10.1038/s41561-022-01116-9

Ito, G., Shen, Y., Hirth, G., & Wolfe, C. J. (1999). Mantle flow, melting, and dehydration of the Iceland mantle plume. Earth and Planetary Science Letters, 165(1), 81–96. https://doi.org/10.1016/S0012-821X(98)00216-7

Jenkins, J., Maclennan, J., Green, R. G., Cottaar, S., Deuss, A. F., & White, R. S. (2018). Crustal Formation on a Spreading Ridge Above a Mantle Plume: Receiver Function Imaging of the Icelandic Crust. Journal of Geophysical Research: Solid Earth, 123(6), 5190–5208. https://doi.org/10.1029/2017JB015121

Jestin, F., Huchon, P., & Gaulier, J. M. (1994). The Somalia plate and the East African Rift System: Present-day kinematics. Geophysical Journal International, 116(3), 637–654.

Koivisto, E. A., Andrews, D. L., & Gordon, R. G. (2014). Tests of fixity of the Indo-Atlantic hot spots relative to Pacific hot spots: Rates of inter-hotspot motion. Journal of Geophysical Research: Solid Earth, 119(1), 661–675. https://doi.org/10.1002/2013JB010413

Krein, S. B., Molitor, Z. J., & Grove, T. L. (2021). ReversePetrogen: A Multiphase Dry Reverse Fractional Crystallization-Mantle Melting Thermobarometer applied to 13,589 Mid-Ocean Ridge Basalt Glasses. Journal of Geophysical Research - Solid Earth.

Kumar, P., Kind, R., Priestley, K., & Dahl-Jensen, T. (2007). Crustal structure of Iceland and Greenland from receiver function studies. Journal of Geophysical Research: Solid Earth, 112(B3).

Lawver, L. A., & Müller, R. D. (1994). Iceland hotspot track. Geology, 22(4), 311–314.

Le Douaran, S., & Francheteau, J. (1981). Axial depth anomalies from 10 to 50° north along the Mid-Atlantic Ridge: Correlation with other mantle properties. Earth and Planetary Science Letters, 54(1), 29–47. https://doi.org/10.1016/0012-821X(81)90066-2

Leroy, S., Razin, P., Autin, J., Bache, F., d'Acremont, E., Watremez, L., Robinet, J., Baurion, C., Denèle, Y., Bellahsen, N., Lucazeau, F., Rolandone, F., Rouzo, S., Kiel, J. S., Robin, C., Guillocheau, F., Tiberi, C., Basuyau, C., Beslier, M.-O., … Lazki, A. A.-. (2013). From rifting to oceanic spreading in the Gulf of Aden: A synthesis. In K. Al Hosani, F. Roure, R. Ellison, & S. Lokier (Eds.), Lithosphere Dynamics and Sedimentary Basins: The Arabian Plate and Analogues (pp. 385–427). Springer Berlin Heidelberg. https://doi.org/10.1007/978-3-642-30609-9_20

Marks, K. M., & Sandwell, D. T. (1991). Analysis of geoid height versus topography for oceanic plateaus and swells using nonbiased linear regression. Journal of Geophysical Research, 96(B5), 8045. https://doi.org/10.1029/91JB00240

McNutt, M. (1988). Thermal and mechanical properties of the Cape Verde Rise. Journal of Geophysical Research: Solid Earth, 93(B4), 2784–2794.

Mitrovica, J. X., & Forte, A. M. (2004). A new inference of mantle viscosity based upon joint inversion of convection and glacial isostatic adjustment data. Earth and Planetary Science Letters, 225(1–2), 177–189. https://doi.org/10.1016/j.epsl.2004.06.005

Monnereau, M., & Cazenave, A. (1990). Depth and geoid anomalies over oceanic hotspot swells: A global survey. Journal of Geophysical Research, 95(B10), 15429. https://doi.org/10.1029/JB095iB10p15429

Montelli, R., Nolet, G., Dahlen, F. A., Masters, G., Engdahl, E. R., & Hung, S. H. (2004). Finite-frequency tomography reveals a variety of plumes in the mantle. Science, 303(5656), 338–343.

Moore, J. G., & Schilling, J.-G. (1973). Vesicles, water, and sulfur in Reykjanes Ridge basalts. Contributions to Mineralogy and Petrology, 41(2), 105–118. https://doi.org/10.1007/BF00375036

Morgan, W. J., & Morgan, J. P. (2007). Plate velocities in the hotspot reference frame. SPECIAL PAPERS-GEOLOGICAL SOCIETY OF AMERICA, 430, 65.

Müller, R. D., Sdrolias, M., Gaina, C., & Roest, W. R. (2008). Age, spreading rates, and spreading asymmetry of the world's ocean crust. Geochemistry, Geophysics, Geosystems, 9(4).

Murton, B. J., Taylor, R. N., & Thirlwall, M. F. (2002). Plume–Ridge Interaction: A Geochemical Perspective from the Reykjanes Ridge. Journal of Petrology, 43(11), 1987–2012. https://doi.org/10.1093/petrology/43.11.1987

Naif, S., Key, K., Constable, S., & Evans, R. L. (2013). Melt-rich channel observed at the lithosphere–asthenosphere boundary. Nature, 495(7441), 356–359. https://doi.org/10.1038/nature11939

Parsons, B., & Daly, S. (1983). The relationship between surface topography, gravity anomalies, and temperature structure of convection. Journal of Geophysical Research: Solid Earth, 88(B2), 1129–1144.
Podolefsky, N. S., Zhong, S., & McNamara, A. K. (2004). The anisotropic and rheological structure of the oceanic upper mantle from a simple model of plate shear. Geophysical Journal International, 158(1), 287–296. https://doi.org/10.1111/j.1365-246X.2004.02250.x
Richards, M. A., Yang, W., Baumgardner, J. R., & Bunge, H. (2001). Role of a low-viscosity zone in stabilizing plate tectonics: Implications for comparative terrestrial planetology. Geochemistry, Geophysics, Geosystems, 2(8), 2000GC000115. https://doi.org/10.1029/2000GC000115
Royden, L. H., & Holt, A. F. (2020). Subduction Dynamics and Mantle Pressure: 1. An Analytical Framework Relating Subduction Geometry, Plate Motion, and Asthenospheric Pressure: 1. An Analytical Framework Relating Subduction Geometry, Plate Motion, and Asthenospheric Pressure. Geochemistry, Geophysics, Geosystems, 21(7). https://doi.org/10.1029/2020GC009032
Rychert, C. A., Harmon, N., Constable, S., & Wang, S. (2020). The Nature of the Lithosphere-Asthenosphere Boundary. Journal of Geophysical Research: Solid Earth, 125(10), e2018JB016463. https://doi.org/10.1029/2018JB016463
Schilling, J. G. (1991). Fluxes and excess temperatures of mantle plumes inferred from their interaction with migrating mid-ocean ridges. Nature, 352(6334), 397–403.
Schilling, J. G., Kingsley, R. H., Hanan, B. B., & McCully, B. L. (1992). Nd-Sr-Pb isotopic variations along the Gulf of Aden: Evidence for Afar mantle plume-continental lithosphere interaction. Journal of Geophysical Research: Solid Earth, 97(B7), 10927–10966.
Schilling, J.-G. (1973). Iceland Mantle Plume: Geochemical Study of Reykjanes Ridge. Nature, 242(5400), 565–571. https://doi.org/10.1038/242565a0
Schmerr, N. (2012). The Gutenberg Discontinuity: Melt at the Lithosphere-Asthenosphere Boundary. Science, 335(6075), 1480–1483. https://doi.org/10.1126/science.1215433
Scoppola, B., Boccaletti, D., Bevis, M., Carminati, E., & Doglioni, C. (2006). The westward drift of the lithosphere: A rotational drag? Geological Society of America Bulletin, 118(1–2), 199–209. https://doi.org/10.1130/B25734.1
Selway, K., Smirnov, M. Y., Beka, T., O'Donnell, J. P., Minakov, A., Senger, K., Faleide, J. I., & Kalscheuer, T. (2020). Magnetotelluric Constraints on the Temperature, Composition, Partial Melt Content, and Viscosity of the Upper Mantle Beneath Svalbard. Geochemistry, Geophysics, Geosystems, 21(5), e2020GC008985. https://doi.org/10.1029/2020GC008985
Shorttle, O., Moussallam, Y., Hartley, M. E., Maclennan, J., Edmonds, M., & Murton, B. J. (2015). Fe-XANES analyses of Reykjanes Ridge basalts: Implications for oceanic crust's role in the solid Earth oxygen cycle. Earth and Planetary Science Letters, 427, 272–285. https://doi.org/10.1016/j.epsl.2015.07.017
Sleep, N. H. (1990). Hotspots and mantle plumes: Some phenomenology. Journal of Geophysical Research: Solid Earth, 95(B5), 6715–6736.
Sleep, N. H. (2006). Mantle plumes from top to bottom. Earth-Science Reviews, 77(4), 231–271. https://doi.org/10.1016/j.earscirev.2006.03.007
Smallwood, J. R., White, R. S., & Minshull, T. A. (1995). Sea-floor spreading in the presence of the Iceland plume: The structure of the Reykjanes Ridge at 61°40′N. Journal of the Geological Society, 152(6), 1023–1029. https://doi.org/10.1144/GSL.JGS.1995.152.01.24
Stamps, D. S., Calais, E., Saria, E., Hartnady, C., Nocquet, J. M., Ebinger, C. J., & Fernandes, R. M. (2008). A kinematic model for the East African Rift. Geophysical Research Letters, 35(5).
Stein, C., & Hansen, U. (2008). Plate motions and the viscosity structure of the mantle—Insights from numerical modelling. Earth and Planetary Science Letters, 272(1–2), 29–40. https://doi.org/10.1016/j.epsl.2008.03.050
Unni, C. K., & Schilling, J.-G. (1978). Cl and Br degassing by volcanism along the Reykjanes Ridge and Iceland. Nature, 272(5648), 19–23. https://doi.org/10.1038/272019a0
W. Jason Morgan. (1972). Deep Mantle Convection Plumes and Plate Motions. AAPG Bulletin, 56. https://doi.org/10.1306/819A3E50-16C5-11D7-8645000102C1865D
Wang, S., Yu, H., Zhang, Q., & Zhao, Y. (2018). Absolute plate motions relative to deep mantle plumes. Earth and Planetary Science Letters, 490, 88–99. https://doi.org/10.1016/j.epsl.2018.03.021

Weir, N. R. W., White, R. S., Brandsdóttir, B., Einarsson, P., Shimamura, H., & Shiobara, H. (2001). Crustal structure of the northern Reykjanes Ridge and Reykjanes Peninsula, southwest Iceland. Journal of Geophysical Research: Solid Earth, 106(B4), 6347–6368. https://doi.org/10.1029/2000JB900358

White, R., & McKenzie, D. (1989). Magmatism at rift zones: The generation of volcanic continental margins and flood basalts. Journal of Geophysical Research, 94(B6), 7685. https://doi.org/10.1029/JB094iB06p07685

Wilson, J. T. (1973). Mantle plumes and plate motions. Tectonophysics, 19(2), 149–164.

Wölbern, I., Rümpker, G., Link, K., & Sodoudi, F. (2012). Melt infiltration of the lower lithosphere beneath the Tanzania craton and the Albertine rift inferred from S receiver functions. Geochemistry, Geophysics, Geosystems, 13(8).

Workman, R. K., & Hart, S. R. (2005). Major and trace element composition of the depleted MORB mantle (DMM). Earth and Planetary Science Letters, 231(1–2), 53–72. https://doi.org/10.1016/j.epsl.2004.12.005

Yamamoto, M., Morgan, J. P., & Morgan, W. J. (2007). Global plume-fed asthenosphere flow-I: motivation and model development. Special Papers-Geological Society of America, 430, 165.

Zhou, H., & Dick, H. J. B. (2013). Thin crust as evidence for depleted mantle supporting the Marion Rise. Nature, 494(7436), 195–200. https://doi.org/10.1038/nature11842

Chapter 3: Melting Near the Slab-Wedge Interface at 2.4 GPa

Abstract

We have investigated the composition of melts of hydrous lherzolite at 2.4 GPa over temperatures of 1000-1175 ˚C. Our experiments all use the starting composition H&Z+SM, which represents a subduction-enriched peridotite containing 0.61 % Na_2O, 0.16 K_2O % (wt. %) with 4.2 wt. % H_2O added (Mitchell and Grove, 2015). All experiments contain the solid phases olivine, orthopyroxene, and an aluminous phase (either garnet or spinel). Experiments at temperatures above ~1000 ˚C contain a measurable glass phase. Clinopyroxene is found in experiments run at temperatures up to 1150 ˚C. The melt phase in the experiments varies in modal proportions from ~4-26%. Melt compositions are typically intermediate between shallow melt compositions (Mitchell and Grove, 2015) and deep mantle melts (Grove and Till, 2019). In particular, the Cao, Na_2O, and K_2O compositions of erupted primitive HMAs require mixing between shallow melts, which are relatively enriched in CaO and depleted in Na_2O and K_2O, and deep melts, which are relatively enriched in Na_2O and K_2O and depleted in CaO. Additionally, by pressure quenching the experiments instead of only turning off the thermocouple at the end of the experiment, we preserve a range of melt textures from low to high temperature experiments. Melt textures of high temperature experiments are characterized by a combination of smooth, continuous glass and vesiculated glass with inferred water contents of ~9 wt.% water. Melt textures of low temperature experiments are characterized by highly vesicular glass and small, isolated melt spheres with inferred water contents of 6-7 wt.% water. These results are consistent with the results of Gavrilenko et al. (2019) which suggest that during quenching and the melt to glass phase transition, more than ~9 wt.% water cannot be preserved in the quenched glass phase, with excess water released during quenching. Melt with water contents between ~6-9 wt.% results in transitional glass textures, with minor amounts of water released during quenching. This finding implies that melt inclusion studies, used to infer magmatic water

contents, are biased toward upper crustal water solubilities and may inaccurately reflect the water contents of deep magmas in the upper mantle or lower crust.

3.1 Introduction

Partial melting in the mantle wedge is thought to result from volatiles released by the subducting oceanic lithosphere (Kushiro, 1972). The fluids released from the subducting slab carry alkalic cations such as Na and K, resulting in the relative enrichment of those elements in hydrous melts from the mantle wedge (Grove et al., 2002). Previous workers have identified so called, ‘primitive,’ erupted rocks which are near equilibrium with peridotite in the mantle wedge (e.g., Baker et al., 1994; Kelemen et al., 2014). There is a large compositional variety of primitive erupted basalts and andesites in subduction arcs (Schmidt and Jagoutz, 2017). The observed compositional variety results from melts at different depths and temperatures in the mantle wedge, while also being dependent on the volume and composition of fluids released from the subducting slab (Mitchell and Grove, 2015; Grove and Till, 2019). The details of melts produced within different parts of the mantle wedge, and how those melts are modified prior to eruption in a subduction arc are still the subject of investigation and debate (Strek et al., 2007; Keleman and Yogodzinski, 2007;Barr et al., 2007; Streck and Leeman, 2018; Phillips and Till, 2022).

Early workers utilized simple systems such as Mg_2SiO_4-SiO_2-H_2O (Kushiro et al., 1968; Kushiro 1968, 1972) to constrain basic systematics of melt composition as a function of variable pressure and temperature. This early work highlighted the importance of water to the melting reaction. Subsequent work demonstrated that by adding 3-6 wt. % H_2O to spinel lherzolite, the silica content of the melt increased by 1 wt.% and the FeO-MgO content decreased by 2 wt. % in comparison to anhydrous peridotite melts (Gaetani and Grove, 1998; 2003). These results supported the hypothesis that magmas with high water contents can form due to upward percolation of fluids through the mantle wedge while maintaining equilibrium with high temperature mantle peridotite. While there is abundant work on melt compositions in the shallow mantle wedge (<2 GPa e.g., Mysen and Boettcher, 1975; Gaetani and Grove, 1998; Grove et al., 2013; Mitchell and Grove, 2015), the composition of deep melts (>2 GPa) and their impact on erupted compositions is the subject of active investigation (e.g., Grove and Till, 2019). Grove et al. (2006) and Till et al. (2012) found that the water-saturated peridotite solidus between 3-6 GPa is located at extremely low temperatures between 800-820 ˚C. Field-based evidence of low-temperature melting in the mantle wedge, consistent with the aforementioned experiments, has been identified in the Japanese Sanbagawa belt (Hattori et al., 2010; Till et al., 2010). Grove and Till (2019) postulated that hydrous arc magmas form over a range of depths starting at the base of the wedge near the top of the subducting slab (3 GPa) and ending in the shallow mantle (~1 GPa). By mixing deep melts with shallow melts in the mantle wedge, they were able to reproduce observed compositional variability in high magnesium andesites and basaltic andesites. In addition, they found that the addition of a small 'slab component' in the form of elevated alkali elements (Na_2O+K_2O) was critical to reproducing observed REE and incompatible element distributions in erupted basalts and andesites.

In this paper, we present the results of experiments at 2.4 GPa (~75 km depth in the mantle wedge) using a lherzolitic starting bulk composition with an added metasomatic component equivalent to ~4.2 wt. % H_2O and ~5 wt. % alkalis. The composition of experimental melts at temperatures ranging from 1000-1175 °C are presented along with phase proportions, which we then compare to previous hydrous lherzolite melting experiments and the compositions of erupted primitive magnesian andesites in subduction arcs globally. Furthermore, we discuss the melt textures and glass compositions which resulted from pressure quenching and how they may explain the observation that erupted primitive glass and melt inclusions almost never have water contents in excess of 9-10 wt.% despite high water solubilities (14-20 wt.%) in the upper mantle.

3.2 Experimental and analytical methods

3.2.1 Starting materials

As a starting material, we used Mix D from Mitchell and Grove (2015), otherwise known as H&Z + SM (Table 3.1). This mix is made from a blend of synthetic oxides that is composed of

71% of an anhydrous Hart and Zindler (1986) primitive mantle composition with an added slab component, and 29% of a hydrous mix (H&Z + H2O) from Grove et al. (2006). The slab component added to Hart and Zindler (1986) is determined in Grove et al. (2002). With this mix composition, we aim to experimentally constrain the melt compositions near the interface of the subduction slab.

3.2.2 Piston cylinder experiments

Melting experiments on H&Z+SM were conducted at 2.4 GPa across a range of temperatures from 1000-1175 °C using a 0.5" end-loaded solid medium piston cylinder (Boyd and England, 1960) in the MIT Experimental Petrology Laboratory. The starting material was packed into a 7/16" long Au capsule, which is then triple-crimped and welded and placed inside an Al_2O_3 ring. The capsule and Al_2O_3 ring were sandwiched between MgO spacers in the midpoint of a cylindrical graphite furnace. A sintered, cylindrical $BaCO_3$ cell surrounds the graphite furnace during the experiment.

Pressure was previously calibrated using the breakdown of Ca-tschermak pyroxene to anorthite + gehlenite + corundum (1350 °C, 1.3 GPa) and using the spinel (sp) to garnet transition in the CMAS peridotite analog system (1500 °C, 2.5 GPa) (Hays 1966; Longhi 2005). This calibration showed that pressure was accurate to ± 0.05 GPa, and that no pressure correction was necessary.

The temperature is controlled and monitored using $W_{97}Re_3/W_{75}Re_{25}$ thermocouples, without correction for the effect of pressure on thermocouple emf. The vertical thermal gradient across the charge has been determined by direct measurement of offset thermocouples as well as temperature mapping using the reaction kinetics of $MgO + Al_2O_3 = MgAl_2O_4$ (Watson et al. 2002; Medard and Grove 2008). Results from these methods indicated a vertical temperature difference of ~ 10 °C across the capsule (hot end on top) in addition to a ~ 20 °C difference between the location of the hotspot in the graphite furnace and the location of the thermocouple 1.5 mm above the capsule. Temperature corrections for this ~ 20 °C difference were applied.

The experiments used the hot piston-in technique (Johannes et al., 1971). At the beginning of each experimental run, the assembly was pressurized at room temperature to 1.0 GPa. Temperature was then raised at a rate of 100 °C/min to 865 °C, where it was held for 6 min. Then, the pressure was raised to the final pressure, and temperature was increased at 50 °C/min to the final temperature of the run. Experiments were held at their final run conditions for 52-175 hrs.

All experiments were terminated by pressure quenching by releasing the piston load and turning off the thermocouple. In contrast to previous experiments at the MIT experimental petrology laboratory (e.g., Grove and Till, 2019) which quenched the run by turning off the power, we performed a pressure quench at the end of each run to better preserve melt textures and prevent quench crystal growth. In the discussion section, we compare our melt textures to previous experimental melt textures and discuss the implications of pressure quenching in regard to the observed water contents in erupted glasses and melt inclusions.

3.2.3 Electron microprobe analysis

At the end of each experiment, we drilled into the capsule prior to epoxy impregnation. Previous hydrous mantle melting experiments released small quantities of water upon drilling (e.g., Grove and Till, 2019), however we did not observe this. This may have important implications for the water contents of erupted primitive glasses and melt inclusions. Following drilling, the gold capsule is impregnated with epoxy before it is cut into four pieces on a diamond wire saw. The four pieces are again impregnated with epoxy to completely fuse the phases to the capsule interior. Each piece is then polished to remove excess epoxy before mounting all four pieces in a 1-inch epoxy disk. Finally, the disk is polished on diamond polishing mylar.

Experimental major element compositions were obtained using wavelength-dispersive spectrometry (WDS) on the 5-spectrometer JEOL 8200 electron microprobe (EMP) at the Massachusetts Institute of Technology. Measurements were acquired using a 15 kV accelerating voltage, 10 nÅ beam current, and 1 to 10 μm spot sizes. Online data reduction utilized the CITZAF correction package (Armstrong, 1995) and the atomic number correction, the absorption coefficients, and the fluorescence correction available in CITZAF.

When determining mineral compositions, 15-20 measurements were made of the target mineral throughout the experimental charge. Low standard deviations of the mineral analyses in Table 3.3 support low compositional variability throughout the experiment. In high temperature experiments (>1050 °C), glass was analyzed by setting up point grids and analyzing hundreds of spots to get an accurate, holistic average of glass compositions in the experiment. At lower temperatures, glass was only present as small spheres and sheets and not large bodies. These were analyzed by setting 1 to 5 spots, depending on the size of the sphere. At the end of the analysis, the compositions of all the spheres were averaged like the high temperature analyses.

3.3 Experimental results

3.3.1 Mineral and melt textures

The temperature conditions and mineral proportions of each experiment are reported in Figure 3.1. Table 3.2 contains experimental run times and phase proportions, and Table 3.3 contains phase compositions of glass, orthopyroxene (opx), clinopyroxene (cpx), garnet, and olivine (oliv). For the bulk composition in this study (H&Z + SM, Table 3.1), the experiments always contain oliv+opx+an aluminous phase (either garnet or spinel). Cpx is present at temperatures lower than 1150 °C, and garnet is present for temperatures at and below 1075 °C. In experiments above 1075 °C, spinel replaces garnet as the aluminous phase in the experiment. The modal abundance of both garnet and cpx decreased with increasing temperature in the experiments, while the modal abundance of liquid increased. All experiments, except E21, contained identifiable glass or quench crystals.

Experimental charges were cut in half and impregnated with epoxy before polishing to preserve small pockets of glass and quench modified melt in between mineral grains. The volume proportion of melt in the experiments increases with increasing experimental temperature. The melt is generally found near the top of the experimental capsule, as this is the highest temperature region of the capsule. Melt frequently collects near crimps in the gold capsule, between the crystalline matrix and wall of the experimental charge (Figure 3.2e). In the lowest temperature experiments, at or below 1050 °C, the melt occurs as large vesiculated bubbles (both isolated and in contact with solid grains, Figure 3.3c) and isolated small spherules (Figure 3.3d and e). The vesiculated bubbles vary in size from 50-200 microns in diameter. The vesicles in the large bubbles, which we interpret as vapor-filled pores within the melt phase, are 10-50 microns in diameter. Isolated melt spheres range in diameter from 1-25 microns (Figure 3.3d and e).

In high temperature experiments (>1100 °C), the melt is preserved as large bodies of glass near the top of the charge with some interstitial melt at the boundary between the melt-rich body and crystalline matrix (Figure 3.3a and b). Two distinct textures are present in the high temperature glasses: 1) a smooth, continuous textures glass with no vesicles and 2) strongly vesicular glass with <10-micron vesicles.

In comparison to similar experiments by Grove and Till (2019) at 3 GPa, we observe the same distribution of phases relative to the top and bottom of the charge. This includes melt in the top of the charge and near crimped edges, high modal amounts of garnet and cpx in the bottom of the charge, and poikiloblastic garnets with opx and oliv inclusions. While we observe melt spheres in our low temperature experiments, they are not high in silica like the high silica melt spherules of Grove and Till (2019) (Table 3.3). They are also not texturally associated with vesicles as shown in Figure 3.3d. These differences may be a product of quenching both pressure and temperature in these experiments as opposed to only temperature in Grove and Till (2019) or related to the contrast in experimental pressure.

The total compositional weight percentages for glass around ~90-95 wt.% suggest ~5-10 wt.% H_2O is present in the final quenched glasses (Table 3.3). This result in conjunction with the lack of high silica melt spheres in our experiments likely results from the loss of exsolved vapor and supercritical fluid during pressure quenching of the experiment. Pressure quenching is likely to result in failure of the gold capsule walls at the end of the experiment due to the rapid change in pressure, resulting in small cracks or holes through which vapor can escape. This would explain why we did not observe the release of vapor on drilling into the capsules. Furthermore, the estimated water contents of 5-10 wt.% are consistent with the study of Gavrilenko et al. (2019). Gavrilenko et al. (2019) found that estimates of magmatic water content from melt inclusions (MIs), which commonly yield water contents <9-10 wt.%, may not accurately reflect the water content of deep, primitive magmas. At depth, hydrous magmas may contain well over 10 wt.% H_2O, and during ascent and emplacement in the upper crust or eruption, the glass may not homogenously quench, exsolving a significant portion of the original water content. Such a finding has significant implications for the cycling and return flux of water in subduction arcs. We discuss the implications of our experimental results relative to the study of Gavrilenko et al. (2019) in the discussion section.

Melt bodies in the high temperature experiments were generally larger in the experiments at 3.2 GPa relative to our experiments at 2.4 GPa. Melt bodies near the top of the charge vary from 50 to ~1000 microns in length and were 50-300 microns wide (Figure 3.3a and b). Both small and large vesicles are present in large melt bodies (Figure 3.3a). Small vesicles are 1-10 microns in diameter, while larger vesicles can reach ~100 microns in diameter. Grove and Till (2019) interpreted vesicles and associated high silica melt spherules as precipitating from supercritical fluid exsolved from the melt phase during quenching, based on the occurrence of high silica spheres within the vesicle. While vesicles are also abundant in our experiments, their proportion relative to the melt phase is dependent on experimental temperature. It is likely these vesicles form during the experiment, and their variable proportion relative to the melt is due to the increasing proportion of supercritical fluid relative to the melt with decreasing temperature. Notably, water was rarely released from our experimental capsules upon drilling into the experiment after quenching. This may be because the water escaped from the capsule during failure of the capsule walls from pressure quenching.

Mineral textures are similar to the results of previous studies (Grove et al., 2006; Till et al., 2012; Grove and Till, 2019). Olivine crystals are subhedral to anhedral (5-100 microns) with larger grains forming at the cold end of the capsule in some experiments (Figure 3.2c). Orthopyroxene and clinopyroxene are subhedral to euhedral (5-30 microns). Garnet occurs as large poikilitic grains, enclosing anhedral olivine and orthopyroxene (100-150 microns). Both garnet and clinopyroxene are present near the bottom (colder) end of the experiment. In some cases, cpx crystallizes directly from the melt phase on quenching (Figure 3.3b). Rutile was absent in our experiments, in comparison to the experiments of Grove and Till (2019) at 3.2 GPa. This is because the rutile-in reaction is strongly temperature dependent at high pressure, suggesting these experiments are not in the low temperature, high pressure rutile stability field (Xiong et al., 2005).

3.3.2 Mineral and melt compositions

For mineral phases, 10-40 analyses of each phase were made throughout the charge. Low standard deviations (Table 3.3) demonstrate the minerals are unzoned and compositionally homogenous. Melt was analyzed two ways, dependent on the size of the melt body. For large melt bodies (>50 μm^2), a grid of points was set up across the body at 8-10 μm intervals. The composition was averaged across the grid and assumed to be representative of the melt composition. In low temperature experiments with thin melt bodies ("honeycombs") and spheres, individual point analyses were made and analyzed at low spot size (~1 micron). The lowest temperature experiment in this study (1000 °C), did not contain and melt phase.

Long experimental durations were necessary to achieve equilibrium, evidenced by: 1) a lack of chemical zoning and homogenous intracrystalline compositions, 2) constant composition of individual minerals regardless of location in the experimental charge, 3) systematic changes in composition with experimental temperature. The Mg# of individual phases, and K_d between olivine and melt also support equilibrium in the experiments (Table 3.3). Olivine-melt K_d's fall between 0.26 and 0.36, which is in the range of expected K_d's in the uppermost mantle during melting (Kinzler and Grove, 1992; Matzen et al., 2011). The Mg# of glass and olivine are also in the expected range, 0.73-0.79 (Tatsumi and Ishizaka, 1982; Grove et al., 2002; Bryant et al., 2010; Mitchell and Grove, 2015).

3.4 Discussion

3.4.1 Melt compositions of near solidus melts of hydrous lherzolite

Figure 3.4 plots the composition of analyzed experimental melt compositions vs. temperature in addition to previous experiments from: Mysen and Boettcher, 1975; Gaetani and Grove, 1998; Till et al., 2012; Green et al., 2014; Mallik et al., 2015; and Grove and Till, 2019. With the exceptions of Mysen and Boettcher (1975) and Gaetani et al. (1998), these past experiments were carried out at higher pressure than experiments in this study. Mysen and Boettcher (1985) and Gaetani et al. (1998) performed experiments primarily around 1-2 GPa. Therefore, the existing literature generally brackets the experiments in this study, with experiments representative of the shallow mantle wedge (1-2 GPa) and the deep mantle wedge (>3 GPa). Melt compositions are intimately related to temperature. SiO_2, TiO_2, Al_2O_3, Na_2O, and K_2O all decrease with increasing experimental temperature in this study (Figure 3.4a, b, c, h, and i). Cr_2O_3, FeO, MgO, and CaO all increase with increasing temperature in this study (Figure 3.4d, e, f, and g). These results are in general agreement with previous studies although the temperature dependent systematics of the alkali elements (Na_2O, and K_2O) are less well-constrained in the existing literature. Notably, CaO content of the melt is strongly dependent on the presence of garnet and not cpx (Figures 3.1 and 3.4). High CaO contents in melt (>10 wt.%) require garnet to be absent. Incompatible elements such as Na_2O and K_2O are also strongly dependent on experimental temperature. For the two lowest temperature experiments (1025-1050 °C), where melt content is <10 vol. %, Na_2O and K_2O are significantly higher (>1 wt% increase) relative to the high temperature experiments. The relationship between temperature and melt composition for SiO_2, FeO, MgO, CaO, Na_2O, and K_2O is not linear, with a significant change in melt composition between 1050 and 1075 °C (Figure 3.4).

Our findings for SiO_2, CaO, and K_2O are similar to the findings of Grove and Till (2019) at 3.2 GPa. At low temperature (<~1050°C), melt silica contents are >50 wt.%, relative to <50 wt.% at higher temperature (Figure 3.4a). This is consistent with experiments by Mysen and Boettcher (1975), Grove and Till (2019), and Till et al. (2012). The transition to high CaO contents in the melt phase occurs at ~1050-1075 °C in our experiments at 2.4 GPa, and at ~1100 °C in experiments at 3.2 GPa (Grove and Till, 2019). Therefore, the Garnet-in reaction decreases in temperature with decreasing pressure (consistent with Grove et al., 2006). The contents of the highly incompatible elements Na_2O and K_2O do not appear linked to a particular mineral phase (Figure 3.1). Rather, these phases are almost always concentrated in the melt phase, with decreasing relative abundance as the melt phase is diluted with other elements such as MgO, FeO, and CaO with increasing temperature and melt fraction. These observations suggest that the compositional systematics of melt with changing temperature in the deep mantle wedge (>2 GPa) are generally similar and strongly dependent on temperature.

The dependence of melt composition on pressure is best represented by MgO and Al_2O_3. As the melting pressure increases, the Al2O3 content decreases (Figure 3.4c). MgO contents increase with increasing pressure. This is characterized by a systematic change in composition between the experiments of Mysen and Boettcher (1.5 GPa, 1975), this study (2.4 GPa), and Grove and Till (3.2 GPa, 2019).

Also of note is the effect of starting composition on melt compositions. Water content and the addition of alkali elements Na_2O and K_2O have a significant effect on melt composition in low temperature experiments. The starting composition of this study and Grove and Till (2019) (H&Z + SM) has additional alkali elements, representing the contribution of an alkali-rich fluid from the dehydrating slab (Grove et al., 2002). The presence of amphibole under the conditions of the Mysen and Boettcher experiments results in high calcium contents at low temperatures, while at high pressure (>2.4 GPa, this study), the absence of amphibole and early amphibole breakdown leads to relatively low calcium contents in the melt. Relatively low Na_2O

and K_2O concentrations at low temperature in previous experiments, particularly Mysen and Boettcher (1975), is likely due to low concentrations in the starting composition, and/or quench-modified melt compositions. There is no strong correlation between the concentration of alkalis in the low temperature melt phase and the melting pressure (Figure 3.4).

3.4.2 Comparison with previous experimental studies on hydrous lherzolite melting

Figures 3.4 and 3.5 compare our results to previous studies versus temperature and MgO content, respectively. High pressure experiments (> 3 GPa) by Tenner et al. (2012), Till et al. (2012), Green et al. (2014), Mallik et al. (2015), and Grove and Till (2019) span SiO2 contents of 40-70 wt. %. High silica spheres of Grove and Till (2019) reach SiO_2 content between 70-80 wt. %. Al_2O_3 contents of high-pressure experiments are generally lower than experiments <3 GPa and less than 16-17 wt.% (this study, Mysen and Boettcher, 1975, Gaetani and Grove, 1998, Mitchell and Grove, 2015). FeO and MgO contents of high-pressure experiments are enriched relative to low pressure experiments, spanning 10-26 wt.%. CaO contents are noticeably lower in the high-pressure experiments in comparison to this study and other shallow experiments (Figure 3.5g). At 10 wt.% MgO, CaO contents of Grove and Till (2019) are ~1-4 wt.% lower than experiments in this study and experiments by Mitchell and Grove (2015). Low melt fraction experiments, which produce high silica melts relative to high temperature experiments, produce melts enriched in Na_2O and K_2O due to their incompatible behavior. Similar to the behavior of CaO, the alkali elements of erupted compositions may form by mixing of deep and shallow mantle melts.

SiO_2 contents of shallow experiments (<2 GPa, Mysen and Boettcher, 1975; Gaetani and Grove, 1998; Mitchell and Grove, 2015) are higher than in the experiments of this study, and transition from low melt fraction composition to high melt fraction composition is not as abrupt. Al_2O_3 content of this study is relatively low in comparison to Mysen and Boettcher (1975) (Figure 3.4) but overlaps with the range of Al_2O_3 in Mitchell and Grove (2015) (Figures 3.4 and 3.5). FeO and MgO contents of low pressure hydrous mantle melts are generally equivalent to or higher than in this study. The FeO and MgO content of Mysen and Boettcher, 1975 is significantly lower than high melt fraction melts in this study but are equivalent to the FeO and MgO composition of low temperature melts in this study at equivalent SiO_2. CaO contents of high temperature, high melt fraction (>10%) melts in this study are much higher than at shallow pressures. However, low temperature, low melt fraction melts have low CaO (consistent with low temperature melts and high silica spheres of Grove and Till, 2019). As mentioned hypothesized, low CaO content melts can explain the relatively low concentrations of CaO in erupted lavas (Grove and Till, 2019), relative to shallow mantle melts from Mitchell and Grove (2015). As with the high-pressure melts, alkali content (Na_2O and K_2O) is strongly dependent on melting temperature and the degree of melting, as opposed to pressure.

3.4.3 Comparison to natural primitive basaltic andesites and magnesian andesites

Figure 3.5 contrasts major element composition of the melt phase in our experiments versus the major element compositions of natural primitive basaltic andesites and magnesian andesites. Our results reinforce the hypothesis that erupted high magnesium andesites are the product of mantle melting, and that the final erupted composition reflects mixing of polybaric melts in the mantle wedge over the dehydrating slab with little to no impact from AFC or crustal assimilation. While most of the major element systematics can be matched by the compositions of hydrous melts of the shallow mantle wedge (Mitchell and Grove, 2015), the low CaO contents of the erupted compositions and the high K_2O are not explained by shallow melts alone. Grove and Till (2019) demonstrated that mixing between deep, low temperature melts near the slab interface with shallow melts can explain the relatively low CaO contents.

The relatively high K_2O contents of erupted magmas compared to shallow mantle melts may in part be explained by mixing with deep, low temperature melts near the slab wedge interface (Figure 3.5, Grove and Till, 2019). Most experimental melts at low pressure (e.g., Mitchell and Grove, 2015) are characterized by low potassium contents below 0.5 wt.%. Low temperature melts, representative of low degrees of melting directly above the slab, are relatively enriched in K_2O, at both low and high MgO concentrations (Figure 3.5). Therefore, the relatively high K2O contents of erupted HMAs is likely the product of mantle mixing between shallow, low K2O melts and deep, low temperature melts with K2O concentrations ≥ 1 wt.%.

As K2O is strongly incompatible with the phases in our experiments (ol, opx, cpx, garnet, and spinel) it is concentrated into the melt phase. Because of this incompatibility, the K2O concentrations of the experimental melts are strongly dependent on the starting composition of the experiment and the added 'slab component' as derived from Grove et al., 2002. The relative concentration of K2O in the melt phase decreases with progressive melting due to the enrichment of FeO, MgO, and CaO.

3.4.4 Water Contents of Erupted Primitive Glasses and Melt Inclusions

While mineral melt equilibria (Sisson and Grove, 1993), direct measurements of MIs (Anderson, 1974; Sisson and Layne, 1993; Wallace, 2005; Gavrilenko et al., 2019), and phase equilibria/phenocryst stability (Rutherford et al., 1985; Moore and Carmichael, 1998; Krawczynski et al., 2012) are all commonly used to constrain the pre-eruptive water contents of silicate melts, this water content may not accurately reflect the water contents of melts in the mantle wedge (Gavrilenko et al., 2019). Our measurements of experimental glasses yield average compositional totals between 90-95 wt.%, suggesting ~5-10 wt.% H_2O in the quenched experimental glass produced during this study. This estimate of water content is broadly consistent with that cited from MI studies in subduction arcs (e.g., Wallace, 2005; Plank et al., 2013; Gavrilenko et al., 2019). However, the solubility of water is expected to be much larger in the lower crust and mantle wedge (Mitchell et al., 2017). Thus, existing studies that rely on MIs or natural glasses may be biased toward magmatic water solubilities in the upper crust. In this section, we discuss how the results in our experiments support high water contents in the deep mantle wedge and provide a mechanism to explain the absence of such high water contents in erupted glasses and Mis similar to that proposed by Gavrilenko et al. (2019).

Water solubility models and experiments for the mantle wedge suggest upper bounds on magmatic water content of 14 to over 20 wt.% (Carmichael, 2002; Krawczynski et al., 2012; Mitchell et al., 2017). Despite this, there are little to no direct measurements of glass or MIs that yield such high water contents. Therefore, we must ask at what point does water leave the melt phase and why.

We posit that water exits the system during abrupt changes in pressure. Gavrilenko et al. (2019) found that experimental mafic glasses, formed with pre-loaded water contents >9-10 wt.%, did not form homogeneous quenched glass, and that the water in excess of ~9-10 wt.% exsolves from the melt phase during quenching. They determined that high-pressure, high-water content (>9 wt.%) magmas were unable to maintain high water contents not because of the change in water solubility as a function of pressure, but rather because of the structural change related to the melt-glass phase transition. Moreover, Gavrilenko et al. (2019) identified a transition point at magmatic water contents of 6-9 wt.% where the melt phase variably quenched to either clear glass or to vesiculated and devitrified glass.

In comparison to Gavrilenko et al. (2019), which performed their experiments at pressures of 1-1.5 GPa, our experiments at 2.4 GPa are also consistent with the observation that water contents in excess of 10 wt.% are unable to be preserved during pressure quenching due to the melt-glass structural transition. We expect the water solubility of melts at 2.4 GPa to be in excess of 20 wt.% based on the experimental constraints on water solubility at 1 GPa (Mitchell et al., 2017). Notably, we observe a temperature dependent transition in glass textures between the highest and lowest temperature experiments. High temperature glasses contain mixed vesicular glass and 'smooth' glass with no vesicles (Figures 3.3A and B). In contrast, low temperature glasses were strongly vesicular or occurred as small, isolated spheres (Figures 3.3C, D, and E). Glass in the low temperature experiments may have contained 9-11 wt.% H_2O, while glass in the high temperature experiments contained only 6-7 wt.% H_2O. This observation is consistent with the findings of Gavrilenko et al. (2019) that at water contents around 6 wt.%, quenched glass textures are transitional between vesiculated and 'smooth' (or optically clear) glass, while melt with >9 wt.% H_2O cannot store the entirety of the water in the quenched glass atomic structure and so it must be released from the melt phase on quenching.

The release of water during pressure quenching of the melt leads to the exsolution of vapor from the melt phase and the creation of strongly vesicular glass. Additionally, in our experiments, the vapor produced during quenching is released from the charge during failure of the Au capsule. The texture in the low temperature experiments consisting of small, isolated spheres may be produced by rapid expansion of the melt and exsolution of vapor during quenching. In addition to water dissolved in the melt, Grove and Till (2019) identified high silica spherules which may have resulted from the presence of a supercritical fluid with high dissolved silica contents. Excess vapor from the quenched glass and any supercritical fluid in our experiments, were likely released during quench, leaving only the concentration of water that was locked into the quenched glass structure.

3.5 Conclusion

The compositions of hydrous lherzolite melts at 2.4 GPa are texturally consistent with melts at 3 GPa. Our results confirm and strengthen the hypothesis that mixing of low temperature melts near the Slab-Wedge interface with melts in the shallow mantle wedge are able to reproduce the compositional characteristics of erupted primitive magnesian andesite. Additionally, our results suggest that high K_2O contents of erupted lavas relative to shallow mantle melts may be explained through the same mixing process. While the compositional systematics are similar to melts at 3 GPa, shallower melts in this study are characterized by higher relative Al_2O_3 and lower relative FeO and MgO. We identify a strong dependence of glass texture on the experimental temperature, and suggest that the textural contrast between experiments is the product of variable dissolved water content in the experimental melt which is partially released from the melt phase during pressure quenching.

References

Anderson, A. T. (1974). Evidence for a Picritic, Volatile-rich Magma beneath Mt. Shasta, California. Journal of Petrology, 15(2), 243–267. https://doi.org/10.1093/petrology/15.2.243

Armstrong, J. T. (1995). CITZAF: a package of correction programs for the quantitative electron microbeam X-ray-analysis of thick polished materials, thin films, and particles. Microbeam Analysis, 4, 177–200.

Baker, M. B., Grove, T. L., & Price, R. (1994). Primitive basalts and andesites from the Mt. Shasta region, N. California: Products of varying melt fraction and water content. Contributions to Mineralogy and Petrology, 118(2), 111–129. https://doi.org/10.1007/BF01052863

Barr, J., Grove, T. L., & Elkins-Tanton, L. (2007). High-magnesian andesite from Mount Shasta: A product of magma mixing and contamination, not a primitive melt: COMMENT AND REPLY: COMMENT. Geology, 35(1), e147–e147. https://doi.org/10.1130/G24058C.1

Boyd, F. R., & England, J. L. (1960). Apparatus for phase-equilibrium measurements at pressures up to 50 kilobars and temperatures up to 1750°C. Journal of Geophysical Research, 65(2), 741–748. https://doi.org/10.1029/JZ065i002p00741

Bryant, J. A., Yogodzinski, G. M., & Churikova, T. G. (2011). High-Mg# andesitic lavas of the Shisheisky Complex, Northern Kamchatka: Implications for primitive calc-alkaline magmatism. Contributions to Mineralogy and Petrology, 161(5), 791–810. https://doi.org/10.1007/s00410-010-0565-4

Carmichael, I. S. (2002). The andesite aqueduct: Perspectives on the evolution of intermediate magmatism in west-central (105–99°W) Mexico. Contributions to Mineralogy and Petrology, 143(6), 641–663. https://doi.org/10.1007/s00410-002-0370-9

Gaetani, G. A., & Grove, T. L. (1998). The influence of water on melting of mantle peridotite. Contributions to Mineralogy and Petrology, 131(4), 323–346. https://doi.org/10.1007/s004100050396

Gaetani, G. A., & Grove, T. L. (2003). Experimental constraints on melt generation in the mantle wedge. In J. Eiler (Ed.), Geophysical Monograph Series (Vol. 138, pp. 107–134). American Geophysical Union. https://doi.org/10.1029/138GM07

Gavrilenko, M., Krawczynski, M., Ruprecht, P., Li, W., & Catalano, J. G. (2019). The quench control of water estimates in convergent margin magmas. American Mineralogist, 104(7), 936–948. https://doi.org/10.2138/am-2019-6735

Green, D. H., Hibberson, W. O., Rosenthal, A., Kovács, I., Yaxley, G. M., Falloon, T. J., & Brink, F. (2014). Experimental Study of the Influence of Water on Melting and Phase Assemblages in the Upper Mantle. Journal of Petrology, 55(10), 2067–2096. https://doi.org/10.1093/petrology/egu050

Grove, T., Chatterjee, N., Parman, S., & Medard, E. (2006). The influence of H2O on mantle wedge melting. Earth and Planetary Science Letters, 249(1–2), 74–89. https://doi.org/10.1016/j.epsl.2006.06.043

Grove, T. L., Holbig, E. S., Barr, J. A., Till, C. B., & Krawczynski, M. J. (2013). Melts of garnet lherzolite: Experiments, models and comparison to melts of pyroxenite and carbonated lherzolite. Contributions to Mineralogy and Petrology, 166(3), 887–910. https://doi.org/10.1007/s00410-013-0899-9

Grove, T. L., & Till, C. B. (2019). H2O-rich mantle melting near the slab–wedge interface. Contributions to Mineralogy and Petrology, 174(10), 80. https://doi.org/10.1007/s00410-019-1615-1

Grove, T. L., Till, C. B., Lev, E., Chatterjee, N., & Médard, E. (2009). Kinematic variables and water transport control the formation and location of arc volcanoes. Nature, 459(7247), 694–697. https://doi.org/10.1038/nature08044

Grove, T., Parman, S., Bowring, S., Price, R., & Baker, M. (2002). The role of an H2O-rich fluid component in the generation of primitive basaltic andesites and andesites from the Mt. Shasta region, N California. Contributions to Mineralogy and Petrology, 142(4), 375–396. https://doi.org/10.1007/s004100100299

Hart, S. R., & Zindler, A. (1986). In search of a bulk-Earth composition. Chemical Geology, 57(3–4), 247–267. https://doi.org/10.1016/0009-2541(86)90053-7

Hattori, K., Wallis, S., Enami, M., & Mizukami, T. (2010). Subduction of mantle wedge peridotites: Evidence from the Higashi-akaishi ultramafic body in the Sanbagawa metamorphic belt: Garnet-bearing peridotite, Sanbagawa. Island Arc, 19(1), 192–207. https://doi.org/10.1111/j.1440-1738.2009.00696.x

Hays, J. F. (1966). Lime-alumina-silica. Carnegie Inst Wash Yearb, 65, 234–239.

Johannes, W., Bell, P. M., Mao, H. K., Boettcher, A. L., Chipman, D. W., Hays, J. F., Newton, R. C., & Seifert, F. (1971). An interlaboratory comparison of piston-cylinder pressure calibration using the albite-breakdown reaction. Contributions to Mineralogy and Petrology, 32(1), 24–38. https://doi.org/10.1007/BF00372231

Kelemen, P. B., Hanghøj, K., & Greene, A. R. (2014). One View of the Geochemistry of Subduction-Related Magmatic Arcs, with an Emphasis on Primitive Andesite and Lower Crust. In Treatise on Geochemistry (pp. 749–806). Elsevier. https://doi.org/10.1016/B978-0-08-095975-7.00323-5

Kelemen, P. B., & Yogodzinski, G. (2007). High-magnesian andesite from Mount Shasta: A product of magma mixing and contamination, not a primitive melt: COMMENT AND REPLY: COMMENT. Geology, 35(1), e149–e150. https://doi.org/10.1130/G24099C.1

Kinzler, R. J., & Grove, T. L. (1992). Primary magmas of mid-ocean ridge basalts 1. Experiments and methods. Journal of Geophysical Research: Solid Earth, 97(B5), 6885–6906. https://doi.org/10.1029/91JB02840

Krawczynski, M. J., Grove, T. L., & Behrens, H. (2012). Amphibole stability in primitive arc magmas: Effects of temperature, H2O content, and oxygen fugacity. Contributions to Mineralogy and Petrology, 164(2), 317–339. https://doi.org/10.1007/s00410-012-0740-x

Kushiro, I. (1968). Compositions of magmas formed by partial zone melting of the Earth's upper mantle. Journal of Geophysical Research, 73(2), 619–634. https://doi.org/10.1029/JB073i002p00619

Kushiro, I. (1972). Effect of Water on the Composition of Magmas Formed at High Pressures. Journal of Petrology, 13(2), 311–334. https://doi.org/10.1093/petrology/13.2.311

Kushiro, I., Syono, Y., & Akimoto, S. (1968). Melting of a peridotite nodule at high pressures and high water pressures. Journal of Geophysical Research, 73(18), 6023–6029. https://doi.org/10.1029/JB073i018p06023

Kushiro, I., & Walter, M. J. (1998). Mg-Fe partitioning between olivine and mafic-ultramafic melts. Geophysical Research Letters, 25(13), 2337–2340. https://doi.org/10.1029/98GL01844

Longhi, J. (2005). Temporal stability and pressure calibration of barium carbonate and talc/pyrex pressure media in a piston-cylinder apparatus. American Mineralogist, 90(1), 206–218. https://doi.org/10.2138/am.2005.1348

Mallik, A., Nelson, J., & Dasgupta, R. (2015). Partial melting of fertile peridotite fluxed by hydrous rhyolitic melt at 2–3 GPa: Implications for mantle wedge hybridization by sediment melt and generation of ultrapotassic magmas in convergent margins. Contributions to Mineralogy and Petrology, 169(5), 48. https://doi.org/10.1007/s00410-015-1139-2

Matzen, A. K., Baker, M. B., Beckett, J. R., & Stolper, E. M. (2011). Fe–Mg Partitioning between Olivine and High-magnesian Melts and the Nature of Hawaiian Parental Liquids. Journal of Petrology, 52(7–8), 1243–1263. https://doi.org/10.1093/petrology/egq089

Médard, E., & Grove, T. L. (2008). The effect of H2O on the olivine liquidus of basaltic melts: Experiments and thermodynamic models. Contributions to Mineralogy and Petrology, 155(4), 417–432. https://doi.org/10.1007/s00410-007-0250-4

Mitchell, A. L., Gaetani, G. A., O'Leary, J. A., & Hauri, E. H. (2017). H2O solubility in basalt at upper mantle conditions. Contributions to Mineralogy and Petrology, 172(10), 85. https://doi.org/10.1007/s00410-017-1401-x

Mitchell, A. L., & Grove, T. L. (2015). Melting the hydrous, subarc mantle: The origin of primitive andesites. Contributions to Mineralogy and Petrology, 170(2), 13. https://doi.org/10.1007/s00410-015-1161-4

Moore, G., & Carmichael, I. S. E. (1998). The hydrous phase equilibria (to 3 kbar) of an andesite and basaltic andesite from western Mexico: Constraints on water content and conditions of phenocryst growth. Contributions to Mineralogy and Petrology, 130(3–4), 304–319. https://doi.org/10.1007/s004100050367

Mysen, B. R. O., & Boettcher, A. L. (1975). Melting of a Hydrous Mantle: II. Geochemistry of Crystals and Liquids Formed by Anatexis of Mantle Peridotite at High Pressures and High Temperatures as a Function of Controlled Activities of Water, Hydrogen, and Carbon Dioxide. Journal of Petrology, 16(1), 549–593. https://doi.org/10.1093/petrology/16.1.549

Phillips, M., & Till, C. B. (2022). Crustal storage and ascent history of the Mt. Shasta primitive magnesian andesite: Implications for arc magma crustal flux rates. Contributions to Mineralogy and Petrology, 177(1), 9. https://doi.org/10.1007/s00410-021-01853-x

Plank, T., Kelley, K. A., Zimmer, M. M., Hauri, E. H., & Wallace, P. J. (2013). Why do mafic arc magmas contain ~4wt% water on average? Earth and Planetary Science Letters, 364, 168–179. https://doi.org/10.1016/j.epsl.2012.11.044

Rutherford, M. J., Sigurdsson, H., Carey, S., & Davis, A. (1985). The May 18, 1980, eruption of Mount St. Helens: 1. Melt composition and experimental phase equilibria. Journal of Geophysical Research: Solid Earth, 90(B4), 2929–2947. https://doi.org/10.1029/JB090iB04p02929

Schmidt, M. W., & Jagoutz, O. (2017). The global systematics of primitive arc melts. Geochemistry, Geophysics, Geosystems, 18(8), 2817–2854. https://doi.org/10.1002/2016GC006699

Sisson, T. W., & Grove, T. L. (1993). Temperatures and H2O contents of low-MgO high-alumina basalts. Contributions to Mineralogy and Petrology, 113(2), 167–184. https://doi.org/10.1007/BF00283226

Sisson, T. W., & Layne, G. D. (1993). H2O in basalt and basaltic andesite glass inclusions from four subduction-related volcanoes. Earth and Planetary Science Letters, 117(3–4), 619–635. https://doi.org/10.1016/0012-821X(93)90107-K

Streck, M. J., & Leeman, W. P. (2018). Petrology of “Mt. Shasta” high-magnesian andesite (HMA): A product of multi-stage crustal assembly. American Mineralogist, 103(2), 216–240. https://doi.org/10.2138/am-2018-6151

Streck, M. J., Leeman, W. P., & Chesley, J. (2007). High-magnesian andesite from Mount Shasta: A product of magma mixing and contamination, not a primitive mantle melt. Geology, 35(4), 351. https://doi.org/10.1130/G23286A.1

Tatsumi, Y., & Ishizaka, K. (1982). Origin of high-magnesian andesites in the Setouchi volcanic belt, southwest Japan, I. Petrographical and chemical characteristics. Earth and Planetary Science Letters, 60(2), 293–304. https://doi.org/10.1016/0012-821X(82)90008-5

Tenner, T. J., Hirschmann, M. M., & Humayun, M. (2012). The effect of H 2 O on partial melting of garnet peridotite at 3.5 GPa. Geochemistry, Geophysics, Geosystems, 13(3), 2011GC003942. https://doi.org/10.1029/2011GC003942

Till, C. B., Elkins-Tanton, L. T., & Fischer, K. M. (2010). A mechanism for low-extent melts at the lithosphere-asthenosphere boundary: MELTING AT THE LITHOSPHERE-ASTHENOSPHERE BOUNDARY. Geochemistry, Geophysics, Geosystems, 11(10), n/a-n/a. https://doi.org/10.1029/2010GC003234

Till, C. B., Grove, T. L., & Withers, A. C. (2012). The beginnings of hydrous mantle wedge melting. Contributions to Mineralogy and Petrology, 163(4), 669–688. https://doi.org/10.1007/s00410-011-0692-6

Wallace, P. J. (2005). Volatiles in subduction zone magmas: Concentrations and fluxes based on melt inclusion and volcanic gas data. Journal of Volcanology and Geothermal Research, 140(1–3), 217–240. https://doi.org/10.1016/j.jvolgeores.2004.07.023

Watson, E., Wark, D., Price, J., & Van Orman, J. (2002). Mapping the thermal structure of solid-media pressure assemblies. Contributions to Mineralogy and Petrology, 142(6), 640–652. https://doi.org/10.1007/s00410-001-0327-4

Figures and Captions

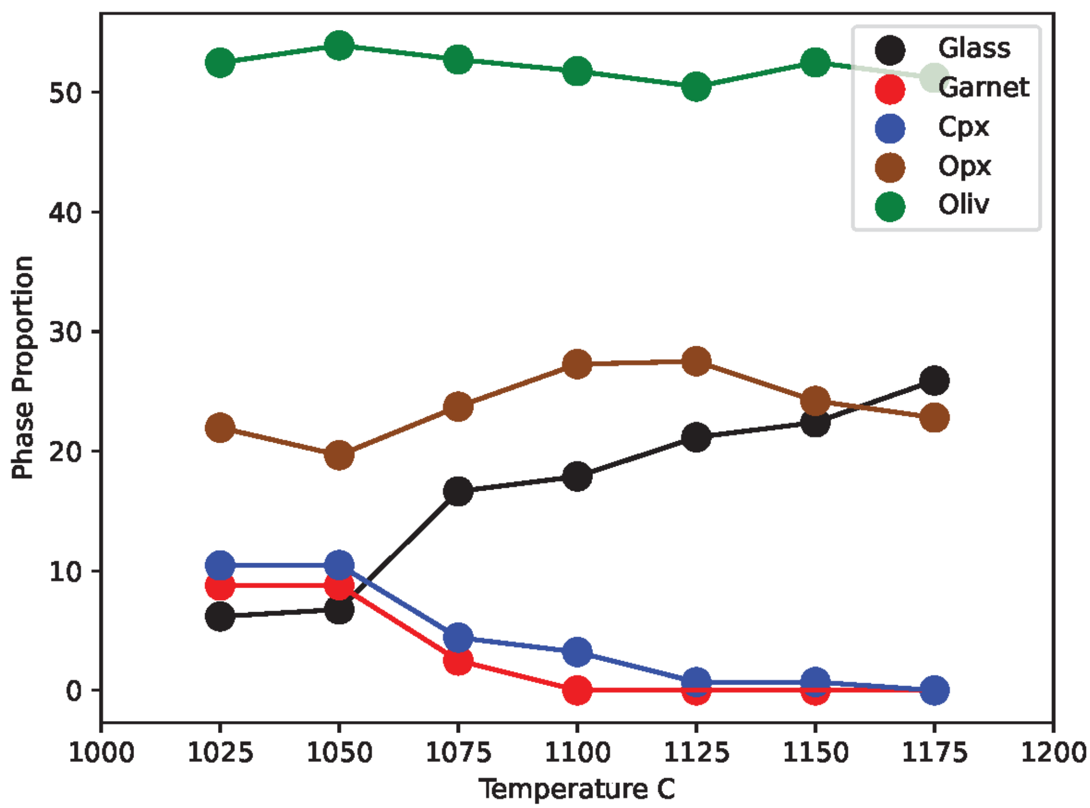

Figure 3.1: Phase proportions of experiments as a function of temperature. The proportions are calculated via mass balance of measured phase compositions (Table 3.3) and the starting mix composition (Table 3.1).

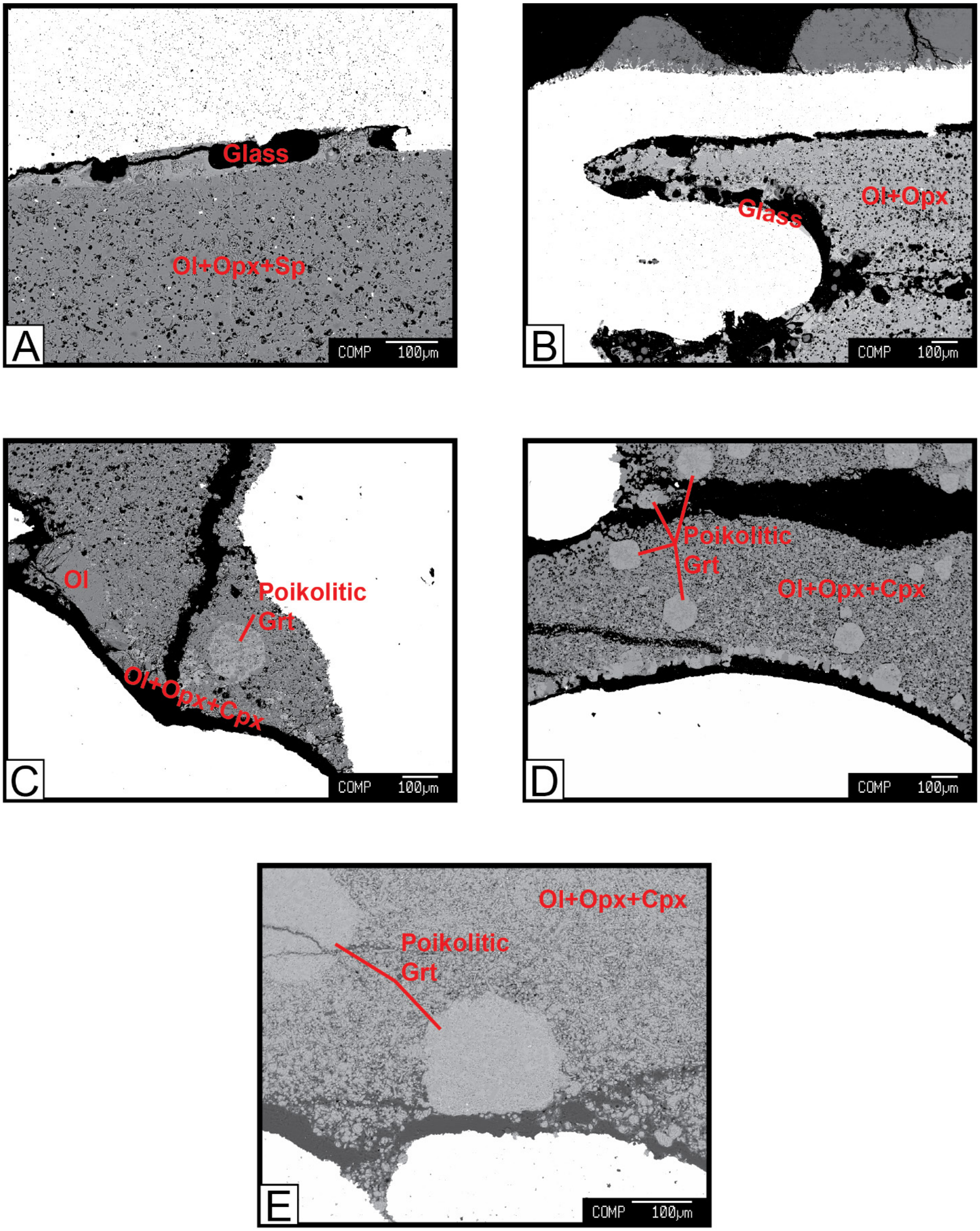

Figure 3.2: Backscattered Electron (BSE) images of selected experimental charges displaying the textural relationships between the solid phases (ol, opx, cpx, and garnet). A) Experiment C647 performed at 1150 ˚C. The top end of the capsule is toward the top of the image. Melt is visible between

the gold capsule (white) and solid phases in the experiment (dark gray BSE region). B) Experiment C649 conducted at 1100 ˚C. The top of the image is also the top of the capsule. Melt is visible around the edges of the gold septum. C) Experiment E16 conducted at 1075 ˚C. Large poikiloblastic garnet in the center of the charge. The top of the charge is toward the top of the image. Large olivine grains are present on the bottom left of the capsule in the image. D) Experiment E18 conducted at 1050 ˚C. The bottom of the capsule is displayed with large opx and ol crystals. Large poikiloblastic garnets occur throughout the entire charge. E) Experiment E21 conducted at 1000 ˚C. No melt was observed in this experiment. The top of the charge is toward the bottom of the image. Euhedral poikiloblastic garnets are well developed and occur throughout the charge.

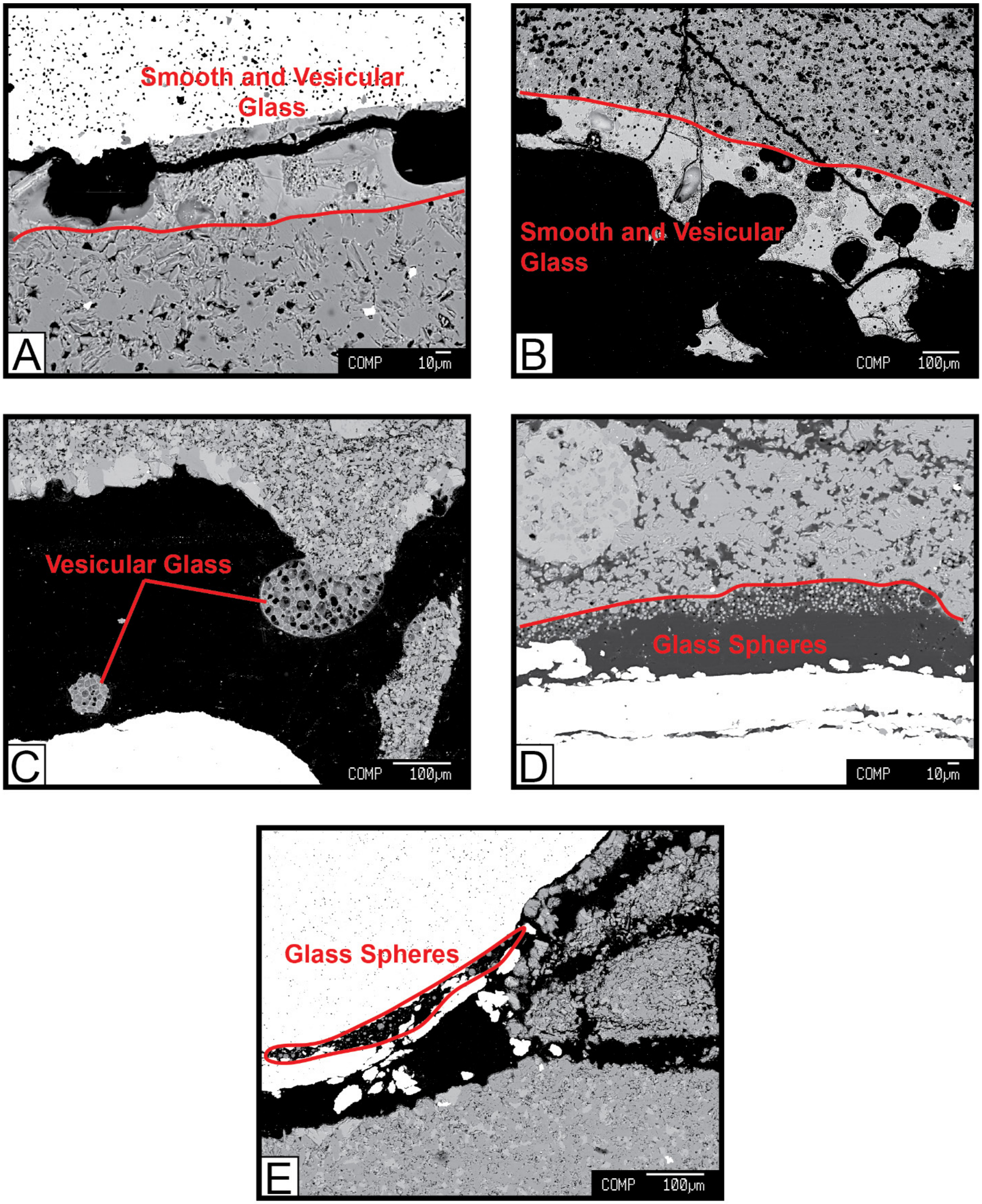

Figure 3.3: Backscattered Electron (BSE) image of melt textures from selected experiments. A) Experiment C647 conducted at 1175 ˚C. A large melt body with vesicular regions at the top of the capsule. Both small and large vesicles occur in the melt. Euhedral opx and ol crystals are visible below the melt body. B) Experiment C648 conducted at 1175 ˚C. A massive body of melt at the top of the charge, with similar textural characteristics to the melt in experiment C647. C) Experiment E18

conducted at 1050 ˚C. This experiment contains a large, vesiculated melt bubble directly below euhedral to subhedral ol, opx, and cpx crystals. The top of the capsule corresponds to the bottom of the image. A smaller vesiculated melt sphere is visible toward the bottom left. D) Experiment E18. A second melt texture visible in the experiment is isolated, small, and spherical bodies. The melt bodies in this texture are smaller than the vesicles visible in panel (C) but are not compositionally distinct. E) Experiment E19 conducted at 1025 ˚C. Small, homogenous, circular bodies of melt within a fold in the gold capsule.

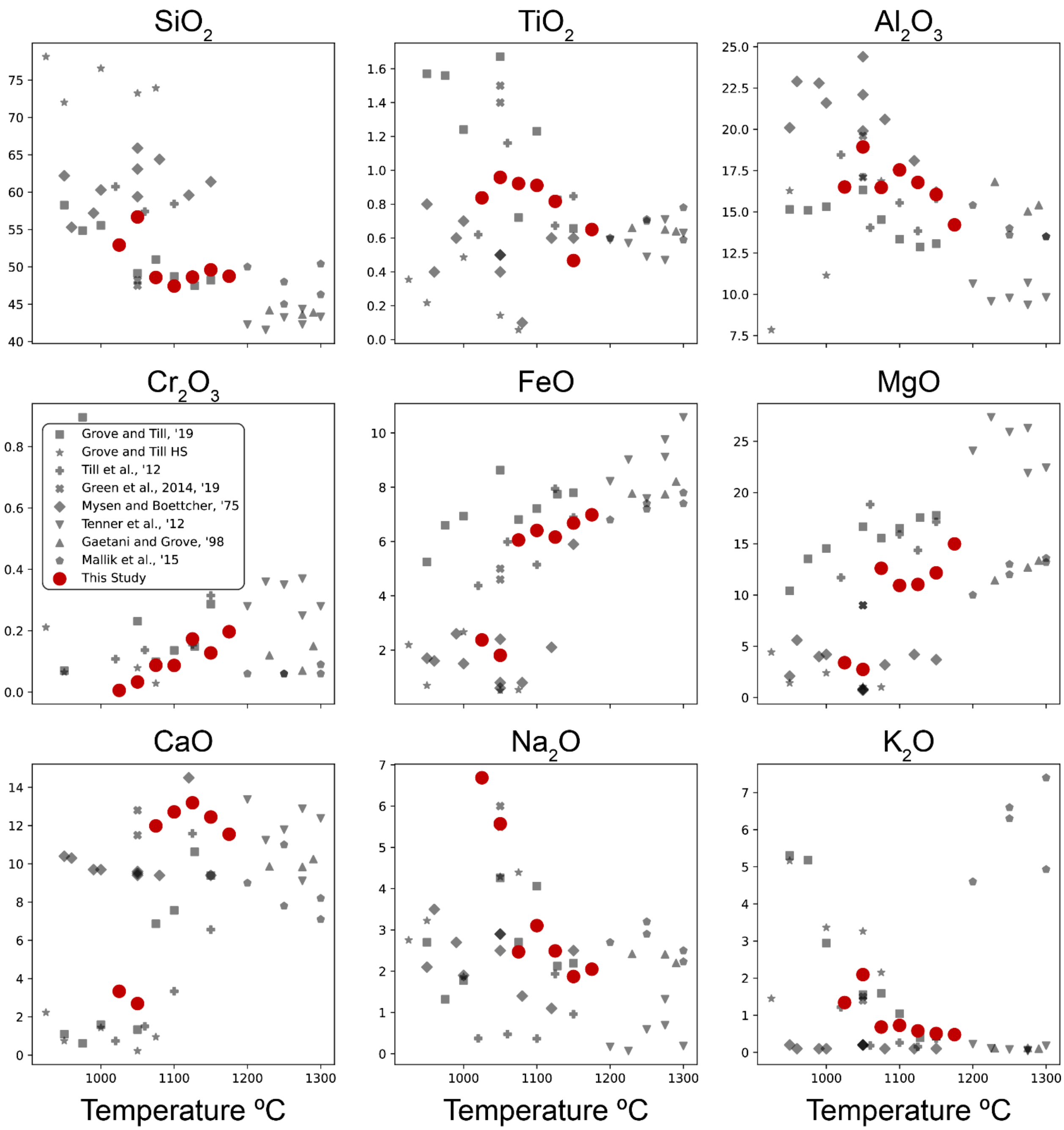

Figure 3.4: Major element composition of experimental glass in wt.% (Table 3.3) plotted versus experimental temperature. Results of this study are compared to similar experiments by Mysen and Boettcher (1975), Gaetani and Grove (1998), Tenner et al., 2012, Till et al. (2012), Green et al., 2015, Mallik et al. (2015), and Grove and Till (2019). Also plotted are the compositions of high silica melt spheres from Grove and Till (2019).

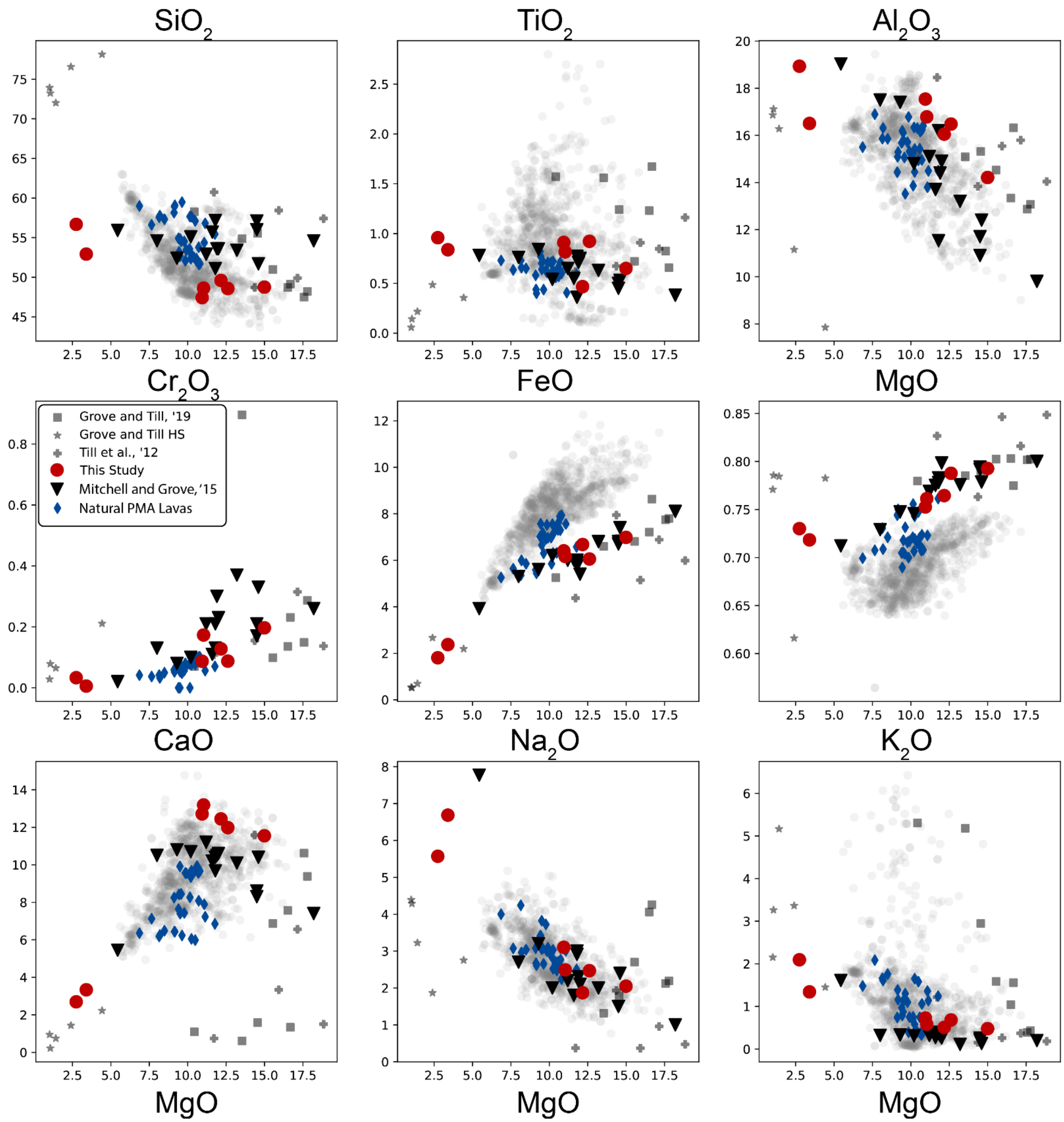

Figure 3.5: Major element composition of experimental glass in wt.% (Table 3.3) plotted versus MgO wt.%. Translucent gray data from Schmidt and Jagoutz, 2015. Mitchell and Grove (2015)

experimental glasses are plotted as inverted black triangles. Till et al. (2012) experimental glasses are plotted as gray pluses. And Grove and Till (2019) experimental glasses and high silica spheres are plotted as gray squares and stars, respectively.

Tables

	SiO_2	*TiO_2*	*Al_2O_3*	*Cr_2O_3*	*FeO*	*MnO*	*MgO*	*CaO*	*Na_2O*	*K_2O*	*NiO*	*sum*	*H_2O*
H&Z +SM	46.30	0.18	4.21	0.40	7.48	0.10	37.18	3.20	0.59	0.15	0.28	100.05	4.21

Table 3.1: Chemical composition of H&Z + SM, the experimental mix used in this paper.

Expt.	*P (kbar)*	*T (C)*	*Mix*	*Date*	*Run Time (hrs)*	*Spinel /garnet*	*Phases*					
							Ol	Opx	Cpx	Grnt	Liq	fO_2
E16	24	1075	H&Z +SM	3/26/2019	144	grnt	52.74	23.72	4.41	2.49	16.64	
E18	24	1050	H&Z +SM	5/6/2019	149	grnt	53.06	20.78	10.42	9.18	6.38	
E19	24	1025	H&Z +SM	5/29/2019	175	grnt	49.82	25.55	10.31	9.79	4.35	
E20	24	1000	H&Z +SM	7/8/2019	169	grnt	N/A	N/A	N/A	N/A	N/A	
E23	24	1125	H&Z +SM	9/11/2019	52	sp	50.47	27.51	0.69	0	21.16	2.24
C647	24	1150	H&Z +SM	10/2/2019	52	sp	52.50	24.26	0.70	0	22.40	2.18
C648	24	1175	H&Z +SM	10/28/2019	53	sp	51.20	22.83	0	0	25.89	2.33
C649	24	1100	H&Z +SM	11/18/2019	101	sp	51.76	27.27	3.20	0	17.88	2.29

Table 3.1 Experiment details and phase proportions.

	# of Analys.	*SiO_2*	*TiO_2*	*Al_2O_3*	*Cr_2O_3*	*FeO*	*MgO*	*MnO*	*CaO*	*Na_2O*	*K_2O*	*NiO*	*Sum*	*Mg #*	*KD $_{FeMg}$*
E16															
grnt	11	41.62	0.18	21.99	2.55	7.44	18.54	0.31	7.39	0.01	0.00		100.03	0.82	0.84
		0.17	0.07	0.20	0.28	0.16	0.25	0.01	0.23	0.01	0.00				
cpx	10	52.92	0.15	3.23	0.97	2.47	17.98	0.08	21.10	0.51	0.02		99.44	0.93	0.29
		0.40	0.02	0.46	0.14	0.10	0.33	0.01	0.67	0.08	0.02				
opx	15	55.78	0.07	3.28	0.74	5.60	33.53	0.11	0.81	0.03	0.00		99.96	0.91	0.35
		0.31	0.01	0.23	0.09	0.13	0.31	0.01	0.08	0.02	0.00				
oliv	11	40.53	0.00	0.01	0.01	8.86	50.40	0.09	0.06			0.07	100.03	0.91	0.37
		0.38	0.00	0.01	0.01	0.10	0.22	0.03	0.01			0.02			
glass	443	43.19	0.82	14.65	0.08	5.38	11.21	0.11	10.65	2.20	0.61		88.90	0.79	
		1.75	0.06	0.65	0.17	0.29	1.39	0.02	0.76	0.40	0.11				
E18															

grnt	16	41.75	0.40	22.69	1.70	7.75	18.51	0.29	7.00	0.04	0.01		100.13	0.81	0.66
		0.26	0.10	0.45	0.44	0.26	0.40	0.02	0.40	0.02	0.01				
cpx	11	53.57	0.34	3.06	0.61	2.40	18.18	0.08	21.37	0.73	0.00		100.34	0.93	0.21
		0.42	0.05	0.50	0.15	0.23	0.37	0.02	0.26	0.08	0.00				
opx	11	55.26	0.15	2.79	0.35	5.45	33.78	0.09	0.71	0.06	0.00		98.65	0.92	0.25
		0.56	0.02	0.65	0.09	0.16	0.51	0.01	0.10	0.02	0.01				
oliv	15	40.39	0.03	0.05	0.04	8.33	50.38	0.09	0.06			0.05	99.42	0.92	0.26
		0.18	0.01	0.15	0.05	0.16	0.29	0.02	0.06			0.04			
glass	38	56.68	0.96	18.94	0.03	1.81	2.74	0.03	2.70	5.57	2.10		91.40	0.74	
		2.41	0.08	0.98	0.04	0.21	0.89	0.02	0.68	1.85	0.35				
E19															
grnt	13	41.73	0.24	23.46	0.82	8.17	19.04	0.29	6.28	0.02	0.00		100.04	0.81	0.65
		0.19	0.06	0.43	0.32	0.10	0.42	0.02	0.63	0.02	0.00				
cpx	10	53.49	0.33	3.11	0.60	2.55	17.74	0.07	21.56	0.72	0.01		100.17	0.93	0.22
		0.36	0.03	0.28	0.15	0.12	0.28	0.01	0.32	0.07	0.01				
opx	15	55.35	0.13	3.13	0.37	6.08	33.47	0.09	0.64	0.07	0.00		99.35	0.91	0.28
		0.59	0.01	0.66	0.09	0.12	0.49	0.01	0.03	0.03	0.00				
oliv	12	40.47	0.01	0.06	0.01	9.22	49.88	0.06	0.07			0.20	99.98	0.91	0.28
		0.26	0.01	0.10	0.01	0.13	0.37	0.02	0.05			0.07			
glass	19	51.04	0.86	16.99	0.00	2.44	3.72	0.02	3.69	10.08	1.63		90.47	0.73	
		1.27	0.05	0.73	0.01	0.14	0.33	0.01	0.59	1.04	0.28				
E20															
grnt	13	42.11	0.66	22.10	1.38	8.43	17.63	0.31	8.48	0.03	0.00		101.13	0.79	
		0.60	0.34	0.96	0.59	0.26	0.47	0.02	1.10	0.03	0.00				
cpx	13	54.09	0.25	2.79	0.45	2.69	17.62	0.06	21.93	0.62	0.01		100.51	0.92	
		0.31	0.05	0.51	0.11	0.13	0.43	0.01	0.30	0.09	0.01				
opx	10	54.49	0.13	4.65	0.54	6.37	32.16	0.09	0.66	0.01	0.00		99.09	0.90	
		0.65	0.02	0.85	0.09	0.13	0.48	0.01	0.07	0.01	0.00				
oliv	10	40.96	0.00	0.05	0.01	9.65	49.63	0.08	0.06			0.25	100.70	0.90	
		0.49	0.00	0.06	0.02	0.12	0.50	0.02	0.03			0.09			
glass	0	N/A	N/A	N/A	N/A	N/A	N/A	N/A	N/A	N/A	N/A	N/A	N/A	N/A	
		N/A	N/A	N/A	N/A	N/A	N/A	N/A	N/A	N/A	N/A	N/A	N/A	N/A	
E23															
cpx	10	53.41	0.09	2.99	1.24	2.68	18.34	0.10	20.69	0.53	0.01		100.08	0.92	0.26
		0.24	0.03	0.16	0.13	0.17	0.41	0.01	0.42	0.07	0.01				
opx	10	55.48	0.04	2.79	0.87	5.44	34.00	0.12	0.91	0.03	0.00		99.68	0.92	0.29
		0.23	0.02	0.10	0.07	0.16	0.26	0.01	0.07	0.02	0.00				
oliv	10	40.63	0.00	0.02	0.06	8.59	50.69	0.11	0.06			0.08	100.23	0.91	0.30
		0.24	0.01	0.01	0.01	0.09	0.26	0.02	0.01			0.03			
spin	1	0.17	0.28	26.01	43.83	13.22	16.88	0.25	0.05			0.08	100.76	0.69	1.44
glass	213	45.49	0.76	15.70	0.16	5.77	10.32	0.13	12.34	2.33	0.54		93.54	0.76	
		1.77	0.06	0.83	0.09	0.26	1.31	0.02	0.59	0.40	0.08				

C647														
cpx	14	53.62	0.08	2.79	1.23	2.72	18.27	0.07	21.12	0.51	0.01		100.43	0.92	0.27
		0.29	0.02	0.22	0.14	0.10	0.30	0.01	0.27	0.04	0.01				
opx	15	56.13	0.05	2.54	0.89	5.51	33.38	0.09	0.96	0.04	0.00		99.59	0.92	0.30
		0.15	0.01	0.17	0.09	0.07	0.20	0.01	0.05	0.02	0.00				
oliv	15	40.65	0.02	0.02	0.02	8.80	50.27	0.12	0.09			0.23	100.22	0.91	0.32
		0.18	0.01	0.02	0.02	0.09	0.30	0.02	0.01			0.03			
spin	5	0.31	0.31	23.48	45.17	15.15	15.57	0.26	0.12			0.16	100.53	0.65	1.77
		0.39	.05	.45	.25	.24	.77	.03	.06			.08			
glass	327	46.10	0.43	14.92	0.12	6.21	11.31	0.07	11.57	1.74	0.47		92.95	0.76	
		2.60	0.33	1.60	0.55	0.76	3.57	0.06	1.44	0.50	0.17				
C648														
opx	13	55.81	0.03	2.39	0.92	5.31	33.14	0.10	0.96	0.03	0.00		98.69	0.92	0.34
		0.24	0.01	0.15	0.11	0.06	0.24	0.01	0.09	0.03	0.00				
oliv	15	40.69	0.01	0.04	0.06	8.36	50.16	0.10	0.09			0.11	99.62	0.91	0.36
		0.15	0.01	0.03	0.02	0.06	0.23	0.03	0.02			0.01			
spin	6	0.32	0.25	21.03	48.11	14.15	16.13	0.19	0.04			0.04	100.25	0.67	1.88
		0.07	0.02	1.01	1.38	0.13	0.67	0.03	0.02			0.01			
glass	534	45.91	0.61	13.38	0.19	6.58	14.12	0.12	10.88	1.93	0.45		94.16	0.79	
		1.27	0.04	0.78	0.04	0.30	1.63	0.02	0.61	0.19	0.07				
C649														
cpx	15	53.34	0.14	3.37	0.97	2.63	17.99	0.07	21.34	0.53	0.00		100.39	0.92	0.25
		0.24	0.02	0.31	0.11	0.06	0.18	0.01	0.23	0.04	0.00				
opx	10	55.91	0.05	3.31	0.82	5.76	32.91	0.11	0.79	0.04	0.01		99.73	0.91	0.30
		0.35	0.02	0.12	0.12	0.03	0.22	0.01	0.08	0.02	0.00				
oliv	13	40.68	0.01	0.01	0.04	9.44	49.87	0.08	0.07			0.16	100.37	0.90	0.32
		0.18	0.01	0.01	0.01	0.10	0.27	0.03	0.03			0.03			
spin	8	0.42	0.26	32.52	35.15	14.45	16.13	0.19	0.04			0.04	100.31	0.68	1.44
		0.63	0.03	1.48	0.97	0.15	0.57	0.01	0.05			0.03			
glass	76	45.60	0.88	16.86	0.08	6.16	10.52	0.13	12.22	2.98	0.70		96.14	0.75	
		0.59	0.05	0.42	0.03	0.18	0.94	0.02	0.45	0.22	0.06				

Table 3.2 Mineral and glass compositions of experiments.

Chapter 4: The Viscosity of a Partially Molten Layer in a Paleo-Orogenic Plateau

Abstract

Orogenic plateaus (e.g., Tibet, Altiplano) are enigmatic features, characterized by broad, flat-top topography at high elevation. Geodynamic models of Tibet hypothesize that a low viscosity mid-lower crustal layer sustains the broad and flat topography associated with the Tibetan plateau. Partial melt is thought to weaken the middle crust of orogenic plateaus, and thus reduce the viscosity of the crust; however, the amount of partial melt and the magnitude of associated weakening remain unconstrained. The New England Appalachians represent an exposed mid- to lower crustal section of a paleo-orogenic plateau, similar to modern-day Tibet. In this study, we utilize the relationship between the spacing of deformation bands and the compaction length to constrain mid-crustal shear viscosity in a late Devonian migmatite. We find that the viscosity of the middle orogenic crust in the paleo-orogenic plateau of the New England Appalachians is $10^{17\text{-}18}$ Pa·s at ~3-9% melt. This finding is consistent with geophysical models of orogenic channel flow and provides field-based evidence for a significant rheologic transition at low melt-fraction. Our results suggest that the key elements for the formation of a weak, mid-crustal layer in orogenic plateaus are an influx of water and temperatures near the hydrous granite solidus.

4.1 Introduction

Orogenic plateaus (e.g., Tibet, Altiplano) are enigmatic features, characterized by broad, flat-top topography at high elevation. Crustal thickening, in association with mid-lower crustal magmatism initiating mid-lower crustal viscous flow, is the most commonly invoked mechanism for plateau formation across tectonic settings (e.g., Orellana-Rovirosa and Richards, 2016 for Galapagos). In particular, geodynamic studies of the Tibetan plateau advocate for a weak, viscous layer ($\eta \leq 10^{18}$ Pa·s) in the mid-lower crust to explain a range of geodetic and seismic observations (Clark and Royden, 2000). The exact origin of these low viscosities, which are approximately five orders of magnitude lower than the viscosity of the crust at the margins of the plateau, is debated. Partial melting (Jamieson et al., 2011) or the circulation of free fluids (Kohlstedt et al., 1995), could in principle result in such low viscosities. Indeed, the presence of a weak, partially molten layer at 20-50 km depth in Tibet is supported by low seismic wave speeds observed in geophysical studies (Hacker et al., 2014). However, how much small melt fractions affect viscosity remains an open, but critical, question. Classically, a threshold of ~20-60% partial melt (Rheologically Critical Melt Percentage (RCMP)) is thought necessary to lower the viscosity over five orders of magnitude (van der Molen and Paterson, 1979).

Alternatively, it has been proposed that the strength of partially molten rocks decreases significantly at low melt fractions (~7% partial melt) (Rosenberg and Handy, 2005). In lab experiments this transition, referred to as the Melt Connectivity Transition (MCT), results in a reduction of less than an order of magnitude, which is borderline insufficient for crustal flow in quartzo-feldspathic rocks (Beaumont et al., 2001). However, experiments are conducted at higher strain rates than observed in nature and do not include the full range of heterogeneity and damage observed in natural systems. Thus, extrapolating laboratory observations to the natural world remains a key open challenge in Geosciences (Breithaupt et al., 2023). While the mid-lower crust of the Tibetan plateau is variably exposed along major faults (Van Buer et al., 2015), there is minimal surface exposure of the postulated lower viscosity region. In contrast, the New England Appalachians expose a continuous section through the mid-lower crust of a Paleozoic orogenic plateau comparable to the Tibetan plateau or Puna-Altiplano (Hillenbrand et al., 2021). Hillenbrand et al. (2021) found that an orogenic plateau developed by 380 Ma in the Acadian orogen exposed in New England. Thus, these exposures provide an unrivaled opportunity to observe and quantify melt fraction and viscosity in the mid-crust of an orogenic plateau by studying exhumed mid-lower crustal rocks. These results in turn provide key ground truthing observations for geodynamic models for crustal flow and the nature of plate-scale deformation.

Here, we studied an exceptional example of near uniformly spaced melt-filled deformation bands in high-grade metasediments in Rumney, New Hampshire (Figure 4.1). The field area in central NH represents the exhumed middle crust of the Acadian-Neoacadian orogen (Chamberlain and Lyons, 1983; Hillenbrand et al., 2021). We utilize a novel method to calculate the shear viscosity of the metasediments by applying the relationship between the compaction length and shear viscosity (McKenzie, 1984). The observed spacing of melt-filled deformation bands provides direct field constraints on the compaction length at the time of melting.

With both the field observations regarding the spacing of melt preserved in the leucosomes, as well as melt viscosity and permeability, we can calculate a macro-scale shear viscosity of the metasediments during Neoacadian deformation (395-350 Ma, Van Staal et al., 2009) completely independent of the lab derived flow laws. Although this method has a number of uncertainties in each component, it provides an independent method to probe the effective rheology of the mid-lower crustal regions with low degrees of melting. In section 4.2, we describe the geological background of the exposed bedrock in central New Hampshire. In section 4.3, we present our workflow and methodology surrounding image analysis constraints on melt fraction and permeability, grain size distribution analysis, thin section textural analysis and justification for constraining melt viscosity, and geochronologic laboratory methods used to constrain the age of melting. In section 4.4, we discuss our observations and results obtained following the methodology and present an initial calculation of shear viscosity for the studied migmatite. Additionally, in section 4.4, we discuss whether *in situ* melting is the source of the late-kinematic leucosomes or if melt is externally sourced from nearby plutons. Finally, we discuss our results in section 4.5, linking our observations with past literature and regional mapping of New Hampshire, presenting a comparison to orogenic plateaus in Tibet and South America, and comparing our estimates of viscosity to those from experimentally constrained flow-laws.

4.2 Geological Background

We studied metatexitic metasediments of the Littleton Formation from the Central Maine Terrane (CMT) of New Hampshire, exceptionally well exposed near Rumney, NH (Figures 4.1 and 4.2). The CMT is a Siluro-Devonian basin that experienced deformation and metamorphism during the Acadian (421-400Ma, Van Staal et al., 2009) and Neoacadian orogenies (395-350Ma, Van Staal et al., 2009). The CMT in New Hampshire spans the upper to middle crust of an Acadian orogenic plateau (~3-6 kbar, Spear et al., 1990; Hillenbrand et al., 2021). Regional metamorphism in central New Hampshire reached temperatures of ~500-800°C and pressures of ~4-6kbar (Chamberlain and Lyons, 1983). Deformation began with early Devonian isoclinal folding and thrusting and at least one additional phase of tight to isoclinal, upright folding about subhorizontal, NE-trending folds (Eusden and Lyons, 1993).

The Acadian orogeny in New England is followed by the proposed collision of Meguma with the trailing margin of Avalonia, termed the Neoacadian orogeny (395-350Ma, van Staal et al., 2009). The Neoacadian orogeny in New Hampshire is characterized by the intrusion of a regional suite of peraluminous granites between 375-350 Ma (Eusden and Barrerio, 1988). Contemporaneous with this regional plutonism, migmatization of the CMT occurred from Maine through central Massachusetts (Figure 4.1, Tracy, 1985; Eusden, 1988; Solar and Brown, 2001; Kohn et al., 2003; Chu et al., 2018). Late Devonian migmatite localities are spatially associated with local hotspots of upper Amphibolite and Granulite facies metamorphism (Tracy, 1985; Chu et al., 2018) as well as the intrusion of the Concord granite series (Eusden, 1988, Figure 4.1). A distinction can be drawn between migmatites in west-central Maine (i.e., Solar and Brown, 2001) and migmatites in central New Hampshire and Massachusetts (Tracy, 1985; Eusden, 1988; This Study). Migmatites in Maine are emplaced in the early Acadian orogeny (>380Ma), prior to the emplacement of Neoacadian peraluminous granites (Solar et al., 1998). Migmatites in central and southeastern New Hampshire are emplaced during the Neoacadian orogeny (<380Ma, Eusden and Barrerio, 1988; Spear et al., 1990). While migmatization and late kinematic plutonism are spatially pervasive throughout central Massachusetts and central New Hampshire, a prominent, orogen perpendicular belt of these plutons and migmatites outcrops in central New Hampshire (Figure 4.1). This belt is characterized by Acadian metamorphic pressures of ~4-5kb and temperatures near the hydrous granite solidus (Eusden, 1988).

The rocks in the field area are anatectic pelitic schists, variably intruded by external granite dikes and in-source leucosomes (Figure 4.2). Small, discordant granite melt patches intrude boudin necks of the earliest, S1 foliation (e.g., Arslan et al., 2008), and are therefore late kinematic relative to Acadian deformation. Petrographic descriptions of the schist and granite melt patches with thin section images are given in Appendix 2(A2.3, Figs. A2.8-A2.10). Synchronous with the intrusion of the discordant granite melt patches, a large pluton of two-mica granite, the Newfound Lake Pluton (364.03 ± .46Ma, Sullivan, 2014), intruded the CMT contemporaneous with the Acadian orogenic plateau. While migmatization is not a rare or unique process, sensu stricto, the exposed migmatite discussed herein presents an unrivaled opportunity to study the processes of partial melting and melt migration during deformation in the initial stages of melting (at low melt fractions). The processes at low melt fraction are expected to continue with increasing melt fraction and will ultimately result in the larger features observed in partially molten rocks such as discordant dikes and layer parallel or stromatic migmatites.

4.3 Workflow and Methodology for the Calculation of Shear Viscosity

To calculate the shear viscosity of a discordant migmatite we use the compaction length, first formulated by McKenzie (1984). The compaction length, δ_c, is a length scale in two phase systems (a system with both a melt phase and solid assemblage) that depends on fundamental material properties of the crystalline matrix and melt phase (McKenzie, 1984). δ_c, is the natural length-scale of magma–solid phase interaction in a viscous two-phase flow and sets the length-scale over which solid matrix compaction occurs when there is either a strong change in flow (e.g., impermeable layer) or a local source of fluid (e.g., melt production). Consequently, compaction length naturally controls the spacing of melt localization features such as shear bands and melt-rich leucosomes (McKenzie, 1984; Katz, 2022). This concept provides a quantitative means to estimate both shear and bulk viscosity (also termed, "compaction viscosity") in experimental and natural settings (e.g., Holtzman et al., 2003; Weinberg et al., 2015). Both the shear and bulk viscosity are required to describe deformation when the mean density of a porous matrix is not constant (as opposed to only shear viscosity when density is constant).

The derivation of the compaction length is well documented in the literature (e.g., McKenzie, 1984; Holtzman et al., 2003; Kohlstedt et al., 2010). The fundamental form of the compaction length is:

$$\delta_c = \sqrt{\frac{\kappa * \left(\zeta + \frac{4}{3}\eta\right)}{\mu}} \quad Eq. 1$$

where, κ, is permeability, ζ, is bulk viscosity, η, is shear viscosity of the crystalline matrix, and μ, is the melt viscosity. In section 4.4.5, we will compare calculated effective viscosity vs shear viscosity. The shear viscosity represents the viscosity, under simple shear, of the solid framework, accounting for the permeability/porosity but not the melt viscosity. The effective viscosity represents the bulk strength of the rock accounting for both the shear viscosity and the melt viscosity. We can assume an upper bound on the effective viscosity based on the Voigt bound (e.g., Ji et al., 2004). The Voigt bound on effective viscosity is a simple geometric mean of the melt viscosity and shear viscosity:

$$\eta_{eff} = \eta(1 - \phi) + \mu(\phi)\ Eq. 2$$

where, η_{eff}, is the effective viscosity in Pa·s and, ϕ, is the melt fraction or porosity (discussed in section 4.3.2).

However, because we are primarily interested in the shear viscosity, we can assume $\zeta \ll \eta$, following the approach of Holtzman et al. (2003). This reduces the equation for compaction length to the form:

$$\delta_c = \sqrt{\frac{\frac{\kappa * 4}{3}\eta}{\mu}}\ Eq. 3$$

and allows us to use the lab based calibration between compaction length and band spacing in a self-consistent manner. For metamorphic rocks, McKenzie and Holness (2000) justify the assumption, $\zeta \ll \eta$, from the assertion that isotropic compaction results in transport across short distances relative to the longer distances required by diffusion transport between crystals under simple shear.

We can relate the compaction length to the observed spacing of melt-filled deformation bands by assuming a linear relationship between melt-filled deformation band spacing and compaction length, constrained by experiments of partially molten aggregates (e.g., Holtzman et al., 2003). For the simplified form of the compaction length (Eq. 3), the scalar value relating observed spacing of deformation bands to the compaction length, hereafter termed, L, is typically 0.14-0.15 (Eq. 4, Holtzman et al., 2003; Kohlstedt et al., 2010). We assume a value of .15 to transpose deformation band spacing and compaction length in our study.

$$L = (.15)\delta_c\ Eq. 4$$

In the following sections we outline the methods used to constrain permeability, melt viscosity, and the spacing of melt-filled deformation bands necessary for calculating shear viscosity from compaction length and briefly discuss the geochronologic methods which are important for contextualizing our analysis relative to the Acadian-Neoacadian orogenic plateau.

4.3.1 Constraining Melt-Filled Deformation Band Spacing

The spacing of melt-filled deformation bands is proportional to the compaction length (Holtzman et al., 2003) and therefore fundamental to our calculation of shear viscosity through Eq. 3. To constrain the spacing, we made direct measurements of the spacing of leucosomes, hosted in sites of foliation boudinage (Arslan et al., 2008), on multiple outcrop surfaces across the field area. Figure 4.2 displays the near uniform spacing of granitic leucosomes on an outcrop surface. The distance between the melt patches was measured from the center of an ellipse that approximates the shape of the melt patch. Two distances were measured: the distance to the next melt patch parallel to the long axis and the distance to the next melt patch parallel to the short axis (Figure 4.4). There is an error of ±1.27cm associated with the spacing measurements based on the precision of the measuring implement used in the field. We present the quantitative results of our measurements and qualitative descriptions of the outcrop structures in Section 4.4.1 (Figure 4.4).

4.3.2 Constraining Permeability

The compaction length is partly dependent upon the permeability of the migmatite during deformation (Eqs. 1 and 2). The permeability can be calculated from porosity, ϕ, and grain size, d, via the following commonly used relationship (Eq. 5, Table 4.2, Wark and Watson, 1998; Katz et al., 2022).

$$\kappa = \frac{d^2\phi^3}{200}\ Eq.5$$

Thus, to calculate permeability, and ultimately shear viscosity, we must constrain porosity and grain size for the field area. We can assume that porosity, or the volume of fluid filled space, is approximately equal to the melt fraction of the migmatite. This assumption generally holds for migmatites as the melt filled pore space is much greater than the vapor filled pore space during migmatization. The grain size can be directly constrained from thin sections of the lithology in the field area using grain size distribution analysis. A detailed description of our analysis methodology for grain size is given in the Appendix (A2.1).

To constrain melt fraction, or the approximate porosity, we segmented outcrop images from the field into leucocratic pixels belonging to granitic leucosomes and meso- and melanocratic pixels corresponding to the schist. We employed the MATLAB "Image Segmenter" application in the image processing toolbox to create a masked image of leucocratic pixels with the "Graph Cut" algorithm. Leucocratic pixels are identified based on abrupt changes in RGB color between neighboring pixel values. "Graph Cut" allows the user to manually select foreground and background objects to refine the image segmentation, which correspond to leucosomes and schist, respectively. The final image mask of leucocratic Type (I) melt patches is then imported into Fiji (Schindelin et al., 2012), where we convert the image mask to a binary image. Before calculating melt fraction, we select only the area of the image where melt patches are well exposed, excluding excess area where there was problematic lighting, dikes, or vegetation. Finally, we calculate the fraction of leucocratic, Type (I) melt patches relative to the size of the selection. The results of the Image Segmentation are discussed in Section 4.4.2, and figures of the image segmentation results for various outcrop faces are given in the Appendix (Figures A2.1-A2.4).

4.3.3 Constraining Melt Viscosity

Melt viscosity is inversely related to compaction length and directly proportional to shear viscosity (Eq. 3). The melt viscosity is strongly dependent on the solubility of water in the melt phase (Giordano et al., 2008; Thomas and Davidson, 2012). To derive an estimate of melt viscosity for the granitic melt preserved in the leucosomes at the time of deformation, we must first derive an estimate of the melt's water content. In the case of water saturation, we can calculate the water content of a felsic melt from the pressure at which the melt is present (Newman and Lowenstern, 2002). This will provide a maximum estimate of water content. The pressure of melting can be roughly constrained with the garnet-biotite-muscovite-plagioclase geobarometer to within a kilobar (Wu et al., 2015).

We can infer water saturation based on the temperature of the melting reaction. In the case of low melting temperatures (600-650˚C) in the NaKFMASH compositional system, the protolith must be vapor saturated (Spear et al., 1999; Weinberg and Hasalova, 2015). As discussed later, we use garnet-biotite equilibrium to calculate the melting temperature of the system. The use of Mg-Fe exchange between garnet and biotite to estimate the temperature of metamorphism is well established (i.e., Hodges and Spear, 1982; Holdaway, 2000; Wu and Cheng, 2006). With an estimate of the water content, given a granitic bulk composition and melting temperature, we can use the model of Giordano et al. (2008) to calculate the melt viscosity at the time of melting.

4.3.4 Zircon Geochronology

Lastly, we present new laser ablation inductively coupled mass spectrometry (LA-ICP-MS) geochronologic data on the timing of melt emplacement in the field area (see Appendix A2.4 for detailed methodology). This is necessary to evaluate the significance of our results in the context of the recently hypothesized Acadian-Neoacadian orogenic plateau (Hillenbrand et al., 2021). Two samples were analyzed for U-Pb in zircon. Sample RY2142 is composed of multiple cores (~1in diameter, ~1-2in long) of the leucosome taken from a roadcut in the field area (43.8020 ˚N, 71.8332 ˚W). Sample RY219 is from the mesocratic schist at the same roadcut. Detrital and metamorphic zircons in sample RY219 can be compared to the population of zircons in sample RY2142 to assess any zircon inheritance in the leucosomes. The results of the U-Pb zircon geochronology are presented in Section 4.4.4.

4.4 Results

In this section, we detail the results of our field observations on melt-filled deformation band spacing, the imaged based constraints on permeability, and the textural and geochemical constraints on melt viscosity.

4.4.1 Field Observations of Melt-Filled Deformation Band Spacing

Two types of melt patches can be identified in the field which we name Type (I) and Type (II). Type (I) are 5-25cm in length and form a conjugate set, with one east dipping and one west dipping population. Type (I) melt patches are strongly discordant relative to the foliation throughout the field area. The melt patches are sub-ellipsoidal in shape, with typical short to long axis ratios of ~3:1. Short and long axes are on average ~5cm and ~15cm, respectively (A2.3, Figure A2.5). Type (II) granite melt patches are significantly smaller (<1 cm) than Type (I) and are sub elliptical to circular on the outcrop face (Figure 4.2 and 4.3). Type (II) melt patches are rimmed by a melanocratic assemblage of biotite+sillimanite±garnet. Furthermore, Type (II) melt patches are uniformly distributed throughout the host aluminous schist layers in the easternmost outcrops of the field area as opposed to quartz and feldspar rich layers less prone to partial melting. The location and internal structure of the small granite leucosomes, relative to the adjacent foliation and lineation, suggests no influence from the deformation that affects the larger melt patches. Discordant and concordant dikes of two-mica granite are present throughout the field area. These dikes consist of equicrystalline, aplitic to pegmatitic, micaceous granitoids with minor garnet. The externally sourced dikes range in width from a few centimeters to four meters, and they range in length from a meter to hundreds of meters across the field area.

On average, Type (I) melt patches are spaced 30-35cm apart regardless of the outcrop orientation and the angle of measurement (Figure 4.4). The spacing of Type (I) melt patches ranges from 10-85cm. Type (II) melt patches are spaced between 1-23cm, with an average spacing of ~5cm (Figure A2.6). The small, individual volume of Type (II) granite leucosomes, in association with melanocratic rims, and their independence from post-depositional structures and dependence on the compositional variability in the protolith, all suggest that *in situ* melting is the source of the late-kinematic granite melt patches. The uniform spacing of Type (I) melt patches and spatial association with deformation bands, in the form of foliation boudinage, suggest that *in situ* melt (Type (II) melt patches) migrated into deformation bands during compaction of the partially molten assemblage.

4.4.2 Constraints on Melt Fraction and Permeability

The melt fraction of Type (I) leucosomes in four outcrops within the field area varies from 2.8 vol.% to 7.0 vol.% (Figures A2.1-A2.4). The melt fraction of Type (I) melt patches increases in outcrops to the southeast (4.1-7.0 vol.%) relative to outcrops in the northwest (2.8-3.4 vol.%). Type (II) melt patches are only present in the southeasternmost outcrops.

After constraining the melt fraction of Type (I) leucosomes, we must account for the melt fraction of the Type (II) leucosomes, which are too small to be resolved during image processing. We used field measurements of the size and spacing of Type (II) leucosomes and assumed a uniform distribution throughout the outcrop (only for outcrops where Type (II) leucosomes are present and near-uniformly distributed across the outcrop face). A small ellipsoid with dimensions of 1.2x1.2x0.5cm can approximate the volume of the Type (II) melt patches (Figure A2.6). This yields an individual volume of ~3cm^3 for each individual Type (II) melt patch. If we consider a cubic volume with a Type (II) melt patch at each corner and a total volume of 125cm^3 (based on the spacing of Type II leucosomes, Figure A2.7), the total melt fraction of the volume from the Type (II) melt patches is ~2%. The total melt fraction of the southeasternmost outcrops (Type (I) and Type (II) leucosomes volume) is 6.1-9.0 vol.%. From these observations we can assume a lower bound of 2.8 vol.% and an upper bound of 9.0 vol.% on the porosity (melt percentage) during melt emplacement and deformation.

To calculate permeability, we use the above constraints on melt fraction and thin section constraints on grain size (Appendix A2.1). Thin section constraints on grain size in the field area suggest a median grain size of 0.25-0.57mm for three thin sections across the field area. From these constraints Eq. 5 yields a range of permeabilities from $1.20\cdot10^{-14}$-$1.18\cdot10^{-12}$m^2. These calculated permeabilities are approximately consistent with the range of migmatite permeabilities constrained by Weinberg et al. (2015).

4.4.3 Pressure-Temperature-Time Constraints and Melt Viscosity

The Littleton schist in the field area is composed of the assemblage quartz (Qtz)+plagioclase (Plag)+biotite (Bt)+sillimanite (Sil)±garnet (Grt)±muscovite (Ms). In Figure 4.3, we observe a Type (II) melt patch on the right side of the section in equilibrium with a melanocratic rim assemblage of Bt+Sil±Grt. This suggests the melt phase is in equilibrium with the melanocratic rim assemblage. The absence of muscovite in equilibrium with the melt phase and the presence of sillimanite in the melting residue is emblematic of vapor saturated muscovite melting (Icenhower and London, 1995; Milord et al., 2001; Weinberg and Hasalova, 2015). In this case, the melting reaction based on the textures in thin section is Qtz+Ms+Plag+H_2O = Bt+Sil+Liq±Grt. Therefore, Bt-Grt geothermometry will constrain the approximate temperature of the melting reaction.

Grt-Bt thermometry (Hodges and Spear, 1982) yields an average temperature of metamorphism of ~609 +/- 34°C, (Figure 4.3). Mineral chemistry of two representative samples (RY202A and RY2130A) is presented in the data repository (Table A2.1). The garnet–biotite–muscovite–plagioclase GBMP barometry (Wu et al., 2015) for both samples yield pressures of ~5kb +/- 1kb, consistent with previous studies of the metamorphic pressure in central New Hampshire based on major element mineral compositions throughout (Chamberlain and Lyons, 1983). A water-saturated, felsic melt at 5kb will contain ~13 wt.% H_2O (Newman and Lowenstern, 2002). The melt viscosity model of Giordano et al. (2008) constrains melt viscosity to ~10^4Pa·s for a granitic bulk composition, with 13 wt.% water, at 650-700°C.

We interpret Type (II) melt patches as *in situ* melts based on the criteria outlined in our prior discussion of field observations. In contrast to Type (II) melt patches, Type (I) melt patches are not associated with melanocratic rims (Figure 4.2), and they are emplaced into boudin necks formed during foliation boudinage (Figure 4.2, Arslan et al., 2008). This suggests that Type (I) melt patches are in-source, but not *in situ* melts of the schist. It is also possible that Type (I) melt patches are externally sourced from the nearby Newfound Lake Pluton (Figure

4.1), especially in consideration of the similarity in intrusive age constrained from zircon U-Pb geochronology (Sullivan, 2014). An external source for the leucosomes is, however, unlikely as the small volume of Type (I) melt patches precludes melt transport over long distances at the near solidus conditions of the host rock. Together, these observations suggest that Type (I) melt patches are sourced from the migration and collection of Type (II) melt patches.

Both the melting temperature and textural observations in thin section support a vapor-saturated melting reaction. Weinberg and Haslova (2015) demonstrate that vapor saturated melting results in a negative volume change. This is consistent with the outcrop structure of the leucosomes in sites of foliation boudinage as the negative volume change would draw *in situ* melts into dilatational sites. While local lithological heterogeneity and preexisting damage zones in the rock may result in a more complex visco-elasto-plastic rheology as opposed to a dominantly viscous rheology assumed for the compaction length, the relationship between the spacing of melt-collection sites and the shear viscosity should still reflect an accurate constraint within the error of our methods as discussed in Section 4.5.1. It is beyond the scope of this study to discuss, in detail, the effects of complex, local variations in rheologic behavior and the effect of specific lithologic and geometric variations on the shear viscosity.

4.4.4 Timing of Melt Migration and Emplacement

The mean age of the melt patch zircons is 361.85 ± 0.71Ma (S4, Figs. A2.11 and A2.12). We did not identify a detrital population in the leucosomes as all zircons are younger than 380 Ma, which is significantly younger than the minimum depositional age of the Siluro-Devonian metasedimentary rocks in the CMT (see Figure A2.14; Bradley and Sullivan, 2017). We interpret the age distribution as reflecting near-contemporaneous intrusion of the melt patches within the error of our analysis. This is reinforced by field observations of cross cutting relationships between melt patches and granite dikes, which suggest relatively contemporaneous intrusion of granitoids into the field area. The distribution of zircon crystallization ages does not preclude incremental melting and melt emplacement (meaning our constraint on melt percentage is a maximum constraint), however this is beyond the scope of this study and the precision of our data.

The age of emplacement of the Type (I) melt patches (361.85 ± 0.71Ma) is contemporaneous with the postulated time of the Acadian orogenic plateau (380-330Ma; Hillenbrand et al., 2021). It is also contemporaneous with the emplacement of individual, Concord granite plutons that were emplaced regionally during the Neoacadian orogeny (~375-354Ma, Eusden and Barrerio, 1988; Sunapee Pluton, 354 ± 5Ma; Harrison et al., 1987; Newfound Lake Pluton, 364.03 ± .46Ma, Sullivan, 2014).

4.4.5 Calculation of Shear Viscosity

The average spacing of Type (I) melt patches is ~30cm (Figure 4.4). For the purposes of our initial shear viscosity calculation, we utilize a grain size of ~0.00033 m as constrained from observations of quartz grain size in thin section (Appendix A2.1, Figures A2.8-A2.10). Additionally, we assume an average porosity of 6%. These constraints yield a permeability of $1.18 \cdot 10^{-13} m^2$. We will discuss the effect of variations in grain size and porosity on the shear viscosity in the next section. We assume melt viscosity is ~10^4Pa·s as discussed in Section 4.4.3. Figure 4.6 displays the results of our initial calculation of shear viscosity based on the permeability, melt fraction, and deformation band spacing constrained in this study. Based on the above constraints (Table 4.1), for a deformation band spacing of ~30cm (Figure 4.4), the shear viscosity of the migmatite at the time of melt emplacement into boudin necks (361.85 ± 0.71Ma) was ~10^{17-18}Pa·s (Figure 4.6).

We take 3-9% of the melt to have segregated into deformation bands based on our image processing results and we set the melt viscosity and shear viscosity as 10^4 and 10^{17}Pa·s. Using the Voigt bound (Eq. 2), we calculate an effective viscosity of $9.4(\pm 0.3) \cdot 10^{16}$Pa·s. The results are not overly sensitive to the exact value of melt porosity since the melt viscosity is thirteen orders of magnitude less than shear viscosity Overall, we find that effective viscosity is not significantly different than shear viscosity, especially when considering the inherent errors to our calculation of shear viscosity in the following section.

4.5 Discussion

4.5.1 Sensitivity of the Compaction Length to Select Parameters

In this section, we discuss the inherent uncertainties associated with the calculation of shear viscosity in this study and the sensitivity of shear viscosity to variations in grain size, melt fraction, melt viscosity, and Type (I) leucosome spacing (Figure 4.7). With any method used to constrain the viscosity of natural rocks, including utilizing experimentally constrained flow laws (Breithaupt et al., 2023), there are inherent large uncertainties. Grain size and melt fraction are utilized in the calculation of permeability while melt viscosity and leucosome spacing are related to the compaction length. In calculating the variation of shear viscosity based on the chosen parameters, we hold constant the initial values discussed in the previous section, only allowing for variation in one of the parameters at a time (Figure 4.7). The method outlined in this study presents an alternative method for constraining natural shear viscosity and effective viscosity, which is especially useful for discordant migmatites.

Our observations of grain size suggest that most grains are 0.25-0.55mm in diameter with the largest population of grains averaging .33mm. The minimum grain size is ~.1 mm, while the maximum grain size is ~.5mm. Allowing for variation in grain size across the observed range in thin section results in a variation in shear viscosity from ~10^{17}-$2 \cdot 10^{18}$Pa·s (Figure 4.7a).

Image segmentation constraints on melt fraction suggest a range in melt fraction from 2.8-9.0 vol.%. Allowing for variation in the compaction length based on this range yields a spread in viscosity from $7 \cdot 10^{16}$ to $2 \cdot 10^{18}$Pa·s (Figure 4.7b). The systematic decrease in melt fraction from east to west across the field area likely resulted in a decrease in local shear viscosity with proximity to the nearby Newfound Lake pluton.

Of the four chosen parameters (Figure 4.7), our estimate of melt fraction has the largest uncertainty due to a lack of direct constraints on melt viscosity from the field. In general, we expect an order of magnitude increase in melt viscosity to correspond to an order of magnitude increase in shear viscosity (Eqs. 1 and 2). The exact melt viscosity for a felsic water saturated melt at ~610˚C may realistically vary between 10^4-10^5Pa·s depending on the exact composition used for the melt. Allowing melt viscosity to vary within these upper and lower bounds yields a variation in shear viscosity from $2 \cdot 10^{17}$ to $2 \cdot 10^{18}$Pa·s (Figure 4.7c).

Finally, we assess the sensitivity of shear viscosity to melt-filled deformation band spacing. We allow for variation between 10 cm and 1 m, corresponding to the observed range in the field (Figure 4.4). This results in a variation in viscosity from $4 \cdot 10^{16}$-$2 \cdot 10^{18}$Pa·s (Figure 4.7d). Altogether, melt viscosity is the least well constrained of our parameters. Despite the uncertainty related to melt viscosity and our other parameters, we can reasonably conclude that the viscosity is significantly reduced relative to a melt-free rheology (Figure 4.8), and in general varies between $10^{17\text{-}18}$Pa·s. In the following discussion, we take shear viscosity to vary within this range and compare our calculated shear viscosity to geophysical and experimental constraints on the viscosity of a partially molten layer in the orogenic crust.

4.5.2 Magnitude of Partial Melt Induced Weakening

Our results establish that partially molten metasediment in the middle crust of the Neoacadian orogenic plateau deformed with a viscosity of $10^{17\text{-}18}$Pa·s during Neoacadian deformation (Figs 6 and 8). To compare these field-based results to a melt-free rheology, we calculate the melt-free viscosity of the metasediment from flow laws for individual rock-forming minerals (quartz, plagioclase, and mica) at typical orogenic strain rates and temperatures using the approach of Huet et al. (2014) as ~10^{20}Pa·s (Figure 4.8). This suggests that the presence of melt resulted in a 2-3 order of magnitude reduction in shear viscosity compared to a melt-free rheology. This reduction is significant given that the melt fraction of the migmatite is low (~6%).

Many geodynamic models assume a 1-2 order of magnitude reduction in viscosity due to melt weakening (e.g., Beaumont et al., 2004) based on experimental deformation of partially molten aggregates (Rosenberg and Handy, 2005). Beaumont et al. (2004) state that while this assumption is a conservative estimate, it is still sufficient to weaken the mid-lower crust of orogens in accordance with channel flow. Our data shows that the reduction in viscosity due to the presence of low volumes of melt may be more significant than the 1-2 orders of magnitude as suggested by some experimental data (Rosenberg and Handy, 2005). Additionally, this work presents field based evidence in support of the MCT of Rosenberg and Handy (2005), which hypothesizes significant melt weakening by 5-7 vol.% melt associated with significant interconnectivity of melt along grain boundaries. This contrasts with the alternative Rheologically Critical Melt Percentage (RCMP) hypothesis, which states melt weakening is not significant (>1 order of magnitude) until >20 vol.% melt is present. Our results also suggest that models of crustal magmatic systems with trans-crustal mushes (e.g., Cashman et al. 2017) can have significant spatio-temporal variations in rheology. These in turn would strongly modulate responses to magma recharge and magma eruptibility (Mittal & Richards, 2019).

4.5.3 Extent of Partial Melting and Intrusion in the Neoacadian Orogenic Plateau

The above discussion establishes that the middle crust of the Neoacadian orogen (emplacement at ~19km and ~360Ma) of New Hampshire was weakened due to the presence of partial melt. However, the question remains whether this is representative of regional mid-crustal flow and anatexis, or a localized partially molten contact areole. In this section, we establish that migmatization and plutonism in central New Hampshire and central Massachusetts are contemporaneous with the migmatite in this study, suggesting significant regional weakening of the Neoacadian middle crust (~4-7kb) due to partial melting and plutonism.

Migmatites and peraluminous, late kinematic Neoacadian granites make up a sizable portion of the map pattern in central New Hampshire, both east and west of the ‘dorsal zone’ established by Eusden et al. (1993) (Figure 4.1). Most Neoacadian migmatites in central NH are spatially associated with the intrusion of the Concord Granite (regionally intruded between 375-350 Ma, Eusden and Barrerio, 1998). We constrained the percentage of partial melt in our field area to between 2.8-9.0%. Other workers have constrained the late Devonian melt percentage in central New Hampshire to between ~5-30% in migmatized and/or heavily intruded outcrops (Eusden, 1988; Kohn et al., 1997). We can estimate a maximum regional melt fraction by calculating the area fraction of mapped late kinematic granitoids relative to surrounding metasediments from the bedrock geologic map of central New Hampshire (Figure 4.1, Lyons, 1997). From this method, we calculate a regional melt fraction between 10-15%. In total, we expect local melt fraction in Neoacadian migmatites and intrusive contact aureoles to vary from ~2.8-30 vol.%.

The instantaneous melt fraction was likely only a percentage of the melt fractions discussed above. However, when considering the near contemporaneous intrusion of these granites and migmatites within error of current geochronologic datasets (Eusden and Barrerio, 1998), the consistent estimates of Neoacadian metamorphic pressures in central NH (4-5kb), and that significant crustal weakening can occur at very low melt fractions (~5 vol.%), the middle crust of the Neoacadian orogen is expected to be relatively weak at this time. Furthermore, partial melting and granite intrusion is well documented in central Massachusetts at metamorphic pressures of 5-7kb. This suggests that the partially molten middle crust may have extended as much as 7km below the NeoAcadian partially molten zone in New Hampshire, lending further credence to the hypothesis of regional ductile channel flow associated with partial melting in the Acadian orogen.

The above constraints on regional melt fraction and metamorphic conditions support the presence of a partially molten, ductile layer at depth in the Acadian-Neoacadian orogenic plateau (Hillenbrand et al., 2021). This finding is not surprising when considering the extensive literature on partial melt induced weakening in the Puna-Altiplano and Tibetan-Himalayan orogenic plateaus. In the next section, we compare our observations and constraints on mid-crustal melt fraction and viscosity to other orogenic plateaus in Tibet and South America.

4.5.4 Mid-Crustal Viscosities of Orogenic Plateaus

Our results support the assertion that orogenic plateaus require low mid-lower crustal viscosities to support broad, flat topography (Clark and Royden, 2000). Low mid-lower crustal viscosities are necessitated underneath the Tibetan plateau and the Puna-Altiplano (Clark and Royden, 2000; Babeyko et al., 2002). Our estimates of melt fraction in New Hampshire are remarkably consistent with seismic and magnetotelluric data for Tibet and the Andes which suggest melt fractions of 3 to 30% (Schmitz et al., 1997; Schilling and Partzsch, 2001; Li et al., 2003; Schilling et al., 2006; Hacker et al., 2014, Xie et al., 2021).

Our derived viscosities are consistent with regional geodynamic models of both the Tibetan and Andean plateaus (Clark and Royden, 2000; Gerbault et al., 2005). Our constraints, as discussed above, suggest viscosity varies from 10^{17}-10^{18}Pa·s in the middle crust of the Neoacadian orogenic plateau. Geodynamic and topographic constraints in the Tibetan plateau assert that the viscosity of a weak ductile layer is $\leq 10^{18}$Pa·s (Clark and Royden, 2000). Similar estimates of crustal viscosity in the Andes suggest higher viscosities ranging from 10^{19} to 10^{21} Pa·s (Husson and Sempere, 2003; Gerbault and Willingshofer, 2004; Gerbault et al., 2005). The overall viscosity structure of the middle crust is likely extremely heterogeneous due to local variations in melt fraction, mineralogy, and temperature. However, as long as the effective viscosity across a large region is sufficiently low, large-scale ductile flow can occur (Beaumont et al., 2004).

Altogether, partial melting is clearly linked with orogenic plateaus. The melt fraction associated with plateaus varies depending on the scale of discussion, but is generally no more than 20-30%, with 5-10% melt sufficient to weaken the middle crust of plateaus and allow for ductile deformation.

4.5.5 The Importance of Water to Partial Melting and Crustal Weakening

The low-temperature of the melting reaction highlights the role of water-fluxed melting and fluid advection to the generation and maintenance of plateau topography. Previous studies on the Acadian orogeny have established the importance of fluid advection for regional metamorphic 'hotspots' (Chu et al., 2018). We constrained the local age of melting and advection to ~360Ma, contemporaneous with an Acadian-Neoacadian orogenic plateau (380-330Ma, Hillenbrand et al., 2021) and the intrusion of the late kinematic Concord granite series (370-350Ma, Eusden and Barrerio, 1988). The spatial correlation between the migmatization and the adjacent, contemporaneous Newfound Lake Pluton, in conjunction with our temperature estimates near the hydrous granitic solidus (Figure 4.5), suggest that fluid exsolution from the nearby pluton may have triggered local fluid-saturated partial melting of the pelitic layers. The distribution of late Devonian migmatites and late-kinematic, Devonian granitoids across central New Hampshire suggests that similar conditions were regionally pervasive at 4-5kb (~15-19km depth) throughout the Neoacadian orogen.

Crystallization of the granite plutonic suite would exsolve significant volumes of water into the middle crust of the Neoacadian orogen (Thomas and Davidson, 2012; Weinberg and Hasalova, 2015). The introduction of large volumes of water in concert with regional amphibolite facies metamorphic temperatures would result in extensive partial melting and fluid advection. These results suggest that fluids, in concert with temperatures near the hydrous granitic solidus, played a key role in weakening the mid-lower crust of the Neoacadian orogen during the presence of an orogenic plateau.

Advection associated with fluid exsolution from plutonism is a much more efficient process for creating spatially extensive, partially molten regions than conduction of heat from intruding plutons combined with radiogenic heating (Baumgartner and Valley, 2001). Future work on the timing and petrogenesis of the NeoAcadian late kinematic granitoids and migmatites in New Hampshire and Massachusetts is necessary to provide explicit constraints on the extent and magnitude of partial melting in the Acadian middle crust.

4.6 Conclusion

We have constrained the mid-crustal viscosity of a paleo-orogenic plateau to 10^{17-18}Pa·s at ~2.8-9.0 vol.% melt. Through a systematic analysis of grain size, melt fraction, melt viscosity, and leucosome spacing, this study reveals critical insights into the nature of mid-crustal deformation during the Neoacadian orogeny. Additionally, our results have global implications for rheology and deformation within orogenic plateaus. The methods presented in this study present an alternative workflow for calculating shear viscosity and effective viscosity as opposed to the commonly utilized experimental flow laws. Our results demonstrate that viscosity can be reduced by ~2-3 orders of magnitude due to the presence of low volumes of partial melt (2.8-9 vol.%). Previous geologic mapping and constraints on melt fraction throughout New Hampshire suggest such conditions were regionally pervasive during the Neoacadian orogeny, however, detailed geochronologic analysis and petrogenetic studies of the Concord granite and other Neoacadian migmatite localities are required to further constrain the temporal relationship between orogenic plateau development and mid-crustal anatexis in New Hampshire.

References

Antonelli, M. A., Mittal, T., McCarthy, A., Tripoli, B., Watkins, J. M., & DePaolo, D. J. (2019). Ca isotopes record rapid crystal growth in volcanic and subvolcanic systems. *Proceedings of the National Academy of Sciences*, *116*(41), 20315–20321. https://doi.org/10.1073/pnas.1908921116

Arslan, A., Passchier, C. W., & Koehn, D. (2008). Foliation boudinage. *Journal of Structural Geology*, *30*(3), 291–309. https://doi.org/10.1016/j.jsg.2007.11.004

Babeyko, A. Y., Sobolev, S. V., Trumbull, R. B., Oncken, O., & Lavier, L. L. (2002). Numerical models of crustal scale convection and partial melting beneath the Altiplano–Puna plateau. *Earth and Planetary Science Letters*, *199*(3–4), 373–388. https://doi.org/10.1016/S0012-821X(02)00597-6

Baumgartner, L. P., & Valley, J. W. (2001). Stable Isotope Transport and Contact Metamorphic Fluid Flow. *Reviews in Mineralogy and Geochemistry*, *43*(1), 415–467. https://doi.org/10.2138/gsrmg.43.1.415

Beaumont, C., Jamieson, R. A., Nguyen, M. H., & Lee, B. (2001). Himalayan tectonics explained by extrusion of a low-viscosity crustal channel coupled to focused surface denudation. *Nature*, *414*(6865), 738–742. https://doi.org/10.1038/414738a

Beaumont, C., Jamieson, R. A., Nguyen, M. H., & Medvedev, S. (2004). Crustal channel flows: 1. Numerical models with applications to the tectonics of the Himalayan-Tibetan orogen. *Journal of Geophysical Research: Solid Earth*, *109*(B6), 2003JB002809. https://doi.org/10.1029/2003JB002809

Bradley, D. C., & O'Sullivan, P. (2017). Detrital zircon geochronology of pre- and syncollisional strata, Acadian orogen, Maine Appalachians. *Basin Research*, *29*(5), 571–590. https://doi.org/10.1111/bre.12188

Breithaupt, T., Katz, R. F., Hansen, L. N., & Kumamoto, K. M. (2023). Dislocation theory of steady and transient creep of crystalline solids: Predictions for olivine. *Proceedings of the National Academy of Sciences*, *120*(8), e2203448120. https://doi.org/10.1073/pnas.2203448120

Cashman, K. V., Sparks, R. S. J., & Blundy, J. D. (2017). Vertically extensive and unstable magmatic systems: A unified view of igneous processes. *Science*, *355*(6331), eaag3055. https://doi.org/10.1126/science.aag3055

Chamberlain, C. P., & Lyons, J. B. (1983). Pressure, temperature and metamorphic zonation studies of pelitic schists in the Merrimack Synclinorium, south-central New Hampshire. *American Mineralogist*, *68*(5–6), 530–540.

Chu, X., Ague, J. J., Tian, M., Baxter, E. F., Rumble, D., & Chamberlain, C. P. (2018). Testing for Rapid Thermal Pulses in the Crust by Modeling Garnet Growth–Diffusion–Resorption Profiles in a UHT Metamorphic 'Hot Spot', New Hampshire, USA. *Journal of Petrology*. https://doi.org/10.1093/petrology/egy085

Clark, M. K., & Royden, L. H. (2000). Topographic ooze: Building the eastern margin of Tibet by lower crustal flow. *Geology*, *28*(8), 703–706. https://doi.org/10.1130/0091-7613(2000)28<703:TOBTEM>2.0.CO;2

Craig, T. J., Kelemen, P. B., Hacker, B. R., & Copley, A. (2020). Reconciling Geophysical and Petrological Estimates of the Thermal Structure of Southern Tibet. *Geochemistry, Geophysics, Geosystems*, *21*(8). https://doi.org/10.1029/2019GC008837

Ebadi, A., & Johannes, W. (1991). Beginning of melting and composition of first melts in the system Qz-Ab-Or-H2O-CO2. *Contributions to Mineralogy and Petrology*, *106*(3), 286–295. https://doi.org/10.1007/BF00324558

Eusden, D. (1988). The bedrock geology of the Gilmanton 15-minute quadrangle, New Hampshire [Ph.D.]. Dartmouth College.

Eusden, D., & Barrerio, B. (1988). The timing of peak high-grade metamorphism in central-eastern New England. *Atlantic Geology*, *24*(3), 241–255.

Eusden, D., & Lyons, J. B. (1993). The sequence of Acadian deformations in central New Hampshire. *Geological Society of America Special Paper*, *275*.

Gerbault, M., Martinod, J., & Hérail, G. (2005). Possible orogeny-parallel lower crustal flow and thickening in the Central Andes. *Tectonophysics*, *399*(1–4), 59–72. https://doi.org/10.1016/j.tecto.2004.12.015

Gerbault, M., & Willingshofer, E. (2004). Lower crust indentation or horizontal ductile flow during continental collision? *Tectonophysics*, *387*(1–4), 169–187. https://doi.org/10.1016/j.tecto.2004.06.012

Giordano, D., Russell, J. K., & Dingwell, D. B. (2008). Viscosity of magmatic liquids: A model. *Earth and Planetary Science Letters*, *271*(1–4), 123–134. https://doi.org/10.1016/j.epsl.2008.03.038

Hacker, B. R., Ritzwoller, M. H., & Xie, J. (2014). Partially melted, mica-bearing crust in Central Tibet. *Tectonics*, *33*(7), 1408–1424. https://doi.org/10.1002/2014TC003545

Harrison, T. M., Aleinikoff, J. N., & Compston, W. (1987). Observations and controls on the occurrence of inherited zircon in Concord-type granitoids, New Hampshire. *Geochimica et Cosmochimica Acta*, *51*(9), 2549–2558. https://doi.org/10.1016/0016-7037(87)90305-X

Hillenbrand, I. W., Williams, M. L., Li, C., & Gao, H. (2021). Rise and fall of the Acadian altiplano: Evidence for a Paleozoic orogenic plateau in New England. *Earth and Planetary Science Letters*, *560*, 116797. https://doi.org/10.1016/j.epsl.2021.116797

Hirth, G., Teyssier, C., & Dunlap, J. W. (2001). An evaluation of quartzite flow laws based on comparisons between experimentally and naturally deformed rocks. *International Journal of Earth Sciences*, *90*(1), 77–87. https://doi.org/10.1007/s005310000152

Hodges, K. V., & Spear, F. S. (1982). Geothermometry, geobarometry and the Al2SiO5 triple point at Mt. Moosilauke, New Hampshire. *American Mineralogist*, *67*(11–12), 1118–1134.

Holdaway, M. J. (2000). Application of new experimental and garnet Margules data to the garnet-biotite geothermometer. *American Mineralogist*, *85*(7–8), 881–892. https://doi.org/10.2138/am-2000-0701

Holtzman, B. K., Groebner, N. J., Zimmerman, M. E., Ginsberg, S. B., & Kohlstedt, D. L. (2003). Stress-driven melt segregation in partially molten rocks: MELT SEGREGATION IN MOLTEN ROCKS. *Geochemistry, Geophysics, Geosystems*, *4*(5), n/a-n/a. https://doi.org/10.1029/2001GC000258

Huang, W. L., & Wyllie, P. J. (1973). Melting relations of muscovite-granite to 35 kbar as a model for fusion of metamorphosed subducted oceanic sediments. *Contributions to Mineralogy and Petrology*, *42*(1), 1–14. https://doi.org/10.1007/BF00521643

Huet, B., Yamato, P., & Grasemann, B. (2014). The Minimized Power Geometric model: An analytical mixing model for calculating polyphase rock viscosities consistent with experimental data. *Journal of Geophysical Research: Solid Earth*, *119*(4), 3897–3924. https://doi.org/10.1002/2013JB010453

Husson, L., & Sempere, T. (2003). Thickening the Altiplano crust by gravity-driven crustal channel flow. *Geophysical Research Letters*, *30*(5), 2002GL016877. https://doi.org/10.1029/2002GL016877

Icenhower, J., & London, D. (1995). An experimental study of element partitioning among biotite, muscovite, and coexisting peraluminous silicic melt at 200 MPa (H_2O). *American Mineralogist*, *80*(11–12), 1229–1251. https://doi.org/10.2138/am-1995-11-1213

Jamieson, R. A., Unsworth, M. J., Harris, N. B. W., Rosenberg, C. L., & Schulmann, K. (2011). Crustal Melting and the Flow of Mountains. *Elements*, *7*(4), 253–260. https://doi.org/10.2113/gselements.7.4.253

Ji, S. (2004). A generalized mixture rule for estimating the viscosity of solid-liquid suspensions and mechanical properties of polyphase rocks and composite materials: A GENERALIZED MIXTURE RULE. *Journal of Geophysical Research: Solid Earth*, *109*(B10). https://doi.org/10.1029/2004JB003124

Katz, R. F., Jones, D. W. R., Rudge, J. F., & Keller, T. (2022). Physics of Melt Extraction from the Mantle: Speed and Style. *Annual Review of Earth and Planetary Sciences*, *50*(1), 507–540. https://doi.org/10.1146/annurev-earth-032320-083704

Kohlstedt, D. L., Evans, B., & Mackwell, S. J. (1995). Strength of the lithosphere: Constraints imposed by laboratory experiments. *Journal of Geophysical Research: Solid Earth*, *100*(B9), 17587–17602. https://doi.org/10.1029/95JB01460

Kohlstedt, D. L., Zimmerman, M. E., & Mackwell, S. J. (2010). Stress-driven Melt Segregation in Partially Molten Feldspathic Rocks. *Journal of Petrology*, *51*(1–2), 9–19. https://doi.org/10.1093/petrology/egp043

Kohn, M. J., Spear, F. S., & Valley, J. W. (1997). Dehydration-Melting and Fluid Recycling during Metamorphism: Rangeley Formation, New Hampshire, USA. *Journal of Petrology*, *38*(9), 1255–1277. https://doi.org/10.1093/petroj/38.9.1255

Kronenberg, A. K., Kirby, S. H., & Pinkston, J. (1990). Basal slip and mechanical anisotropy of biotite. *Journal of Geophysical Research*, *95*(B12), 19257. https://doi.org/10.1029/JB095iB12p19257

Li, S., Unsworth, M. J., Booker, J. R., Wei, W., Tan, H., & Jones, A. G. (2003). Partial melt or aqueous fluid in the mid-crust of Southern Tibet? Constraints from INDEPTH magnetotelluric data.

Geophysical Journal International, *153*(2), 289–304. https://doi.org/10.1046/j.1365-246X.2003.01850.x

Lyons, J. B., Bothner, W., Moench, R. H., & Thompson, J. B., Jr. (1997). *Bedrock geologic map of New Hampshire* [Map]. U.S. Geological Survey.

McKENZIE, D. (1984). The Generation and Compaction of Partially Molten Rock. *Journal of Petrology*, *25*(3), 713–765. https://doi.org/10.1093/petrology/25.3.713

Milord, I., Sawyer, E. W., & Brown, M. (2001). Formation of Diatexite Migmatite and Granite Magma during Anatexis of Semi-pelitic Metasedimentary Rocks: An Example from St. Malo, France. *Journal of Petrology*, *42*(3), 487–505. https://doi.org/10.1093/petrology/42.3.487

Mittal, T., & Richards, M. A. (2019). Volatile Degassing From Magma Chambers as a Control on Volcanic Eruptions. *Journal of Geophysical Research: Solid Earth*, *124*(8), 7869–7901. https://doi.org/10.1029/2018JB016983

Monteiro, A., Duraiswami, R. A., Mittal, T., Pujari, S., Low, U., & Absar, A. (2021). Cooling history and emplacement dynamics within rubbly lava flows, southern Deccan Traps: Insights from textural variations and crystal size distributions. *Bulletin of Volcanology*, *83*(11), 67. https://doi.org/10.1007/s00445-021-01485-w

Newman, S., & Lowenstern, J. B. (2002). VolatileCalc: A silicate melt–H2O–CO2 solution model written in Visual Basic for excel. *Computers & Geosciences*, *28*(5), 597–604. https://doi.org/10.1016/S0098-3004(01)00081-4

Orellana-Rovirosa, F., & Richards, M. (2016). Evidence and models for lower crustal flow beneath the G alápagos platform. *Geochemistry, Geophysics, Geosystems*, *17*(1), 113–142. https://doi.org/10.1002/2015GC006136

Patino Douce, A. E., & Johnston, A. D. (1991). Phase equilibria and melt productivity in the pelitic system: Implications for the origin of peraluminous granitoids and aluminous granulites. *Contributions to Mineralogy and Petrology*, *107*(2), 202–218. https://doi.org/10.1007/BF00310707

Pullen, A., Ibáñez-Mejia, M., Gehrels, G. E., Giesler, D., & Pecha, M. (2018). Optimization of a Laser Ablation-Single Collector-Inductively Coupled Plasma-Mass Spectrometer (Thermo Element 2) for Accurate, Precise, and Efficient Zircon U-Th-Pb Geochronology. *Geochemistry, Geophysics, Geosystems*, *19*(10), 3689–3705. https://doi.org/10.1029/2018GC007889

Rosenberg, C. L., & Handy, M. R. (2005). Experimental deformation of partially melted granite revisited: Implications for the continental crust. *Journal of Metamorphic Geology*, *23*(1), 19–28. https://doi.org/10.1111/j.1525-1314.2005.00555.x

Rybacki, E., Gottschalk, M., Wirth, R., & Dresen, G. (2006). Influence of water fugacity and activation volume on the flow properties of fine-grained anorthite aggregates: INFLUENCE OF WATER ON ANORTHITE STRENGTH. *Journal of Geophysical Research: Solid Earth*, *111*(B3), n/a-n/a. https://doi.org/10.1029/2005JB003663

Schilling, F. R., & Partzsch, G. M. (2001). Quantifying partial melt fraction in the crust beneath the central andes and the Tibetan plateau. *Physics and Chemistry of the Earth, Part A: Solid Earth and Geodesy*, *26*(4–5), 239–246. https://doi.org/10.1016/S1464-1895(01)00051-5

Schilling, F. R., Trumbull, R. B., Brasse, H., Haberland, C., Asch, G., Bruhn, D., Mai, K., Haak, V., Giese, P., Muñoz, M., Ramelow, J., Rietbrock, A., Ricaldi, E., & Vietor, T. (2006). Partial Melting in the Central Andean Crust: A Review of Geophysical, Petrophysical, and Petrologic Evidence. In O. Oncken, G. Chong, G. Franz, P. Giese, H.-J. Götze, V. A. Ramos, M. R. Strecker, & P. Wigger (Eds.), *The Andes* (pp. 459–474). Springer Berlin Heidelberg. https://doi.org/10.1007/978-3-540-48684-8_22

Schindelin, J., Arganda-Carreras, I., Frise, E., Kaynig, V., Longair, M., Pietzsch, T., Preibisch, S., Rueden, C., Saalfeld, S., Schmid, B., Tinevez, J.-Y., White, D. J., Hartenstein, V., Eliceiri, K., Tomancak, P., & Cardona, A. (2012). Fiji: An open-source platform for biological-image analysis. *Nature Methods*, *9*(7), 676–682. https://doi.org/10.1038/nmeth.2019

Schmitz, M., Heinsohn, W.-D., & Schilling, F. R. (1997). Seismic, gravity and petrological evidence for partial melt beneath the thickened Central Andean crust (21–23°S). *Tectonophysics*, *270*(3–4), 313–326. https://doi.org/10.1016/S0040-1951(96)00217-X

Solar, G. S., & Brown, M. (2001). Deformation partitioning during transpression in response to Early Devonian oblique convergence, northern Appalachian orogen, USA. *Journal of Structural Geology*, *23*(6–7), 1043–1065. https://doi.org/10.1016/S0191-8141(00)00175-9

Spear, F. S., Hickmott, D. D., & Selverstone, J. (1990). Metamorphic consequences of thrust emplacement, Fall Mountain, New Hampshire. *GSA Bulletin*, *102*(10), 1344–1360.

Sullivan, N. C. (2014). Advances in samarium-neodymium geochronology: Applications to early earth garnet, hydrothermal carbonate, and high temperature metamorphic systems [Ph.D.]. Boston University.

Thomas, R., & Davidson, P. (2012). Water in granite and pegmatite-forming melts. *Ore Geology Reviews*, *46*, 32–46. https://doi.org/10.1016/j.oregeorev.2012.02.006

Tracy, R. J. (1985). Migmatite occurrences in New England. In J. R. Ashworth (Ed.), *Migmatites* (pp. 204–224). Springer US. https://doi.org/10.1007/978-1-4613-2347-1_6

Van Buer, N. J., Jagoutz, O., Upadhyay, R., & Guillong, M. (2015). Mid-crustal detachment beneath western Tibet exhumed where conjugate Karakoram and Longmu–Gozha Co faults intersect. *Earth and Planetary Science Letters*, *413*, 144–157. https://doi.org/10.1016/j.epsl.2014.12.053

van der Molen, I., & Paterson, M. S. (1979). Experimental deformation of partially-melted granite. *Contributions to Mineralogy and Petrology*, *70*(3), 299–318. https://doi.org/10.1007/BF00375359

van Staal, C. R., Whalen, J. B., Valverde-Vaquero, P., Zagorevski, A., & Rogers, N. (2009). Pre-Carboniferous, episodic accretion-related, orogenesis along the Laurentian margin of the northern Appalachians. *Geological Society, London, Special Publications*, *327*(1), 271–316. https://doi.org/10.1144/SP327.13

Virgin, W. W. (1964). THE STRUCTURE AND PETROGRAPHY OF THE CONCORD GRANITE IN THE CONCORD AREA,NEW HAMPSHIRE [Ph.D.]. Lehigh University.

Wark, D. A., & Watson, E. B. (1998). Grain-scale permeabilities of texturally equilibrated, monomineralic rocks. *Earth and Planetary Science Letters*, *164*(3–4), 591–605. https://doi.org/10.1016/S0012-821X(98)00252-0

Weinberg, R. F., & Hasalová, P. (2015). Water-fluxed melting of the continental crust: A review. *Lithos*, *212–215*, 158–188. https://doi.org/10.1016/j.lithos.2014.08.021

Weinberg, R. F., Veveakis, E., & Regenauer-Lieb, K. (2015). Compaction-driven melt segregation in migmatites. *Geology*, *43*(6), 471–474. https://doi.org/10.1130/G36562.1

Wu, C. M. (2015). Revised empirical garnet-biotite-muscovite-plagioclase geobarometer in metapelites. *Journal of Metamorphic Geology*, *33*(2), 167–176. https://doi.org/10.1111/jmg.12115

Wu, C.-M., & Cheng, B.-H. (2006). Valid garnet–biotite (GB) geothermometry and garnet–aluminum silicate–plagioclase–quartz (GASP) geobarometry in metapelitic rocks. *Lithos*, *89*(1–2), 1–23. https://doi.org/10.1016/j.lithos.2005.09.002

Xie, C., Jin, S., Wei, W., Ye, G., Jing, J., Zhang, L., Dong, H., & Yin, Y. (2021). Middle Crustal Partial Melting Triggered Since the Mid-Miocene in Southern Tibet: Insights From Magnetotelluric Data. *Journal of Geophysical Research: Solid Earth*, *126*(9), e2021JB022435. https://doi.org/10.1029/2021JB022435

Figures and Captions

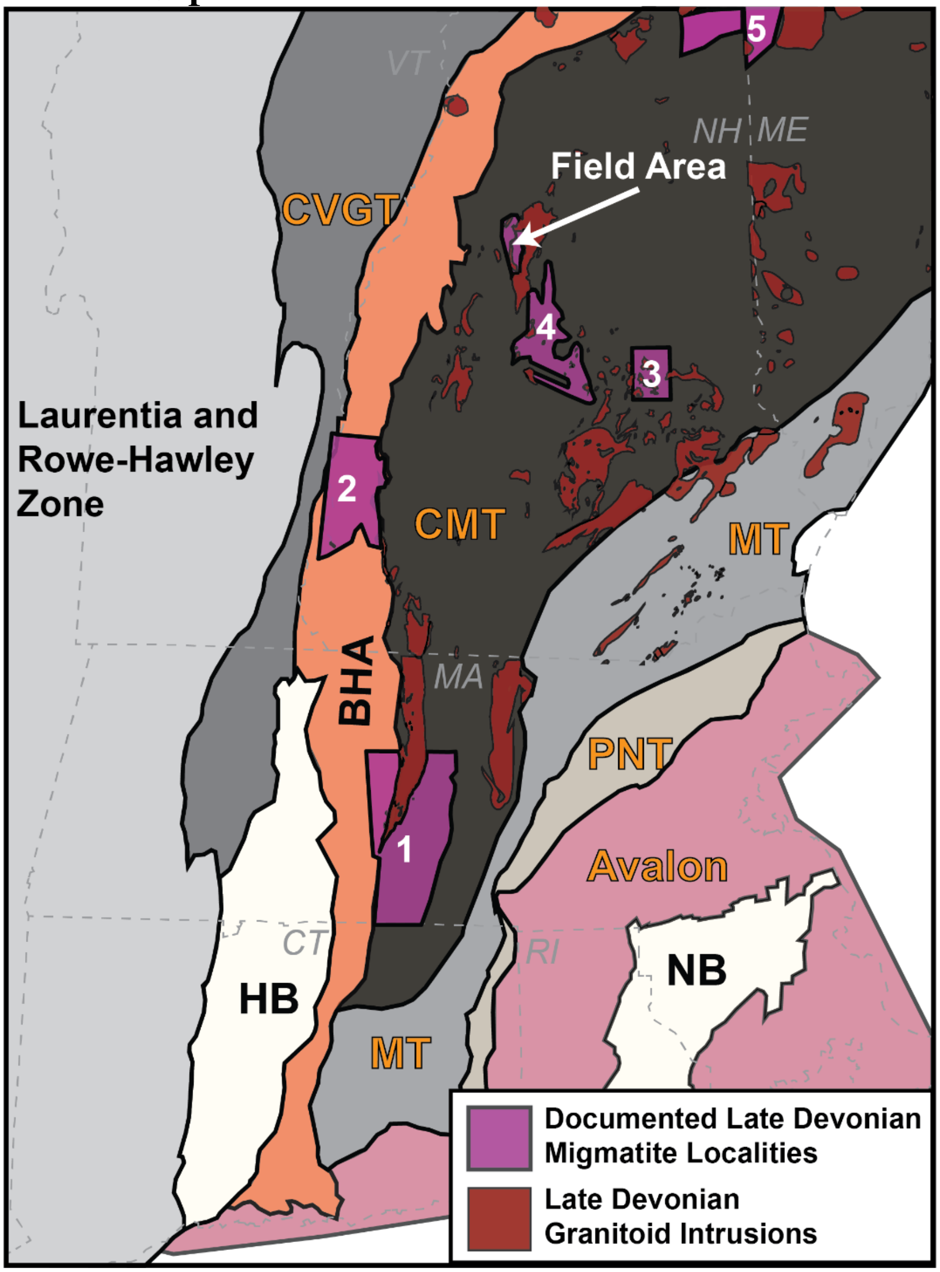

Figure 4.1: Regional geologic map of major New England terranes showing the distribution of late Devonian magmatism within the Central Maine Terrane (CMT), modified from Aleinikoff, 2007 and Lyons and Livingston, 1977. Abbreviations are as follows: CVGT-Connecticut Valley Gaspe Trough, BHA-Bronson Hill Anticlinorium, HB-Hartford Basin, MT-Merrimack Terrane, PNT-Putnam-Nashoba Terrane, NB-Narragansett Basin.

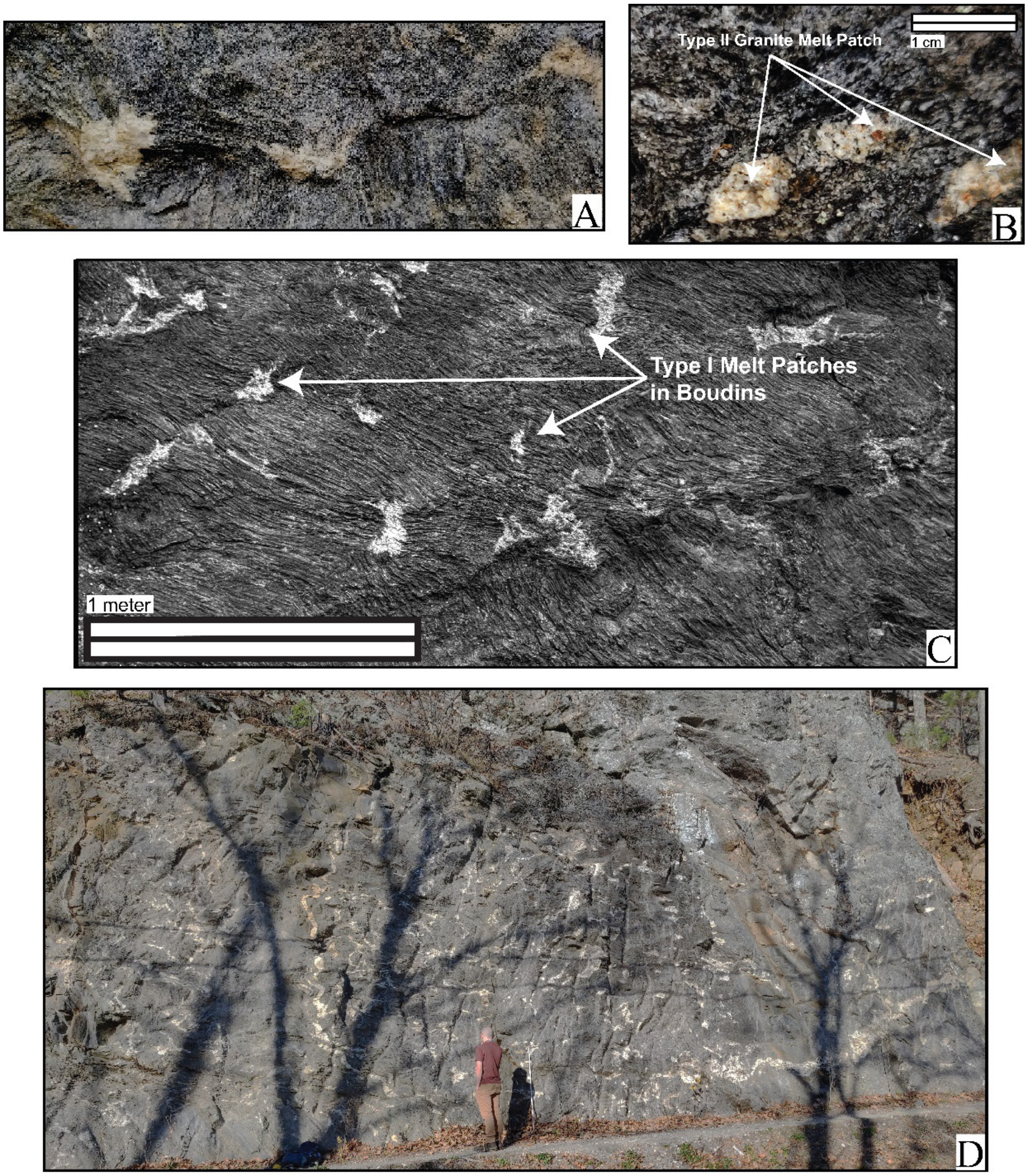

Figure 4.2: Outcrop images of the field area near Rumney, NH. A) Examples of foliation boudinage as defined by Arslan et al., 2008. B) Close-up photograph of Type (II) granite melt patches. C) Grayscale photograph of Type (I) granite melt patches highlighting the characteristic spacing and orientations. D) Photo of large roadcut through migmatite in field area.

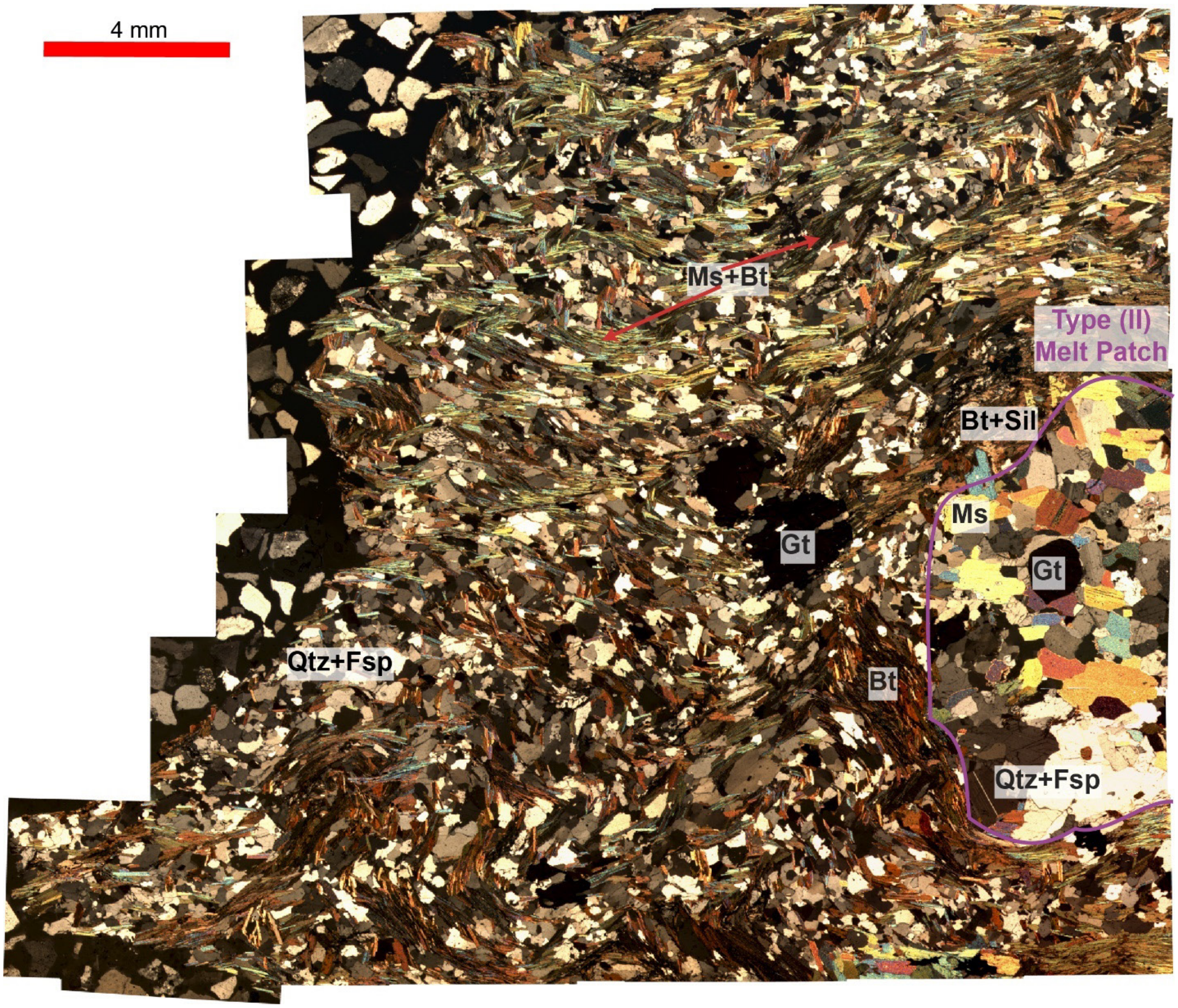

Figure 4.3: Thin section image of sample RY202 showcasing a Type (II) melt patch on the right side. Major phases include Quartz (Qtz), Feldspar (Fsp), Biotite (Bt), Muscovite (Ms), Garnet (Grt), and Sillimanite (Sil). Note the occurrence of a melanocratic rim of Bt+Sil+Grt directly adjacent to the Type (II) melt patch.

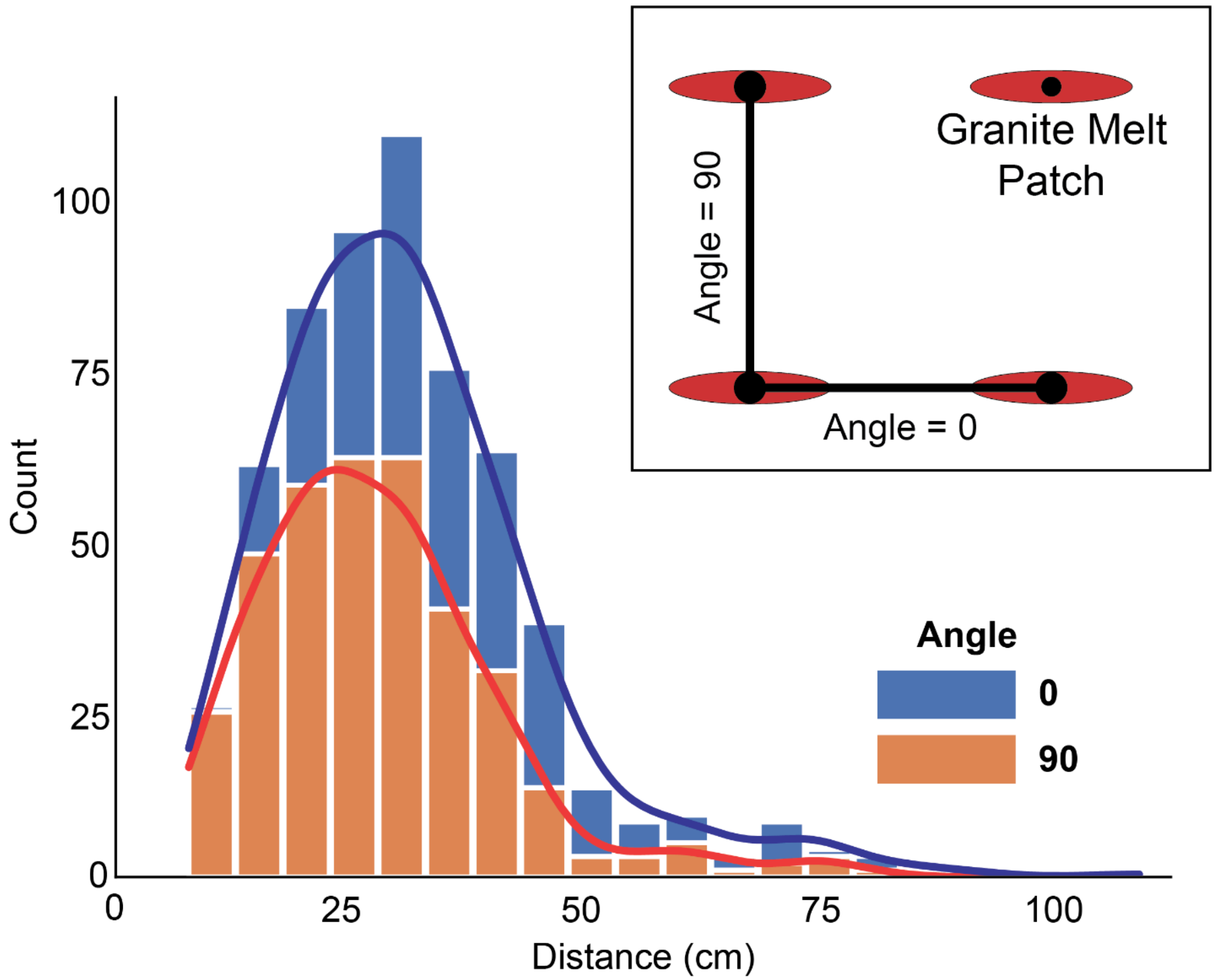

Figure 4.4: Histogram of Type (I) melt patch spacing. The schematic diagram shows the orientation of the measured spacing relative to the long axis of the leucosomes.

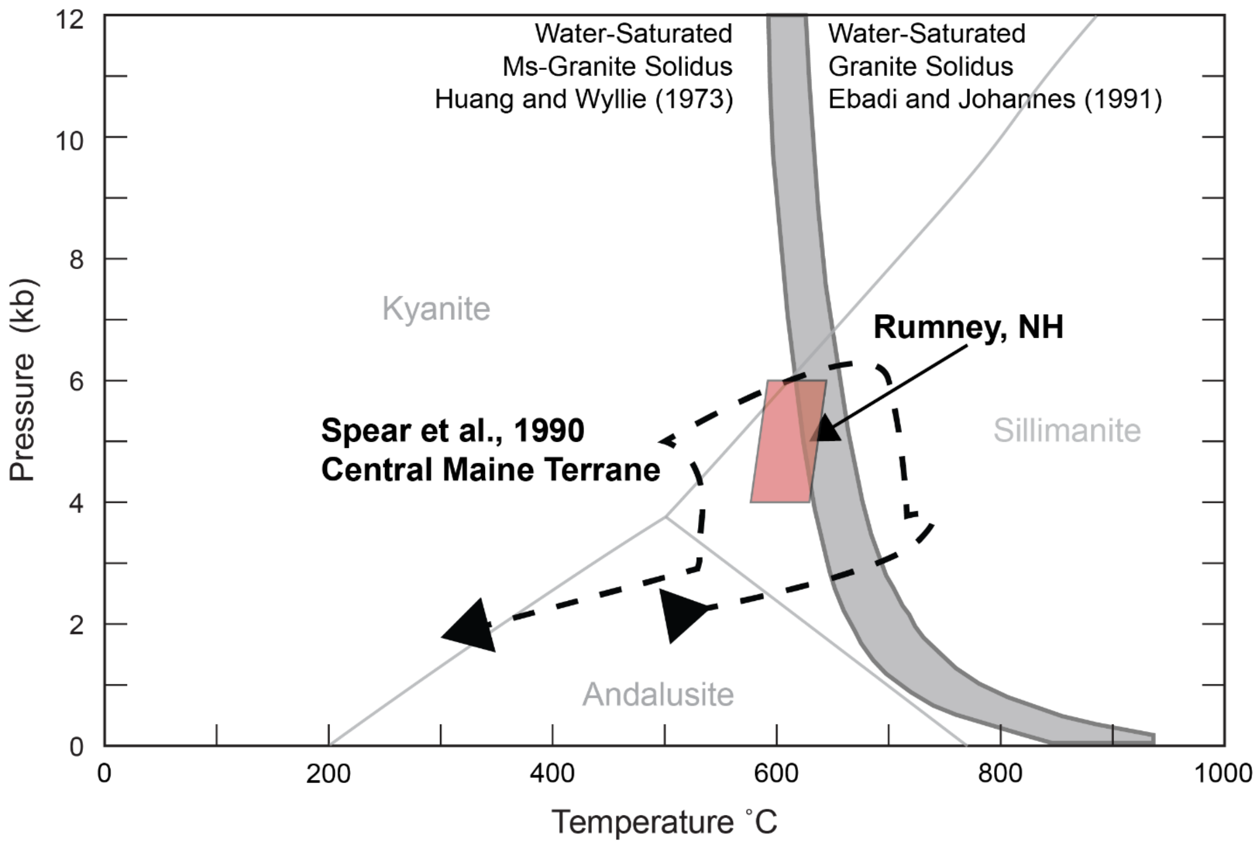

Figure 4.5: Geothermobarometry results (red box). Constraints on the water-saturated granite solidus are plotted as gray curves (Huang and Wyllie, 1973; Ebadi and Johannes, 1991). Counterclockwise PT path from Spear et al. (1990).

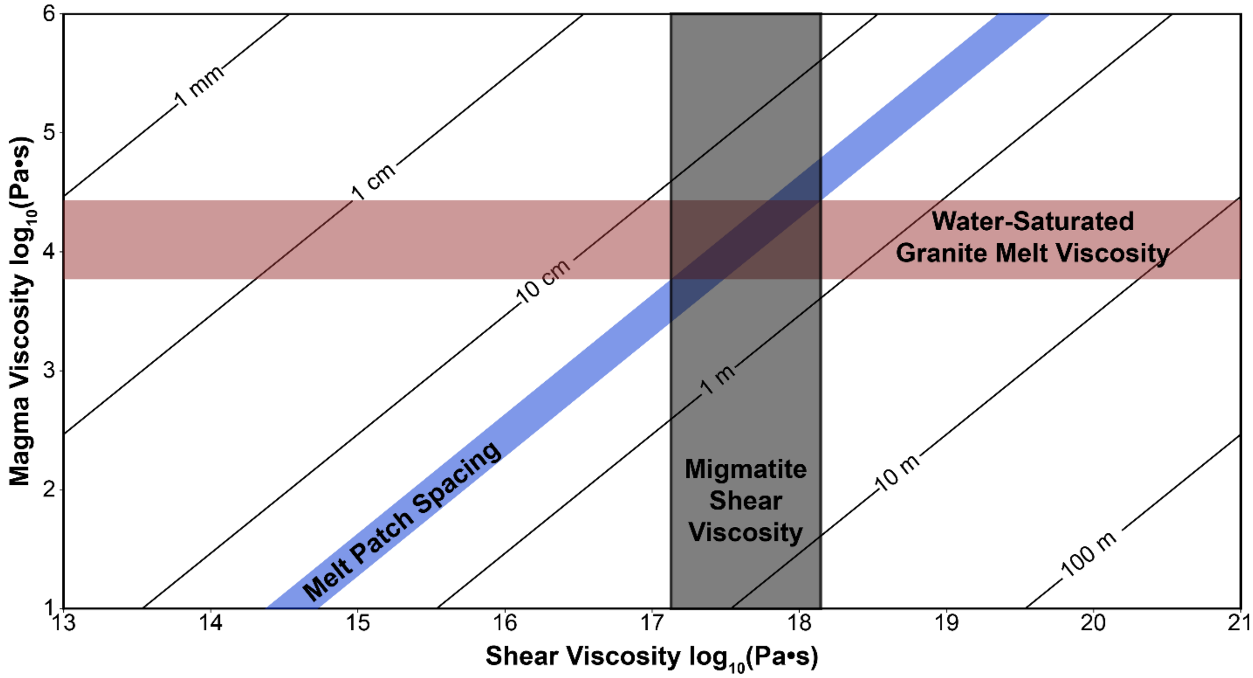

Figure 4.6: Contour plot of log shear viscosity vs magma viscosity. Contours correspond to the spacing of melt-filled deformation bands, and the observed average spacing in the field area is highlighted in blue.

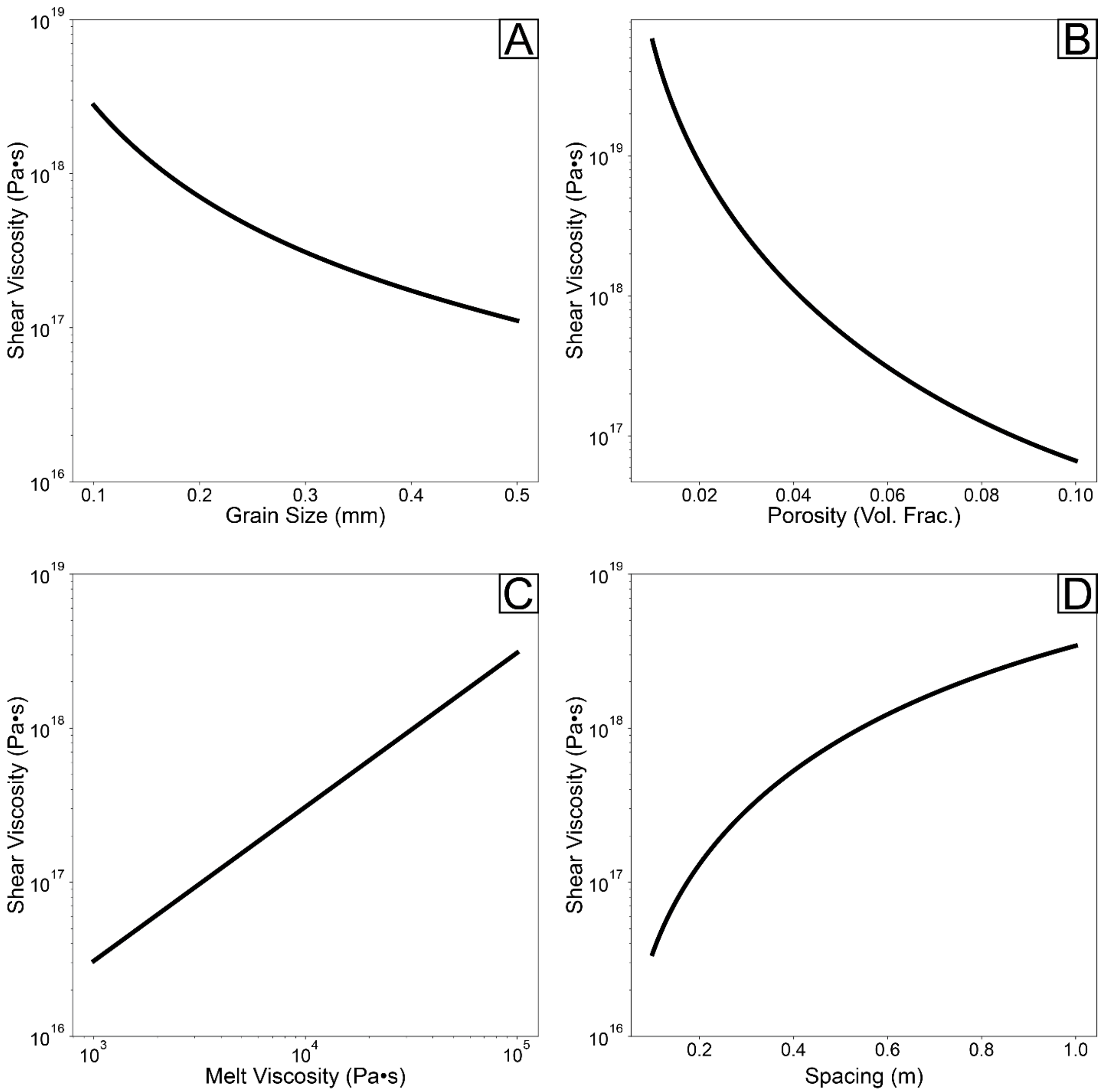

Figure 4.7: Effect of grain size (A), porosity (B), melt viscosity (C), and leucosome spacing (D) on calculated shear viscosity.

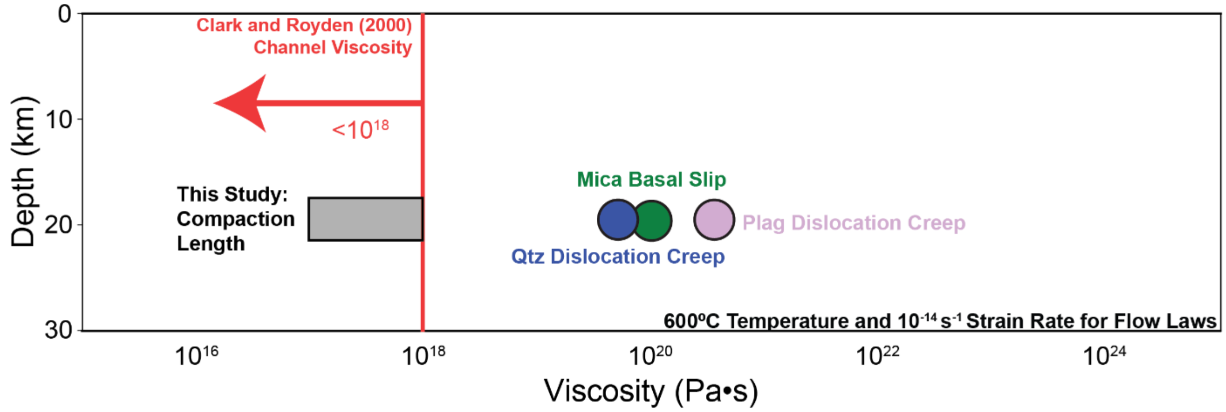

Figure 4.8: The shear viscosity estimated in this study compared to geophysical estimates of mid-lower crustal viscosity from Tibet (Clark and Royden, 2000) and monomineralic viscosities calculated from flow laws for mica, quartz, and plagioclase from Kronenberg et al. (1990), Hirth et al. (2001), and Rybacki et al. (2006), respectively.

Tables

Table 1: Equations and values used in the calculation of compaction length.

	DESCRIPTION	VALUE	CONSTRAINT ON VALUE
EQUATIONS			
$\boldsymbol{\delta_c}$	Compaction length-scale	$\sqrt{\frac{\kappa * \eta}{\mu}}$	Simplified form for compaction length (see Holtzman et al., 2003).
$\boldsymbol{\kappa}$	Permeability	$\frac{d^2\phi^3}{200}$ $\approx$**5.6 $\cdot 10^{-14}$ m^2**	Dependent on grain size and porosity constraints. C = 200 according to Wark and Watson (1998).
L	Spacing of Deformation Bands	$L = (.15)\delta_c$	Scalar value of .14-.15 from Kohlstedt et al. (2010) and Holtzman and Kohlstedt (2007)
VARIABLES			
L	Spacing of deformation bands	25-30 cm	Mean value of Type (I) melt patch spacing from outcrop measurements (see Figure 4.4)
$\boldsymbol{\phi}$	Porosity	2.8-9%	Constrained by the observed melt fraction at Rumney.
$\boldsymbol{d}$	Grain Size	.33 mm = .00033 m	Constrained from thin section measurements of quartz and feldspar grain size.
$\boldsymbol{\mu}$	Melt viscosity	~10^4 Pa·s	Constrained with the melt viscosity calculator of Giordano et al. (2008). Utilized water solubility in melt calculated from Newman and Lowenstern (2002).

Chapter 5: Testing Models of Depth-Dependent Conjugate Strike-Slip Shear in the New England Appalachian Orogen with Implications for the Relative Motion Between Gondwana and Laurasia

Abstract

The mid-lower crustal structure of conjugate orogenic strike-slip fault systems, such as the Karakorum-Altyn Tagh fault system in the Tibetan-Himalaya, remains a topic of widespread debate. End-member models of orogenic strike-slip fault systems propose either trans-lithospheric strike-slip, or alternatively, upper crustal strike-slip terminating in a shallowly dipping to subhorizontal mid-crustal shear zone or weak layer (Tapponnier et al., 2001 and Van Buer et al., 2015, respectively). The exhumed Acadian-Alleghenian orogen in the southern New England Appalachians presents an unparalleled opportunity to investigate extensive exposure of the orogenic mid-lower crust. The exhumed crust in this region underwent deformation and metamorphism during orogenic conjugate strike-slip shear along the Norumbega (dextral) and Western Bronson Hill (sinistral) shear zones during the Carboniferous Alleghenian orogeny (Massey and Moecher, 2013; McWilliams et al., 2013). The distribution of Alleghenian deformation and metamorphism in New England exhibits a distinct north-to-south variation in Neoacadian and Alleghenian metamorphic grade and deformation style. This variation allows for direct observations of an orogenic conjugate strike-slip shear system as a function of depth in the orogen. We present new regional macro-structural analysis, microstructural observations, Electron Backscatter Diffraction (EBSD) data, and in situ monazite and titanite U-Pb geochronology, suggesting the spatial distribution of Alleghenian deformation and metamorphism in the New England Appalachians is the result of rigid indentation of Gondwana to the south and highly oblique convergence to the north. This resulted in upper crustal strike-slip conjugate shear terminating on a low angle mid-lower crustal decollement and moderately west dipping coaxial shear zone. These observations of mid-lower crustal structure in

association with an upper crustal conjugate shear system support an end-member model akin to that proposed by Van Buer et al. (2015), wherein upper crustal deformation is decoupled from the mid-lower crust along mid-lower crustal structures.

5.1 Introduction

Conjugate fault or shear systems are prevalent in planetary lithospheres throughout the solar system including on Earth, Venus, and Mars (e.g., Ivanov and Head, 2006; Montgomery et al., 2009; Yin and Taylor, 2011). On Earth, many conjugate shear systems are found in plate boundary regions, particularly in orogenic belts (e.g., Sengor and Kidd, 1979; Tapponnier et al., 1981; Jackson and McKenzie, 1984; Ratschbacher et al., 1991; Alavi, 1994; Leloup et al., 1995; Brookfield and Hashmat, 2001; Morley, 2001; Calais et al., 2003; Allen et al., 2004; Cunningham, 2005; Backe et al., 2006; Dhont et al., 2006; Yin and Taylor, 2011; Van Buer et al., 2015). Traditionally, conjugate shear systems are interpreted through the Coulomb fracture criterion or Andersonian fault theory (Anderson, 1905).

Many such systems, notably modern orogenic conjugate strike-slip fault systems, are inconsistent with these classical interpretations of conjugate shear and necessitate alternative models which depend on the crustal structure as well as the distribution of deformation in the lithosphere and uppermost mantle (e.g., Yin and Taylor, 2011). While the upper crustal brittle structure and behavior of these systems is well understood, observational constraints regarding their mid-lower crustal structure and behavior are lacking. A long-standing debate revolves around whether these systems are trans-lithospheric (e.g., Tapponnier, 2001) or terminate in mid-crustal weak zones such as detachments or decollements (e.g., Van Buer et al., 2015). Moreover, it is not well understood how strength variations corresponding to depth in the crust (i.e., a weak mid-lower crustal layer) correspond to observed changes in deformation style and intensity.

Furthermore, the dynamic mechanism through which these conjugate shear systems occur is variably attributed to ductile flow in the lower crust or mantle (Yin and Taylor, 2011);

bookshelf faulting and regional rotation under oblique collision (Badham, 1982) or rigid indentation (Tapponnier, 1986); or inherited preexisting structures in the lithosphere (Sibson, 1990). The identification of the mechanism through which conjugate faulting is initiated requires an understanding of the depth-dependent behavior of the system, the direction and mode of deformation, the direction of plate motion, and the orientation of the plate boundary (Yin and Taylor, 2011).

The New England Appalachians preserve a tilted and exhumed mid-lower crustal section through a Carboniferous orogenic conjugate strike-slip shear system (Wintsch et al., 2003, Massey and Moecher, 2013; McWilliams et al., 2013; Hillenbrand et al., 2021). This exposure provides an unprecedented opportunity to study the depth-dependent structure of an orogenic conjugate strike-slip fault system. The tilted crustal section allows for discrimination between trans-lithospheric/trans-crustal faulting (Tapponnier, 2001) and termination in a mid-lower crustal weak zone (Van Buer et al., 2015). Additionally, we investigate the dynamical origin of orogenic conjugate shear systems by testing the aforementioned hypotheses (i.e., Badham, 1982; Tapponnier, 1986; Yin and Taylor, 2011; Sibson, 1990) through structural and kinematic analysis across the Appalachian system.

We present a macro- to micro-scale structural analysis of the conjugate strike-slip shear system preserved in the New England Appalachians. The macro-scale structural data is compiled from existing bedrock maps and supplemented by new field work in Connecticut, Central Massachusetts, and Southern New Hampshire. Additionally, we present new microstructural analysis and electron backscatter diffraction (EBSD) data within the conjugate shear zones and medial block. These compilations of structural data and analyses from the conjugate shear system are contextualized with *in situ* geochronology and geochemical analysis of synkinematic monazite and titanite growth before and during the late Paleozoic Alleghenian orogeny (Dallmeyer, 1982; Wintsch, 1992).

5.2 Geologic Background

The New England Appalachians record the composite Paleozoic orogenesis between ~500-260 Ma which culminated in the development of the supercontinent Pangea following closure of the Rheic ocean (Bird and Dewey, 1970; Zartman, 1988; Wintsch et al., 1992; Domeier and Torsvik, 2014; Young et al., 2019). This orogenesis can be subdivided into three major orogenic episodes: the Taconic Orogeny (Rodgers, 1971; MacDonald, 2014), the Acadian Orogeny (Robinson et al., 1998; van Staal et al., 2009), and the Alleghenian Orogeny (Dallmeyer, 1982; Wintsch et al., 1992). Some evidence exists for minor orogenic events between each major episode including the Salinic Orogeny (~450-423 Ma) and the Neoacadian orogeny (~395-350 Ma) (van Staal et al., 2009). Although much of the evidence for these subsequent orogenic episodes exists only in the Appalachian orogen of Eastern Canada as opposed to the New England Appalachians. Following the Alleghenian orogeny in the Permo-Carboniferous, continental rifting begins in the Triassic (Schlische, 1993). Continental rifting is followed by continental breakup and the formation of the Atlantic Ocean basin starting at ~200 Ma (Withjack et al., 2020; Kinney et al., 2022).

The oldest Taconic Orogen is preserved and largely unaffected by subsequent orogenesis in westernmost New England within Eastern New York, Western Vermont, Western Massachusetts, and Western Connecticut (Van Staal et al., 2009; MacDonald et al., 2014; Karabinos et al., 2017; Valley et al., 2020; Figure 5.1). Taconic plutons are also uplifted and exposed along the Bronson Hill Anticlinorium between two Siluro-Devonian basins (Karabinos et al., 2017; Valley et al., 2020). Central New England (Eastern Vermont, New Hampshire, Central-Western Maine, Central Massachusetts, and Central-Eastern Connecticut) is thought to preserve deformation from the accretion of Ganderia, directly following the main phase of Taconic orogenesis, through the accretion of Avalonia and Meguma in the Devonian Acadian and Neoacadian orogenies (van Staal et al., 2009). The extent of Ganderian basement beneath

Central New England is debated due to limited basement exposures, however, it may extend as far as coastal Connecticut (Kay et al., 2017).

Following accretion of Ganderia, two Siluro-Devonian basins were deposited on Ganderian basement: the Central Maine Terrane (CMT) and the Connecticut Valley Gaspe Trough (CVGT) (Figure 5.1; Bradley and Sullivan, 2017; Hepburn et al., 2021). The Siluro-Devonian Merrimack Terrane is also deposited at about the same time (Hepburn et al., 2021). Deposition within these basins terminates with the onset of Acadian subduction and collision of Avalonia (Eusden and Lyons, 1993; van Staal et al., 2009; Tassara and Ague, 2021). The beginning of the Acadian orogeny was marked by synkinematic arc granitoid intrusion contemporaneous with regional high temperature metamorphism (Tassara and Ague, 2021). High temperature metamorphism is followed by burial and tight to isoclinal folding best preserved adjacent to the Ordovician age Bronson Hill Anticlinorium (BHA) (Spear et al., 1990; Eusden and Lyons, 1993). Peak Acadian metamorphism and deformation is followed by late-kinematic granite intrusion and retrograde metamorphism (Eusden, 1988; Moecher et al., 2021). Classically, workers have found that dextral transpression is the best deformation model to explain regional macrostructural and shear sense observations in both the southern and northern Appalachians (Ferrill and Thomas, 1988; Gates et al., 1988; West and Hubbard, 1997; Robinson et al., 1998; Solar and Brown, 2001; Valentino and Gates, 2001; Merschat et al., 2005; Massey et al., 2017). Detailed kinematic models for the Acadian orogeny, constrained through the analysis of EBSD and microstructural datasets still endorse an approximately NW-SE convergence direction for the Devonian (Bradley, 1983; Kruckenberg et al., 2019). The Neoacadian orogeny is best defined in Eastern Canada (van Staal et al., 2009), however the nature of late Devonian orogeny and the extent of Meguma further south to New England is not well constrained. The southward extent of Meguma is typically extrapolated along the subaqueous Nauset magnetic anomaly and is based on the presence of Ediacaran granites in the basement of Cape Cod, Massachusetts (Hutchinson et al., 1988; van Staal et al., 2009; White et al., 2010). The extrapolation is not well founded as Ediacaran granites are present on multiple peri-Gondwana terranes and could also represent a previously unrecognized northwest African crustal block (Kuiper, 2017).

The Alleghenian orogeny in New England is well preserved in Central-Eastern Connecticut, Rhode Island, and Southeastern Massachusetts. The Alleghenian orogeny is the product of collision between Gondwana and Laurasia, preserved from southeastern North America through the Hercynian orogen in Eastern Europe. This orogeny resulted in the formation of the supercontinent Pangea and the closure of the Rheic ocean by ~330-320 Ma (Hatcher, 2010; Domeier and Torsvik, 2014; Young et al., 2019). Alleghenian amphibolite facies deformation and metamorphism overprints preexisting Acadian metamorphism and deformation in the Merrimack Terrane of Connecticut and within the Bronson Hill Anticlinorium. In fact, Alleghenian metamorphism and deformation is documented within the Bronson Hill Anticlinorium as far as Northeastern Vermont and Coastal Maine (West and Lux, 1993; McWilliams et al., 2013). Avalonia, as currently exposed in Eastern Connecticut, Rhode Island, and Eastern Massachusetts, was metamorphosed at high temperatures (>500 ˚C) for the first time in the in the late Paleozoic during the Alleghenian orogeny, culminating in peak metamorphism at ~300-290 Ma (Wintsch et al., 2007). Deformation and subsidence from Alleghenian deformation in Connecticut and western Rhode Island resulted in the deposition of the Narragansett Basin, the only regionally extensive Carboniferous basin preserved in New England (Murray et al., 2004).

In the early Alleghenian orogen, a conjugate strike-slip shear system developed on the margins of the CMT (Figure 5.1). A sinistral shear zone is documented from Central Massachusetts to Central Vermont, termed the Western Bronson Hill Shear Zone (WBHSZ; Massey and Moecher, 2013; McWilliams et al., 2013). A contemporaneous dextral shear zone is well documented along the Norumbega shear zone (e.g., West and Lux, 1993; West and Hubbard, 1997; Wang and Ludman, 2002). There were also large dextral shear systems active in the Maritimes Basin in Canada and Morocco during the Alleghenian orogeny (Houari and Hoepffner et al., 2003; Waldron et al., 2015). The Norumbega shear zone may have transitioned to an oblique, sinistral and reverse slip fault at the end of the Alleghenian orogeny (West and Hubbard, 1997).

The depth of exposure of the shear system increases from north to south in New England as a product of differential Alleghenian uplift (Wintsch et al., 2003; Massey and Moecher, 2013; McWilliams et al., 2013). Existing estimates of the depth of Carboniferous metamorphism in eastern Connecticut suggest metamorphic pressures of ~7 kb near Willimantic, CT (Moecher, 1999), and >10 kb in the southern BHA (Wintsch et al., 2003) corresponding to a range in depth from ~27-40 km in the crust. Contemporaneous with high T, high P metamorphism in southern New England, metamorphism in northern New England occurred at significantly lower pressures (<4 kb) (Holdaway et al., 1988).

The Alleghenian orogeny and formation of Pangea were followed by Triassic-Jurassic continental rifting and the formation of the Atlantic Ocean. The plate boundary geometry of the Atlantic Ocean inherited much of the crustal structure from the previous orogenic episodes (Withjack et al., 2020), and the pre-rifting continental geometry is easily reconstructed by retro-deforming the Atlantic Ocean along lineaments in the paleomagnetic stripes (e.g., Seton et al., 2012). Triassic-Jurassic rift basins are preserved along the entire Appalachian belt, notably in the central Appalachians (around Gettysburg, PA) and southern New England (the Hartford Basin, Schlische, 1993).

5.3 Data and Methods

To test between models of translithospheric faulting (e.g., Tapponnier et al., 2001) and the termination of strike-slip conjugate faulting in a mid-crustal weak zone (e.g., Van Buer et al., 2015) we compiled macro-structural data from existing bedrock maps supplemented by our own field work (Figure 5.2; Section 5.4.1), performed microstructural analysis on mutually perpendicular thin sections throughout the southern New England Appalachians, and analyzed thin sections by electron backscatter diffraction (EBSD) to quantify ductile deformation throughout the system (Figures 5 and 6; Section 5.4.2). Furthermore, we analyzed in situ syn- to post-kinematic monazite and titanite for trace elements and isotope ratios (Figures 5.10, 5.11, 5.12, and 5.13; Section 5.4.3) to characterize the timing of deformation relative to existing constraints on the timing of conjugate faulting (i.e., Massey and Moecher, 2013; Massey et al., 2017). This dataset elucidates the regional dynamic context under which the conjugate fault system was active, enabling evaluation of models of lower crustal and upper mantle flow (Yin and Taylor, 2011), regional rotation or bookshelf shear (Badham, 1982; Tapponnier, 1986), and the role of preexisting structures (Sibson, 1990).

We present a new macro-structural data compilation for the southern New England Appalachians in Southern New Hampshire, Central Massachusetts, and Eastern Connecticut (Figures 5.2 and 5.4). Macro-structural data for much of central Massachusetts is sparse due to a lack of bedrock outcroppings and existing bedrock geologic maps. The macro-structural data is compiled from existing bedrock geologic maps in the region as well as new supplemental field work. The macro-structural data includes the dominant generation of the foliation (S_n), mineral lineations (L_m), and fold hinge lineations (L_f). The structural data is plotted on both maps, through ArcGIS Pro, and stereonets, through the Orient program (Vollmer, 1995). We present the results of our compilation in section 5.4.1 and discuss the implications for the structure of the Carboniferous conjugate shear system preserved in New England in section 5.5.5.

5.3.1 Electron-backscatter diffraction (EBSD) and quantitative vorticity analysis

New electron backscatter diffraction (EBSD) data is presented along with microstructural analysis and qualitative characterization of quartz deformation textures for samples within the conjugate shear zones and the medial Central Maine and Merrimack Terranes. Nine samples were analyzed for quartz, feldspar, mica, monazite, and titanite crystallographic orientations in oriented thin sections. Prior to EBSD analysis, two mutually perpendicular sections were cut (both perpendicular to foliation, and one parallel to the macroscopic lineation if visible). In the absence of a macroscopic lineation, we cut a subhorizontal and subvertical section for steeply dipping samples and N-S and E-W vertical sections for shallowly dipping samples. The thin sections were qualitatively analyzed for microstructural simple shear indicators and structural asymmetry prior to EBSD analysis (see section 5.4.1). Following qualitative microstructural analysis, the thin sections were prepped for EBSD analysis by polishing with colloidal silica. We utilized a variable pressure mode at 40 Pa (as opposed to carbon coating) to prevent charging during EBSD analysis. EBSD data were collected at the Marine Biological Laboratory (Woods Hole, MA) using a Zeiss Supra 40VP field emission gun scanning electron microscope (FEG-SEM) equipped with an Oxford Instruments Symmetry EBSD detector. EBSD maps were collected at 30 kV accelerating voltage, 15.53–19.17 mm working distance, 70° sample tilt, and 0.5–12 μm step size, depending on the sample grain size.

EBSD data post-processing was conducted in the open-source MTEX toolbox for MATLAB (Bachmann et al., 2010). We calculated fabric strength, or the strength of the crystallographic preferred orientations (CPO) relative to a uniform distribution of orientations using both the M-index (0-1, Skemer et al., 2005) and J-index (1-infinity, Bunge, 1982). Where increasing values of the fabric strength indices correspond to increasing fabric strength. To quantitatively characterize the c-axis distributions for quartz, we performed eigenvalue analysis using the P (point), G (girdle), R (random) statistics of Vollmer (1990), and the shape characteristic, K, of Woodcock (1977). These two methods provide quantitative estimates of the shape of crystallographic fabrics as point maxima ($P>G$, $K>1$) versus girdle distributions ($P<G$, $K<1$). For crystallographic fabrics dominated by a point maxima component, we calculated the modal orientation (e.g., red squares Figure 6; Mainprice et al., 2015). For girdle distributions we calculated the five most volumetrically significant components to adequately characterize single and/or cross girdle distributions. From the ODF components, we can calculate the angle between the c-axis point maxima or girdle bisector and the dominant foliation in the sample.

With the calculated angle between the foliation and quartz c-axis fabric as well as an estimate of the ratio of the maximum (X) and minimum (Z) finite strain axes, Rxz, on the vorticity normal section, we estimate a vorticity number, Wm, for the sample (e.g., Wallis, 1992; Wallis, 1995; Xypolias, 2012). Strain ratios on the X-Z plane—that is, the vorticity-normal section, or lineation-parallel and foliation-perpendicular section—were based primarily on boudin geometries both in the field and in thin section (e.g., Figures 5.3 and 5.5). The strain ratio can be estimated from boudins by assuming that the observed maximum thickness of the boudin is the initial and uniform thickness of the deformed layer or object, and then calculating the magnitude of strain required to reproduce the observed change in width between the initial object/layer and the observed width of the boudins in question (Ramsay, 1967).

To further characterize the strain regime, in addition to Wm, we calculated intracrystalline vorticity axes using the crystallographic vorticity analysis (CVA) method of Michels et al. (2015). The direction of the sample-scale vorticity vector from Michels et al. (2015) corresponds to the orientation of the axis of dispersion of the crystallographic axes in each grain. After constraining the vorticity axis for each map, we rotated the EBSD data into a vorticity-normal section with the foliation oriented horizontally (VNS or XZ section, Figure 5.6). By rotating the EBSD data in Euclidean space, we can limit the uncertainty in strain analysis for samples lacking a macroscopic lineation, or samples from complex transpressional or highly asymmetric strain regimes.

We also estimate quartz deformation temperatures through a combination of microtextural analysis (following Stipp et al., 2002, for instance) and quartz slip system analysis within the VNS (e.g., Toy et al., 2008). Additionally, we estimate differential stress from recrystallized grain size piezometry (Cross et al., 2017) and subgrain size piezometry (Goddard et al., 2020). Subgrain size piezometry is advantageous because subgrain sizes are relatively insensitive to grain boundary pinning by secondary mineral phases and, thus, can be applied to polymineralic samples (Goddard et al., 2023), unlike recrystallized grain size piezometry, which is limited to monomineralic layers. Goddard et al. (2023) also argue that subgrain sizes are established after less strain than recrystallized grain sizes—thus, by combining subgrain size piezometry and recrystallized grain size piezometry, we may be able to disentangle the stress history of our samples. Stress estimates, when combined with rough estimates of metamorphic grade, can also be used as a proxy for crustal depth (e.g., Behr and Platt, 2011).

5.3.2 Electron microprobe (EPMA) X-ray mapping

Prior to *in situ* analysis of monazite and titanite via LA-ICP-MS, we produced compositional maps of selected late-kinematic monazite and synkinematic titanite in four samples. Backscattered electron (BSE) images and elemental x-ray maps from wavelength dispersive spectrometry (WDS) were obtained with the JEOL 8200 electron microprobe (EMPA) at the Massachusetts Institute of Technology (MIT). For monazite, we produced maps of Ca, Ce, Th, and Y as well as backscattered electron (BSE) maps. For titanite, we produced compositional maps of Al, Ce, Fe, and Nb as well as BSE. The compositional maps are given in figures 5.8 and 5.9 for monazite and titanite, respectively.

5.3.3 Laser-ablation inductively coupled plasma mass spectrometry (LA-ICP-MS)

Lastly, we analyzed in situ titanite and monazite isotope and trace element compositions through laser ablation inductively coupled plasma mass spectrometry (LA-ICP-MS). The goal was to obtain U-Pb ages and geochronologic constraints on the age of deformation and metamorphism contemporaneous with mid-lower crustal orogenic conjugate shear in southern New England. Analyses were performed at the University of Maine MicroAnalytical Geochemistry and Isotope Characterization (MAGIC) laboratory. Trace element and U-Pb data were collected using an ESI NWR193UC excimer laser ablation system coupled to an Agilent 8900 ICP-MS based on the methodology of Walters et al. (2022).

Both deformed and undeformed titanite and undeformed late kinematic monazite were analyzed on polished sections. Titanite was ablated using a 15 μm spot at 10 Hz with a beam energy density of 2 J cm^{-2}. Monazite was ablated using an 8 μm spot at 10 Hz with a beam energy density of 1.7 J cm^{-2}. Each analysis was acquired over 15 s (monazite) or 20 s (titanite) with 17 s of washout in between analyses. Fifteen unknown monazite analyses were bracketed by two analyses each of reference monazites USGS 44069, TS-Mnz, and Moacyr, and USGS basalt glass GSE-1G. U-Pb and Pb-Pb isotope ratios were calculated relative to the reference monazite USGS 44069 (Aleinikoff et al. 2006).

Monitored isotopes and their dwell times (ms) for monazite analyses were 29Si (5), 43Ca (1), 44Ca (1), 49Ti (5), 88Sr (1), 89Y (1), 90Zr (1), 139La (1), 140Ce (1), 141Pr (1), 146Nd (1), 147Sm (1), 153Eu (1), 157Gd (1), 159Tb (1), 163Dy (1), 165Ho (1), 166Er (1), 169Tm (1), 172Yb (1), 175Lu (1), 202Hg (40), 204Pb (1), 206Pb (55), 207Pb (85), 208Pb (35), 232Th (5), 235U (1), and 238U (30). Monitored isotopes for titanite analyses were 29Si (1), 43Ca (1), 44Ca (1), 49Ti (1), 56Fe (1), 88Sr (1), 89Y (1), 90Zr (5), 93Nb (1), 137Ba (1), 139La (1), 140Ce (1), 141Pr (1), 146Nd (1), 147Sm (1), 153Eu (1), 157Gd (1), 159Tb (1), 163Dy (1), 165Ho (1), 166Er (1), 169Tm (1), 172Yb (1), 175Lu (1), 178Hf (1), 181Ta (1), 202Hg (1), 204Pb (1), 206Pb (45), 207Pb (75), 208Pb (2), 232Th (5), 235U (1), and 238U (5). Time-resolved signals were processed using the iolite4 software package (Paton et al. 2011). Trace element mass fractions were determined relative to GSD-1G using the Trace Elements DRS assuming a Ca content of 19.25 %m/m in titanite as the internal calibration element. Trace element mass fractions in monazite were determined semi-quantitatively relative to Bananeira monazite using the Trace Elements DRS (Gonçalves et al., 2016). Isotope ratios were calculated using the U-Pb Geochronology DRS relative to MKED-1 for titanite and USGS 44069 for monazite. U-Pb dates were calculated in IsoplotR (Versmeesch 2018) using the measured $^{207}Pb/^{235}U$, $^{206}Pb/^{238}U$, and $^{207}Pb/^{206}Pb$ compositions and calculating either concordant ages (monazite) or discordant isochrons anchored at Stacey Kramers common lead composition (e.g., Figures 5.12 and 5.13). All associated errors for titanite and monazite ages in figures and discussed in the text are given as two standard deviations from the best fit age ($\pm 2\sigma$).

Concordia dates for secondary reference materials were calculated to be within reference values; Moacyr gave a date of 515 ± 3 Ma (2s), consistent with the recent TIMS age of 513 ± 1 Ma, (Palin et al. 2013). The calculated TS-Mnz concordia date of 904 ± 5 Ma (2s) is within uncertainty of the TIMS date of 910.42 ± 0.34 Ma (Budzyń et al. 2021). Unknown titanite analyses were bracketed by two analyses each of reference titanites MKED-1, McClure Mountain Ttn, and CKHB, and USGS basalt glass GSE-1G. U-Pb and Pb-Pb isotope ratios in titanite were calculated relative to the reference titanite MKED-1 (Spandler et al. 2016; 1518.87 ± 0.32 Ma). Concordia dates of secondary titanite reference materials are within published reference values; McClure Mountain titanite gave a date of 522 ± 3 Ma (523.26 ± 0.65 Ma, Schoene and Bowring, 2006). Titanite CKHB gave a date of 93 ± 10 Ma, consistent with the published TIMS age of 94.3 ± 0.15 Ma (Fisher et al. 2020).

To constrain the approximate temperature of metamorphism and subsequent deformation, we calculate the temperature of titanite growth from Zirconium (Zr) in titanite concentrations according to the Zr-in-ttn (sphene) geothermometer (Hayden et al., 2008). This thermometer requires constraints on pressure, TiO_2 and SiO_2 activities, and the measured Zr in the crystal. All the samples containing titanite also contained quartz as a major phase, and therefore we assume that $a(SiO_2) \approx 1$. Rutile is not an equilibrium phase with titanite in our samples and therefore we assume $a(SiO_2) \approx 0.75 \pm 0.25$ (Ghent and Stout, 1984; Kapp et al., 2009; Chambers and Kohn, 2012; Moser et al., 2022). The pressure of titanite growth during Alleghenian metamorphism is the largest uncertainty in calculating titanite crystallization temperatures. Previous studies on Alleghenian metamorphism in eastern Connecticut suggest pressures of metamorphism of 7 ± 3kb (Moecher, 1997; Wintsch et al., 2003). We ascribe a relatively large error to these pressure estimates due to the lack of sample coverage and detailed petrogenetic modelling.

As the conjugate fault system was active between ~330-275 Ma (McWilliams et al., 2013; Massey et al., 2017), we want to characterize the deformation style throughout the system during this time period. Additionally, we want to assess any change in deformation style at the beginning and end of this time period to better constrain the mechanism that led to the development of the conjugate fault system in the Carboniferous, and its subsequent termination in the Permian.

5.4 Results

5.4.1 Macroscale Structural Analysis of Southern New England

The bedrock structure of the New England Appalachians changes fundamentally from north to south based on compiled foliation, mineral lineation, and fold axis data from bedrock maps in Eastern Connecticut, Central Massachusetts, and Southern New Hampshire (Figures 5.2 and 5.4). The sinistral WBHSZ and the dextral Norumbega shear zone define steeply dipping conjugate shear zones on the west and east margins of the CMT, respectively. We aim to demonstrate how the structure of the conjugate fault system, both in the bounding shear zones (WBHSZ and Norumbega shear zone) and medial block (CMT), changes with depth in the Alleghenian orogen by characterizing the modern-day macroscale structure of the New England Appalachians. The Acadian-Neoacadian and Alleghenian orogens in southern New England were progressively tilted and uplifted during late Paleozoic orogenesis (Winstch et al., 2003). As the Alleghenian orogeny is the last major episode of high temperature ductile deformation in New England, we do not need to account for significant modification of the internal structure during subsequent rifting and continental breakup.

Much of the internal structure of the CMT reflects Acadian-Neoacadian deformation prior to the Alleghenian orogeny (Eusden and Barrerio, 1988; Eusden and Lyons, 1993; Massey and Moecher, 2013; Massey et al., 2017; Hillenbrand et al., 2021; Moecher et al., 2021). The pattern of moderately-to-steeply west-dipping foliations and shallow-to-subhorizontal north-south plunging mineral lineations and fold axes is traditionally interpreted as reflecting transpressional deformation (Fossen and Tikoff, 1998; Massey et al., 2017). Massey et al. (2017) interpret the structure of Central Massachusetts as reflecting dextral transpression during the Neoacadian orogeny in the late Devonian and early Carboniferous. A component of dextral simple shear is inferred from asymmetric fold patterns on horizontal outcrop planes and microstructural shear sense indicators on the subhorizontal plane. The Neoacadian metamorphic assemblages in Central Massachusetts and Northeastern Connecticut are crosscut by a series of late Devonian to Carboniferous high angle faults (Zen et al., 1983; Rodgers, 1985). These fault zones sole out on the Eastford thrust fault at the southern terminus of the CMT in Connecticut (Figures 5.1 and 5.2). Outcrop observations on vertical, E-W striking faces in proximity to these fault zones, including asymmetric feldspar sigmoids, asymmetric west-side-up folding, and low-angle shallowly west dipping shear bands suggest early top-to-SE reverse faulting. The top-to-SE reverse faulting is likely contemporaneous with inferred shallow top-to-SE thrusting on the Eastford fault based on the regional map pattern and macrostructural relationships between thrust faults in the field (Figures 5.1 and 5.3).

While the presence of shallow mineral lineations parallel to fold hinges is well established (e.g., Peterson and Robinson, 1993; Massey et al., 2017), it is not clear to what extent a component of strike-slip deformation was active within the CMT during the late Neoacadian and Alleghenian orogenies. This uncertainty is in part due to the lack of detailed crystallographic analysis and quantitative characterization of ductile deformation in Central Massachusetts. Traditional semi-quantitative structural analysis can be ambiguous or misleading in terms of identifying the vorticity normal section for kinematic analysis and making inferences about the 3-dimensional strain regime (Tikoff and Fossen, 1995; Fossen and Tikoff, 1999; Lin et al., 1998; Czeck and Hudleston, 2003; Michels et al., 2015; Fossen and Cavalcante, 2017). During our own field work, we identified mostly sinistral shear bands crosscutting the peak Acadian-Neoacadian metamorphic assemblage on subhorizontal outcrop faces in the Eastern CMT near Sturbridge, MA. This would seem to contradict the model of late regional dextral transpression for the CMT. Furthermore, there is no documented dextral strike-slip shear zone on the eastern margin of the CMT or Merrimack Terrane correlating to the Norumbega fault zone to the north. While asymmetric shear sense indicators are identified on subhorizontal outcrop faces throughout southern New England, the outcrop textures are dominantly symmetric. An alternative regime, which may explain the conflicting shear senses on the subhorizontal outcrop planes, dominantly symmetric fabrics, and subhorizontal mineral and fold hinge lineations, would be regional constriction (Fossen and Tikoff, 1999). In the case of constriction, the lineation would correspond to the maximum strain axis, X, which is along strike and orogen-parallel in this case. We can further test this idea through the analysis of microstructures and crystallographic preferred orientation in section 5.4.2.

The sinistral WBHSZ extends from Northeastern Vermont, along the Westminster West fault zone (Armstrong, 1997; McWilliams et al., 2013), to Central Connecticut within the Bolton synform (Massey and Moecher, 2013; Figures 5.1 and 5.2). The WBHSZ is steeply west dipping to subvertical until Central Connecticut, where the shear zone gradually rotates toward a moderate to shallowly west dipping orientation (Figure 5.2). The southern terminus of the WBHSZ, relating to its extent with depth in the Alleghenian orogen based on the metamorphic pressure estimates of Wintsch et al. (2003), is not well constrained. Previous work suggests that a sinistral shear system is present to the south of the Eastford fault and Bolton synform in the Cremation Hill Fault Zone (London, 1988). However, there are no robust geochronologic constraints on the timing of this proposed deformation. There is a clear shift in the orientation of foliations throughout the Bronson Hill Anticlinorium beyond the southern terminus of the adjacent CMT (Figure 5.2). While the foliations are steeply to moderately dipping in the Central Massachusetts and Vermont segments of the WBHSZ, the dip begins to shallow north of Bolton, CT and remains shallow until at least the southern tip of the Bolton synform near East Hampton, CT. Moreover, the mineral lineations within the Bolton synform rotate from the strike toward the dip direction to the south. This suggests a transition in the overall deformation corresponding to either changing strain magnitude or a change in the deformation style (Fossen and Tikoff, 1998). Asymmetric kinematic indicators on both subvertical and subhorizontal outcrop surfaces become increasingly rare to the south, although symmetric boudins are abundant. The abundance of symmetric boudins, change in mineral lineation orientation, and rotation of the foliation all suggest that the sinistral strike-slip shear documented to the north wanes in Central-Eastern Connecticut with the disappearance of the CMT across the Eastford fault.

In Eastern Connecticut, the structural style transitions from moderately-to-steeply dipping fabrics within the CMT to subhorizontal and shallowly-dipping fabrics in the underlying Merrimack Terrane across the Eastford fault (Figure 5.2). The Eastford fault is moderately west-dipping along strike and to the north of its southernmost extent in Connecticut and may correlate to Alleghenian strike-slip deformation on the subvertical Norumbega shear zone in Southeastern Maine. The Eastford fault crosscuts both the CMT and Merrimack Terrane as a shallow N-NW dipping to subhorizontal decollement directly south of the CMT. There is little to no macroscopic evidence of strike-slip shear along the Eastford fault based on the outcrop structure of subhorizontal surfaces. We document well-developed and pervasive top-to-southeast shear sense indicators on the subvertical NW-SE striking faces near the Eastford fault, supporting top-to-southeast thrusting (Figure 5.3).

The subhorizontal nature of the Merrimack Terrane precludes a significant component of inclined or subvertical strike-slip shear as opposed to pure shear flattening or subhorizontal simple shear. Outcrop observations on E-W and N-S striking planes within the Merrimack Terrane reflect largely symmetric strain with abundant symmetric boudins and virtually no pervasive asymmetric shear sense indicators (Figure 5.3). Asymmetry is only present through a secondary cleavage plane, prominent in the quartzo-feldspathic Devonian intrusions throughout the Merrimack terrane, which dips shallowly west. Lineations, boudin necks, and fold hinges vary significantly within the subhorizontal plane (Figure 5.4). This may be a function of late, gentle to open folding about Willimantic dome. In general, most of the linear structures trend in the NE and SW quadrants.

The Alleghenian metamorphic grade of the Merrimack Terrane is also unique, in that Alleghenian amphibolite facies metamorphism in eastern Connecticut strongly overprints Neoacadian metamorphism (Wintsch et al., 2007). While existing literature is abundant in studying deformation and metamorphism proximal to Willimantic dome and along the Honey Hill-Lake Char fault system (e.g., Wintsch et al., 1992; Moecher, 1999), there is little existing study of the internal deformation and detailed metamorphic evolution of the terrane. From the macro-structural observations, we can say that there is little to no component of inclined or vertical strike-slip deformation, and that deformation reflects largely pure shear strain based on the abundance of symmetric fabrics.

The Honey Hill-Lake Char fault system on the east and south margins of the Merrimack Terrane represents early Alleghenian underthrusting of Avalonia (Wintsch et al., 1992) followed by late Alleghenian (Permian) gravitational collapse and detachment faulting (i.e., Ma et al., 2023). The Honey Hill-Lake Char fault system has been well studied by past and current workers (e.g., Wintsch et al., 1992; Luo et al., 2022). Previous mapping efforts identified conflicting top-to-north and top-to-south shear sense along the Honey Hill fault zone and inferred that the top-to-south motion was most significant during the Carboniferous and Permian (Goldstein et al., 1989). Our own outcrop observations also suggest that top-to-north deformation is most significant during late Alleghenian (Permian) localized ductile deformation and uplift. We observe well developed and pervasive top-to-north asymmetric feldspar sigmoids and shearbands in a quartzo-feldspathic mylonite of the Honey Hill Fault (Figure 5.3). In contrast to the Merrimack Terrane, Avalonia did not experience high grade Acadian-Neoacadian metamorphism. The metamorphism of Avalonia, as exposed at the surface, did not occur until the late Carboniferous and early Permian (Wintsch et al., 1992). The Narragansett Basin was deposited in the early Carboniferous consistent with top-to-SE underthrusting of Avalonia leading to flexurally-induced subsidence and deposition of Carboniferous sediments to the east of the thrust fault.

To summarize, the Carboniferous strike-slip shear zones apparent in central and northern New England do not extend beyond the Eastford fault and Merrimack Terrane which represent, at a minimum, the middle crust of the Alleghenian orogen. While the WBHSZ extends as far as Central-Northern Connecticut, the Norumbega shear zone does not extend through Central-Eastern Massachusetts or Eastern Connecticut along the margin of the CMT. Rather, the eastern margin of the CMT transitions from dextral strike-slip faulting in the north, along the Norumbega fault zone, to top-to-SE thrusting along the Eastford fault and Eastern margin of the CMT in Massachusetts and Connecticut. The earlier southward termination of the Norumbega shear zone relative to the WBHSZ may in part be due to a change in regional strike from NW-SE to N-S assuming a near-constant maximum horizontal compressive stress orientation (discussed further in section 5.5.2). At the southern terminus of the CMT in Northeastern Connecticut, the Eastford fault is observed to cut westward to the BHA, dividing the CMT from the Merrimack Terrane. Below the Eastford fault, the structural style changes dramatically. Evidence of strike-slip deformation within the Bronson Hill and WBHSZ wanes to the south of the Eastford fault, corresponding to a marked shallowing in foliation dips along the Bronson Hill Anticlinorium (Figure 5.2). Top-to-SE deformation and extensional dip-slip deformation are proposed to continue on the eastern margin of the Merrimack Terrane related to deformation on the Honey Hill-Lake Char fault zone (Wintsch et al., 1992; Severson, 2020). However, much of the evidence of conjugate strike-slip deformation is absent in the Bronson Hill, CMT, and Merrimack Terranes in Central Massachusetts and Connecticut. This suggests that the conjugate strike-slip fault zone does not crosscut the entire orogenic crust, let alone the lithosphere, and gradually terminates in a mid-crustal decollement. In the following section, we analyze microstructural and EBSD data throughout Southern New England to quantitatively establish the transition from upper crustal strike-slip faulting to mid-lower crustal general or pure shear.

5.4.2 Microstructural and EBSD Analysis of Deformed Schist and Gneiss

To quantitatively characterize changes in deformation with depth in the orogen we assessed microstructures and EBSD data in nine samples across the proposed orogenic conjugate shear system. From the EBSD data we calculated crystallographic vorticity vectors (via crystallographic vorticity analysis, CVA, Michels et al., 2015) and kinematic vorticity numbers, W_m (Wallis et al., 1992). The vorticity number and vector allow us to discriminate between bulk coaxial and noncoaxial deformation while providing a quantitative constraint on convergence direction during Alleghenian deformation. Based on the qualitative observation of dominant symmetric fabrics in the Merrimack Terrane and southernmost Bronson Hill Anticlinorium relative to strongly asymmetric fabrics in Northern New England, we expect that the vorticity number of shear zones at the margins of the CMT should decrease to the south. To determine changes in crustal strength with depth through the orogenic system, we also estimate differential stress using quartz recrystallized grain size (Cross et al., 2017) and subgrain size (Goddard et al., 2020) paleopiezometry analyses. Microstructural 'regimes' in quartz, strongly dependent on both deformation temperature and strain rate, can be identified through microstructural analysis of quartz in thin section (Hirth and Tullis, 1992; Stipp et al., 2002). With the results of paleopiezometry analyses and microstructural observations in thin section we can determine deformation temperatures for quartz based on the dominant quartz recrystallization mechanism: bulge recrystallization (BLG, ~275-420 ˚C), subgrain rotation recrystallization (SGR, ~420-530 ˚C), or grain boundary migration (GBM, >530 ˚C) (Stipp et al., 2002). Furthermore, the quartz vorticity vector and vorticity number (W_m), can also be used to demonstrate a change in the orientation of the maximum compressive stress relative to the foliation. Based on the above constraints, we can show through qualitative and quantitative analysis of quartz deformation how the deformation regime and style changes with depth in the conjugate shear system.

We performed EBSD analysis on two samples within the CMT, one in Central Massachusetts (MA2207) and another in Northeast Connecticut (CT2207). Sample MA2207 from the Paxton Formation quartzo-feldspathic orthogneiss in Central Massachusetts features two symmetric and conjugate c-axis maxima at low angle to the macroscopic lineation based on quartz EBSD CPOs (Figure 5.6). The a-axes thus form two symmetric and conjugate girdles perpendicular to the macroscopic lineation and foliation. This pattern is associated with strongly coaxial deformation, most likely constrictional deformation, based on the c-axis distribution (e.g., Lister and Hobbs, 1980; Schmid and Casey, 1986; Barth et al., 2010). The CVA axis is ambiguous, forming a sample scale girdle of vorticities parallel to the foliation. This implies that either the sample records multiple deformation episodes, or a single rotational axis is not sufficient to quantify the strain geometry of the sample. The latter case would be consistent with a constrictional strain regime. Sample MA2207 also contains abundant recrystallized quartz with amoeboid grain boundaries and subgrains. These quartz microstructures suggest a combination of grain boundary migration (GBM) and subgrain rotation (SGR) recrystallization. The abundance of amoeboid grain boundaries relative to subgrains indicates GBM was the dominant deformation mechanism. As the c-axis maxima are subparallel to the macroscopic lineation and perpendicular to the vorticity vector, sample MA2207 deformed via prism-[c] slip. Quartz deforming under prism-[c] slip and dominant GBM reflects a deformation temperature of ≥ 600 °C (Stipp et al., 2002). This deformation temperature is further supported by weak-to-moderate internal deformation of plagioclase, which becomes ductile only at temperatures above ~600 °C (Tullis and Yund, 1992).

Sample CT2207, while still within the Central Maine Terrane, is located much closer to Eastford fault zone and the region of significant Alleghenian tectonism in Eastern Connecticut (Figures 5.2 and 5.6). Similar to sample MA2207, quartz microstructures are characterized by abundant amoeboid grain boundaries and subgrains. The relative number of amoeboid grains is nearly equal to the abundance of subgrains. This suggests that the dominant deformation in this sample reflects conditions near the GBM to SGR transition at ~500 °C (Stipp et al., 2002). For this sample, there was no macroscopic lineation; however, the subvertical section analyzed was the correct VNS as verified following the CVA method. On the VNS, the c-axes lie within the foliation plane and are approximately parallel to the vorticity vector, forming a central point maximum (Figure 5.6). The a-axes form approximately six point maxima lying within the VNS, suggesting prism-<a> slip. Prism-<a> slip occurs at temperatures of ~450–500 °C, consistent with the textural interpretation. Under coaxial strain in prism-<a> slip, the six a-axes are expected to be symmetric about the foliation (e.g., Toy et al., 2008; Barth et al., 2010); however, the a-axis pattern in this sample is rotated ~10–15° counterclockwise from symmetry. The error on the sample orientation is ~10°, so this deviation suggests a minor component of dip-slip simple shear. As the sample is cut looking south, this pattern results from top to the east/southeast rotation or east-vergent reverse shear, consistent with the strike-parallel and subhorizontal vorticity vector from crystallographic vorticity analysis. This is in contrast to sample MA2207 (Central Massachusetts) for which we inferred constriction.

We analyzed three samples along the sinistral WBHSZ proposed to extend from Northeastern Vermont to Connecticut (Figure 5.6). The northernmost sample (TH2107) was taken from the mylonitized Partridge Formation near Lake Morey, VT. The lithologies on the eastern edge of Lake Morey are traditionally mapped as phyllites of the Ordovician Partridge Fm (e.g., Ratcliffe et al., 2011). However, in thin section it is apparent that these rocks are quartz-rich mylonites and ultramylonites (Figures 5.5A, B, and C). The Meetinghouse Slate member of the Gile Mountain Formation and the Ordovician Partridge Fm broadly correlate with the mapped sinistral Westminster West fault zone to the south (Ratcliffe et al., 2011; McWilliams et al., 2013). Therefore, we anticipate EBSD analysis of these samples to suggest a significant component of noncoaxial sinistral deformation if the WBHSZ extends North of Haverhill, NH.

Microstructures and EBSD data for Sample TH2107, from the Ordovician Partridge Fm are strongly indicative of sinistral strike-slip deformation in the upper crust (Figures 5.5B, 5.5C, and 5.6). The extreme grain size reduction in the sample suggests relatively low-temperature quartz deformation undergoing a combination of bulge recrystallization and cataclastic flow. Such conditions occur at deformation temperatures of ~300–400 °C (Stipp et al., 2002). Quartz pole figures are characterized by a singular c-axis maximum highly asymmetric to the foliation plane (Figure 5.6), while the a-axes form a girdle of orientations ~40° to the macroscopic foliation, and highly asymmetric to the same degree as the c-axes (Figure 5.6). These textures are indicative of basal-<a> slip, supporting the microstructural evidence for low deformation temperatures (~400 ˚C). The high asymmetry of the crystallographic axes relative to the macroscopic structures is representative of significant simple shear (e.g., Toy et al.., 2008; Barth et al., 2010), as endorsed by crystallographic vorticity analysis which yields a subvertical vorticity vector. West-side-south asymmetric boudins and shear bands in thin section suggest a significant sinistral simple shear component (Figures 5.5B and C). We can calculate a vorticity number from the angle between the c-axis maxima and normal to the foliation plane as well as the strain magnitude on the VNS, Rxz, following the method of Wallis (1992; 1995). Boudins in thin section can be used to estimate a minimum Rxz magnitude of ~1.5 (Figure 5.5A). The c-axis maximum is ~45° from the normal to the foliation plane based on the calculated maximum ODF components. These constraints yield a vorticity number, W_m, estimate of 1 (±0.1), indicating dominant simple shear (Wallis, 1992). As inferred also by McWilliams et al. (2013), these results suggest that the mylonitic section of the WBHSZ, corresponding to the Westminster West fault zone in Vermont, extends at least as far north as the Piermont Allochthon, and represents sinistral strike-slip fault zone mylonite under greenschist facies conditions.

In Connecticut, we analyzed two samples on the proposed WBHSZ, south of the type locality in Palmer, MA (Massey and Moecher, 2013). Sample CT2203 is from the Silurian Clough Quartzite. Amoeboid quartz boundaries are abundant in this sample relative to subgrain boundaries, suggesting GBM is the dominant deformation mechanism, and that the deformation temperature is >530 °C. EBSD on the VNS yields a relatively complex c-axis CPO generally in the plane of the foliation or inclined to the foliation at an angle of ~45-50˚ (Figure 5.6). The a-axes are typically near perpendicular to the foliation plane (Figure 5.6). These observations are broadly consistent with prism-[c] slip, which occurs at temperatures >550-600 °C (Toy et al., 2008), consistent with the microstructural interpretations of deformation temperature. Similar to the Vermont sample, we can estimate a vorticity number from the c-axis distribution. The c-axes form a girdle distribution in this sample (P>G and K<1). The five largest components of the ODF define two girdles, with one outlier in the SE quadrant (Figure 5.6). We measure the angle between the bisector of the girdles and the inferred shear plane, yielding an asymmetry of ~15°. We estimate the minimum Rxz as ~1.4-1.9 from the deformation of boudins in outcrops with the BHA (e.g., Figure 5.3E, D, and H). These estimates yield a vorticity number of 0.6-0.7 (±0.1). While there is still a component of sinistral simple shear based on the c-axis asymmetry, this is indicative of general shear with dominant simple shear In comparison to sample TH2107 in Vermont, the vorticity number has decreased to the south, corresponding to increasing depth in the orogenic system and increasing proximity to the Long Island Promontory in New York. The lack of well-developed and pervasive shear sense indicators in outcrop and in thin section support our calculated vorticity number in that we would not expect dominant simple shear and high vorticity numbers.

The final sample within the WBHSZ, near the southernmost end of the Bolton Synform (Figure 5.6) is from the Devonian Littleton Schist (CT2217). The abundance of mica causes grain boundary pinning in quartz. Nevertheless, subgrains are still rare in comparison to amoeboid grain boundaries, suggesting dominant GBM. On the VNS, the EBSD data yield a c-axis maximum in the plane of the foliation and perpendicular to the vorticity vector, indicative of prism-[c] slip. The vorticity vector is strongly oblique to both the horizontal and vertical planes, suggesting either oblique simple shear, deformation with triclinic symmetry, or flattening strain with oblique extrusion (Fossen and Tikoff, 1995). The a-axes CPO, while typically representative of a girdle distribution due to the tri-fold symmetry of quartz a-axes, is characteristic of a point maxima near perpendicular to the foliation plane. Altogether, these crystallographic textures are indicative of prism-[c] slip, suggesting a deformation temperatures >550-600 °C (Toy et al., 2008) and endorsing the microstructural interpretations. Both the c and a-axes are symmetric relative to the macroscopic structures indicating strongly coaxial deformation. Additionally, pressure shadows on the lineation parallel and foliation perpendicular face are symmetric about biotite and garnet porphyroblasts supporting coaxial deformation (Figures 5.5F and G). The absence of significant plastic deformation in the garnet precludes late ultra-high temperature deformation in the Bolton Synform. From the crystallographic axes, we interpret the deformation regime as coaxial flattening (e.g., Toy et al., 2008; Barth et al., 2010). There is only a slight 2° asymmetry between the c-axis maxima and foliation, well within the error of the constrain on foliation orientation. The slight asymmetry yields a vorticity number estimate of 0.1 (±0.1) (Wallis, 1992). This continues the trend of decreasing vorticity number to the south along the WBHSZ, and therefore decreasing noncoaxiality with depth in the orogen.

In summary, deformation transitions from noncoaxial sinistral strike slip in Vermont to coaxial flattening in Connecticut along the WBHSZ. We observe increasing deformation temperature and metamorphic grade from Vermont to Connecticut based on the dominant quartz slip system and deforming metamorphic assemblage (Figure 5.6; McWilliams et al., 2013; Massey et al., 2017; Wintsch et al., 2003). The range of deformation temperatures and metamorphic grade spans the greenschist through amphibolite facies, corresponding to the upper crust and middle crust, respectively. Further EBSD analysis of the Eastford fault zone and Merrimack Terrane below delineates the nature of deformation in the middle crust of the Alleghenian orogenic conjugate fault zone. We do not present new EBSD data for the Norumbega fault zone, as there is a plethora of existing studies and data establishing the timing of strongly noncoaxial dextral deformation in SE Maine (i.e., West and Lux, 1993; Ludman et al., 1999; Johnson et al., 2009; Price et al., 2016). The existing data for the Norumbega fault zone is strongly reminiscent of our data for the mylonitic section of the WBHSZ in Vermont, with similar published vorticity numbers and deformation ages.

On the Eastford Fault Zone at the southern terminus of the CMT, we analyzed microstructures and EBSD data for two samples (CT2205 and CT2208). Sample CT2205 is from the Ordovician Brimfield Schist near Gurleyville, CT (Figure 5.6). As discussed in section 5.4.1, there is abundant outcrop-scale evidence for top-to-SE thrusting (e.g., Figure 5.3E), consistent with the mapped shear direction of the Eastford fault. In thin section, there is microstructural evidence for GBM and SGR, as with the other samples in Central Massachusetts and Connecticut, suggesting deformation temperatures of >420 °C (Stipp et al., 2002). EBSD data on the VNS yield a c-axis maximum subparallel to the vorticity axis and macroscopic fold hinges. The a-axes form a distribution of ~6 clusters lying within the VNS. These observations are indicative of prism-<a> slip and deformation temperatures of ~450-600 °C (Schmid and Casey, 1986; Toy et al., 2008). Similar to sample CT2207 which is directly north of this sample, the a-axes are rotated ~10° from symmetry with the foliation (Figure 5.6). This supports the outcrop-scale interpretation of top-to-SE dip-slip simple shear. The similar degree of asymmetry between sample CT2207 and this sample, suggests that the top-to-SE deformation partly overprints prior Acadian-Neoacadian deformation in Northeastern Connecticut within the CMT. However, the absence of such deformation throughout central Massachusetts suggests that Alleghenian deformation did not overprint preexisting ductile structures in the CMT within Central Massachusetts.

To the east along the Eastford fault, we sampled from the Southbridge Fm near Ashford, CT (CT2208, Figure 5.6). This is a sample of micaceous quartzite with no well-developed macroscopic lineation. Compositional bedding is pronounced in outcrop and is parallel to the observed grain size variation in thin section (Figure 5.5E). Here, quartz deforms under a combination of GBM and SGR suggesting deformation temperatures of 500–600 °C. The EBSD data on the VNS yield a singular, broad c-axis maxima parallel to the vorticity vector and subhorizontal, while the a-axes form six clusters lying within the VNS. This is indicative of prism-<a> slip and is strongly reminiscent of the texture in sample CT2205. In contrast to sample CT2205, there is little to no asymmetry of the crystallographic axes, implying coaxial deformation. The lack of evidence for top-to-SE deformation on this segment of the Eastford fault indicates late flattening or pure shear strain as opposed to the top-to-SE simple shear observed further south. The coarse bedding and lack of sheet silicates may have hindered significant noncoaxial deformation of our sample. Regardless, there is no evidence of strike-slip or dip-slip late Paleozoic shear along this segment of the Eastford fault.

Within the Merrimack Terrane we analyzed two samples: CT2223 and CT2229. Sample CT2229 is from the Devonian Canterbury Gneiss, a deformed early Acadian intrusion (Wintsch et al., 2007). Quartz and feldspar microstructures are highly variable with textures ranging from myrmeckite (Figure 5.5H) to quartz subgrain development (SGR) (Figure 5I). Myrmeckite likely reflects the conditions of igneous intrusion and crystallization during the early Acadian orogeny as opposed to subsequent Alleghenian orogenesis and amphibolite facies metamorphism, while SGR records the latest recrystallization of quartz in the section. This suggests that the final deformation event in this sample is characterized by a deformation temperature of ~420–490 °C (Stipp et al., 2002) (consistent with the observed temporal trend in Zr-in-titanite temperatures discussed in section 4.3). EBSD data on the VNS are relatively complex as would be expected from the microstructures (Figure 5.6). There are abundant small inclusions of quartz in plagioclase in the sample. Most quartz inclusions are < 120 um in diameter, therefore we filter for grains larger than this size and only consider the EBSD orientations of these large grains. Quartz c-axes are parallel to the VNS and oriented subperpendicular to the foliation. The a-axes define a girdle subparallel to the foliation with ~15–20° of asymmetry. This CPO is indicative of basal-<a> slip, which reflects relatively low temperatures of ~450 °C in comparison to the other samples in eastern Connecticut. While there is no outcrop-scale evidence for subhorizontal simple shear, the quartz CPO suggests noncoaxial top-to-SE deformation. This may reflect distributed simple shear between the rigid overlying CMT (separated by the Top-to-SE Eastford fault) and underthrusting Avalonia in the early Alleghenian orogeny.

Sample CT2223 is from the Waterford Group Gneiss which mantles Willimantic Dome in Central-Eastern Connecticut (Figures 5.2 and 5.6). The provenance of the Waterford Group is not well constrained; however, it is underlain by a pop-up of Avalonian Crust in the core of the dome. This suggests the Waterford group either represents a portion of the Avalonian crust, or a strongly metamorphosed and thinned section of the Putnam-Nashoba Terrane. The latter is more likely as no such intermediate-mafic assemblage is extensive in the exposed Avalonian basement of Rhode Island and southern Connecticut. This sample is unique in that quartz is not an abundant and interconnected mineral, therefore the deformation is primarily accommodated in the dominant amphibole and plagioclase phases. Macroscopic shear sense indicators in the Williamantic area are sparse. While evidence of simple shear is documented (e.g., Getty and Gromet, 1992), our own field investigation of the Waterford Gneiss documented primarily symmetric boudinage and little to no asymmetry within the amphibole-plagioclase gneiss (e.g., Figure 5.3H). CVA of plagioclase and amphibole yields a vorticity pole similar to sample CT2229. However, the pole is rotated relative to the nearby Willimantic dome, suggesting the deformation is early kinematic relative to Alleghenian uplift of Willimantic. While quartz was not modally abundant, the quartz EBSD data on the VNS is notable in that Dauphiné twinning produced a characteristic texture of the rhomb planes, {r} and {z}. As the {r}- and {z}-planes have different elastic properties, under deformation they will undergo dauphine twinning to reorient the more elastically compliant {r}-planes parallel to the maximum compressive stress. It has been proposed that this process can be used to estimate the paleostress direction (i.e., Rahl et al., 2018). As one direction is parallel to the foliation, we infer the maximum compressive paleo-stress direction corresponds to the subvertical population of {r}-faces. This suggests that paleostress was subvertical during late kinematic deformation around Willimantic dome in the Alleghenian orogeny. This would represent late rotation from the earlier episode of subhorizontal top-to-SE shear documented within the Merrimack Terrane in sample CT2229.

As a further estimate of depth within in the orogenic system, we calculated differential stress using quartz recrystallized grain size piezometry and subgrain size piezometry following the methods of Cross et al. (2017) and Goddard et al. (2020), respectively. For sample TH2107 in Vermont, there are no subgrains, so we utilize only the recrystallized grain size piezometer of Cross et al. (2017). The recrystallized grain size in TH2107 is ~1.92 µm, which corresponds to a differential stress of ~299 MPa. While high, this sample is almost entirely composed of quartz and plagioclase. This is particularly apparent when viewing the sample in cross polarized light due to the relative lack of high birefringence minerals. Sample CT2203 in Connecticut has a mean subgrain size of 98 µm corresponding to an effective stress of ~5 MPa (Goddard et al., 2021). Sample CT2217 at the southern end of the WBHSZ has a subgrain size of 57 µm, corresponding to an effective stress of ~8 MPa. From this data we observe a decrease in crustal strength moving southward along the WBHSZ. Crustal strength is broadly related to depth in the orogen, with peak crustal strength typically at the brittle-ductile transition in the mid-crust (Behr and Platt, 2011). The stress for the sample in Vermont is indicative of upper crustal deformation at a depth of ~10–15 km and strain rate of ~10^{-10} s^{-1} under strike-slip deformation (Figure 5.7). Samples in Connecticut yield low stresses of ~5–8 MPa, corresponding to viscous deformation in the mid-lower crust (>25 km) at strain rates between 10^{-12}–10^{-14} s^{-1}. The piezometric stress estimates for samples on the Eastford fault and within the Merrimack Terrane yield similarly low values (<6 MPa) demarcating an extensive mid-lower crustal weak zone in southern New England.

In the following sections, we place U-Pb geochronologic constraints on the timing of the deformation episodes discussed in this section based on *in situ* analysis of late- to post-kinematic monazite and synkinematic titanite grains in four sections from Eastern Connecticut and Central Massachusetts.

5.4.3 In situ Geochemistry and Geochronology of Monazite and Titanite in Southern New England

We analyzed U-Pb isotope and trace element compositions for *in situ* monazite and titanite in four samples at the southern terminus of the conjugate shear system to constrain the timing of deformation relative to hypothesized orogenic conjugate shear (i.e., Massey and Moecher, 2013). Two samples within the CMT (MA2207) and on the Eastford Fault (CT2205) were analyzed for *in situ* monazite, while two samples within the Merrimack Terrane (CT2223 and CT2229) were analyzed for *in situ* titanite via LA-ICP-MS. To assess the degree of ductile deformation in each grain and rule out the possibility of U-Pb diffusion during deformation we analyzed the monazite and titanite grains via EBSD. Unfortunately, the monazite grains did not index well with traditional published match units for monazite solid solution endmembers (i.e., Reddy et al., 2010; Erickson et al., 2015). Available monazite EBSD data suggests <1-2° of internal misorientation in both samples containing monazite. The relative lack of internal deformation in the monazites supports late or post kinematic (re)crystallization in the two studied samples. All the measured titanites are characterized by <5-10° of internal misorientation. While U-Pb resetting or disturbance can occur for such degrees of deformation in titanite (e.g., Moser et al., 2022), much of the titanite growth appears synkinematic with the foliation observed in thin section, and therefore the growth and deformation may have been largely contemporaneous.

Monazite in sample MA2207 is largely post-kinematic, with growth postdating much of the deformation and peak metamorphic assemblage in the sample. In addition, available EBSD data suggests <2° of internal misorientation in the post-kinematic monazite grains. Therefore, monazite in this sample should date the absolute latest moderate-high temperature (>400 °C, Williams et al., 2011) deformation episode. Monazite in this sample is characterized by weak to absent zoning in BSE in 3 of the selected grains, with one grain displaying pronounced concentric zoning. The three grains with muted zoning in BSE display lobate to patchy zoning of Ca and Th with little to no variation in Ce or Y (Figure 5.8). The only grain with well-developed concentric zoning in BSE displays similar concentric zones in Ca and Th and is also characterized by the presence of a low-Y core, in contrast to the other grains. The pronounced Ca and Th zoning in all four grains is indicative of the brabantite or cheralite [$(Ca,Th)(PO_4)_2$] substitution for REE in the monazite crystal lattice, a common substitution in metamorphic monazite (Williams and Jecyrnovic, 2007).

In contrast to sample MA2207, the monazite in sample CT2205, taken from the CMT in Northeastern Connecticut, is characterized by well-developed concentric zoning and lobate rim growth in BSE, with bright, resorbed cores present in at least three of the grains (Figure 5.14). Similar to the monazite in MA2207, the Ce maps display little to no zoning. Much of the zoning in BSE can be explained by the variations in Ca and Th due to the cheralite substitution for REEs as in the Central Massachusetts sample (Figure 8). In stark contrast to the monazite in MA2207, monazites in sample CT2205 are characterized by pronounced late growth of Y-rich lobate rims (Figure 8). The concentration of Y in monazite is generally related to the stability of garnet and/or xenotime in the bulk metamorphic assemblage (e.g., Hacker et al., 2019). Therefore, this variation may reflect a decrease in garnet stability (typically correlated to decreasing temperature) during late monazite crystallization. While there is no garnet in section CT2205 it is documented as being variably present in the sampled lithology and in other lithologies in proximity (Pease, 1988).

For titanite in sample CT2223 from the Waterford group mantling Willimantic dome, we observe very little zoning in both BSE and the compositional maps (Figures 5.9 and 5.14). There is fine lamellar to concentric zoning, particularly prominent in the third grain (Figure 5.9), however this zoning is below the resolution of the laser utilized during subsequent LA-ICP-MS analysis. The titanites in sample CT2223 are synmetamorphic and interstitial with surrounding epidote, amphibole, and plagioclase.

The titanites in sample CT2229 from the Devonian Canterbury Gneiss display a variety of complex zoning patterns (Figures 5.9 and 5.14). Two of the grains, which grew contemporaneously with the biotite foliation based on textures in thin section, are characterized by concentric and lobate rim growth in BSE (Figure 5.14). This pattern appears to primarily result from the compositional zoning in Al and Nb (Figure 5.9). Titanite grain 1 in this sample, while there is a bright BSE rim similar to the aforementioned two grains, also displays pronounced sector zoning due to the compositional variation of Nb. Lastly, the third grain is characterized by an anomalously bright BSE core surrounded by concentrically zoned titanite growth adjacent to the rim of the main grain. This grain is notable in that it displays pronounced Ce and Fe zoning between the core and rim growth suggesting different growth conditions than the other grains (Figure 5.9). High concentrations of Ce and Fe in titanite are most common in titanites grown during igneous crystallization (Gros et al., 2020), and therefore we anticipate that U-Pb isotopic ages in this section of the grain will yield results similar to the published zircon crystallization age of the Canterbury Gneiss (~414 Ma, Wintsch et al., 2007). Following EPMA mapping of the above grains, we analyzed the individual compositional domains with LA-ICP-MS.

In sample MA2207 we observe largely late Devonian and early Carboniferous U-Pb ages in all but one sample. For the three grains with little to no zoning in BSE, we observe a singular maximum in the kernel distribution function of spot ages in the grains (Figure 5.11). These maxima range from ~349-358 Ma, indicative of late Neoacadian growth. Much of this growth would seem to just predate retrograde metamorphism (~350-340 Ma) in the CMT of central Massachusetts based on recently published detailed geochronologic analysis of metamorphic and igneous monazites in Central Massachusetts (Moecher et al., 2021). This suggests that very little pervasive, moderate-high temperature deformation occurs during retrograde conditions. The trace element compositions of the monazite are largely uniform in this sample, with a relatively high slope for the HREEs (Dy-Lu). Such a trace element composition is generally interpreted as resulting from the presence of garnet during monazite growth (Hacker et al., 2019). These observations lead us to conclude that deformation within Central Massachusetts is not distributed at 350-360 Ma and has already begun to migrate to discrete amphibolite facies shear zones to the south and on the margins of the terrane (i.e., the WBHSZ). Of interest in this sample is grain 4 with significant zoning in BSE (Figure 5.14). This grain displays a singular maximum in the KDE at ~366 Ma, significantly older than the other grains. In contrast to the other three grains, this grain is preserved as an inclusion within synmetamorphic plagioclase in the sample. The concentric zoning pattern and older KDE maximum age of this grain seems to result from the preservation of Neoacadian metamorphic growth prior to retrograde metamorphism. The age of late growth in this grain overlaps with the maxima of the other three grains, displaying concentric rim growth from 335-360 Ma during the latest stages of the Neoacadian orogeny. In summary, sample MA2207 records primarily late- to post-kinematic monazite growth in the Neoacadian orogeny, however, records no growth during the Alleghenian orogeny after ~330 Ma contemporaneous with the conjugate orogenic shear system.

Monazite in sample CT2205 from the Eastford fault in Northeast Connecticut records a latest early-mid Carboniferous growth episode and a more complex Devonian crystallization history than those in sample MA2207. The most significant growth in all monazite grains in sample CT2205 occurred throughout the Acadian-Neoacadian orogeny. Primary maxima in the KDE occur at ~410, 378, 377, and 372 Ma for grains 1-4, respectively (Figure 5.11). The oldest monazite growth in this sample, in grain 1, records early Acadian (early Devonian) growth at ~420 Ma, contemporaneous with regional synkinematic intrusion of arc intrusive rocks such as the Kinsman Granitoid in New Hampshire and mafic-ultramafic cumulates in northeast Connecticut (Tassara et al., 2021). Both grains 1 and 4 have relatively old cores with approximate crystallization ages of 410 and 403 Ma, respectively. This early growth is indicative of early Acadian metamorphism. The youngest monazite growth occurs between 342-316 Ma on the rims of the grains (Figures 5.11 and 5.14). The U-Pb isotope compositions of the latest growth are notable in that their ages are partly discordant due to higher concentrations of common lead. Discordant monazite compositions can result from a variety of secondary processes (Hawkins and Bowring, 1997) such as fluid mineral interaction (Black et al., 1984;

Parrish, 1990; DeWolf et al., 1993), hydrothermal growth (Davis et al., 1994), and deformation (Getty and Gromet, 1992). All of these processes may have been active during Carboniferous orogenesis, however available EBSD data suggests little to no internal deformation. Therefore, the discordant rim growth likely results from fluid related interactions, which may be indirectly related to deformation on nearby shear zones. In addition to the younger ages, the trace element signatures of monazite in sample CT2205, while relatively uniform, are characterized by shallow HREE slopes. This is indicative of garnet breakdown or the absence of garnet during metamorphic growth as inferred from compositional maps of Y in the grains. The high Y, bright BSE rim domains always correspond to the youngest domains (<350 Ma) (Figure 5.14) which indicates some degree of garnet breakdown or open system compositional exchange due to fluid advection or partial melting and extraction (Yakymchuk and Brown, 2014) associated with late Devonian and early Carboniferous retrograde metamorphism or amphibolite facies metamorphism.

Titanite growth in sample CT2229 from the Canterbury Gneiss is relatively complex in contrast to published titanite ages for the Merrimack Terrane as a function of both U-Pb compositions and Zr-in-ttn temperatures of crystallization (Wintsch et al., 2007). We expect most of the titanite U-Pb compositions to be discordant when plotted on Tera-Wasserburg diagrams due to the incorporation of common lead (e.g., Essex and Gromet, 2000; Moser et al., 2022; Walters et al., 2022); however, we can utilize the slope of contemporaneous titanite growth in individual domains based on the BSE zoning and intragranular trace element compositions to constrain both the age of crystallization and the approximate common lead composition (e.g., Walters et al., 2022). Unanchored discordant age models for all the domains result in $^{207}Pb/^{206}Pb$ intercepts near the Stacey-Kramers common lead value from 500-250 Ma (~.85-.87, Stacey and Kramers, 1975).

For the two grains with the simplest concentric zoning of Al and Nb (Grains 2 and 4, Figure 5.9), we observe dominant crystallization during the early Alleghenian orogeny between

~315-290 Ma (Figure 5.12) at temperatures between 600-700 °C (Figure 5.14b) assuming a pressure of 7kb +/-3 kb (Wintsch et al., 1992; Moecher, 1997). Grain 2 crystallized at 309.3 ± 2.7 Ma while grain 4 crystallized at 317 ± 3.4 Ma (Figure 5.12), corresponding to early Alleghenian deformation and metamorphism contemporaneous with conjugate strike-slip shear in northern New England.

Titanite grain 1 in sample CT2229 is characterized by two dominant crystallization episodes (Figure 5.12). Older crystallization is associated with the prominent sector zoning of Nb (also visible in BSE, Figure 5.10) and flat LREE (La-Sm) profiles for spots in the core of the grain. The sector zoning is contemporaneous within error of the oldest growth in grain 1, and aside from the relative variation in Nb only displays gradual variations in trace element enrichment between sectors. The oldest compositional domain in this grain crystallized at 388.1 ± 1.6 Ma and at temperatures of >600-750 °C (Figures 5.12 and 5.14). A few points on the rim of grain 1, characterized by relatively low $^{238}U/^{206}Pb$ ratios, may reflect Neoacadian crystallization postdating the primary crystallization at ~388 Ma (Figure 5.14), however, these points are not compositionally distinct from the rest of the core spots. The younger domain in titanite grain 1 exhibits much greater scatter in U-Pb composition (MSWD = 10, Figure 5.12). This may be due in part to low degrees of deformation-induced resetting (i.e., Moser et al., 2021) or relatively continuous crystallization. The titanite growth in the youngest domain is dated to 323.3 ± 3.4 Ma and crystallized at conditions of 650-700 °C. Therefore, the rim growth, also corresponding to the most deformed sections of the crystal as determined by EBSD analysis, is contemporaneous with conjugate strike-slip shear in New England and early Alleghenian metamorphism.

Titanite grain 3 is the most complex of the four measured grains. The oldest crystallization in grain 3, associated with strongly enriched trace element compositions and a negative Eu anomaly, occurs at 390.9 ± 3.2 Ma and at temperatures >750 °C (Figures 5.12 and 5.14). This likely reflects crystallization during or just postdating igneous intrusion of the sampled lithology in the early Acadian orogeny based on the published zircon crystallization age of the Canterbury Gneiss (Wintsch et al., 2007) and the temperature of crystallization from Zr-in-ttn thermometry. This is the only grain in which we identified a prominent Neoacadian growth both in terms of U-Pb isotopic composition (Figure 5.12) and based on trace element compositions with flat LREE profiles and no negative Eu anomaly (Figure 5.10). This Neoacadian growth is found in the dark BSE rim domains that mantle the central Fe and Ce rich core domain (Figure 5.14). The Neoacadian rim growth occurred at 360.4 ± 6.6 Ma and temperatures of ~600-700 °C, suggesting crystallization during Neoacadian metamorphism. Final crystallization and rim growth in grain 3 occurred at 299.4 ± 5.1 Ma and temperatures of ~650-700 °C, broadly contemporaneous with growth in grains 2 and 4 during Alleghenian orogenesis and conjugate shearing.

Altogether, titanite in sample CT2229 reflects continuous crystallization from the early Acadian through the Alleghenian orogeny. Furthermore, Zr-in-ttn temperatures suggest that these lithologies (from the Merrimack Terrane) remained relatively hot (>600 °C) and deep (>4 kb) for over 100 Myrs of orogenesis (Figure 5.14). Cores in grains 1 and 3 preserve the conditions of igneous crystallization and peak Acadian metamorphism in the Devonian, while their rim domains and grains 2 and 4 record synkinematic titanite crystallization during the Alleghenian orogeny while the proposed conjugate fault system was active (~330-275 Ma, Massey and Moecher, 2013). The titanite crystallization temperatures for the rim domains and grains 2 and 4 suggest the U-Pb ages reflect crystallization immediately prior to the deformation discussed in section 5.4.2, which primarily occurred at temperatures between 500-600 °C.

Sample CT2223 contains three titanite grains with relatively uniform crystallization ages reflecting a single episode of growth in the mid-late Alleghenian orogeny and are late to post kinematic relative to orogenic conjugate shear (Figures 5.13 and 5.14). All three grains are characterized by LREE depleted and flat MREE and HREE profiles. Crystallization in the three grains occurred at 287.8 ± 4 Ma and at temperatures of 600-700 °C (assuming a similar range of pressures to sample CT2229 based on previous studies of Alleghenian metamorphism, Moecher, 1997; Wintsch et al., 2003). These grains are relatively young in comparison to the titanite growth in sample CT2229 with almost all spot ages younger than ~300 Ma (Figure 5.14) and no record of prior crystallization in the Acadian or Neoacadian orogenies. This growth would be pre to synkinematic with the observed dauphine twinning in quartz that implies a subvertical paleostress, and synkinematic with amphibole and plagioclase deformation that yields a subhorizontal to shallow vorticity vector reflecting early-mid Alleghenian deformation. Therefore, this growth just predates the transition to a subvertical maximum compressive stress as suggested by the dauphine twinning in the quartz discussed in section 5.4.2.

The transition from subhorizontal top-to-SE subhorizontal shear observed in sample CT2229 to subvertical collapse and extension documented in the quartz in sample CT2223 likely occurred between ~290-260 Ma in the mid-late Alleghenian orogen directly following peak metamorphism of Avalonia (Wintsch et al., 1992, Wintsch et al., 2014). This suggests a relationship between peak metamorphism of the underthrusting block (Avalonia) and the transition from crustal thickening and conjugate shear to orogenic collapse. These ages are comparatively young when considering the published Ar-Ar Hbl cooling ages for the Willimantic region which suggest regional temperatures of 500 °C by ~260 Ma. This implies amphibolite facies conditions were pervasive around Willimantic dome until 260-280 Ma, after which rapid uplift and cooling began.

5.5 Discussion

5.5.1 Mid-Lower Crustal Architecture of Conjugate Orogenic Strike-Slip Shear Systems

The conjugate strike-slip shear system composed of the sinistral WBHSZ and dextral Norumbega fault zone in the northern and central New England Appalachians terminates in a weak subhorizontal decollement in the middle crust of the Alleghenian orogen, exposed in southern New England. Our structural observations of the middle crust of the Alleghenian orogen in the New England Appalachians preclude transcrustal or translithospheric strike-slip faulting as the structure in the BHA, CMT, and Merrimack Terrane rotates from moderately to steeply dipping fabrics in Massachusetts, NH, and VT to subhorizontal and shallowly dipping fabrics in Connecticut. Microstructural and EBSD constraints on the orientation of the vorticity vector (Michels et al., 2015) and the vorticity number (Wallis, 1992), together with the macrostructural observations, demarcate a transition from strike-slip shear (transpression) in central Massachusetts and Vermont to pure shear/flattening deformation in Connecticut (Figure 5.6) representative of late Carboniferous deformation in the early Alleghenian orogeny.

The crustal architecture of the New England conjugate shear system is reminiscent of that proposed by Van Buer et al. (2015) for the Karakorum-Altyn Tagh conjugate shear system in Tibet. The depth of the proposed mid-crustal weak zone preserved in New England, approximately 7 kb, is nearly the same as the depth of the exposed weak zone in Tibet (~ 6.4 kb, Van Buer et al., 2015). The only contrast between the crustal architecture proposed herein and that proposed by Van Buer et al. (2015) is that the middle crust of New England represents a compressional decollement system instead of an extensional detachment.

The crustal structure and rheology of the conjugate shear system in New England is characterized by upper crustal mylonitization and semi-brittle strike-slip deformation in northern New England and subhorizontal simple shear and flattening in a very weak (<9 MPa) mid-crustal layer directly below the conjugate shear system in the upper crust (Figure 5.7). We can subdivide the modern-day system into three regimes based on strength and deformation style (Figures 5.6 and 5.7). The northernmost regime is characterized by rigid behavior of the medial block with subvertical shear zone mylonites deforming under dominant simple shear on the margins. This behavior is reminiscent of the upper crustal structure documented in central Tibet and southeast Asia (Morley, 2001; Yin and Taylor, 2011; Van Buer et al., 2015). The central regime is characterized by semi-rigid behavior of the medial block (CMT) with general and flattening shear zones on the margins. The southernmost regime, preserved in the Merrimack Terrane and BHA, represents the underlying mid-crustal weak zone characterized by a combination of inclined flattening strains and top-to-southeast shear due to the relative motion of the underthrusting Avalonia block and overriding CMT. The Merrimack Terrane, Eastford fault, and BHA in Southern New England are all characterized by extremely low strengths corresponding to a weak mid-lower crust (Figure 5.7).

Each of these three zones is also characterized by a pronounced variation in the vorticity number, or relative amounts of simple and pure shear, along strike of the WBHSZ. Ultimately, the variation in vorticity number likely reflects a combination of changing plate boundary orientation and vertical strain partitioning between the upper, middle, and lower crust (e.g., Figure 5.15). It is reasonable to conclude that deformation is horizontally as well as vertically partitioned (e.g., Northrup and Burchfield, 1996). While a large-scale rotation of the maximum horizontal stress direction may result from along-strike variations in plate-boundary orientation (e.g., Faure et al., 1996), abrupt changes in horizontal stress azimuth, such as that required between the WBHSZ and Norumbega fault zone are more readily explained by deformation partitioning (see Figure 5.15 and section 5.5.2 for a discussion of paleo-stress directions, convergence direction, and plate boundary orientation). Therefore, from our observations of Carboniferous deformation in southern New England versus northern New England, we conclude that strike-slip and orogen parallel deformation is strongly partitioned into the upper crust, while the weak middle crust accommodates slip and pure shear near parallel to the convergence direction in the late Paleozoic (Figure 15, Young et al., 2019). Furthermore, if deformation is vertically partitioned, it would explain why strike-slip deformation is abundant throughout the upper crust exposed in northern New England, Eastern Canada, and NW Africa while it is nearly absent in mid-lower crust exposed in southern New England.

The presence of a subhorizontal weak zone in the orogenic middle crust endorses the classical 'jelly sandwich' model of orogenic rheology, where the upper (CMT) and lower (Avalonia/Ganderia) crust are decoupled along a weak layer in the middle crust (Merrimack Terrane) (Figure 5.7). Although, we did not identify an underlying rigid lower crust. Wintsch et al. (2014) suggest that Avalonia remained relatively rigid until after prograde metamorphism at ~300-290 Ma. Thus, Avalonia and the lithologies on the south side of the Honey Hill fault may represent the feldspar rich, strong lower crust. It is unclear from our results whether a weak mid-crustal layer is sufficient to inhibit transcrustal or translithospheric strike-slip shear, or if the regional kinematics and deformation regime are also important.

The subhorizontal weak zone in the middle crust and associated subhorizontal fabric developed no earlier than the early Alleghenian orogeny in the mid-late Carboniferous while high temperature metamorphism may have persisted from the previous Acadian-Neoacadian orogeny based on Zr-in-ttn constraints on the temperature of metamorphism (Figure 5.14). The temperature-time data from the studied titanites implies over 100 Myrs of high temperatures in the middle crust, however the subhorizontal weak layer may not have been present for the entirety of this period. Therefore, metamorphism alone cannot explain the development of such a subhorizontal weak layer in the middle crust, as there is no evidence for a similar layer during Acadian-Neoacadian orogenesis which achieved comparable mid-crustal conditions to those documented in the Alleghenian middle crust (Chu et al., 2018).

The regional kinematics and deformation style must play an important role in the creation of the subhorizontal layer due to its absence during previous Acadian-Neoacadian deformation which occurred at similar temperatures. It is likely that one of two factors is required to produce a subhorizontal layer in the weak middle crust, either 1) flattening in the orogenic hinterland resulting from orogenic collapse or significant upper crustal loading or 2) orogen parallel simple shear between the upper and lower crust due to depth-dependent partitioning or paired general shear (Yin and Taylor, 2011).

5.5.2 Gondwana-Laurasia Permo-Carboniferous Stress Field and Kinematics

We hypothesize that conjugate strike-slip shear in the early Alleghenian orogeny and the significant regional contrast between the northern and southern Appalachians resulted primarily from the variation in plate boundary geometry during the collision of Gondwana and

Laurasia. Where the plate boundary in the northern Appalachians reflects strongly oblique convergence in comparison to near head-on collision in the southern Appalachians (Figure 5.15). The structure of the northern and southern Appalachians is fundamentally different both in terms of their macroscale structure and the spatial distribution of metamorphism. Previous studies commonly invoke a regional regime of dextral transpression for both the Acadian-Neoacadian and early Alleghenian orogenies in the northern and southern Appalachians (Ferrill and Thomas, 1988; Gates et al., 1988; West and Hubbard, 1997; Robinson et al., 1998; Solar and Brown, 2001; Valentino and Gates, 2001; Merschat et al., 2005; Massey et al., 2017). Gates et al. (1988) previously hypothesized that an extrusion model for the northern Appalachians is inconsistent with the absence of major sinistral shear zones. However, with the work of Massey and Moecher (2013), McWilliams et al. (2013), and the results of this study, it is clear that a major sinistral shear zone is present in the western BHA. The identification of this major sinistral shear zone by Massey and Moecher (2013) leads us to reevaluate the regional deformation regime during Carboniferous orogenesis and quantitatively assess the relationship between the convergence direction of Gondwana and Laurasia and the local stress field required by deformation on Alleghenian faults.

We can determine the local direction of the maximum horizontal stress through a simple relationship between vorticity number and the angle of the flow apophyses (Fossen and Cavalcante, 2017). Vorticity number is directly equal to the cosine of the angle between the flow apophyses. Assuming that one of the flow apophyses is representative of the foliation plane, then the other corresponds to the direction of the maximum principal stress. Therefore, we can use our estimates of vorticity number to map out the regional variation in maximum compressive stress directions in New England and compare our results to estimates of stress direction in the southern Appalachians, the convergence direction between Gondwana and Laurasia, and the plate boundary orientation.

The results of our calculated maximum compressive stress orientations are shown on Figure 5.11 relative to the regional structures associated with the collision of Laurasia and Gondwana. We observe a significant variation in principal stress orientation within New England, with the northern WBHSZ and Norumbega fault zones yielding near perpendicular results. Further south, the horizontal stress directions are closer to the overall convergence direction between Gondwana and Laurasia as determined from the plate kinematic model of Young et al. (2019). The contrasting stress directions in the northern Appalachians required by deformation on the WBHSZ and Norumbega fault zone likely reflect significant strain partitioning in the upper crust as inferred in the previous section. If we knew the relative displacements on these two fault zones, we could attempt to calculate the convergence direction based on the relative amounts of deformation partitioned onto the two shear zones; however, it is extremely difficult to estimate displacements with any certainty on the strike parallel WBHSZ. If the shear zones have near equal displacements, their sum would yield a total stress azimuth near the convergence direction.

The two calculated stress directions for southern New England reflect decreasing degrees of strain partitioning with increasing depth in the orogen as they are near parallel to the convergence direction. The sample at ~30° degrees to the convergence direction is CT2203, which records general shear in the WBHSZ. In concert with the flattening shear zone on the eastern margin of the CMT (based on deformation analysis of sample CT2208), the E-W convergence in central Massachusetts and northern Connecticut may have still been largely accommodated on the margins of the CMT. The southernmost stress direction of this study, from sample CT2217, is almost exactly parallel to the convergence direction. This result together with the vorticity vector for sample CT2229 which also suggests near E-W horizontal stress strongly suggests that the convergence between Gondwana and Laurasia is not partitioned in the weak mid-crustal layer with dip-slip and flattening in the direction of bulk convergence.

Stress direction estimates for the southern Appalachians yield a similar result to the southernmost sample discussed above. Figure 5.15 displays the stress direction estimated by analyzing Carboniferous-Permian joint set directions in the southern Appalachians (Engelder and Whitaker, 2006). The direction of bulk convergence and estimates of horizontal stress direction in the southern Appalachians are consistent with observations of dextral transpressive deformation along major structures such as the Brevard Fault Zone (Merschat et al., 2005).

While the convergence direction does not change dramatically between the south and north Appalachians, the plate boundary orientation rotates up to 80° in the northern Appalachians and NW Africa from the plate boundary between the Suwannee terrane and Laurasia in the southern Appalachians (Figure 5.15, Young et al., 2019). This obviously explains why dextral strike-slip shear zones are so prevalent in the northern Appalachians and NW Africa as commonly discussed in the literature, however, the presence of a sinistral shear zone conjugate to the Norumbega is enigmatic. Sinistral deformation on the WBHSZ would seem inconsistent with the bulk convergence direction in the Carboniferous. The lack of underlying orogen-parallel flow is inconsistent with models which invoke basal tractions such as paired general shear (Yin and Taylor, 2011). Based on these results, we favor a model where the sinistral shear zone is necessary as an antithetic shear zone accommodating deformation between the adjacent and relatively juvenile Paleozoic terranes and the rigid and old Laurasian cratonic lithosphere. The sinistral WBHSZ in tandem with the dextral Norumbega fault zone serves to facilitate extrusion of the relatively rigid CMT to the north and away from the zone of direct convergence in the southern Appalachians.

In addition to accommodating deformation on the margin of the Laurasian craton, the extrusion of the CMT between conjugate strike-slip shear zones would serve to facilitate convergence between Gondwana and Laurasia. The near perpendicular convergence to the south likely produced significantly greater crustal thicknesses in comparison to the northern Appalachians, prohibiting significant orogen-parallel transport from north to south. The variation in crustal thickness (based on studies of Alleghenian metamorphism) between the relatively thicker southern New England Appalachians versus the comparatively thin northern Appalachians would serve to drive N-S, orogen-parallel transport away from the region of elevated crustal thickness (Hillenbrand et al., 2021).

Therefore, ascribing a regional deformation regime of dextral transpression for the Alleghenian orogeny in New England is perhaps misleading given the diversity of shear zones documented in this study. Alleghenian shear zones in New England range from strike-slip dominant dextral and sinistral regimes to flattening and dip-slip zones. The spatial pattern of coaxial dominant deformation, or 'pinching,' in the south transitioning to upper crustal conjugate strike-slip in the north is consistent with a northward extrusion model for deformation in the northern Appalachians during, at least, the early Alleghenian orogeny (~330-280 Ma). The extrusion results from the relatively head-on collision, or indentation, of Gondwana to the south, with strongly oblique convergence in the north. Future work should focus on reevaluating the spatio-temporal variation in Alleghenian metamorphism in the southern Appalachians to place precise constraints on the P-T conditions associated with changing deformation regimes in the Merrimack Terrane and underlying Avalonia.

5.6 Conclusions

We have found that spatio-temporal variations in Permo-Carboniferous deformation in the New England Appalachians are consistent with a model of orogenic conjugate strike-slip shear similar to that proposed by Van Buer et al. (2015) for the Tibetan plateau. Upper crustal strike-slip shear zone mylonites in northern New England transition to general and flattening shear zones in the weak middle crust of the Alleghenian orogen, reflecting decreasing degrees of deformation partitioning with depth in the orogenic system relative to the convergence direction in the late Carboniferous. Furthermore, our results support an upper crustal extrusion model, similar to commonly invoked extrusion models in the Eastern Himalayas and SE Asia. The presence of a major sinistral shear zone and significant flattening and dip-slip deformation in

New England suggest inferences of regional dextral transpression in the late Paleozoic present in incomplete picture of trans-crustal deformation.

References

Aitken, J. M. (1955). *The bedrock geology of the Rockville quadrangle with map* [Map]. Connecticut Geological and Natural History Survey.

Alavi, M. (1994). Tectonics of the zagros orogenic belt of iran: New data and interpretations. *Tectonophysics*, *229*(3–4), 211–238. https://doi.org/10.1016/0040-1951(94)90030-2

Aleinikoff, J. N., Schenck, W. S., Plank, M. O., Srogi, L., Fanning, C. M., Kamo, S. L., & Bosbyshell, H. (2006). Deciphering igneous and metamorphic events in high-grade rocks of the Wilmington Complex, Delaware: Morphology, cathodoluminescence and backscattered electron zoning, and SHRIMP U-Pb geochronology of zircon and monazite. *Geological Society of America Bulletin*, *118*(1–2), 39–64. https://doi.org/10.1130/B25659.1

Allen, M., Jackson, J., & Walker, R. (2004). Late Cenozoic reorganization of the Arabia-Eurasia collision and the comparison of short-term and long-term deformation rates. *Tectonics*, *23*(2), 2003TC001530. https://doi.org/10.1029/2003TC001530

Anderson, E. M. (1905). The dynamics of faulting. *Transactions of the Edinburgh Geological Society*, *8*(3), 387–402. https://doi.org/10.1144/transed.8.3.387

Armstrong, T. R. (1997). *Preliminary bedrock geologic map of the Vermont part of the 7.5 x 15 minute Bellows Falls Quadrangle, Windham and Windsor counties, Vermont* (Open-File Report 97–284; Open-File Report). US Geological Survey.

Bachmann, F., Hielscher, R., & Schaeben, H. (2010). Texture Analysis with MTEX – Free and Open Source Software Toolbox. *Solid State Phenomena*, *160*, 63–68. https://doi.org/10.4028/www.scientific.net/SSP.160.63

Backé, G., Dhont, D., & Hervouët, Y. (2006). Spatial and temporal relationships between compression, strike-slip and extension in the Central Venezuelan Andes: Clues for Plio-Quaternary tectonic escape. *Tectonophysics*, *425*(1–4), 25–53. https://doi.org/10.1016/j.tecto.2006.06.005

Badham, J. P. N. (1982). Strike-slip orogens—An explanation for the Hercynides. *Journal of the Geological Society*, *139*(4), 493–504. https://doi.org/10.1144/gsjgs.139.4.0493

Barth, N. C., Hacker, B. R., Seward, G. G. E., Walsh, E. O., Young, D., & Johnston, S. (2010). Strain within the ultrahigh-pressure Western Gneiss region of Norway recorded by quartz CPOs. *Geological Society, London, Special Publications*, *335*(1), 663–685. https://doi.org/10.1144/SP335.27

Behr, W. M., & Platt, J. P. (2011). A naturally constrained stress profile through the middle crust in an extensional terrane. *Earth and Planetary Science Letters*, *303*(3–4), 181–192. https://doi.org/10.1016/j.epsl.2010.11.044

Bird, J. M., & Dewey, J. F. (1970). Lithosphere Plate-Continental Margin Tectonics and the Evolution of the Appalachian Orogen. *Geological Society of America Bulletin*, *81*(4), 1031. https://doi.org/10.1130/0016-7606(1970)81[1031:LPMTAT]2.0.CO;2

Black, L. P., Fitzgerald, J. D., & Harley, S. L. (1984). Pb isotopic composition, colour, and microstructure of monazites from a polymetamorphic rock in Antarctica. *Contributions to Mineralogy and Petrology*, *85*(2), 141–148. https://doi.org/10.1007/BF00371704

Bradley, D. C., & O'Sullivan, P. (2017). Detrital zircon geochronology of pre- and syncollisional strata, A cadian orogen, M aine A ppalachians. *Basin Research*, *29*(5), 571–590. https://doi.org/10.1111/bre.12188

Brookfield, M. E., & Hashmat, A. (2001). The geology and petroleum potential of the North Afghan platform and adjacent areas (northern Afghanistan, with parts of southern Turkmenistan, Uzbekistan and Tajikistan). *Earth-Science Reviews*, *55*(1–2), 41–71. https://doi.org/10.1016/S0012-8252(01)00036-8

Budzyń, B., Sláma, J., Corfu, F., Crowley, J., Schmitz, M., Williams, M. L., Jercinovic, M. J., Kozub-Budzyń, G. A., Konečny, P., Rzepa, G., & Włodek, A. (2021). TS-Mnz – A new monazite age reference material for U-Th-Pb microanalysis. *Chemical Geology*, *572*, 120195. https://doi.org/10.1016/j.chemgeo.2021.120195

Bunge, H.-J. (1982). *Texture Analysis in Materials Science* (H.-J. Bunge, Ed.). Butterworth-Heinemann. https://doi.org/10.1016/B978-0-408-10642-9.50020-9

Calais, E., Vergnolle, M., San'kov, V., Lukhnev, A., Miroshnitchenko, A., Amarjargal, S., & Déverchère, J. (2003). GPS measurements of crustal deformation in the Baikal-Mongolia area (1994–2002): Implications for current kinematics of Asia. *Journal of Geophysical Research: Solid Earth*, *108*(B10), 2002JB002373. https://doi.org/10.1029/2002JB002373

Chambers, J. A., & Kohn, M. J. (2012). *Titanium in muscovite, biotite, and hornblende: Modeling, thermometry, and rutile activities of metapelites and amphibolites*. *97*(4), 543–555. https://doi.org/10.2138/am.2012.3890

Chu, X., Ague, J. J., Tian, M., Baxter, E. F., Rumble, D., & Chamberlain, C. P. (2018). Testing for Rapid Thermal Pulses in the Crust by Modeling Garnet Growth–Diffusion–Resorption Profiles in a UHT Metamorphic 'Hot Spot', New Hampshire, USA. *Journal of Petrology*. https://doi.org/10.1093/petrology/egy085

Collins, G. E. (1954). *The bedrock geology of the Ellington quadrangle with map* [Map]. Connecticut Geological and Natural History Survey.

Cross, A. J., Prior, D. J., Stipp, M., & Kidder, S. (2017). The recrystallized grain size piezometer for quartz: An EBSD-based calibration. *Geophysical Research Letters*, *44*(13), 6667–6674. https://doi.org/10.1002/2017GL073836

Cunningham, D. (2005). Active intracontinental transpressional mountain building in the Mongolian Altai: Defining a new class of orogen. *Earth and Planetary Science Letters*, *240*(2), 436–444. https://doi.org/10.1016/j.epsl.2005.09.013

Czeck, D. (2003). Testing models for obliquely plunging lineations in transpression: A natural example and theoretical discussion. *Journal of Structural Geology*, *25*(6), 959–982. https://doi.org/10.1016/S0191-8141(02)00079-2

Dallmeyer, R. D. (1982). 40Ar/39Ar ages from the Narragansett Basin and southern Rhode Island basement terrane: Their bearing on the extent and timing of Alleghenian tectonothermal events in New England. *GSA Bulletin*, *93*(11), 1118–1130. https://doi.org/10.1130/0016-7606(1982)93<1118:AAFTNB>2.0.CO;2

Davis, D. W., Schandl, E. S., & Wasteneys, H. A. (1994). U-Pb dating of minerals in alteration halos of Superior Province massive sulfide deposits: Syngenesis versus metamorphism. *Contributions to Mineralogy and Petrology*, *115*(4), 427–437. https://doi.org/10.1007/BF00320976

Deasy, R. T., & Wintsch, R. P. (2019). *Draft Bedrock Geologic Map of the Deep River Quadrangle, New London and Middlesex Counties, Connecticut, USA* [Map]. Connecticut Geological and Natural History Survey.

DeWolf, C. P., Belshaw, N., & O'Nions, R. K. (1993). A metamorphic history from micron-scale 207Pb/206Pb chronometry of Archean monazite. *Earth and Planetary Science Letters*, *120*(3–4), 207–220. https://doi.org/10.1016/0012-821X(93)90240-A

Dhont, D., Chorowicz, J., & Luxey, P. (2006). Anatolian escape tectonics driven by Eocene crustal thickening and Neogene–Quaternary extensional collapse in the eastern Mediterranean region. In Y. Dilek & S. Pavlides, *Postcollisional Tectonics and Magmatism in the Mediterranean Region and Asia*. Geological Society of America. https://doi.org/10.1130/2006.2409(21)

Dixon, H. R. (1965). *Bedrock geologic map of the Plainfield quadrangle, Windham and New London Counties, Connecticut* [Map]. U.S. Geological Survey. https://doi.org/10.3133/gq481

Dixon, H. R. (1968). *Bedrock geologic map of the Danielson quadrangle, Windham County, Connecticut* [Map]. U.S. Geological Survey. https://doi.org/10.3133/gq696

Dixon, H. R. (1974). *Bedrock geologic map of the Thompson quadrangle, Windham County, Connecticut, and Providence County, Rhode Island* [Map]. U.S. Geological Survey. https://doi.org/10.3133/gq1165

Dixon, H. R. (1982). *Bedrock geologic map of the Putnam quadrangle, Windham County, Connecticut* [Map]. U.S. Geological Survey. https://doi.org/10.3133/gq1562

Dixon, H. R., & Felmlee, J. K. (1986). *Bedrock geologic map of the Jewett City quadrangle, New London County, Connecticut* [Map]. U.S. Geological Survey. https://doi.org/10.3133/gq1575

Dixon, H. R., & Pessl, F. (1966). *Geologic map of the Hampton quadrangle, Windham County, Connecticut* [Map]. U.S. Geological Survey. https://doi.org/10.3133/gq468

Dixon, H. R., & Shaw, C. E. (1965). *Geologic map of the Scotland quadrangle, Connecticut* [Map]. U.S. Geological Survey. https://doi.org/10.3133/gq392

Domeier, M., & Torsvik, T. H. (2014). Plate tectonics in the late Paleozoic. *Geoscience Frontiers*, *5*(3), 303–350. https://doi.org/10.1016/j.gsf.2014.01.002

Eaton, G. P., & Rosenfeld, J. L. (1972). *Preliminary bedrock geologic map of the Middle Haddam quadrangle, Middlesex County, Connecticut* [Map]. U.S. Geological Survey.

Engelder, T., & Whitaker, A. (2006). Early jointing in coal and black shale: Evidence for an Appalachian-wide stress field as a prelude to the Alleghanian orogeny. *Geology*, *34*(7), 581. https://doi.org/10.1130/G22367.1

Erickson, T. M., Pearce, M. A., Taylor, R. J. M., Timms, N. E., Clark, C., Reddy, S. M., & Buick, I. S. (2015). Deformed monazite yields high-temperature tectonic ages. *Geology*, *43*(5), 383–386. https://doi.org/10.1130/G36533.1

Essex, R. M., & Gromet, L. P. (2000). U-Pb dating of prograde and retrograde titanite growth during the Scandian orogeny. *Geology*, *28*(5), 419–422. https://doi.org/10.1130/0091-7613(2000)28<419:UDOPAR>2.0.CO;2

Eusden, J., & Barrerio, B. (1988). The timing of peak high-grade metamorphism in central-eastern New England. *Atlantic Geology*, *24*(3), 241–255. Érudit.

Eusden, J. D., Jr. (1988). The bedrock geology of the Gilmanton 15-minute quadrangle, New Hampshire [Ph.D., Dartmouth College]. In *ProQuest Dissertations and Theses* (303701407). ProQuest Dissertations & Theses Global. https://www.proquest.com/dissertations-theses/bedrock-geology-gilmanton-15-minute-quadrangle/docview/303701407/se-2?accountid=12492

Eusden, J. D., & Lyons, J. B. (1993). The sequence of Acadian deformations in central New Hampshire. In *Geological Society of America Special Papers* (Vol. 275, pp. 51–66). Geological Society of America. https://doi.org/10.1130/SPE275-p51

Fahey, R. J., & Pease, M. H. (1977). *Preliminary Bedrock Geologic Map of the South Coventry Quadrangle, Tolland County, Connecticut* [Map]. Connecticut Geological and Natural History Survey.

Faure, S., Tremblay, A., & Angelier, J. (1996). Alleghanian paleostress reconstruction in the northern Appalachians: Intraplate deformation between Laurentia and Gondwana. *GSA Bulletin*, *108*(11), 1467–1480. https://doi.org/10.1130/0016-7606(1996)108<1467:APRITN>2.3.CO;2

Feininger, T. (1965). *Bedrock geologic map of the Voluntown quadrangle, New London County, Connecticut, and Kent and Washington Counties, Rhode Island* [Map]. U.S. Geological Survey. https://doi.org/10.3133/gq436

Ferrill, B. A., & Thomas, W. A. (1988). Acadian dextral transpression and synorogenic sedimentary successions in the Appalachians. *Geology*, *16*(7), 604–608. https://doi.org/10.1130/0091-7613(1988)016<0604:ADTASS>2.3.CO;2

Fisher, C. M., Bauer, A. M., Luo, Y., Sarkar, C., Hanchar, J. M., Vervoort, J. D., Tapster, S. R., Horstwood, M., & Pearson, D. G. (2020). Laser ablation split-stream analysis of the Sm-Nd and U-Pb isotope compositions of monazite, titanite, and apatite – Improvements, potential reference materials, and application to the Archean Saglek Block gneisses. *Chemical Geology*, *539*, 119493. https://doi.org/10.1016/j.chemgeo.2020.119493

Fossen, H., & Cavalcante, G. C. G. (2017). Shear zones – A review. *Earth-Science Reviews*, *171*, 434–455. https://doi.org/10.1016/j.earscirev.2017.05.002

Fossen, H., & Tikoff, B. (1998). Extended models of transpression and transtension, and application to tectonic settings. *Geological Society, London, Special Publications*, *135*(1), 15–33. https://doi.org/10.1144/GSL.SP.1998.135.01.02

Gates, A. E., Speer, J. A., & Pratt, T. L. (1988). The Alleghanian Southern Appalachian Piedmont: A transpressional model. *Tectonics*, *7*(6), 1307–1324. https://doi.org/10.1029/TC007i006p01307

Getty, S. R., & Gromet, L. P. (1992). Evidence for extension at the Willimantic Dome, Connecticut; implications for the late Paleozoic tectonic evolution of the New England Appalachians. *American Journal of Science*, *292*(6), 398–420. https://doi.org/10.2475/ajs.292.6.398

Ghent, E. D., & Stout, M. Z. (1984). TiO2 activity in metamorphosed pelitic and basic rocks: Principles and applications to metamorphism in southeastern Canadian Cordillera. *Contributions to Mineralogy and Petrology*, *86*(3), 248–255. https://doi.org/10.1007/BF00373670

Goddard, R. M., Hansen, L. N., Wallis, D., Stipp, M., Holyoke, C. W., Kumamoto, K. M., & Kohlstedt, D. L. (2020). A Subgrain-Size Piezometer Calibrated for EBSD. *Geophysical Research Letters*, *47*(23), e2020GL090056. https://doi.org/10.1029/2020GL090056

Goldsmith, R. (1967a). *Bedrock geologic map of the Montville quadrangle, New London County, Connecticut* [Map]. U.S. Geological Survey. https://doi.org/10.3133/gq609

Goldsmith, R. (1967b). *Bedrock geologic map of the Uncasville quadrangle, New London County, Connecticut* [Map]. U.S. Geological Survey. https://doi.org/10.3133/gq576

Goldstein, A. G. (1989). Tectonic significance of multiple motions on terrane-bounding faults in the northern Appalachians. *GSA Bulletin*, *101*(7), 927–938. https://doi.org/10.1130/0016-7606(1989)101<0927:TSOMMO>2.3.CO;2

Gonçalves, G. O., Lana, C., Scholz, R., Buick, I. S., Gerdes, A., Kamo, S. L., Corfu, F., Marinho, M. M., Chaves, A. O., Valeriano, C., & Nalini, H. A. (2016). An assessment of monazite from the Itambé

pegmatite district for use as U–Pb isotope reference material for microanalysis and implications for the origin of the “Moacyr” monazite. *Chemical Geology*, *424*, 30–50. https://doi.org/10.1016/j.chemgeo.2015.12.019
Gros, K., Słaby, E., Birski, Ł., Kozub-Budzyń, G., & Sláma, J. (2020). Geochemical evolution of a composite pluton: Insight from major and trace element chemistry of titanite. *Mineralogy and Petrology*, *114*(5), 375–401. https://doi.org/10.1007/s00710-020-00715-x
Hacker, B., Kylander-Clark, A., & Holder, R. (2019). REE partitioning between monazite and garnet: Implications for petrochronology. *Journal of Metamorphic Geology*, *37*(2), 227–237. https://doi.org/10.1111/jmg.12458
Harwood, D. S., & Goldsmith, R. (1971). *Bedrock geologic map of the Oneco quadrangle, Connecticut-Rhode Island* [1:24000]. U.S. Geological Survey. https://doi.org/10.3133/gq930
Hatcher, R. D. (2010). The Appalachian orogen: A brief summary. In R. P. Tollo, M. J. Bartholomew, J. P. Hibbard, & P. M. Karabinos, *From Rodinia to Pangea: The Lithotectonic Record of the Appalachian Region*. Geological Society of America. https://doi.org/10.1130/2010.1206(01)
Hawkins, D. P., & Bowring, S. A. (1997). U-Pb systematics of monazite and xenotime: Case studies from the Paleoproterozoic of the Grand Canyon, Arizona. *Contributions to Mineralogy and Petrology*, *127*(1–2), 87–103. https://doi.org/10.1007/s004100050267
Hayden, L. A., Watson, E. B., & Wark, D. A. (2008). A thermobarometer for sphene (titanite). *Contributions to Mineralogy and Petrology*, *155*(4), 529–540. https://doi.org/10.1007/s00410-007-0256-y
Hepburn, J. C., Kuiper, Y. D., McClary, K. J., Loan, M. L., Tubrett, M., & Buchwaldt, R. (2021). Detrital zircon ages and the origins of the Nashoba terrane and Merrimack belt in southeastern New England, USA. *Atlantic Geology*, *57*, 343–396. https://doi.org/10.4138/atlgeol.2021.016
Herz, N. (1955). *The bedrock geology of the Glastonbury quadrangle with map* [Map]. Connecticut Geological and Natural History Survey.
Hillenbrand, I. W., Williams, M. L., Li, C., & Gao, H. (2021). Rise and fall of the Acadian altiplano: Evidence for a Paleozoic orogenic plateau in New England. *Earth and Planetary Science Letters*, *560*, 116797. https://doi.org/10.1016/j.epsl.2021.116797
Hirth, G., & Tullis, J. (1992). Dislocation creep regimes in quartz aggregates. *Journal of Structural Geology*, *14*(2), 145–159. https://doi.org/10.1016/0191-8141(92)90053-Y
Holdaway, M. J., Dutrow, B. L., & Hinton, R. W. (1988). Devonian and Carboniferous metamorphism in west-central Maine; the muscovite-almandine geobarometer and the staurolite problem revisited. *American Mineralogist*, *73*(1–2), 20–47.
Houari, M.-R., & Hoepffner, C. (2003). Late Carboniferous dextral wrench-dominated transpression along the North African craton margin (Eastern High-Atlas, Morocco). *Journal of African Earth Sciences*, *37*(1–2), 11–24. https://doi.org/10.1016/S0899-5362(03)00085-X
Hutchinson, D. R., Klitgord, K. D., Lee, M. W., & Trehu, A. M. (1988). U.S. Geological Survey deep seismic reflection profile across the Gulf of Maine. *GSA Bulletin*, *100*(2), 172–184. https://doi.org/10.1130/0016-7606(1988)100<0172:USGSDS>2.3.CO;2
Ivanov, M. A., & Head, J. W. (2011). Global geological map of Venus. *Planetary and Space Science*, *59*(13), 1559–1600. https://doi.org/10.1016/j.pss.2011.07.008
Jackson, J., & McKenzie, D. (1984). Active tectonics of the Alpine—Himalayan Belt between western Turkey and Pakistan. *Geophysical Journal International*, *77*(1), 185–264. https://doi.org/10.1111/j.1365-246X.1984.tb01931.x
Johnson, S. E., Lenferink, H. J., Marsh, J. H., Price, N. A., Koons, P. O., & West, D. P. (2009). Kinematic vorticity analysis and evolving strength of mylonitic shear zones: New data and numerical results. *Geology*, *37*(12), 1075–1078. https://doi.org/10.1130/G30227A.1
Kapp, P., Manning, C. E., & Tropper, P. (2009). Phase-equilibrium constraints on titanite and rutile activities in mafic epidote amphibolites and geobarometry using titanite–rutile equilibria. *Journal of Metamorphic Geology*, *27*(7), 509–521. https://doi.org/10.1111/j.1525-1314.2009.00836.x
Karabinos, P., Macdonald, F. A., & Crowley, J. L. (2017). Bridging the gap between the foreland and hinterland I: Geochronology and plate tectonic geometry of Ordovician magmatism and terrane accretion on the Laurentian margin of New England. *American Journal of Science*, *317*(5), 515–554. https://doi.org/10.2475/05.2017.01

Kay, A., Hepburn, J. C., Kuiper, Y. D., & Baxter, E. F. (2017). Geochemical evidence for a Ganderian arc/back-arc remnant in the Nashoba Terrane, SE New England, USA. *American Journal of Science*, *317*(4), 413–448. https://doi.org/10.2475/04.2017.01

Kinney, S. T., MacLennan, S. A., Szymanowski, D., Keller, C. B., VanTongeren, J. A., Setera, J. B., Jaret, S. J., Town, C. F., Strauss, J. V., Bradley, D. C., Olsen, P. E., & Schoene, B. (2022). Onset of long-lived silicic and alkaline magmatism in eastern North America preceded Central Atlantic Magmatic Province emplacement. *Geology*, *50*(11), 1301–1305. https://doi.org/10.1130/G50181.1

Kruckenberg, S. C., Michels, Z. D., & Parsons, M. M. (2019). From intracrystalline distortion to plate motion: Unifying structural, kinematic, and textural analysis in heterogeneous shear zones through crystallographic orientation-dispersion methods. *Geosphere*, *15*(2), 357–381. https://doi.org/10.1130/GES01585.1

Kuiper, Y. D., Thompson, M. D., Barr, S. M., White, C. E., Hepburn, J. C., & Crowley, J. L. (2017). Detrital zircon evidence for Paleoproterozoic West African crust along the eastern North American continental margin, Georges Bank, offshore Massachusetts, USA. *Geology*, *45*(9), 811–814. https://doi.org/10.1130/G39203.1

Leloup, P. H., Lacassin, R., Tapponnier, P., Schärer, U., Zhong, D., Liu, X., Zhang, L., Ji, S., & Trinh, P. T. (1995). The Ailao Shan-Red River shear zone (Yunnan, China), Tertiary transform boundary of Indochina. *Tectonophysics*, *251*(1–4), 3–84. https://doi.org/10.1016/0040-1951(95)00070-4

Lin, S., Jiang, D., & Williams, P. F. (1998). Transpression (or transtension) zones of triclinic symmetry: Natural example and theoretical modelling. *Geological Society, London, Special Publications*, *135*(1), 41–57. https://doi.org/10.1144/GSL.SP.1998.135.01.04

Lister, G. S., & Hobbs, B. E. (1980). The simulation of fabric development during plastic deformation and its application to quartzite: The influence of deformation history. *Journal of Structural Geology*, *2*(3), 355–370. https://doi.org/10.1016/0191-8141(80)90023-1

London, D. (1988). Characteristics and regional significance of the Cremation Hill ductile fault zone at the Bronson Hill-Merrimack boundary, south-central Connecticut. *American Journal of Science*, *288*(4), 353–375. https://doi.org/10.2475/ajs.288.4.353

Ludman, A., & Gibbons, S. (1999). Multistage shearing of the Deblois granite in the Kellyland fault zone, eastern Maine. In A. Ludman & D. P. West, *Norumbega Fault System of the Northern Appalachians*. Geological Society of America. https://doi.org/10.1130/0-8137-2331-0.41

Lundgren, L. (1979). *The bedrock geology of the Haddam quadrangle with map* [Map]. Connecticut Geological and Natural History Survey.

Lundgren, L., & Ashmead, L. P. (1966). *The bedrock geology of the Hamburg quadrangle with map* [Map]. Connecticut Geological and Natural History Survey.

Lundgren, L., Ashmead, L. P., & Snyder, G. L. (1971). *The bedrock geology of the Moodus and Colchester quadrangles with maps* [Map]. Connecticut Geological and Natural History Survey.

Luo, Y., Long, M. D., Rondenay, S., Karabinos, P., & Kuiper, Y. D. (2022). Wavefield Migration Imaging of Moho Geometry and Upper Mantle Structure Beneath Southern New England. *Geophysical Research Letters*, *49*(13), e2022GL099013. https://doi.org/10.1029/2022GL099013

Ma, C., Hames, W. E., Foster, D. A., Xiao, W., Mueller, P. A., & Steltenpohl, M. G. (2023). Transformation of eastern North America from compression to extension in the Permian–Triassic. In S. J. Whitmeyer, M. L. Williams, D. A. Kellett, & B. Tikoff, *Laurentia: Turning Points in the Evolution of a Continent* (pp. 577–592). Geological Society of America. https://doi.org/10.1130/2022.1220(28)

Macdonald, F. A., Ryan-Davis, J., Coish, R. A., Crowley, J. L., & Karabinos, P. (2014). A newly identified Gondwanan terrane in the northern Appalachian Mountains: Implications for the Taconic orogeny and closure of the Iapetus Ocean. *Geology*, *42*(6), 539–542. https://doi.org/10.1130/G35659.1

Mainprice, D., Bachmann, F., Hielscher, R., & Schaeben, H. (2015). Descriptive tools for the analysis of texture projects with large datasets using MTEX: Strength, symmetry and components. *Geological Society, London, Special Publications*, *409*(1), 251–271. https://doi.org/10.1144/SP409.8

Massey, M. A., Moecher, D. P., Walker, T. B., O'Brien, T. M., & Rohrer, L. P. (2017). The role and extent of dextral transpression and lateral escape on the post-Acadian tectonic evolution of south-central New England. *American Journal of Science*, *317*(1), 34–94. https://doi.org/10.2475/01.2017.02

McWilliams, C. K., Kunk, M. J., Wintsch, R. P., & Bish, D. L. (2013). Determining ages of multiple muscovite-bearing foliations in phyllonites using the 40Ar/39Ar step heating method:

Applications to the Alleghanian orogeny in central New England. *American Journal of Science*, *313*(10), 996–1016. https://doi.org/10.2475/10.2013.02

Merschat, A. J., Hatcher, R. D., & Davis, T. L. (2005). The northern Inner Piedmont, southern Appalachians, USA: Kinematics of transpression and SW-directed mid-crustal flow. *Journal of Structural Geology*, *27*(7), 1252–1281. https://doi.org/10.1016/j.jsg.2004.08.005

Michels, Z. D., Kruckenberg, S. C., Davis, J. R., & Tikoff, B. (2015). Determining vorticity axes from grain-scale dispersion of crystallographic orientations. *Geology*, *43*(9), 803–806. https://doi.org/10.1130/G36868.1

Moecher, D. P. (1999). The Distribution, Style, and Intensity of Alleghanian Metamorphism in South-Central New England: Petrologic Evidence from the Pelham and Willimantic Domes. *The Journal of Geology*, *107*(4), 449–471. https://doi.org/10.1086/314359

Moecher, D. P., McCulla, J. K., & Massey, M. A. (2021). Zircon and monazite geochronology in the Palmer zone of transpression, south-central New England, USA: Constraints on timing of deformation, high-grade metamorphism, and lithospheric foundering during late Paleozoic oblique collision in the Northern Appalachian orogen. *GSA Bulletin*, *133*(5–6), 1021–1038. https://doi.org/10.1130/B35744.1

Montgomery, D. R., Som, S. M., Jackson, M. P. A., Schreiber, B. C., Gillespie, A. R., & Adams, J. (2006). Continental-scale salt tectonics on Mars and the origin of Valles Marineris and associated outflow channels. *Geological Society of America Bulletin*, *preprint*(2008), 1. https://doi.org/10.1130/B26307.1

Moore, G. (1983). *Bedrock geologic map of the East Killingly quadrangle, Connecticut and Rhode Island* [Map]. U.S. Geological Survey. https://doi.org/10.3133/gq1571

Morley, C. K. (2001). Combined escape tectonics and subduction rollback–back arc extension: A model for the evolution of Tertiary rift basins in Thailand, Malaysia and Laos. *Journal of the Geological Society*, *158*(3), 461–474. https://doi.org/10.1144/jgs.158.3.461

Moser, A. C., Hacker, B. R., Gehrels, G. E., Seward, G. G. E., Kylander-Clark, A. R. C., & Garber, J. M. (2022). Linking titanite U–Pb dates to coupled deformation and dissolution–reprecipitation. *Contributions to Mineralogy and Petrology*, *177*(3), 42. https://doi.org/10.1007/s00410-022-01906-9

Murray, D. P., Skehan, J. W., & Raben, J. (2004). Tectonostratigraphic relationships and coalification trends in the Narragansett and Norfolk Basins, New England. *Journal of Geodynamics*, *37*(3–5), 583–611. https://doi.org/10.1016/j.jog.2004.02.006

Northrup, C. J., & Burchfiel, B. C. (1996). Orogen-parallel transport and vertical partitioning of strain during oblique collision, Efjorden, north Norway. *Journal of Structural Geology*, *18*(10), 1231–1244. https://doi.org/10.1016/S0191-8141(96)00040-5

Palin, R. M., Searle, M. P., Waters, D. J., Parrish, R. R., Roberts, N. M. W., Horstwood, M. S. A., Yeh, M. -W., Chung, S. -L., & Anh, T. T. (2013). A geochronological and petrological study of anatectic paragneiss and associated granite dykes from the D ay N ui C on V oi metamorphic core complex, N orth V ietnam: Constraints on the timing of metamorphism within the R ed R iver shear zone. *Journal of Metamorphic Geology*, *31*(4), 359–387. https://doi.org/10.1111/jmg.12025

Parrish, R. R. (1990). U–Pb dating of monazite and its application to geological problems. *Canadian Journal of Earth Sciences*, *27*(11), 1431–1450. https://doi.org/10.1139/e90-152

Paton, C., Hellstrom, J., Paul, B., Woodhead, J., & Hergt, J. (2011). Iolite: Freeware for the visualisation and processing of mass spectrometric data. *Journal of Analytical Atomic Spectrometry*, *26*(12), 2508. https://doi.org/10.1039/c1ja10172b

Pease, M. H. (1988). *Bedrock geologic map of the Spring Hill quadrangle, Connecticut* (Geologic Quadrangle Map) [GQ-1650]. U.S. Geological Survey. https://doi.org/10.3133/gq1650

Peper, P. D., & Pease, M. H. (1975). *Geologic map of the Westford quadrangle, Connecticut* [Map]. U.S. Geological Survey. https://doi.org/10.3133/gq1214

Peterson, V. L., & Robinson, P. (1993). Progressive evolution from uplift to orogen-parallel transport in a late-acadian, upper amphibolite- to granulite-facies shear zone, south-central Massachusetts. *Tectonics*, *12*(2), 550–567. https://doi.org/10.1029/92TC00822

Price, N. A., Song, W. J., Johnson, S. E., Gerbi, C. C., Beane, R. J., & West, D. P. (2016). Recrystallization fabrics of sheared quartz veins with a strong pre-existing crystallographic preferred orientation from a seismogenic shear zone. *Tectonophysics*, *682*, 214–236. https://doi.org/10.1016/j.tecto.2016.05.030

Rahl, J. M., McGrew, A. J., Fox, J. A., Latham, J. R., & Gabrielson, T. (2018). Rhomb-dominated crystallographic preferred orientations in incipiently deformed quartz sandstones: A potential paleostress indicator for quartz-rich rocks. *Geology*, *46*(3), 195–198. https://doi.org/10.1130/G39588.1

Ramsay, J. G. (1967). *Folding and fracturing of rocks* ([7th print.]). McGraw-Hill.

Ratcliffe, N., Stanley, R., Gale, M. H., Thompson, P. J., & Walsh, G. J. (n.d.). *Bedrock Geologic Map of Vermont* [Map]. U.S. Geological Survey.

Ratschbacher, L., Frisch, W., Linzer, H., & Merle, O. (1991). Lateral extrusion in the eastern Alps, PArt 2: Structural analysis. *Tectonics*, *10*(2), 257–271. https://doi.org/10.1029/90TC02623

Reddy, S. M., Clark, C., Timms, N. E., & Eglington, B. M. (2010). Electron backscatter diffraction analysis and orientation mapping of monazite. *Mineralogical Magazine*, *74*(3), 493–506. https://doi.org/10.1180/minmag.2010.074.3.493

Robinson, P., Tucker, R. D., Bradley, D., Berry, H. N., & Osberg, P. H. (1998). Paleozoic orogens in New England, USA. *GFF*, *120*(2), 119–148. https://doi.org/10.1080/11035899801202119

Rodgers, J. (1971). The Taconic Orogeny. *Geological Society of America Bulletin*, *82*(5), 1141. https://doi.org/10.1130/0016-7606(1971)82[1141:TTO]2.0.CO;2

Rodgers, J. (1985). *Bedrock geological map of Connecticut* [Map]. Connecticut Geological and Natural History Survey.

Schlische, R. W. (1993). Anatomy and evolution of the Triassic-Jurassic Continental Rift System, eastern North America. *Tectonics*, *12*(4), 1026–1042. https://doi.org/10.1029/93TC01062

Schmid, S. M., & Casey, M. (1986). Complete fabric analysis of some commonly observed quartz C-axis patterns. In B. E. Hobbs & H. C. Heard (Eds.), *Geophysical Monograph Series* (Vol. 36, pp. 263–286). American Geophysical Union. https://doi.org/10.1029/GM036p0263

Schoene, B., & Bowring, S. A. (2006). U–Pb systematics of the McClure Mountain syenite: Thermochronological constraints on the age of the 40Ar/39Ar standard MMhb. *Contributions to Mineralogy and Petrology*, *151*(5), 615–630. https://doi.org/10.1007/s00410-006-0077-4

Şengör, A. M. C., & Kidd, W. S. F. (1979). Post-collisional tectonics of the Turkish-Iranian plateau and a comparison with Tibet. *Tectonophysics*, *55*(3–4), 361–376. https://doi.org/10.1016/0040-1951(79)90184-7

Seton, M., Müller, R. D., Zahirovic, S., Gaina, C., Torsvik, T., Shephard, G., Talsma, A., Gurnis, M., Turner, M., Maus, S., & Chandler, M. (2012). Global continental and ocean basin reconstructions since 200Ma. *Earth-Science Reviews*, *113*(3–4), 212–270. https://doi.org/10.1016/j.earscirev.2012.03.002

Severson, A. R. (2020). *Across- and along-strike structural and geochronological variations of the Nashoba-Putnam and Avalon terranes, eastern Massachusetts, Connecticut, and Rhode Island, southeastern New England Appalachians*. Colorado School of Mines. Arthur Lakes Library. https://hdl.handle.net/11124/174210

Sibson, R. H. (1990). Rupture nucleation on unfavorably oriented faults. *Bulletin of the Seismological Society of America*, *80*(6A), 1580–1604. https://doi.org/10.1785/BSSA08006A1580

Skemer, P., Katayama, I., Jiang, Z., & Karato, S. (2005). The misorientation index: Development of a new method for calculating the strength of lattice-preferred orientation. *Tectonophysics*, *411*(1–4), 157–167. https://doi.org/10.1016/j.tecto.2005.08.023

Snyder, G. L. (1961). *Bedrock geology of the Norwich quadrangle, Connecticut* [Map]. U.S. Geological Survey. https://doi.org/10.3133/gq144

Snyder, G. L. (1964a). *Bedrock geology of the Willimantic quadrangle, Connecticut* [Map]. U.S. Geological Survey. https://doi.org/10.3133/gq335

Snyder, G. L. (1964b). *Petrochemistry and bedrock geology of the Fitchville quadrangle, Connecticut* [Map]. U.S. Geological Survey. https://doi.org/10.3133/b1161I

Snyder, G. L. (1967). *Bedrock geologic map of the Columbia quadrangle, east-central Connecticut* [Map]. U.S. Geological Survey. https://doi.org/10.3133/gq592

Snyder, G. L. (1970). *Bedrock geologic and magnetic maps of the Marlborough quadrangle, east-central Connecticut* [Map]. U.S. Geological Survey. https://doi.org/10.3133/gq791

Solar, G. S., & Brown, M. (2001). Deformation partitioning during transpression in response to Early Devonian oblique convergence, northern Appalachian orogen, USA. *Journal of Structural Geology*, *23*(6–7), 1043–1065. https://doi.org/10.1016/S0191-8141(00)00175-9

Spandler, C., Hammerli, J., Sha, P., Hilbert-Wolf, H., Hu, Y., Roberts, E., & Schmitz, M. (2016). MKED1: A new titanite standard for in situ analysis of Sm–Nd isotopes and U–Pb geochronology. *Chemical Geology*, *425*, 110–126. https://doi.org/10.1016/j.chemgeo.2016.01.002

SPEAR, F. S., HICKMOTT, D. D., & SELVERSTONE, J. (1990). Metamorphic consequences of thrust emplacement, Fall Mountain, New Hampshire. *GSA Bulletin*, *102*(10), 1344–1360. https://doi.org/10.1130/0016-7606(1990)102<1344:MCOTEF>2.3.CO;2

Stacey, J. S., & Kramers, J. D. (1975). Approximation of terrestrial lead isotope evolution by a two-stage model. *Earth and Planetary Science Letters*, *26*(2), 207–221. https://doi.org/10.1016/0012-821X(75)90088-6

Stewart, D. B., Wright, B. E., Unger, J. D., Phillips, J. D., & Hutchinson, D. R. (1991). *Global Geoscience Transect 8, Quebec-Maine-Gulf of Maine transect, southeastern Canada, northeastern United States of America* (Open-File Report 91–353). U.S. Geological Survey.

Stipp, M., Stünitz, H., Heilbronner, R., & Schmid, S. M. (2002). Dynamic recrystallization of quartz: Correlation between natural and experimental conditions. *Geological Society, London, Special Publications*, *200*(1), 171–190. https://doi.org/10.1144/GSL.SP.2001.200.01.11

Sun, S. -s., & McDonough, W. F. (1989). Chemical and isotopic systematics of oceanic basalts: Implications for mantle composition and processes. *Geological Society, London, Special Publications*, *42*(1), 313–345. https://doi.org/10.1144/GSL.SP.1989.042.01.19

Tapponnier, P., Mercier, J. L., Proust, F., Andrieux, J., Armijo, R., Bassoullet, J. P., Brunel, M., Burg, J. P., Colchen, M., Dupré, B., Girardeau, J., Marcoux, J., Mascle, G., Matte, P., Nicolas, A., Tingdong, L., Xuchang, X., Chenfa, C., Paoyu, L., … Hongrong, Q. (1981). The Tibetan side of the India–Eurasia collision. *Nature*, *294*(5840), 405–410. https://doi.org/10.1038/294405a0

Tapponnier, P., Peltzer, G., & Armijo, R. (1986). On the mechanics of the collision between India and Asia. *Geological Society, London, Special Publications*, *19*(1), 113–157. https://doi.org/10.1144/GSL.SP.1986.019.01.07

Tapponnier, P., Zhiqin, X., Roger, F., Meyer, B., Arnaud, N., Wittlinger, G., & Jingsui, Y. (2001). Oblique Stepwise Rise and Growth of the Tibet Plateau. *Science*, *294*(5547), 1671–1677. https://doi.org/10.1126/science.105978

Tassara, S., Ague, J. J., & Valencia, V. (2021). The deep magmatic cumulate roots of the Acadian orogen, eastern North America. *Geology*, *49*(2), 168–173. https://doi.org/10.1130/G47887.1

Tikoff, B., & Fossen, H. (1995). The limitations of three-dimensional kinematic vorticity analysis. *Journal of Structural Geology*, *17*(12), 1771–1784. https://doi.org/10.1016/0191-8141(95)00069-P

Tikoff, B., & Fossen, H. (1999). Three-dimensional reference deformations and strain facies. *Journal of Structural Geology*, *21*(11), 1497–1512. https://doi.org/10.1016/S0191-8141(99)00085-1

Toy, V. G., Prior, D. J., & Norris, R. J. (2008). Quartz fabrics in the Alpine Fault mylonites: Influence of pre-existing preferred orientations on fabric development during progressive uplift. *Journal of Structural Geology*, *30*(5), 602–621. https://doi.org/10.1016/j.jsg.2008.01.001

Tullis, J., & Yund, R. (1992). Chapter 4 The Brittle-Ductile Transition in Feldspar Aggregates: An Experimental Study. In *International Geophysics* (Vol. 51, pp. 89–117). Elsevier. https://doi.org/10.1016/S0074-6142(08)62816-8

Valentino, D. W., & Gates, A. E. (2001). Asynchronous extensional collapse of a transpressional orogen: The Alleghanian central Appalachian Piedmont, USA. *Journal of Geodynamics*, *31*(2), 145–167. https://doi.org/10.1016/S0264-3707(00)00028-4

Valley, P. M., Walsh, G. J., Merschat, A. J., & McAleer, R. J. (2020). Geochronology of the Oliverian Plutonic Suite and the Ammonoosuc Volcanics in the Bronson Hill arc: Western New Hampshire, USA. *Geosphere*, *16*(1), 229–257. https://doi.org/10.1130/GES02170.1

Van Buer, N. J., Jagoutz, O., Upadhyay, R., & Guillong, M. (2015). Mid-crustal detachment beneath western Tibet exhumed where conjugate Karakoram and Longmu–Gozha Co faults intersect. *Earth and Planetary Science Letters*, *413*, 144–157. https://doi.org/10.1016/j.epsl.2014.12.053

Van Staal, C. R., Whalen, J. B., Valverde-Vaquero, P., Zagorevski, A., & Rogers, N. (2009). Pre-Carboniferous, episodic accretion-related, orogenesis along the Laurentian margin of the northern Appalachians. *Geological Society, London, Special Publications*, *327*(1), 271–316. https://doi.org/10.1144/SP327.13

Vollmer, F. W. (1990). An application of eigenvalue methods to structural domain analysis. *GSA Bulletin*, *102*(6), 786–791. https://doi.org/10.1130/0016-7606(1990)102<0786:AAOEMT>2.3.CO;2

Vollmer, F. W. (1995). C program for automatic contouring of spherical orientation data using a modified Kamb method. *Computers & Geosciences*, *21*(1), 31–49. https://doi.org/10.1016/0098-3004(94)00058-3

Waldron, J. W. F., Barr, S. M., Park, A. F., White, C. E., & Hibbard, J. (2015). Late Paleozoic strike-slip faults in Maritime Canada and their role in the reconfiguration of the northern Appalachian orogen: STRIKE SLIP, NORTHERN APPALACHIANS. *Tectonics*, *34*(8), 1661–1684. https://doi.org/10.1002/2015TC003882

Wallis, S. (1995). Vorticity analysis and recognition of ductile extension in the Sanbagawa belt, SW Japan. *Journal of Structural Geology*, *17*(8), 1077–1093. https://doi.org/10.1016/0191-8141(95)00005-X

Wallis, S. R. (1992). Vorticity analysis in a metachert from the Sanbagawa Belt, SW Japan. *Journal of Structural Geology*, *14*(3), 271–280. https://doi.org/10.1016/0191-8141(92)90085-B

Walters, J. B., Cruz-Uribe, A. M., Song, W. J., Gerbi, C., & Biela, K. (2022). Strengths and limitations of in situ U–Pb titanite petrochronology in polymetamorphic rocks: An example from western Maine, USA. *Journal of Metamorphic Geology*, *40*(6), 1043–1066. https://doi.org/10.1111/jmg.12657

Wang, C., & Ludman, A. (2003). Evidence for post-Acadian through Alleghanian deformation in eastern Maine: Multiple brittle reactivation of the Norumbega Fault system. *Atlantic Geology*, *38*(1), 32–52. Érudit.

West, D. P., & Hubbard, M. S. (1997). Progressive localization of deformation during exhumation of a major strike-slip shear zone: Norumbega fault zone, south-central Maine, USA. *Tectonophysics*, *273*(3–4), 185–201. https://doi.org/10.1016/S0040-1951(96)00306-X

West, D. P., & Lux, D. R. (1993). Dating mylonitic deformation by the 40Ar-39Ar method: An example from the Norumbega Fault Zone, Maine. *Earth and Planetary Science Letters*, *120*(3–4), 221–237. https://doi.org/10.1016/0012-821X(93)90241-Z

White, C. E. (2010). Stratigraphy of the Lower Paleozoic Goldenville and Halifax groups in the western part of southern Nova Scotia. *Atlantic Geology*, *46*, 136–154. https://doi.org/10.4138/atlgeol.2010.008

Williams, M. L., Jercinovic, M. J., Harlov, D. E., Budzyń, B., & Hetherington, C. J. (2011). Resetting monazite ages during fluid-related alteration. *Chemical Geology*, *283*(3–4), 218–225. https://doi.org/10.1016/j.chemgeo.2011.01.019

Williams, M. L., Jercinovic, M. J., & Hetherington, C. J. (2007). Microprobe Monazite Geochronology: Understanding Geologic Processes by Integrating Composition and Chronology. *Annual Review of Earth and Planetary Sciences*, *35*(1), 137–175. https://doi.org/10.1146/annurev.earth.35.031306.140228

Wintsch, R. P. (2003). P-T-t paths and differential Alleghanian loading and uplift of the Bronson Hill terrane, South Central New England. *American Journal of Science*, *303*(5), 410–446. https://doi.org/10.2475/ajs.303.5.410

Wintsch, R. P., Aleinikoff, J. N., Walsh, G. J., Bothner, W. A., Hussey, A. M., & Fanning, C. M. (2007). Shrimp U-Pb evidence for a Late Silurian age of metasedimentary rocks in the Merrimack and Putnam-Nashoba terranes, eastern New England. *American Journal of Science*, *307*(1), 119–167. https://doi.org/10.2475/01.2007.05

Wintsch, R. P., Sutter, J. F., Kunk, M. J., Aleinikoff, J. N., & Dorais, M. J. (1992). Contrasting P-T-t paths: Thermochronologic evidence for a Late Paleozoic final assembly of the Avalon Composite Terrane in the New England Appalachians. *Tectonics*, *11*(3), 672–689. https://doi.org/10.1029/91TC02904

Wintsch, R. P., Yi, K., & Dorais, M. J. (2014). Crustal thickening by tectonic wedging of the Ganderian rocks, southern New England, USA: Evidence from cataclastic zircon microstructures and U–Pb ages. *Journal of Structural Geology*, *69*, 428–448. https://doi.org/10.1016/j.jsg.2014.07.019

Withjack, M., Malinconico, M., & Durcanin, M. (2020). The “Passive” Margin of Eastern North America: Rifting and the Influence of Prerift Orogenic Activity on Postrift Development. *Lithosphere*, *2020*(1), 8876280. https://doi.org/10.2113/2020/8876280

Woodcock, N. H. (1977). Specification of fabric shapes using an eigenvalue method. *GSA Bulletin*, *88*(9), 1231–1236. https://doi.org/10.1130/0016-7606(1977)88<1231:SOFSUA>2.0.CO;2

Yakymchuk, C., & Brown, M. (2014). Behaviour of zircon and monazite during crustal melting. *Journal of the Geological Society*, *171*(4), 465–479. https://doi.org/10.1144/jgs2013-115

Yin, A., & Taylor, M. H. (2011). Mechanics of V-shaped conjugate strike-slip faults and the corresponding continuum mode of continental deformation. *Geological Society of America Bulletin*, *123*(9–10), 1798–1821. https://doi.org/10.1130/B30159.1

Young, A., Flament, N., Maloney, K., Williams, S., Matthews, K., Zahirovic, S., & Müller, R. D. (2019). Global kinematics of tectonic plates and subduction zones since the late Paleozoic Era. *Geoscience Frontiers*, *10*(3), 989–1013. https://doi.org/10.1016/j.gsf.2018.05.011

Zartman, R. E. (1988). Three decades of geochronologic studies in the New England Appalachians. *GSA Bulletin*, *100*(8), 1168–1180. https://doi.org/10.1130/0016-7606(1988)100<1168:TDOGSI>2.3.CO;2

Zen, E., Goldsmith, R., Ratcliffe, N., Robinson, P., Stanley, R., Hatch, N., Shride, A., Weed, E., & Wones, D. (1983). *Bedrock Geologic Map of Massachusetts* [Map]. United States Geologic Survey.

Figures and Captions

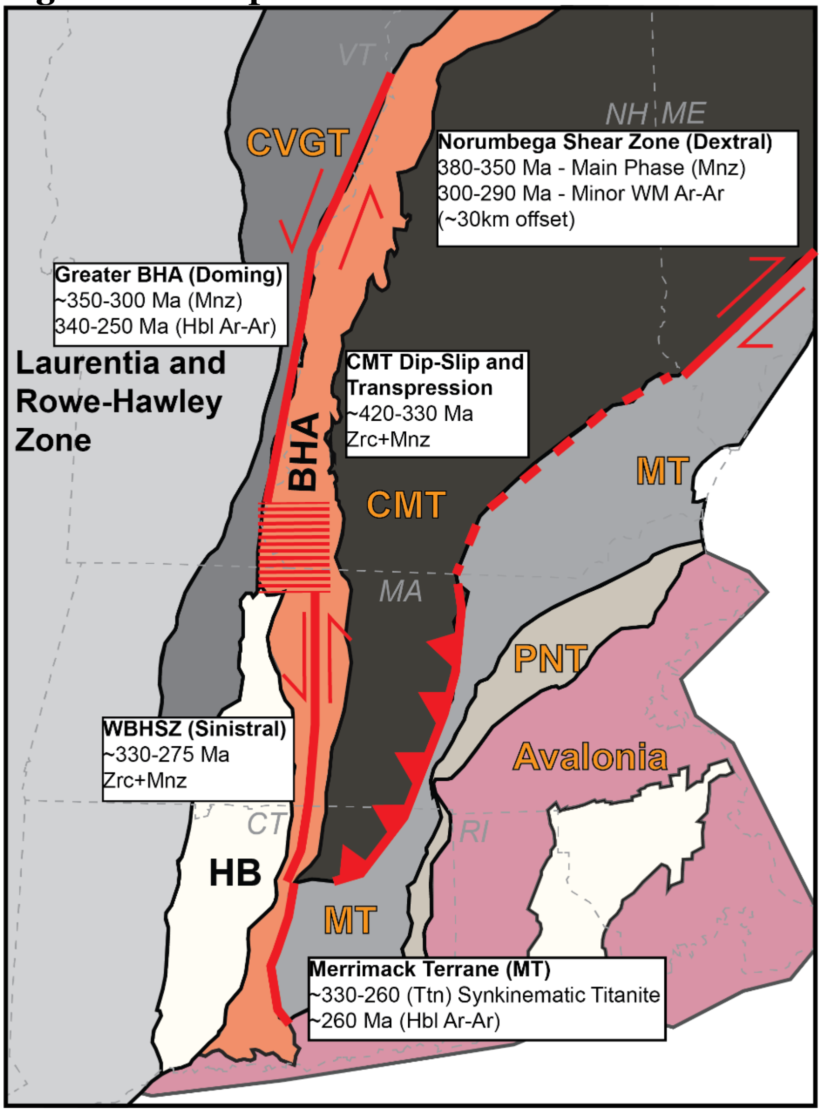

Figure 5.1: Regional map of New England and major terranes, modified from Aleinikoff et al. (2007). Published age constraints for major shear zones and internal deformation of the terranes are given in the associated white boxes. Age constraints for the Norumbega are from West and Lux (1993) and Gerbi and West (2007). Ages for the BHA from Spear et al. (2008) (Mnz) and Wintsch et al. (2003). Ages for the CMT from Moecher et al. (2021), and the WBHSZ from Massey et al. (2017). Acronyms are as follows: BHA-Bronson Hill Anticlinorium, CVGT-Connecticut Valley Gaspe Trough, CMT-Central Maine Terrane, HB-Hartford Basin, MT-Merrimack Terrane, PNT-Putnam Nashoba Terrane.

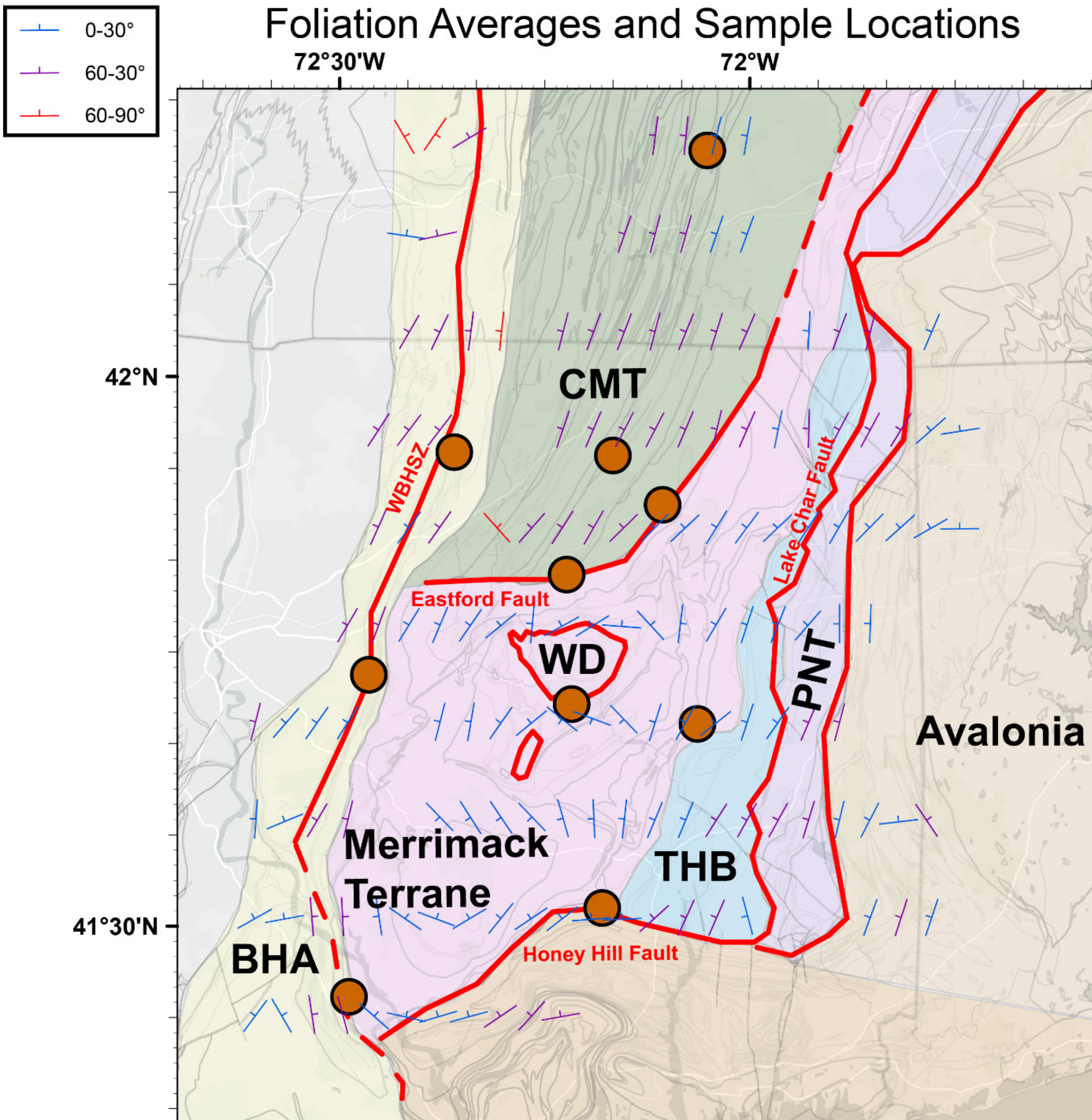

Figure 5.2: Compiled macroscopic foliation data from Connecticut and Massachusetts bedrock geologic maps. The compiled foliations are averaged into a grid for visualization. Acronyms are the same as Figure 1 except for WD-Willimantic Dome and THB-Tatnic Hill Belt. Bedrock data references are as follows: Collins (1954), Aiken (1955), Herz (1955), Snyder (1961), Snyder (1964a), Snyder (1964b), Dixon (1965), Dixon and Shaw (1965), Feininger (1965), Dixon and Pessl (1966), Lundgren and Ashmead (1966), Goldsmith (1967a), Goldsmith (1967b), Snyder (1967), Dixon (1968), Snyder (1970), Harwood and Goldsmith (1971), Lundgren et al. (1971), Eaton and Rosenfeld (1972), Dixon (1974), Peper and Pease (1975), Fahey and Pease (1977), Lundgren (1979), Dixon (1982), Moore (1983), Dixon and Felmlee (1986), Pease (1988), and Deasy and Wintsch (2019).

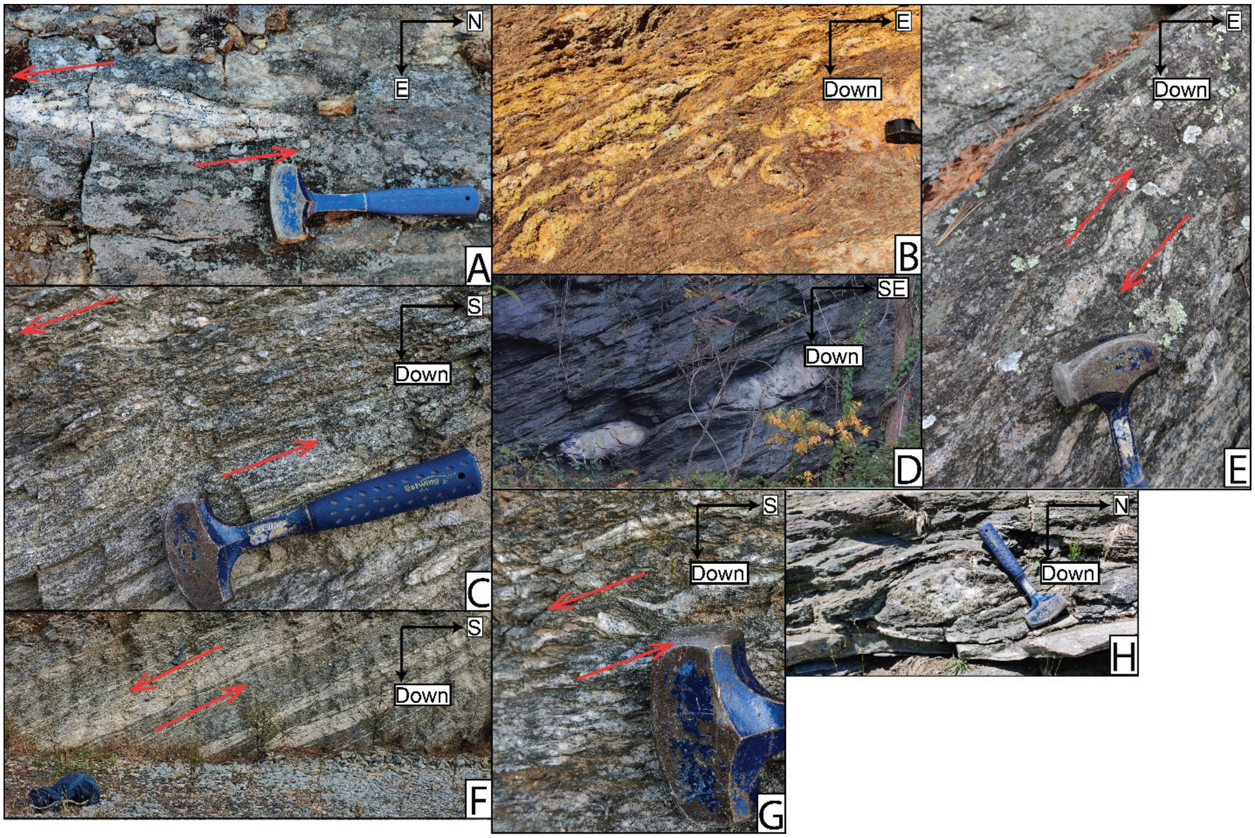

Figure 5.3: Outcrop photos of structures in southern New England. A) West side south, sinistral asymmetric boudin on a subhorizontal plane near Sturbridge, MA. B) Structures on the subvertical plane at the same outcrop as A), displaying west side up asymmetric folding and largely symmetric boudinage. C, F, and G) Top to the north shear sense indicators on an outcrop through the Honey Hill fault zone in southeastern CT. D) Symmetric boudinage in the core of the Bolton synform in Bolton Notch State Park, CT. E) Top to the SE asymmetric boudins near the Eastford fault in northeast Connecticut. H) Symmetric boudin of a coarse amphibole and plagioclase layer directly south of Willimantic, CT.

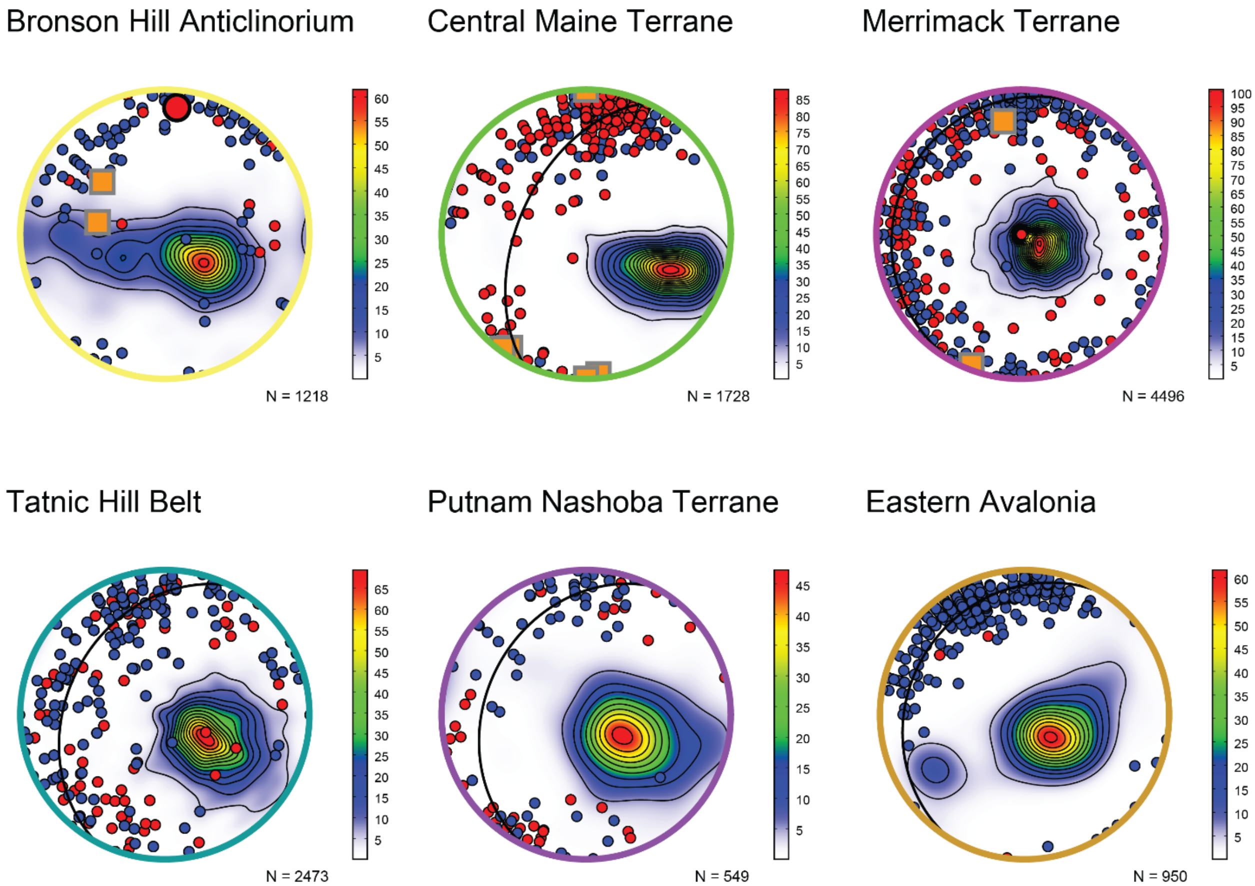

Figure 5.4: Stereonets of the compiled foliations (S_n, contoured by multiples of uniform density, m.u.d.), mineral lineations (L_m, blue poles), and fold axes (L_f, red poles) separated by the tectonic domains on Figure 2. The average foliation plane is shown as a black plane, except for the BHA. Due to the large-scale folding within the BHA, we plot the calculated fold axis as a large red circle. The vorticity vector from CVA analysis (Michels et al., 2015) is plotted as an orange square with a gray border.

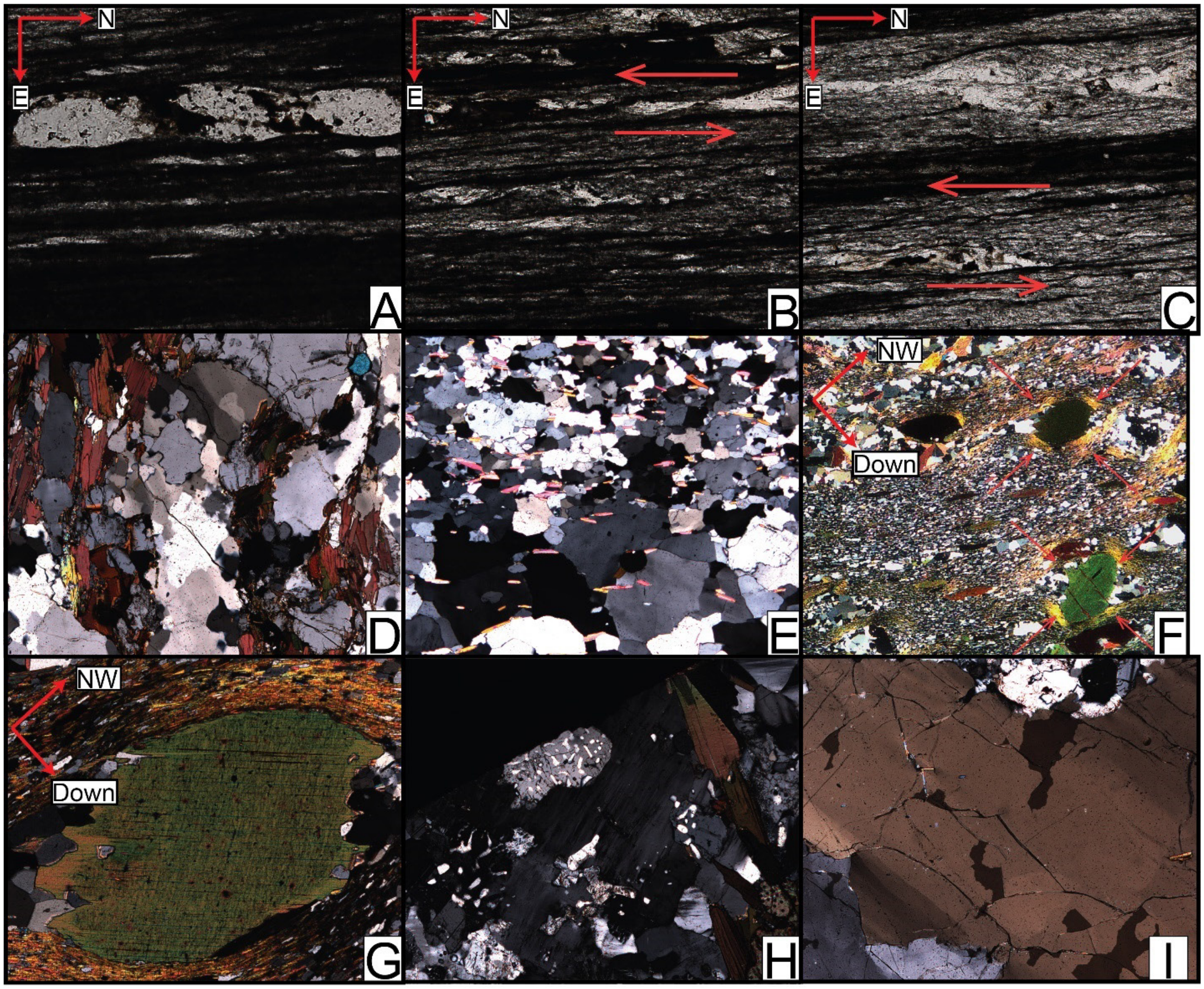

Figure 5.5: Thin section photographs of sample TH2107 (A, B, and C), MA2207 (D), CT2208 (E), CT2217 (F and G), and CT2229 (H and I). Orientations and shear sense are shown in red for samples with well-developed microscopic shear sense indicators discussed in the text.

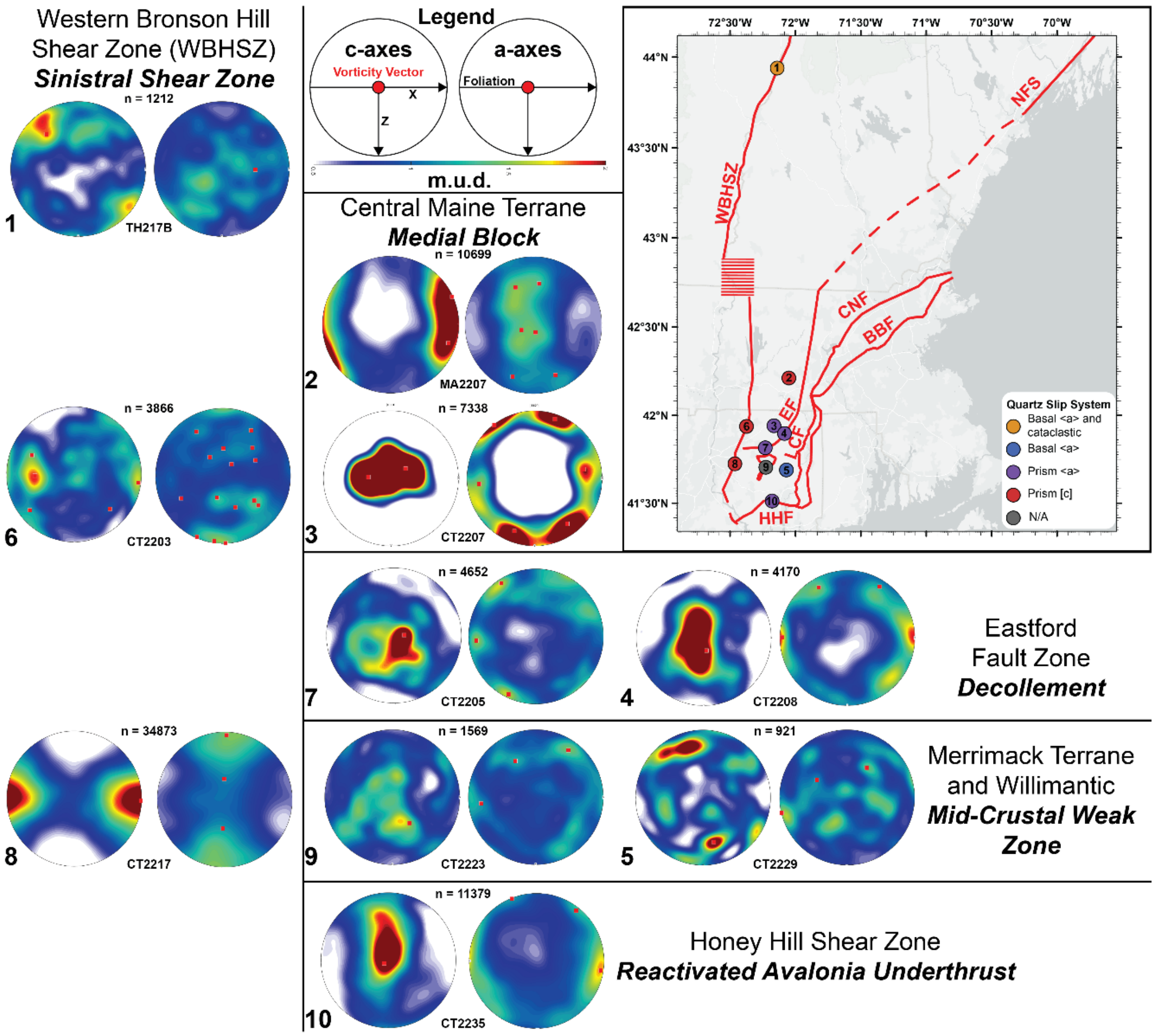

Figure 5.6: EBSD pole figures of the vorticity normal section (VNS) for the specified samples in this study. Pole figures are arranged according to their approximate relative positions in New England (visible on the map). Red squares are the results of component analysis of the orientation distribution function in MTEX (Bachmann et al., 2011). The included map displays the sample locations (numbered), as well as major shear zones/terrane boundaries in New England. Samples are colored according to the dominant quartz slip system on the VNS. Abbreviations are as follows: WBHSZ-Western Bronson Hill Shear Zone, NFS-Norumbega fault system, CNF-Clinton Newbury Fault, BBF-Bloody Bluff Fault, EF-Eastford fault, LCF-Lake Char fault, HHF-Honey Hill fault.

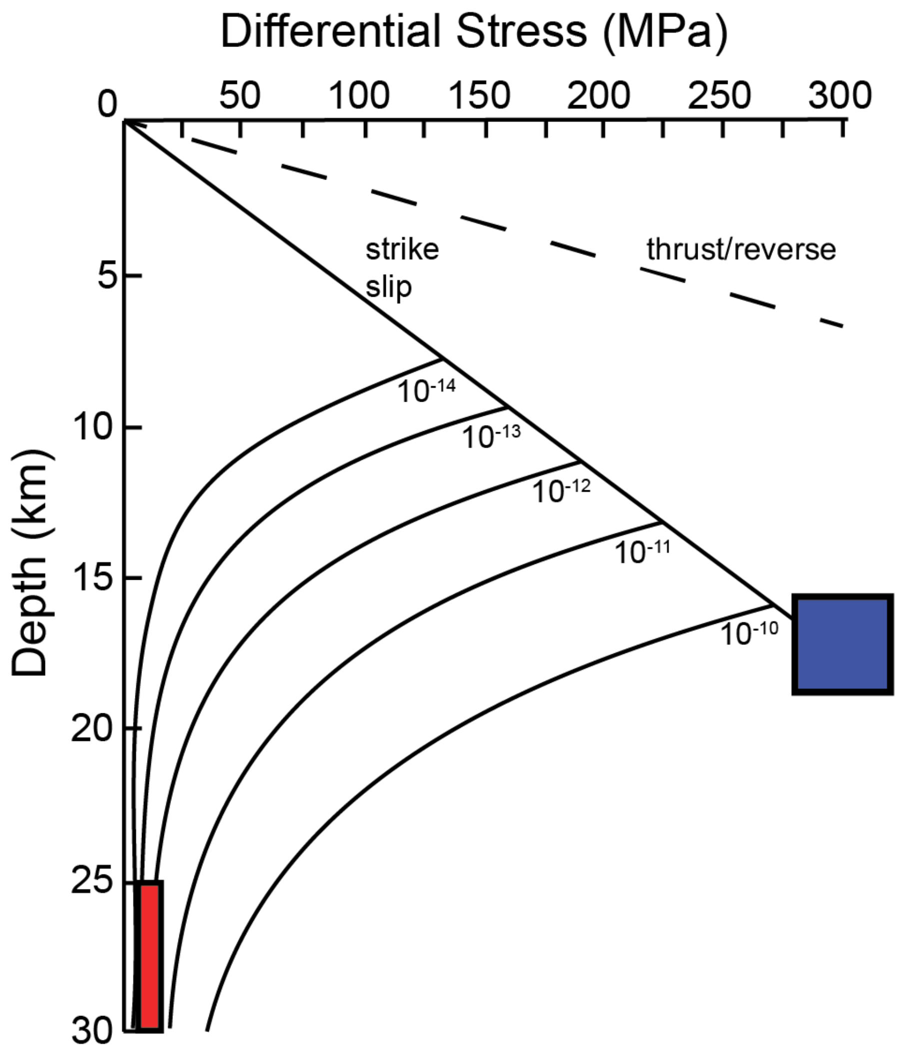

Figure 5.7: Depth vs differential stress modified from Behr and Platt (2011). Brittle failure curves for strike-slip (solid) and thrust regimes (dashed) are labelled. Ductile failure curves according to the labelled strain rate (s^{-1}). The blue box represents the stress estimate from the recrystallized grain size piezometer of Cross et al. (2017) for sample TH2107. The red box represents the range of approximate depth from (Moecher, 1997) and the stress from the subgrain size piezometer of Goddard et al. (2020) for samples CT2203, CT2205, CT2208, CT2217, and CT2229.

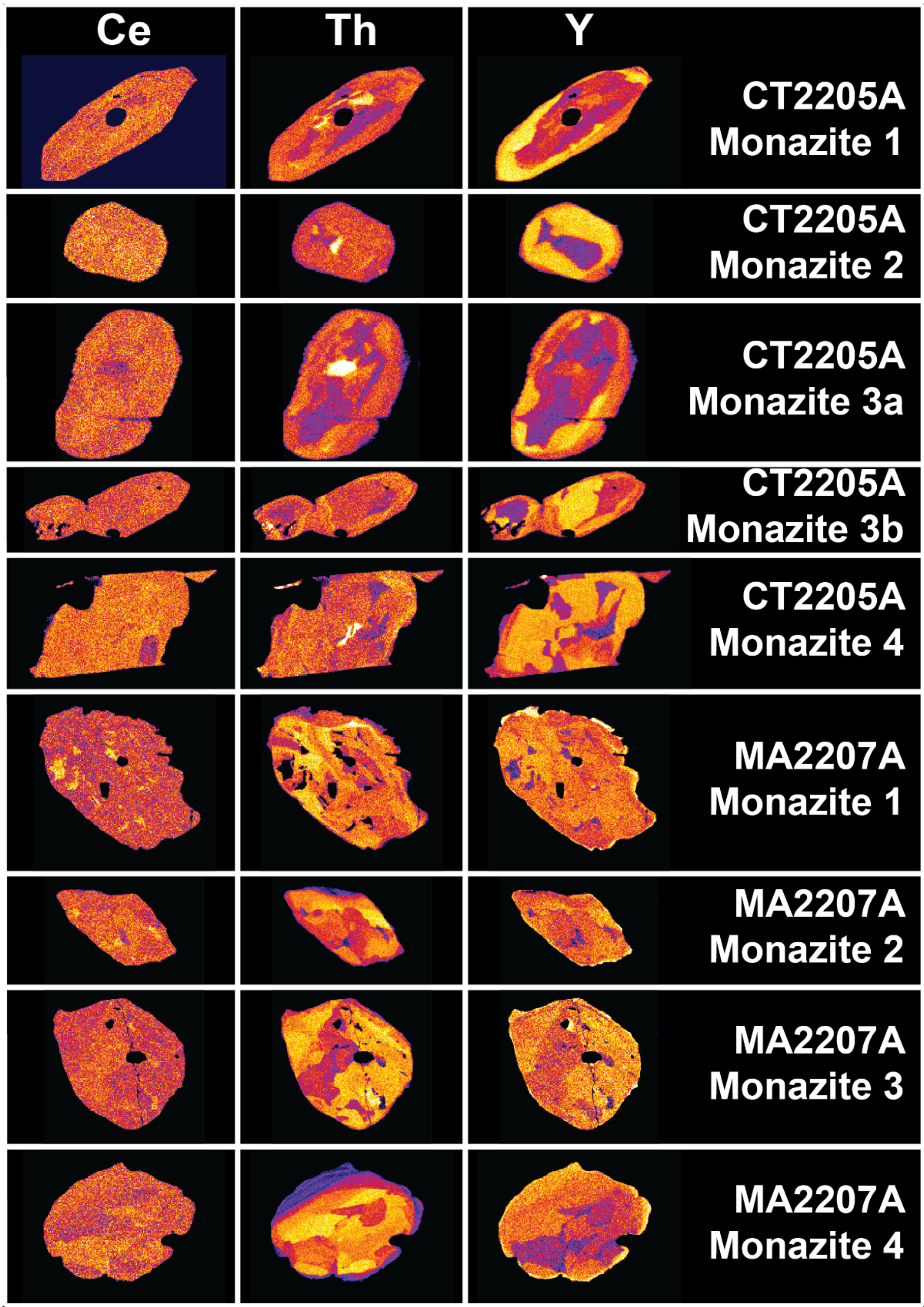

Figure 5.8: Elemental x-ray maps from wavelength dispersive spectrometry (WDS) for monazite grains.

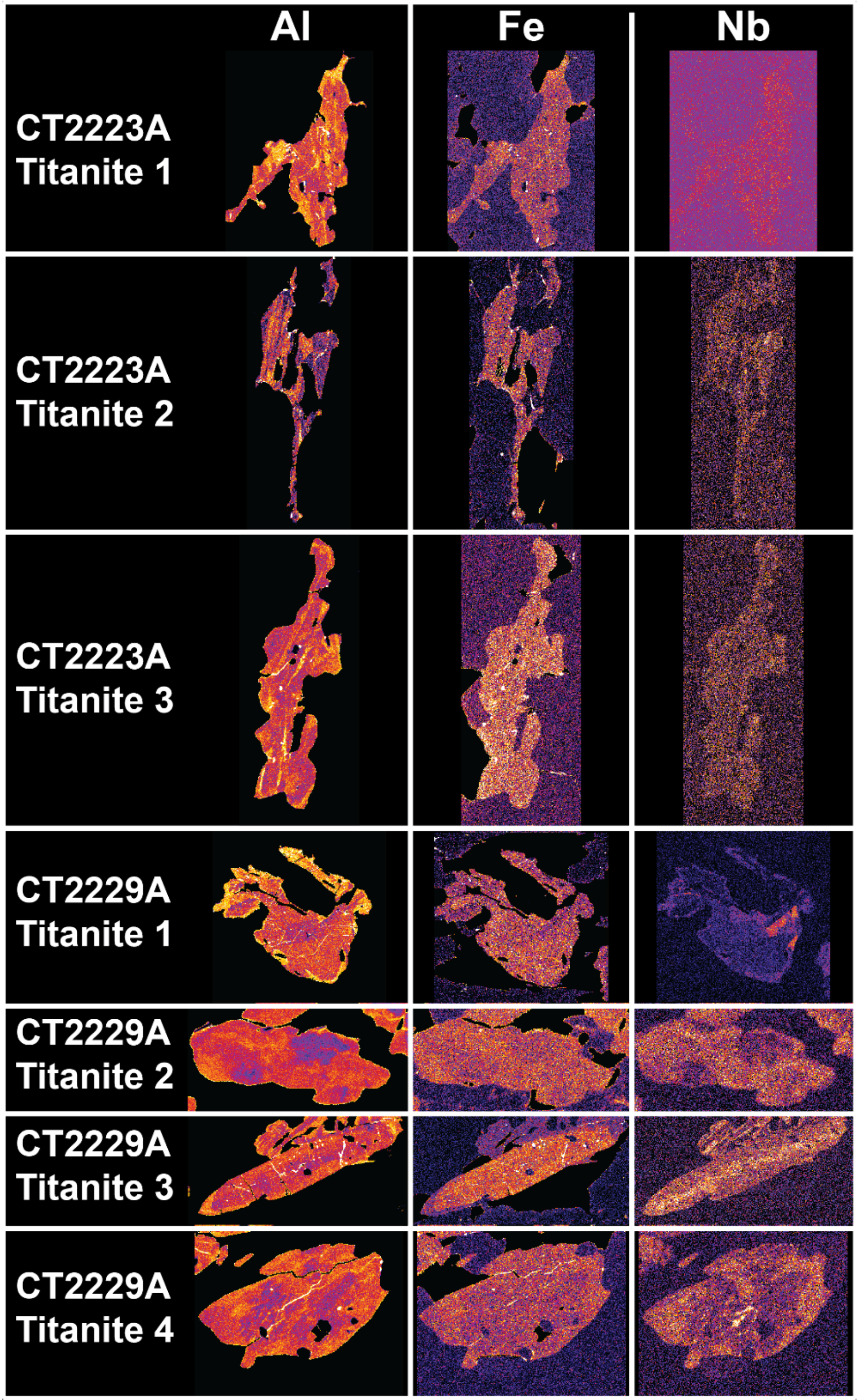

Figure 5.9: Elemental x-ray maps from wavelength dispersive spectrometry (WDS) for titanite grains.

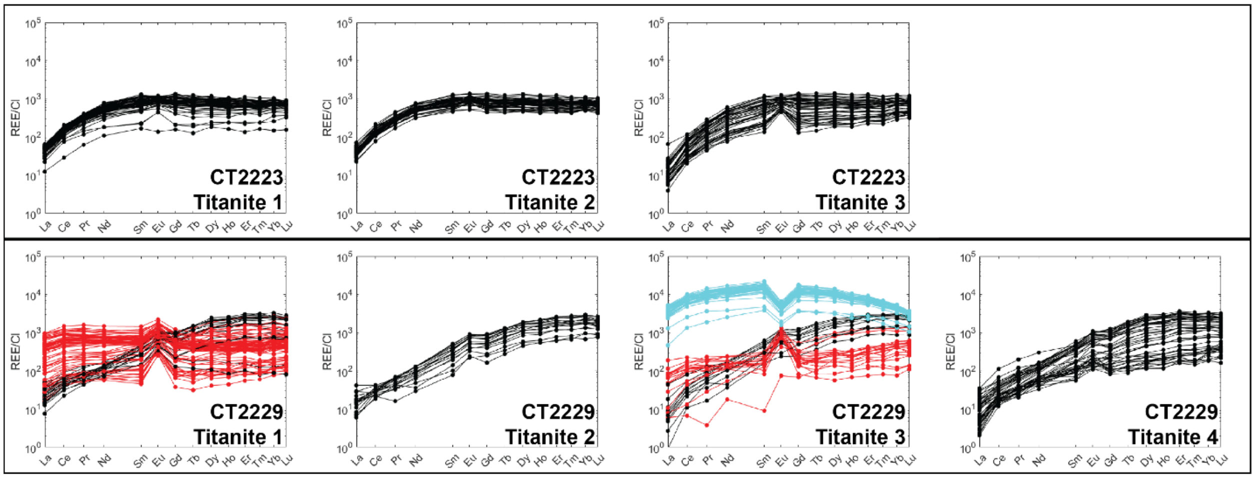

Figure 5.10: Chondrite normalized (Sun and McDonough, 1989) rare earth element (REE) diagrams for titanite grains in samples CT2223 and CT2229. Colors represent different compositional domains used for age calculation in Figure 5.11. Black represents the youngest compositional domain. Red represents the next oldest compositional domain. And blue represents the oldest compositional domain (only Titanite 3 in sample CT2229 has three distinct compositional domains).

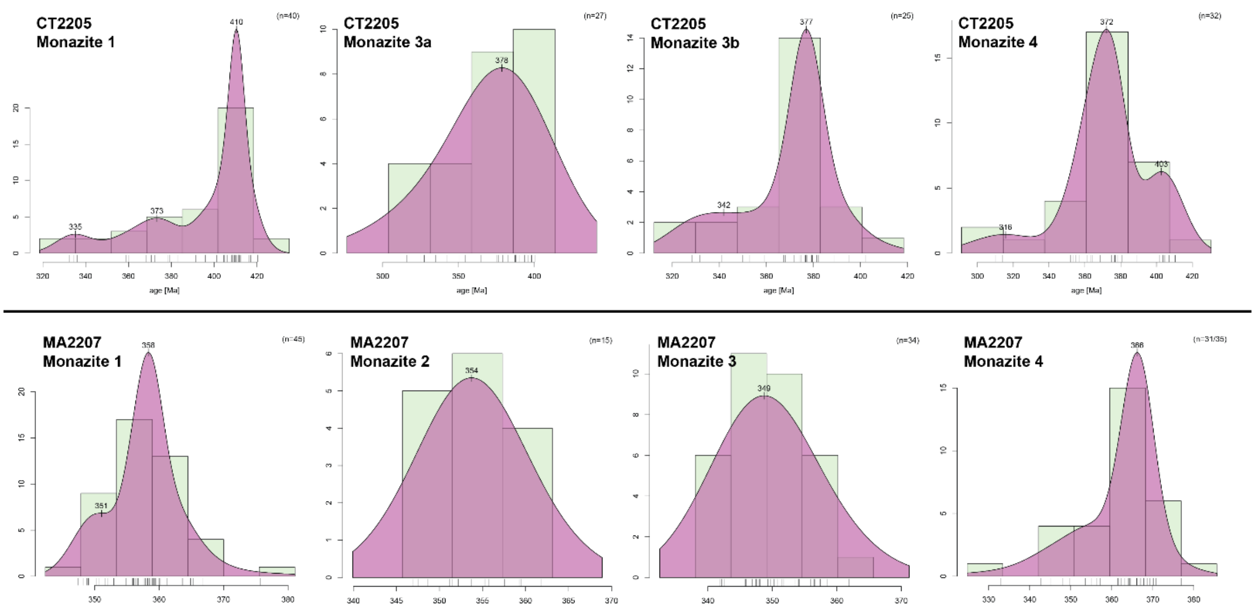

Figure 5.11: Histograms and kernel density estimates (KDE) of monazite spot ages for individual grains plotted with IsoplotR (Vermeesch, 2018). Local maxima in the KDE are labelled.

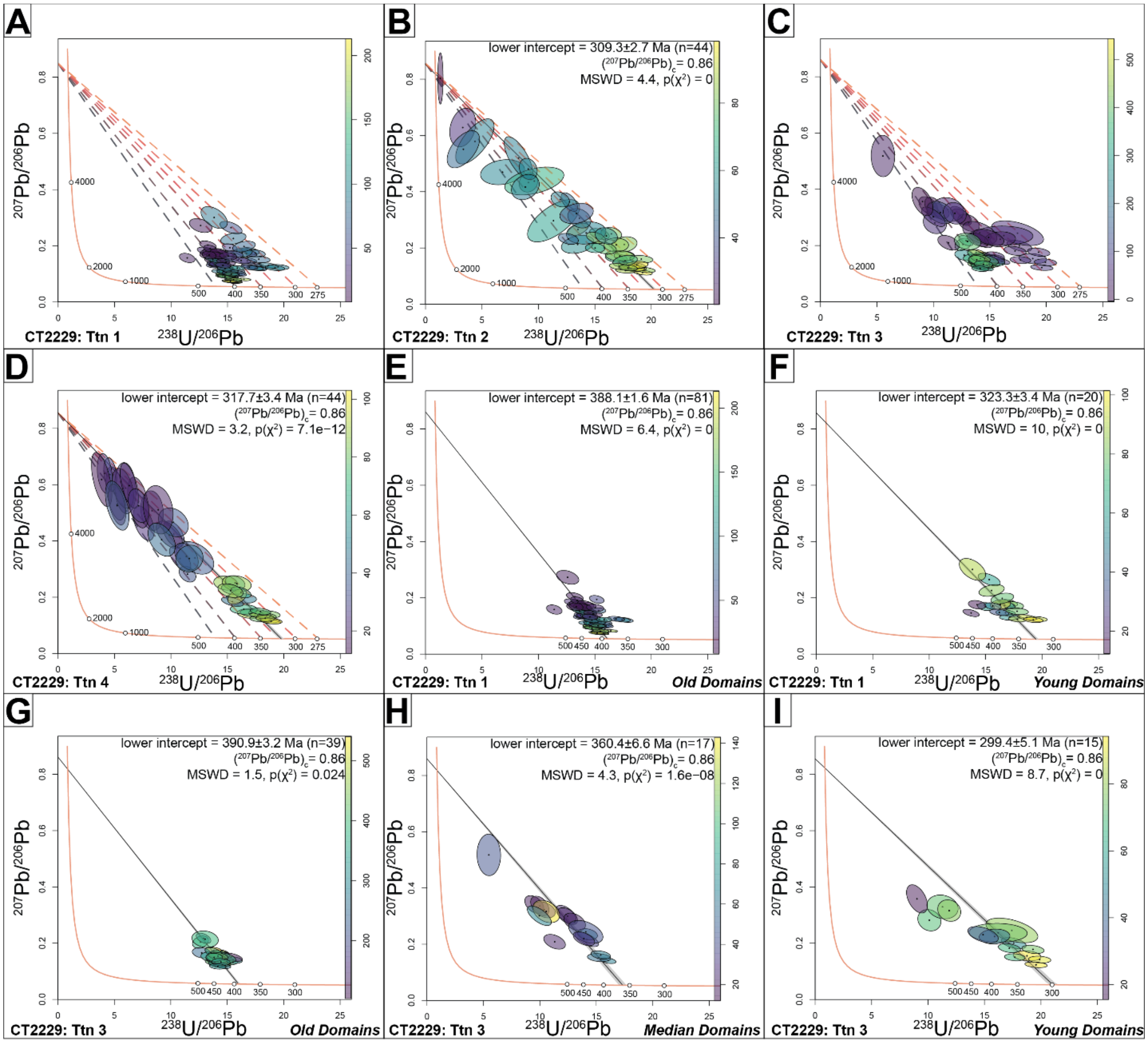

Figure 5.12: Tera-Waserberg *diagrams for U-Pb isotope compositions in four titanite grains from sample CT2229 plotted in IsoplotR (Vermeesch, 2018). A, B, C, and D) plot the results of all spots for the four grains with the 450, 400, 350, 300, and 275 Ma discordant isochrons anchored at Stacey-Kramers common lead composition between 250-500 Ma (~0.86, Stacey and Kramers, 1975). E, F, G, H, and I) display the domain segregated isochron fits, anchored at Stacey-Kramers common lead for grains 1 and 3. For grains 2 and 4, and the individual domain data, the discordant age model is plotted as a black line with a gray error region.*

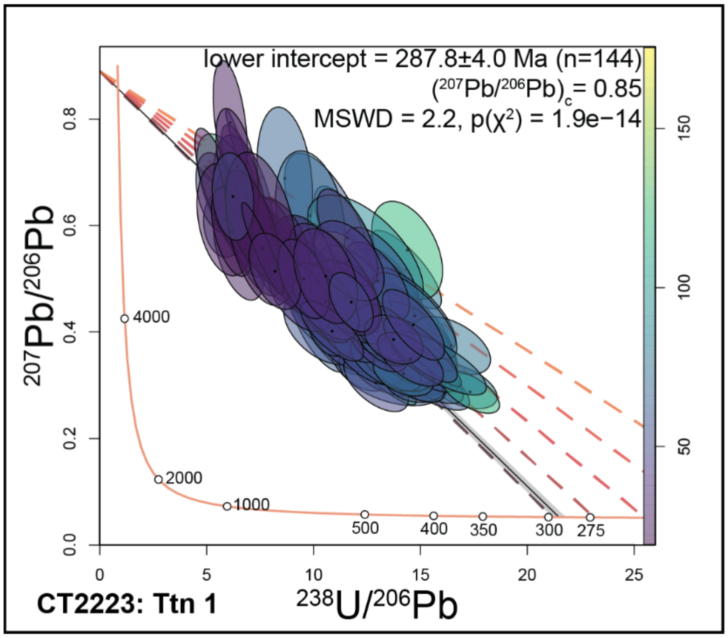

Figure 5.13: Tera-Waserberg *diagram for U-Pb isotope compositions in three titanite grains from sample CT2223 plotted in IsoplotR (Vermeesch, 2018). Discordant isochron models at 300, 275, 250, 225, and 200 Ma, anchored at Stacey-Kramers common lead (Stacey and Kramers, 1975), are shown as dashed lines. The discordant isochron fits through the data of the three grains is plotted as a black line with associated error in gray.*

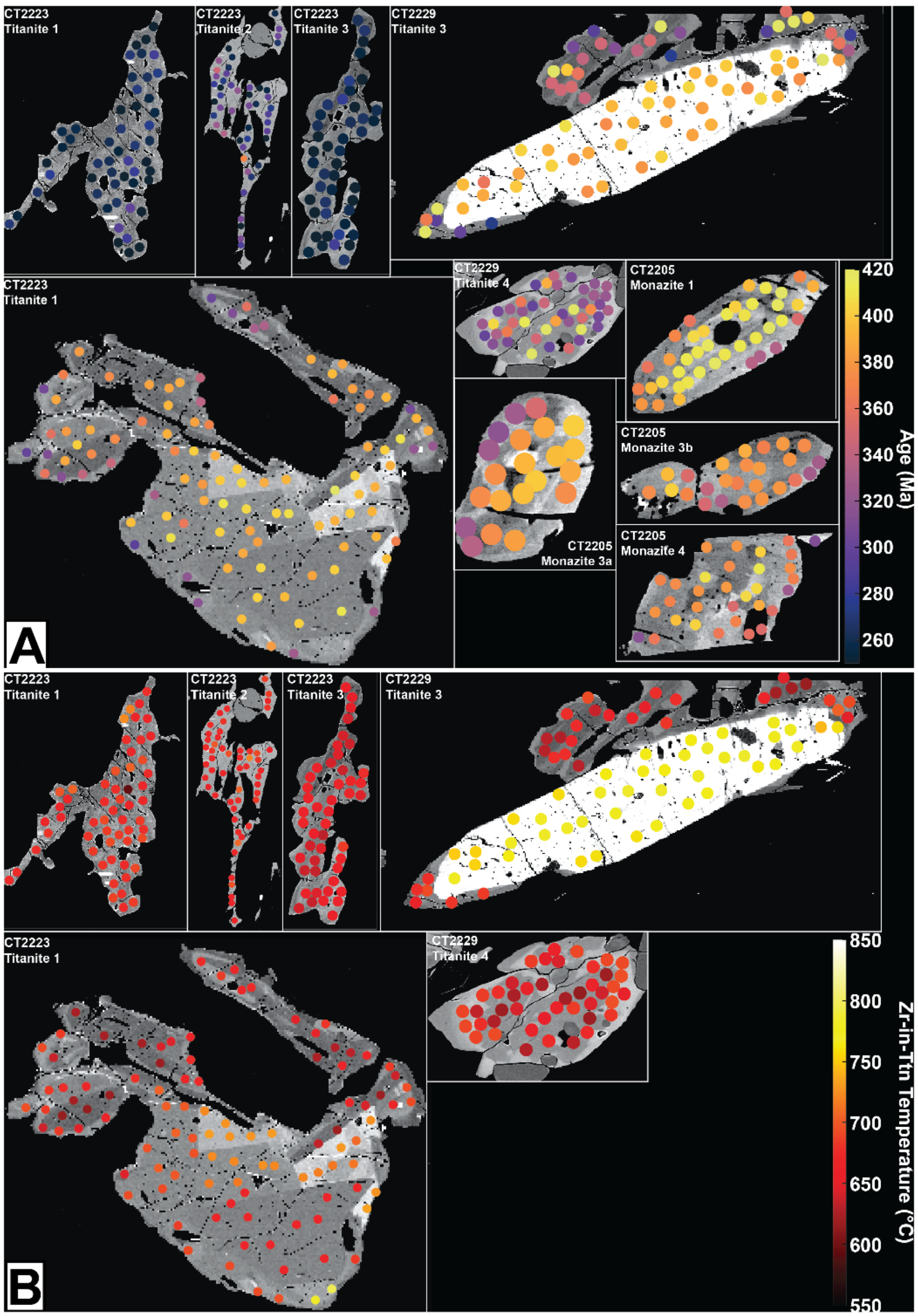

Figure 5.14: BSE maps of select titanite and monazite grains from samples CT2223 and CT2229 with spot locations overlayed. A) Displays the concordant age fit of each point (assuming a $^{207}Pb/^{206}Pb$ intercept of ~0.86 for titanite or concordia age for monazite) calculated in IsoplotR (Vermeesch, 2018). B) Displays the Zr-in-ttn temperature (Hayden et al., 2008) assuming a pressure of titanite growth of ~7kb (Moecher, 1997), only for titanite grains.

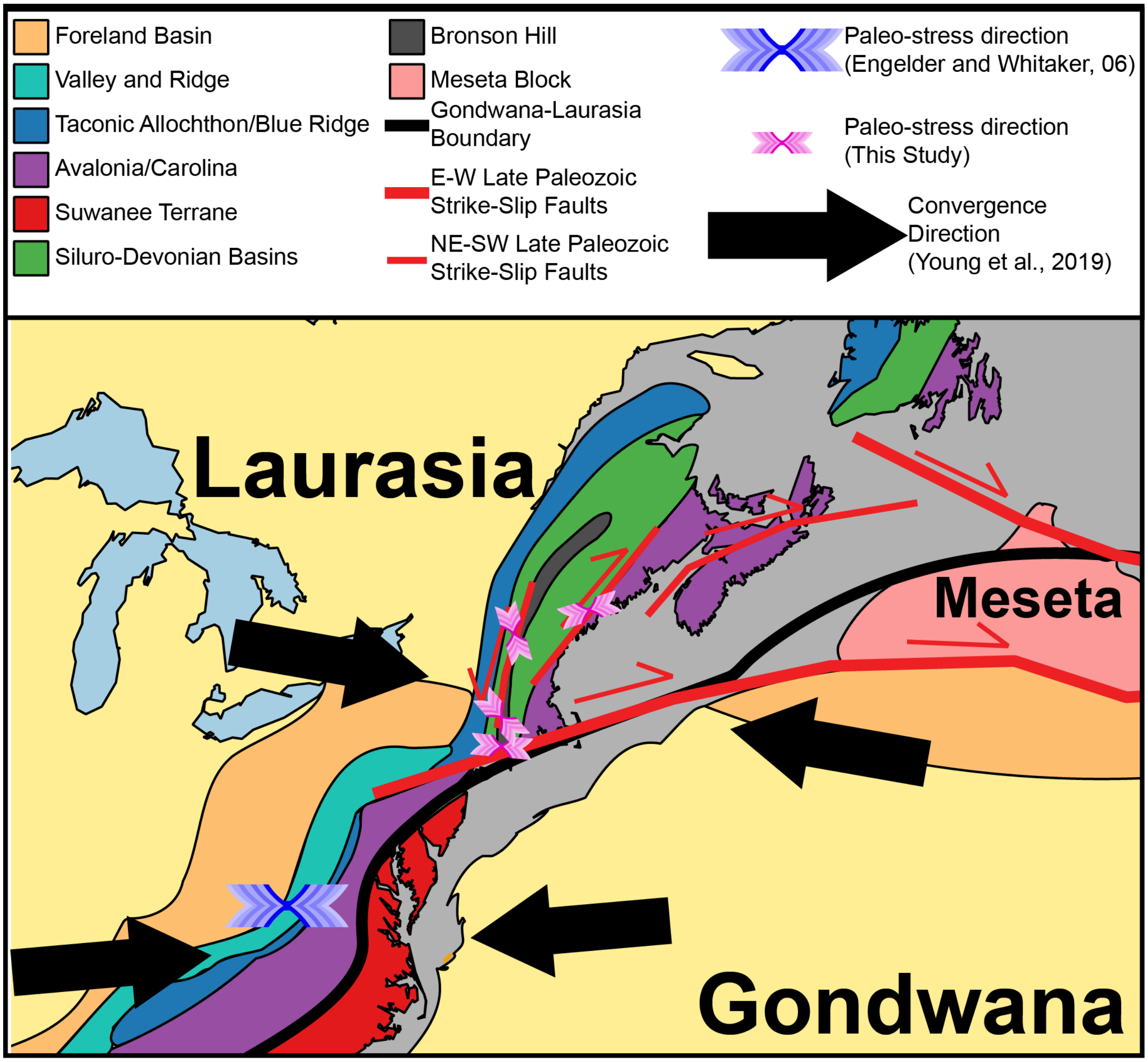

Figure 5.15: Regional tectonic reconstruction at 320 Ma. The modern-day coastlines are reconstructed to their relative positions at 320 Ma according to the kinematic model of Young et al. (2019). Late Carboniferous stress directions, corresponding to early Alleghenian deformation, are plotted as inward pointing fletchings.

Appendix 1: Additional Background and Methodology for Chapter 2

A1.1: Additional Details of Model Derivation for Hele Shaw Flow

This section adds detail to the derivation of the quantitative model described in Section 5 of the main text.

Beginning with eqs. 5ab in the main text, we solve for the constants A_u and A_ℓ so that the horizontal velocity and shear stress are equal at the interface between the upper and lower channels, giving:

$$A_u = -\frac{P_\ell}{\partial r}\left(\frac{\mu_u c_\ell{}^2}{2\mu_u(c_u\mu_\ell + \mu_u c_\ell)}\right) - \frac{\partial P_u}{\partial r}\left(\frac{\mu_\ell c_u{}^2 + 2\mu_u c_u c_\ell}{2\mu_u(c_u\mu_\ell + \mu_u c_\ell)}\right) \qquad (\mathrm{A}-1)$$

$$A_\ell = \frac{\partial P_u}{\partial r}\left(\frac{\mu_\ell c_u{}^2}{2\mu_\ell(c_\ell\,\mu_u + \mu_\ell\,c_u)}\right) + \frac{\partial P_\ell}{\partial r}\left(\frac{\mu_u c_\ell{}^2 + 2\mu_\ell c_\ell c_u}{2\mu_\ell(c_\ell\,\mu_u + \mu_\ell\,c_u)}\right) \qquad (\mathrm{A}-2)$$

We integrate eqs. (5ab) in the main text over z, from the top to bottom of each channel, to find the total flux:

$$\int_0^{c_u} v_u(z)\,dz = \frac{1}{\mu_u}\frac{\partial P_u}{\partial r}\left(\frac{c_u{}^3}{6}\right) + A_u\frac{c_u{}^2}{2} \qquad (\mathrm{A}-3)$$

$$\int_0^{c_u} v_\ell(z)\,dz = \frac{1}{\mu_\ell}\frac{\partial P_\ell}{\partial r}\left(\frac{c_\ell{}^3}{6}\right) - A_\ell\frac{c_\ell{}^2}{2} \qquad (\mathrm{A}-4)$$

Finally, we take the divergence to obtain the change in thickness of the upper and lower channels through time. Substituting for P_u, P_ℓ, A_u, and A_ℓ yields:

$$\frac{\partial c_u}{\partial t} = \frac{1}{r}\frac{\partial}{\partial r}\left(rB_u\left(\frac{\partial T}{\partial r}\right)\right) + \frac{1}{r}\frac{\partial}{\partial r}\left(rC_u\frac{\partial c_{ex}}{\partial r}\right) + \frac{1}{r}\frac{\partial}{\partial r}\left(rD_u\frac{\partial c_u}{\partial r}\right) \qquad (\mathrm{A}-5)$$

where:

$$B_u = \frac{(\rho_u - \rho_w)g(\mu_\ell c_u{}^4 + 4\mu_u c_\ell c_u{}^3) + (\rho_\ell - \rho_w)g(3\mu_u c_\ell{}^2 c_u{}^2)}{12\mu_u(c_u\mu_\ell + \mu_u c_\ell)}$$

$$C_u = \frac{(\rho_u - \rho_{ex})g(\mu_\ell c_u{}^4 + 4\mu_u c_\ell c_u{}^3) + (\rho_\ell - \rho_{ex})g(3\mu_u c_\ell{}^2 c_u{}^2)}{12\mu_u(c_u\mu_\ell + \mu_u c_\ell)}$$

$$D_u = \frac{(\rho_u - \rho_\ell)g(\mu_u c_\ell{}^2 c_u{}^2)}{4\mu_u(c_u\mu_\ell + \mu_u c_\ell)}$$

and:

$$\frac{\partial c_\ell}{\partial t} = \frac{1}{r}\frac{\partial}{\partial r}\left(rB_\ell\left(\frac{\partial T}{\partial r}\right)\right) + \frac{1}{r}\frac{\partial}{\partial r}\left(rC_\ell\frac{\partial c_{ex}}{\partial r}\right) + \frac{1}{r}\frac{\partial}{\partial r}\left(rD_\ell\frac{\partial c_u}{\partial r}\right) \qquad (\mathrm{A}-6)$$

$$B_\ell = \frac{(\rho_\ell - \rho_w)g(\mu_u {c_\ell}^4 + 4\mu_\ell c_u {c_\ell}^3) + (\rho_u - \rho_w)g(3\mu_\ell {c_\ell}^2 {c_u}^2)}{12\mu_\ell(c_u\mu_\ell + \mu_u c_\ell)}$$

$$C_\ell = \frac{(\rho_\ell - \rho_{ex})g(\mu_u {c_\ell}^4 + 4\mu_\ell c_u {c_\ell}^3) + (\rho_u - \rho_{ex})g(3\mu_\ell {c_\ell}^2 {c_u}^2)}{12\mu_\ell(c_u\mu_\ell + \mu_u c_\ell)}$$

$$D_\ell = \frac{(\rho_u - \rho_\ell)g(\mu_u {c_\ell}^4 + 4\mu_\ell c_u {c_\ell}^3)}{12\mu_\ell(c_u\mu_\ell + \mu_u c_\ell)}$$

Using the relationship between dynamic pressure and vertical velocity at the base of the lower channel (see following section):

$$\frac{\partial c_u}{\partial t} + \frac{\partial c_\ell}{\partial t} - \frac{\partial T}{\partial t} = fP_\ell \qquad (\mathrm{A}-7)$$

where f is a parameter with units of m Pa^{-1}s^{-1}. We rewrite to solve for the time derivative of c_ℓ

and substitute into eq. (A-6):

$$\left(fP_\ell + \frac{\partial T}{\partial t} - \frac{\partial c_u}{\partial t}\right) = \left[\frac{1}{r}\frac{\partial}{\partial r}\left(rB_\ell\frac{\partial T}{\partial r}\right) + \frac{1}{r}\frac{\partial}{\partial r}\left(rD_\ell\frac{\partial c_u}{\partial r}\right)\right] \qquad (\mathrm{A}-8)$$

Adding eqs. (A-5) and (A-8) and moving fP_ℓ to the right-hand side, we obtain an expression for the time derivative of T:

$$\frac{\partial T}{\partial t} = \frac{1}{r}\frac{\partial}{\partial r}\left(r(B_u + B_\ell)\frac{\partial T}{\partial r}\right) + \frac{1}{r}\frac{\partial}{\partial r}\left(r(C_u + C_\ell)\frac{\partial c_r}{\partial r}\right) + \frac{1}{r}\frac{\partial}{\partial r}\left(r(D_u + D_\ell)\frac{\partial c_u}{\partial r}\right) - fP_\ell$$

and finally, substituting for P_ℓ:

$$\frac{\partial T}{\partial t} = \frac{1}{r}\frac{\partial}{\partial r}\left(r(B_u + B_\ell)\frac{\partial T}{\partial r}\right) + \frac{1}{r}\frac{\partial}{\partial r}\left(r(C_u + C_\ell)\frac{\partial c_r}{\partial r}\right) + \frac{1}{r}\frac{\partial}{\partial r}\left(r(D_u + D_\ell)\frac{\partial c_u}{\partial r}\right)$$

$$-f\big([gT(\rho_\ell - \rho_w) - c_r g(\rho_\ell - \rho_{cr})] - c_u g(\rho_\ell - \rho_u)\big) \qquad (\mathrm{A}-9)$$

We used eq. (A-9) to solve for the new value of T at each timestep using implicit finite differencing, and the eq. (A-5) to solve for the new value of c_u using explicit finite differencing.

A1.2: Horizontal and Vertical Velocities in a Viscous Medium from Stream Function Analysis

In this section we derive an “exact” solution for flow in a two-layer medium. We then apply conditions similar to those in the main text, with a relatively thin, low-viscosity upper layer and a thicker, high-viscosity lower layer. This allows us to examine how well the Hele-Shaw approximation captures the rate of horizontal flow in the upper layer when it is underlain by material with thickness and viscosity similar to that of the lower mantle, and to estimate how vertical velocity at the base of the channel is related to the dynamic pressure in the channel. For simplicity we use a simple, two-dimensional Cartesian geometry, and note how a spherical shell geometry might be expected to modify the results from the Cartesian analysis.

Note that the “layers” in this section are a weak upper layer assumed to be immediately beneath the lithosphere and a lower layer extending to the base of the lower mantle. In the main text the upper layer is further divided into two separate layers, or “channels” comprised of weaker plume material above and normal asthenosphere beneath.

We begin with a stream function that satisfies the Stokes equation for (linear) viscous flow in the x-z plane, with wavenumber k in the x-direction:

$$\psi = (A\cosh(kz) + B\sinh(kz) + Ckz\cosh(kz) + Dkz\sinh(kz))\sin(kx) \qquad (\mathrm{A}-10)$$

where A-D are constants to be determined from the boundary conditions. The x- and z-components of velocity (v_x, v_z), shear stress (τ_{xz}), viscous pressure (P), and deviatoric stresses (σ_{xx}, σ_{zz}) are:

$$v_x = \frac{\partial\psi}{\partial z}; \quad v_z = -\frac{\partial\psi}{\partial x}; \quad \tau_{xz} = \mu\left(\frac{\partial v_x}{\partial z} + \frac{\partial v_z}{\partial x}\right)$$

$$(P + \sigma_{zz}) = \int \frac{\partial \tau_{xz}}{\partial x}\, dz; \quad \sigma_{zz} = -\sigma_{xx} = \frac{\partial^2 v_x}{\partial x^2} \qquad (\mathrm{A}-11)$$

where μ is viscosity.

The constants A-D in (A-10) can be written in terms of the velocity, shear stress and total vertical stress evaluated at z=0, as indicated by the naught-subscript on each variable:

$$Ak = -\frac{v_{zo}}{k} \qquad B = \frac{P_o + \sigma_{zzo}}{2\mu k^2}$$

$$C = \frac{v_{xo}}{k} - \frac{P_o + \sigma_{zzo}}{2\mu k^2} \qquad D = \frac{v_{zo}}{k} + \frac{\tau_{xzo}}{2\mu k^2} \qquad (A-12)$$

Evaluation of the stream function yields expressions for velocity and stress, given in the box below for the benefit of the reader.

General expressions for velocity and stress as derived from the stream function (X1):

$$v_x(z,\mu) = \left(v_{xo}\big(\cosh(kz) + kz\sinh(kz)\big) + v_{zo}kz\cosh(kz) + \left(\frac{\tau_o}{2\mu k}\right)\big(\sinh(kz) + kz\cosh(kz)\big) - \left(\frac{f_{zzo}}{2\mu k}\right) kz\sinh(kz) \right) \sin(kx)$$

$$v_z(z,\mu) = \left(-v_{xo}kz\cosh(kz) + v_{zo}(\cosh(kz) - kz\sinh(kz)) - \left(\frac{\tau_o}{2\mu k}\right) kz\sinh(kz) + \left(\frac{f_{zzo}}{2\mu k}\right)\big(kz\cosh(kz) - \sinh(kz)\big) \right) \cos(kx)$$

$$\tau_{xy}(z,\mu) = \Big(2\mu k v_{xo}\big(\sinh(kz) + kz\cosh(kz)\big) + 2\mu k v_{zo} kz\sinh(kz) + \tau_{xo}(\cosh(kz) + kz\sinh(kz)) - f_{zzo} kz\cosh(kz)\Big)\sin(kx)$$

$$f_{zz}(z,\mu) = \Big(2\mu k v_{xo} kz\sinh(kz) + 2\mu k v_{zo}\big(kz\cosh(kz) - \sinh(kz)\big) + \tau_{xo} kz\cosh(kz) + f_{zzo}\big(\cosh(kz) - kz\sinh(kz)\big)\Big)\cos(kx)$$

$$\sigma_{zz}(z,\mu) = \Big(2\mu k v_{xo}\big(\cosh(kz) + kz\sinh(kz)\big) + 2\mu k v_{zo} kz\cosh(kz) + \tau_{\mathrm{o}}\big(\sinh(kz) + kz\cosh(kz)\big) - f_{zzo} kz\sinh(kz)\Big)\cos(kx)$$

$$P(z,\mu) = (-2\mu k v_{xo}\cosh(kz) - 2\mu k v_{zo}\sinh(kz) - \tau_{xo}\sinh(kz) + f_{zzo}\cosh(kz))\cos(kx)$$

It is convenient to set the interface between the two viscous layers at z=0, and the equations apply to both layers provided that the appropriate value of viscosity (μ) is used in each layer. At *z*=0, velocity and appropriate stresses (τ_{xy} and f_{zz}) are continuous across the interface.

We consider an upper layer with thickness h and viscosity μ_h and a lower layer of thickness H and viscosity μ_H. We apply a boundary condition of no horizontal velocity at the top of the upper layer (v_x=0 at *z*= -*h*) and no horizontal or vertical velocity at the base of the lower layer (v_x=v_z=0 at *z*= *H*). Similar results to those presented below are obtained if we apply a zero-shear stress condition at the base of the lower layer, rather than zero horizontal velocity.

Here we show results for two configurations that are relevant to the analysis in the main text. The first case treats the upper layer as approximately corresponding to most of the upper mantle and a viscosity that is generally accepted to be representative of the upper mantle: h=400 km, μ_h= 10^{20} Pa s. The second case decreases the thickness and the viscosity of the upper layer by a factor of 10: h=40 km, μ_h= 10^{19} Pa s. In both cases the combined thickness of the layers, h+H, is 3000 km unless otherwise noted.

For the plumes in this paper examined in this, the diameter of the topographic swells is ~3000 km, yielding an approximate value of k in the range of 10^{-6} m^{-1}, but spanning a range of wavenumbers within an order of magnitude of this value. In the calculation below we use a k=10^{-6} m^{-1}.

We first examine how well flow in the upper, low-viscosity layer can be approximated as Hele-Shaw flow with zero horizontal velocity at its top and base. For z between -h and 0, the Hele-Shaw expression for horizontal velocity is:

$$v_x = \frac{P_o}{2\mu}(z^2 + hz) \qquad (A-13)$$

In this approximation, deviatoric stresses for z between -h and 0 are assumed to be negligible and pressure invariant with depth. For both configurations we use the stream function solutions to that σ_{zz} and the variation in pressure with depth are less than 1% of the surface pressure, and thus satisfy the assumptions of Hele-Shaw flow.

Figure A1.1 shows the horizontal velocity in the upper layer as a function of depth (for wavenumber k= 10^{-6} m^{-1}), comparing the "exact" velocity computed from the stream function (A-10 to A-12) with the velocity computed using the Hele-Shaw approximation with v_x set to zero at the top and bottom of the layer (A-13). These velocities are normalized by the Hele-Shaw velocity in (A-13) computed halfway through the layer, at z = -h/2.

For both layer configurations, v_x computed from the stream function is similar to that computed from the Hele-Shaw approximation, although the stream function yields velocities that are slightly larger and the velocity at the base of the layer is not zero. For h=400 km (μ_h= 10^{20} Pa s), the stream function velocity throughout is quite close to the approximate solution and the total flux (integral of velocity with depth) is within ~3% of the total flux for the approximate solution. For h =40 km (μ_h= 10^{19} Pa s), the maximum horizontal velocity computed from the stream function is approximately 13% greater than for the approximate solution and the total flux is ~20% greater than for the approximate solution.

These results indicate that using the Hele-Shaw approximation for flow in the upper layer, with v_x set to zero at the upper and lower boundaries may underestimate the total flux by ~ 20 % as compared to the exact solution that includes the high viscosity lower layer. Alternatively, the approximate solution will yield an overestimate of the upper layer viscosity by up to 20%, which is fairly small compared with uncertainties in mantle viscosity.

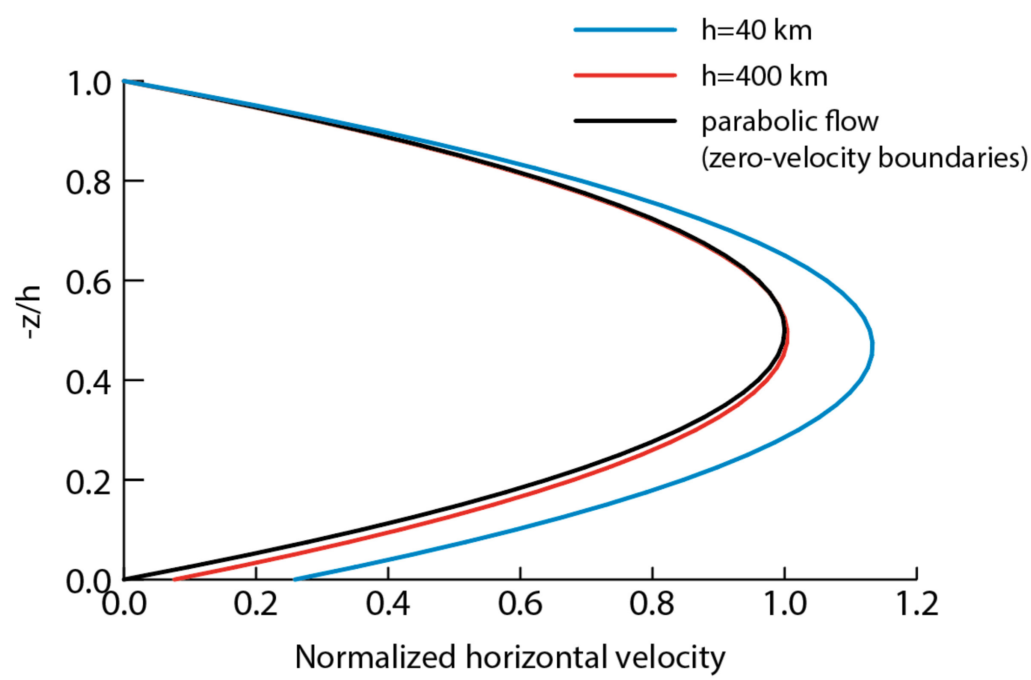

Figure A1.1. Normalized horizontal velocity for simple parabolic flow as computed in (A-13) (black line) compared to the "exact" solutions (blue and red lines) from the stream function (A11-A13) for the two configurations described in the text. The combined thickness of the upper and lower layer is fixed at 3000 km.

There is a vertical velocity at the base of the upper layer that scales with the viscous pressure at the interface between layers. When the upper layer is thinner and much less viscous than the lower layer, as in the cases considered here, the vertical velocity at base of the upper layer is controlled by flow in the lower layer and is mostly independent of the thickness and viscosity of the upper layer. It is however sensitive to wavenumber, *k,* and scales **inversely with the viscosity of the lower layer**. For a lower layer viscosity of $5x10^{22}$ Pa s, the ratio of vertical velocity at the base of the upper layer to the pressure in the upper layer is shown in the plot below (where we divide by a factor of two to allow for three-dimensional flow).

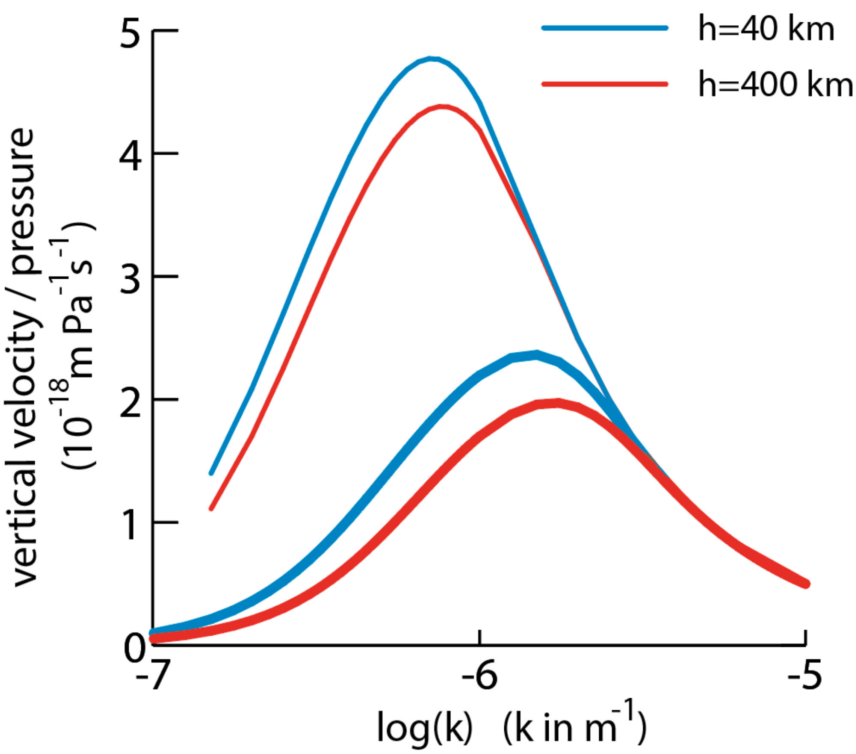

Figure A1.2. The ratio of vertical velocity (in m/s) to pressure in the upper layer (in Pa) for the two viscosity structures examined in this section. Thinner lines are for a total thickness of the two-layers of 3000 km, thicker lines for a total thickness of 1500 km.

The assumption of Cartesian geometry is not particularly good for a layer that extends to the base of the lower mantle (thinner lines in plot above), where the radius at the base of the mantle is approximately half that of the Earth. If we instead put the base of the lower layer halfway down through the mantle, at 1500 km below the top of the upper layer (thicker lines in plot above), the ratio between vertical velocity and pressure is smaller by a factor of two or three at the wavelengths of interest. In either case, the ratio between vertical velocity at the base of the upper layer for wavenumbers near 10^{-6} m^{-1} is expected to be in the general vicinity of 10^{-18} m Pa^{-1} s-^{1} for a lower layer viscosity of 5×10^{22} Pa s. The ratio of velocity to pressure at the base of the upper layer is, for the geometries and upper layer viscosities used here, varies approximately linearly with the reciprocal of the (effective) viscosity of the lower layer, which is probably within a factor of two or three of 5×10^{22} Pa, adding a comparable uncertainty to the results derived in this supplemental section.

A1.3: Further Development of the Constraints on Viscosity and Thickness of a Weak Layer in the Upper Mantle

Quantitative modeling of mantle flux away from upwelling plumes has the potential to better constrain upper mantle viscosity structure beneath young oceanic lithosphere. A variety of interdisciplinary studies have produced evidence favoring the presence of a low viscosity immediately underlying oceanic lithosphere. For example, Hager and O'Connell, 1979; Kawakatsu et al., 2002; Podolefsky et al., 2004; Bagley and Revenaugh, 2008; Stein and Hansen, 2008; Barnhoorn et al., 2011; Schmerr, 2012; Naif et al., 2013; Becker, 2017; Rychert et al., 2020; Selway et al., 2020; Hua et al., 2023**.** This study in this paper the potential to distinguish between (nearly parabolic) channel flow that is distributed across much of the upper mantle and channel flow that may be predominantly confined to a low viscosity zone located beneath the (young) oceanic lithosphere. In the latter case, this study has the potential to constrain the thickness and viscosity of a sub-lithospheric low-viscosity layer.

The primary published constraints on upper mantle viscosity are based, directly or indirectly, on estimates of the shear stresses acting on the base of the plates and are largely determined from plate velocities incorporated into models of plate motion, subduction, and mantle convection (Hager and O'Connell, 1981; Richards et al., 2001; Podolefsky et al., 2004; Becker, 2006; Conrad and Behn, 2010). Under conditions of simple shear, shear stress in uniform through the channel and horizontal velocity is related to shear stress and viscosity by:

$$\frac{\Delta v}{\tau_{rz}} = \int_0^h \frac{dz}{\mu(z)} \qquad (\mathrm{A}-14)$$

where Δv is the difference in velocity across the layer (i.e., between the plates and the deep mantle). If, for example, one assumes that viscosity is uniform throughout the deforming layer, then:

$$\frac{\Delta v}{\tau_{rz}} = \left(\frac{h_{ef}}{\mu_{ef}}\right) \qquad (\mathrm{A}-15)$$

where the "effective viscosity" μ_{ef} is equal to the layer viscosity and the "effective layer thickness" h_{ef} is equal to the entire layer thickness. However, many other, non-uniform viscosity distributions are capable of the same value of $\left(h_{ef}/\mu_{ef}\right)$ under conditions of simple shear. In particular, the value of the integral in eq. (A-14) will be dominated by any sub-layers of exceptionally low viscosity relative to the rest of the channel.

Many studies, over a wide range of disciplines constrain the ratio $\left(h_{ef}/\mu_{ef}\right)$ to be approximately 10^{-15} Pa^{-1} s^{-1} m. For example, Mitrovica and Forte (2004), Conrad and Lithgow-Bertelloni (2006), Holt and Becker (2016), Behr et al. (2022), and Holt and Royden (2020) all obtain similar estimates for $\left(h_{ef}/\mu_{ef}\right)$. For a uniform viscosity upper mantle, this yields an effective upper mantle viscosity in the vicinity of ~5×10^{20} Pa s (Mitrovica and Forte, 2004; Holt and Royden, 2020). However, it is clear that a wide range of viscosity structures could result in the same value of $\left(h_{ef}/\mu_{ef}\right)$. For example, an upper mantle with a thickness of 50 km and a viscosity of ~5x10^{19} Pa s, underlain by material with a much larger viscosity.

Distinguishing among various mantle viscosity structures that satisfy this scaling relationship is possible because scaling relations among stress, viscosity, velocity, and layer thickness are different in the pure shear mode (on which most estimates of upper mantle viscosity depend) and channelized flow as we propose to occur adjacent to the mantle plumes examined in this paper. For example, integrating eqn. (2) in the main text over z, twice, and setting the horizontal velocity at the top and base of the layer yields:

$$v(z) = \frac{\partial P}{\partial r}\int_0^z \frac{z\,dz}{\mu(z)} - \frac{\partial P}{\partial r}\left(\frac{z}{h}\right)\int_0^h \frac{z\,dz}{\mu(z)} \qquad (\mathrm{A}-16)$$

where we have used the approximation that dynamic pressure does not vary significantly with depth in the channel. Integrating again to find the lateral flux of material yields:

$$\int_0^h v(z)\;dz = \frac{\partial P}{\partial r}\int_0^h \int_0^z \frac{z\,dz}{\mu(z)} - \frac{\partial P}{\partial r}\left(\frac{h^2}{2h}\right)\int_0^h \frac{z\,dz}{\mu(z)} \qquad (\mathrm{A}-17)$$

As is also the case for eq. (A-14), the value of the integral in eq. (A-16) will be dominated by any sub-layers of exceptionally low viscosity relative to the rest of the channel. For a layer of thickness μ_{ef} and uniform viscosity μ_{ef} (and zero velocity at the top and base of the layer), this expression simplifies to:

$$\int_0^h v(z)\;dz = -\frac{1}{12}\frac{\partial P}{\partial r}\left(\frac{{h_{ef}}^3}{\mu_{ef}}\right) \qquad (\mathrm{A}-18)$$

Therefore the net flux in the channel (integral on the left side of equation A-10) is related to the radial pressure (or topography) gradient through a term that scales as $\left({h_{ef}}^3/\mu_{ef}\right)$. This ratio will, for example, differ by two orders of magnitude for flux in a channel with viscosity 5x10^{20} Pa s and 500 km thick and flux in a channel with viscosity 5x10^{19} Pa s and 50 km thick.

Thus, modeling of channel flux around upwelling plumes offers a means of better constraining the viscosity structure of the upper mantle, and in particular, probing for the effect of a low viscosity channel beneath young oceanic lithosphere.

A1.4: References for Basalt Geochemical Data

Below we list references for basalt geochemical data referenced and utilized in this paper. Geochemistry was sourced from Gale et al. (2013) and the EarthChem database. Three individual searches were used to query EarthChem for basaltic glass on mid-ocean ridges around Iceland, the Azores, and Afar.

The bounding box for the Iceland EarthChem search criteria is described by the following points:

13.1396484374413 71.9445601552263; -10.3710937499533 71.5729232899962; -17.0947265624232 66.4285209439412; -16.7431640624251 65.1963401562555; -18.0615234374194 64.4666244223293; -21.8408203124022 63.7168693889327; -23.466796874895 62.9466527199747; -32.8271484373526 56.7143116971714; -34.0576171873478 52.9638897237709; -36.5185546873364 52.751095431679; -36.1669921873383 56.2278508799088; -25.9716796873832 63.6840117601881; -19.6435546874118 65.2021476538783; -18.5888671874165 67.9945127881309; -15.2490234374309 70.9505994610655

The second search was for the north Mid-Atlantic ridge around the Azores. The bounding box for this search is bracketed with the following points:

-26.1035156248836 48.5206054408768; -26.1914062498827 46.3746951245416; -27.949218749875 42.2109498121905; -28.037109374875 40.2875472144183; -23.8183593748932 37.6114964222421; -27.3339843748779 37.1907935661516; -30.7617187498626 37.1907935661516; -33.5742187498502 35.0518216004004; -38.0566406248301 32.6319663471255; -40.6933593748178 30.1442049610711; -43.1542968748072 27.1992019704469; -44.7363281248006 24.0927864206346; -43.6816406248044 22.5506526053997; -45.2636718747977 15.7056849311194; -46.2304687497939 15.0234461371042; -47.5488281247872 15.6205292938914; -47.5488281247872 21.649718788159; -46.845703124791 25.3770797298878; -42.4511718748101 32.4830995960703; -33.8378906248483 38.3073607113961; -29.7509765623669 46.3005697107838; -29.5751953123669 48.3323868380523

We performed two individual EarthChem searches for Afar. The first search was for basalt and basaltic andesite whole rock and glass isotope data. The second search included basalt glass major element data for the Red Sea and Gulf of Aden spreading ridges, and additional basalt whole rock data for the Afar Depression in Ethiopia. Three separate bounding boxes for the EarthChem search are given below. The same bounding boxes were used for both searches, however we also searched for whole rock data in the Red Sea and Gulf of Aden to increase the amount of isotope data.

Red Sea Bounding Box:

4735426.7763021 1524927.9691153; 4767224.5800686 1510252.0596846; 4784346.4744044 1549387.8181664; 4742764.7310174 1652119.1841812; 4615573.5159514 1860027.901116; 4483490.3310753 2038584.7991894; 4405218.8141116 2178005.9387809; 4317163.3575274 2251385.4859343; 4270689.6443303 2367886.1740851; 4241337.8254689 2558672.996684; 4138606.4594541 2680972.2419398; 4079902.8217313 2791041.5626699; 4072564.867016 2908448.8381155; 4048105.0179649 2950030.5815024; 3889115.9991324 3160385.2833423; 3830412.3614096 3106573.6154297; 3996739.3349574 2817947.3966262; 4094578.731162 2639390.4985528; 4170404.2632206 2546443.0721585; 4231553.8858485 2299398.5967419; 4297595.4782866 2174653.366581; 4380758.9650605 2074367.9854713; 4461476.4669292 1915378.9666389; 4605789.576331 1736822.0685655

Gulf of Aden Bounding Box:

57.150878905995 13.3958132001013; 58.0737304684907 13.4603379190535; 57.0410156247452 14.6400914259492; 55.6567382810017 15.0248273440645; 54.3823242185078 15.0034713626188; 53.569335937261 14.7897931912684; 52.932128906014 14.661483753364; 52.0971679685174 14.9180258617422; 51.1962890622715 13.5248450301839; 50.251464843526 13.7826958422921; 49.5483398435289 13.5248450301839; 48.273925781035 12.9867527893844; 46.7138671872915 12.6201716343548; 45.5712890622963 12.2098336876435; 44.2968749998025 12.2530578844318; 43.4838867185556 12.0368656623745; 43.2751464841823 11.9384048780741; 43.1378173826201 11.8680783893044; 42.9125976560589 11.7544352837559; 42.8961181638709 11.6948889486814; 43.1103515623077 11.7219570771335; 43.2531738279317 11.7869096108259; 43.6157226560551 11.9275866185567; 44.5001220701139 11.9546314471081; 45.593261718547 11.9492227001912; 47.3840332029135 12.2007070502338; 49.3395996091547 12.7405073845426; 51.4050292966456 12.82676879254; 52.2180175778925 14.2456215386417; 53.8439941403853 13.9239138229127; 55.2502441403787 14.3527548696591; 56.3708496091241 14.0097473467034

Afar Bounding Box:

35.4638671873403 25.6912345834175; 36.7822265623345 22.9940061330809; 37.8808593748302 20.1581979282513; 39.5947265623221 17.3959149093818; 40.6933593748169 15.7856710319012; 40.3417968748188 14.1194872035694; 40.2978515623192 9.61929973653363; 44.165039062302 10.6208016823807; 45.7910156247949 11.4456426740284; 50.0976562497758 12.6998741161649; 51.4160156247692 12.786149556919; 52.5585937497644 13.9478707714567; 55.1513671872534 14.1194872035694; 56.2499999997481 13.9478707714567; 56.5136718747472 15.2317404476021; 54.3164062497567 15.3170581041161; 52.6464843747643 15.0182933999524; 51.5039062497691 14.5907534279789; 50.976562499772 13.7761249639833; 44.7802734372992 12.4840561620865; 43.6816406248044 12.4840561620865; 43.0664062498064 13.0878773224541; 42.4072265623097 14.1194872035694; 42.2753906248102 15.657974819973; 41.396484374814 17.1425821766187; 38.6718749998264 21.1921213145263; 37.8369140623297 23.5623692754653; 36.4746093748359 25.73104561007

Geochemical References

Agranier, A., Blicherttoft, J., Graham, D., Debaille, V., Schiano, P., & Albarede, F. (2005). The spectra of isotopic heterogeneities along the mid-Atlantic Ridge. *Earth and Planetary Science Letters*, *238*(1–2), 96–109. https://doi.org/10.1016/j.epsl.2005.07.011

Al Kwatli, M. A., Gillot, P. Y., Zeyen, H., Hildenbrand, A., & Al Gharib, I. (2012). Volcano-tectonic evolution of the northern part of the Arabian plate in the light of new K–Ar ages and remote sensing: Harrat Ash Shaam volcanic province (Syria). *Tectonophysics*, *580*, 192–207. https://doi.org/10.1016/j.tecto.2012.09.017

Andres, M., Blichert-Toft, J., & Schilling, J.-G. (2004). Nature of the depleted upper mantle beneath the Atlantic: Evidence from Hf isotopes in normal mid-ocean ridge basalts from 79°N to 55°S. *Earth and Planetary Science Letters*, *225*(1–2), 89–103. https://doi.org/10.1016/j.epsl.2004.05.041

Antonini, P., Petrini, R., & Contin, G. (1998). A segment of sea-floor spreading in the central Red Sea: Basalts from the Nereus Deep (23°00′–23°20′N). *Journal of African Earth Sciences*, *27*(1), 107–114. https://doi.org/10.1016/S0899-5362(98)00049-9

Arevalo, R., & McDonough, W. F. (2008). Tungsten geochemistry and implications for understanding the Earth's interior. *Earth and Planetary Science Letters*, *272*(3–4), 656–665. https://doi.org/10.1016/j.epsl.2008.05.031

Arevalo, R., McDonough, W. F., & Luong, M. (2009). The K/U ratio of the silicate Earth: Insights into mantle composition, structure and thermal evolution. *Earth and Planetary Science Letters*, *278*(3–4), 361–369. https://doi.org/10.1016/j.epsl.2008.12.023

Ashchepkov, I. V., Pokhilenko, N. P., Vladykin, N. V., Logvinova, A. M., Afanasiev, V. P., Pokhilenko, L. N., Kuligin, S. S., Malygina, E. V., Alymova, N. A., Kostrovitsky, S. I., Rotman, A. Y., Mityukhin, S. I., Karpenko, M. A., Stegnitsky, Y. B., & Khemelnikova, O. S. (2010). Structure and evolution of the lithospheric mantle beneath Siberian craton, thermobarometric study. *Tectonophysics*, *485*(1–4), 17–41. https://doi.org/10.1016/j.tecto.2009.11.013

Aumento, F. (1968). The Mid-Atlantic Ridge near 45° N. II. Basalts from the area of Confederation Peak. *Canadian Journal of Earth Sciences*, *5*(1), 1–21. https://doi.org/10.1139/e68-001

Aumento, F., Melson, W. G., & et al. (1977). *Initial Reports of the Deep Sea Drilling Project, 37* (Vol. 37). U.S. Government Printing Office. https://doi.org/10.2973/dsdp.proc.37.1977

Ayalew, D., Jung, S., Romer, R. L., Kersten, F., Pfänder, J. A., & Garbe-Schönberg, D. (2016). Petrogenesis and origin of modern Ethiopian rift basalts: Constraints from isotope and trace element geochemistry. *Lithos*, *258–259*, 1–14. https://doi.org/10.1016/j.lithos.2016.04.001

Baragar, W. R. A. (1968). Major-element geochemistry of the Noranda volcanic belt, Quebec-Ontario. *Canadian Journal of Earth Sciences*, *5*(4), 773–790. https://doi.org/10.1139/e68-076

Barberi, F., Bizouard, H., & Varet, J. (1971). Nature of the clinopyroxene and iron enrichment in alkalic and transitional basaltic magmas. *Contributions to Mineralogy and Petrology*, *33*(2), 93–107. https://doi.org/10.1007/BF00386108

Barberi, F., Civetta, L., & Varet, J. (1980). Sr isotopic composition of Afar volcanics and its implication for mantle evolution. *Earth and Planetary Science Letters*, *50*(1), 247–259. https://doi.org/10.1016/0012-821X(80)90136-3

Barberi, F., Ferrara, G., Santacroce, R., Treuil, M., & Varet, J. (1975). A Transitional Basalt-Pantellerite Sequence of Fractional Crystallization, the Boina Centre (Afar Rift, Ethiopia). *Journal of Petrology*, *16*(1), 22–56. https://doi.org/10.1093/petrology/16.1.22

Barberi, F., Santacroce, R., & Varet, J. (1974). Silicic peralkaline volcanic rocks of the afar depression (Ethiopia). *Bulletin Volcanologique*, *38*(2), 755–790. https://doi.org/10.1007/BF02596907

Barrat, J. A., Fourcade, S., Jahn, B. M., Cheminée, J. L., & Capdevila, R. (1998). Isotope (Sr, Nd, Pb, O) and trace-element geochemistry of volcanics from the Erta'Ale range (Ethiopia). *Journal of Volcanology and Geothermal Research*, *80*(1–2), 85–100. https://doi.org/10.1016/S0377-0273(97)00016-4

Barrat, J. A., Jahn, B. M., Fourcade, S., & Joron, J. L. (1993). Magma genesis in an ongoing rifting zone: The Tadjoura Gulf (Afar area). *Geochimica et Cosmochimica Acta*, *57*(10), 2291–2302. https://doi.org/10.1016/0016-7037(93)90570-M

Barrat, J. A., Joron, J. L., Taylor, R. N., Fourcade, S., Nesbitt, R. W., & Jahn, B. M. (2003). Geochemistry of basalts from Manda Hararo, Ethiopia: LREE-depleted basalts in Central Afar. *Lithos*, *69*(1–2), 1–13. https://doi.org/10.1016/S0024-4937(03)00044-6

Barry, P. H., Hilton, D. R., Füri, E., Halldórsson, S. A., & Grönvold, K. (2014). Carbon isotope and abundance systematics of Icelandic geothermal gases, fluids and subglacial basalts with implications for mantle plume-related CO_2 fluxes. *Geochimica et Cosmochimica Acta*, *134*, 74–99. https://doi.org/10.1016/j.gca.2014.02.038

Beier, C., Haase, K. M., Abouchami, W., Krienitz, M.-S., & Hauff, F. (2008). Magma genesis by rifting of oceanic lithosphere above anomalous mantle: Terceira Rift, Azores: MAGMA GENESIS BY RIFTING ABOVE ANOMALOUS MANTLE. *Geochemistry, Geophysics, Geosystems*, *9*(12), n/a-n/a. https://doi.org/10.1029/2008GC002112

Beier, C., Haase, K. M., & Hansteen, T. H. (2006). Magma Evolution of the Sete Cidades Volcano, São Miguel, Azores. *Journal of Petrology*, *47*(7), 1375–1411. https://doi.org/10.1093/petrology/egl014

Beier, C., Haase, K. M., & Turner, S. P. (2012). Conditions of melting beneath the Azores. *Lithos*, *144–145*, 1–11. https://doi.org/10.1016/j.lithos.2012.02.019

Beier, C., Stracke, A., & Haase, K. M. (2007). The peculiar geochemical signatures of São Miguel (Azores) lavas: Metasomatised or recycled mantle sources? *Earth and Planetary Science Letters*, *259*(1–2), 186–199. https://doi.org/10.1016/j.epsl.2007.04.038

Bézos, A., & Humler, E. (2005). The $Fe^{3+}/\Sigma Fe$ ratios of MORB glasses and their implications for mantle melting. *Geochimica et Cosmochimica Acta*, *69*(3), 711–725. https://doi.org/10.1016/j.gca.2004.07.026

Bizouard, H., Barberi, F., & Varet, J. (1980). Mineralogy and Petrology of Erta Ale and Boina Volcanic Series, Afar Rift, Ethiopia. *Journal of Petrology*, *21*(2), 401–436. https://doi.org/10.1093/petrology/21.2.401

Blichert-Toft, J., Agranier, A., Andres, M., Kingsley, R., Schilling, J.-G., & Albarède, F. (2005). Geochemical segmentation of the Mid-Atlantic Ridge north of Iceland and ridge-hot spot interaction in the North Atlantic: RIDGE-HOT SPOT INTERACTION. *Geochemistry, Geophysics, Geosystems*, *6*(1), n/a-n/a. https://doi.org/10.1029/2004GC000788

Bougault, H., Cambon, P., Corre, O., Joron, J. L., & Treuil, M. (1979). Evidence for variability of magmatic processes and upper mantle heterogeneity in the axial region of the Mid-Atlantic Ridge near 22° and 36° N. *Tectonophysics*, *55*(1–2), 11–34. https://doi.org/10.1016/0040-1951(79)90333-0

Bougault, H., Dmitriev, L., Schilling, J. G., Sobolev, A., Joron, J. L., & Needham, H. D. (1988). Mantle heterogeneity from trace elements: MAR triple junction near 14°N. *Earth and Planetary Science Letters*, *88*(1–2), 27–36. https://doi.org/10.1016/0012-821X(88)90043-X

Bourdon, B., Goldstein, S. J., Bourlès, D., Murrell, M. T., & Langmuir, C. H. (2000). Evidence from ^{10}Be and U series disequilibria on the possible contamination of mid-ocean ridge basalt glasses by sedimentary material: CONTAMINATION OF MORB GLASSES. *Geochemistry, Geophysics, Geosystems*, *1*(8), n/a-n/a. https://doi.org/10.1029/2000GC000047

Bourdon, B., Langmuir, C. H., & Zindler, A. (1996). Ridge-hotspot interaction along the Mid-Atlantic Ridge between 37°30′ and 40°30′N: The UTh disequilibrium evidence. *Earth and Planetary Science Letters*, *142*(1–2), 175–189. https://doi.org/10.1016/0012-821X(96)00092-1

Brandl, P. A., Genske, F. S., Beier, C., Haase, K. M., Sprung, P., & Krumm, S. H. (2015). Magmatic Evidence for Carbonate Metasomatism in the Lithospheric Mantle underneath the Ohře (Eger) Rift. *Journal of Petrology*, *56*(9), 1743–1774. https://doi.org/10.1093/petrology/egv052

Brandl, P. A., Regelous, M., Beier, C., & Haase, K. M. (2013). High mantle temperatures following rifting caused by continental insulation. *Nature Geoscience*, *6*(5), 391–394. https://doi.org/10.1038/ngeo1758

Brandon, A. D., Graham, D. W., Waight, T., & Gautason, B. (2007). ^{186}Os and ^{187}Os enrichments and high-$^{3}He/^{4}He$ sources in the Earth's mantle: Evidence from Icelandic picrites. *Geochimica et Cosmochimica Acta*, *71*(18), 4570–4591. https://doi.org/10.1016/j.gca.2007.07.015

Breddam, K., Kurz, M. D., & Storey, M. (2000). Mapping out the conduit of the Iceland mantle plume with helium isotopes. *Earth and Planetary Science Letters*, *176*(1), 45–55. https://doi.org/10.1016/S0012-821X(99)00313-1

Bryan, W. B. (1979). Regional Variation and Petrogenesis of Basalt Glasses from the FAMOUS Area, Mid-Atlantic Ridge. *Journal of Petrology*, *20*(2), 293–325. https://doi.org/10.1093/petrology/20.2.293

Bryan, W. B., Thompson, G., & Ludden, J. N. (1981). Compositional variation in normal MORB from 22°–25°N: Mid-Atlantic Ridge and Kane Fracture Zone. *Journal of Geophysical Research*, *86*(B12), 11815. https://doi.org/10.1029/JB086iB12p11815

Bryan, W. B., Thompson, G., & Michael, P. J. (1979). Compositional variation in a steady-state zoned magma chamber: Mid-Atlantic Ridge at 36°50′N. *Tectonophysics*, *55*(1–2), 63–85. https://doi.org/10.1016/0040-1951(79)90335-4

Burnard, P. (1999). The bubble-by-bubble volatile evolution of two mid-ocean ridge basalts. *Earth and Planetary Science Letters*, *174*(1–2), 199–211. https://doi.org/10.1016/S0012-821X(99)00254-X

Burnard, P., Harrison, D., Turner, G., & Nesbitt, R. (2003). Degassing and contamination of noble gases in Mid-Atlantic Ridge basalts: CONTAMINATION OF NOBLE GASES. *Geochemistry, Geophysics, Geosystems*, *4*(1), 1–20. https://doi.org/10.1029/2002GC000326

Cann, J. R. (1970). Petrology of basalts dredged from the Gulf of Aden. *Deep Sea Research and Oceanographic Abstracts*, *17*(3), 477–482. https://doi.org/10.1016/0011-7471(70)90062-8

Carlson, R. W., Macdougall, J. D., & Lugmair, G. W. (1978). Differential SM/ND evolution in oceanic basalts. *Geophysical Research Letters*, *5*(4), 229–232. https://doi.org/10.1029/GL005i004p00229

Cartigny, P., Pineau, F., Aubaud, C., & Javoy, M. (2008). Towards a consistent mantle carbon flux estimate: Insights from volatile systematics (H2O/Ce, δD, CO2/Nb) in the North Atlantic mantle (14° N and 34° N). *Earth and Planetary Science Letters*, *265*(3–4), 672–685. https://doi.org/10.1016/j.epsl.2007.11.011

Charlier, B., Namur, O., & Grove, T. L. (2013). Compositional and kinetic controls on liquid immiscibility in ferrobasalt–rhyolite volcanic and plutonic series. *Geochimica et Cosmochimica Acta*, *113*, 79–93. https://doi.org/10.1016/j.gca.2013.03.017

Chase, R. L. (1969). Basalt from the Axial Trough of the Red Sea. In E. T. Degens & D. A. Ross (Eds.), *Hot Brines and Recent Heavy Metal Deposits in the Red Sea* (pp. 122–128). Springer Berlin Heidelberg. https://doi.org/10.1007/978-3-662-28603-6_12

Chaussidon, M., & Jambon, A. (1994). Boron content and isotopic composition of oceanic basalts: Geochemical and cosmochemical implications. *Earth and Planetary Science Letters*, *121*(3–4), 277–291. https://doi.org/10.1016/0012-821X(94)90073-6

Chaussidon, M., & Marty, B. (1995). Primitive Boron Isotope Composition of the Mantle. *Science*, *269*(5222), 383–386. https://doi.org/10.1126/science.269.5222.383

Cheminee, J. L. (1970). Distribution de l'uranium, du thorium et du potassium dans les roches volcaniques de l'Afar septentrional (Ethiopie). *Bulletin Volcanologique*, *34*(1), 168–195. https://doi.org/10.1007/BF02597784

Chesner, C. A., & Luhr, J. F. (2010). A melt inclusion study of the Toba Tuffs, Sumatra, Indonesia. *Journal of Volcanology and Geothermal Research*, *197*(1–4), 259–278. https://doi.org/10.1016/j.jvolgeores.2010.06.001

Christie, D. M., Carmichael, I. S. E., & Langmuir, C. H. (1986). Oxidation states of mid-ocean ridge basalt glasses. *Earth and Planetary Science Letters*, *79*(3–4), 397–411. https://doi.org/10.1016/0012-821X(86)90195-0

Chu, Z.-Y., Wu, F.-Y., Walker, R. J., Rudnick, R. L., Pitcher, L., Puchtel, I. S., Yang, Y.-H., & Wilde, S. A. (2009). Temporal Evolution of the Lithospheric Mantle beneath the Eastern North China Craton. *Journal of Petrology*, *50*(10), 1857–1898. https://doi.org/10.1093/petrology/egp055

Cohen, R. S., Evensen, N. M., Hamilton, P. J., & O'Nions, R. K. (1980). U–Pb, Sm–Nd and Rb–Sr systematics of mid-ocean ridge basalt glasses. *Nature*, *283*(5743), 149–153. https://doi.org/10.1038/283149a0

Cohen, R. S., & O'Nions, R. K. (1982). The Lead, Neodymium and Strontium Isotopic Structure of Ocean Ridge Basalts. *Journal of Petrology*, *23*(3), 299–324. https://doi.org/10.1093/petrology/23.3.299

Colin, A., Moreira, M., Gautheron, C., & Burnard, P. (2015). Constraints on the noble gas composition of the deep mantle by bubble-by-bubble analysis of a volcanic glass sample from Iceland. *Chemical Geology*, *417*, 173–183. https://doi.org/10.1016/j.chemgeo.2015.09.020

Condomines, M., Grönvold, K., Hooker, P. J., Muehlenbachs, K., O'Nions, R. K., Óskarsson, N., & Oxburgh, E. R. (1983). Helium, oxygen, strontium and neodymium isotopic relationships in Icelandic volcanics. *Earth and Planetary Science Letters*, *66*, 125–136. https://doi.org/10.1016/0012-821X(83)90131-0

Condomines, M., Morand, P., & Allègre, C. J. (1981). 230Th-238U radioactive disequilibria in tholeiites from the FAMOUS zone (Mid-Atlantic Ridge, 36°50′N): Th and Sr isotopic geochemistry. *Earth and Planetary Science Letters*, *55*(2), 247–256. https://doi.org/10.1016/0012-821X(81)90104-7

Corazzato, C., Francalanci, L., Menna, M., Petrone, C. M., Renzulli, A., Tibaldi, A., & Vezzoli, L. (2008). What controls sheet intrusion in volcanoes? Structure and petrology of the Stromboli sheet complex, Italy. *Journal of Volcanology and Geothermal Research*, *173*(1–2), 26–54. https://doi.org/10.1016/j.jvolgeores.2008.01.006

Costa, A. C. G., Hildenbrand, A., Marques, F. O., Sibrant, A. L. R., & Santos de Campos, A. (2015). Catastrophic flank collapses and slumping in Pico Island during the last 130 kyr (Pico-Faial ridge, Azores Triple Junction). *Journal of Volcanology and Geothermal Research*, *302*, 33–46. https://doi.org/10.1016/j.jvolgeores.2015.06.008

Cottrell, E., & Kelley, K. A. (2011). The oxidation state of Fe in MORB glasses and the oxygen fugacity of the upper mantle. *Earth and Planetary Science Letters*, *305*(3–4), 270–282. https://doi.org/10.1016/j.epsl.2011.03.014

Cottrell, E., & Kelley, K. A. (2013). Redox Heterogeneity in Mid-Ocean Ridge Basalts as a Function of Mantle Source. *Science*, *340*(6138), 1314–1317. https://doi.org/10.1126/science.1233299

Craig, H., & Lupton, J. E. (1976). Primordial neon, helium, and hydrogen in oceanic basalts. *Earth and Planetary Science Letters*, *31*(3), 369–385. https://doi.org/10.1016/0012-821X(76)90118-7

Crovisier, J.-L., Honnorez, J., Fritz, B., & Petit, J.-C. (1992). Dissolution of subglacial volcanic glasses from Iceland: Laboratory study and modelling. *Applied Geochemistry*, *7*, 55–81. https://doi.org/10.1016/S0883-2927(09)80064-4

Czamanske, G. K., & Moore, J. G. (1977). Composition and phase chemistry of sulfide globules in basalt from the Mid-Atlantic Ridge rift valley near 37°N lat. *Geological Society of America Bulletin*, *88*(4), 587. https://doi.org/10.1130/0016-7606(1977)88<587:CAPCOS>2.0.CO;2

Danyushevsky, L. V., Falloon, T. J., Crawford, A. J., Tetroeva, S. A., Leslie, R. L., & Verbeeten, A. (2008). High-Mg adakites from Kadavu Island Group, Fiji, southwest Pacific: Evidence for the mantle origin of adakite parental melts. *Geology*, *36*(6), 499. https://doi.org/10.1130/G24349A.1

Daoud, M. A., Maury, R. C., Barrat, J.-A., Taylor, R. N., Le Gall, B., Guillou, H., Cotten, J., & Rolet, J. (2010). A LREE-depleted component in the Afar plume: Further evidence from Quaternary Djibouti basalts. *Lithos*, *114*(3–4), 327–336. https://doi.org/10.1016/j.lithos.2009.09.008

Daux, V., Crovisier, J. L., Hemond, C., & Petit, J. C. (1994). Geochemical evolution of basaltic rocks subjected to weathering: Fate of the major elements, rare earth elements, and thorium. *Geochimica et Cosmochimica Acta*, *58*(22), 4941–4954. https://doi.org/10.1016/0016-7037(94)90223-2

Daux, V., Crovisier, J. L., & Petit, J. C. (1990). Rare Earth Elements Behaviour During Alteration of Basaltic Glasses: Case of the Weathering of Icelandic Hyaloclastites. *MRS Proceedings*, *212*, 107. https://doi.org/10.1557/PROC-212-107

David, K., Schiano, P., & Allègre, C. J. (2000). Assessment of the Zr/Hf fractionation in oceanic basalts and continental materials during petrogenetic processes. *Earth and Planetary Science Letters*, *178*(3–4), 285–301. https://doi.org/10.1016/S0012-821X(00)00088-1

Debaille, V., Blichert-Toft, J., Agranier, A., Doucelance, R., Schiano, P., & Albarede, F. (2006). Geochemical component relationships in MORB from the Mid-Atlantic Ridge, 22–35°N. *Earth and Planetary Science Letters*, *241*(3–4), 844–862. https://doi.org/10.1016/j.epsl.2005.11.004

Delaney, J. R., Muenow, D. W., & Graham, D. G. (1978). Abundance and distribution of water, carbon and sulfur in the glassy rims of submarine pillow basalts. *Geochimica et Cosmochimica Acta*, *42*(6), 581–594. https://doi.org/10.1016/0016-7037(78)90003-0

Deniel, C., Vidal, P., Coulon, C., Vellutini, P.-J., & Piguet, P. (1994). Temporal evolution of mantle sources during continental rifting: The volcanism of Djibouti (Afar). *Journal of Geophysical Research: Solid Earth*, *99*(B2), 2853–2869. https://doi.org/10.1029/93JB02576

Déruelle, B., Dreibus, G., & Jambon, A. (1992). Iodine abundances in oceanic basalts: Implications for Earth dynamics. *Earth and Planetary Science Letters*, *108*(4), 217–227. https://doi.org/10.1016/0012-821X(92)90024-P

Des Marais, D. J., & Moore, J. G. (1984). Carbon and its isotopes in mid-oceanic basaltic glasses. *Earth and Planetary Science Letters*, *69*(1), 43–57. https://doi.org/10.1016/0012-821X(84)90073-6

Detrick, R., Honnorez, J., Bryan, W. B., Juteau, T., & et al. (Eds.). (1990). *Proceedings of the Ocean Drilling Program, 106/109 Scientific Results* (Vol. 106109). Ocean Drilling Program. https://doi.org/10.2973/odp.proc.sr.106109.1990

Devey, C. W., Albarede, F., Cheminée, J.-L., Michard, A., Mühe, R., & Stoffers, P. (1990). Active submarine volcanism on the society hotspot swell (west Pacific): A geochemical study. *Journal of Geophysical Research*, *95*(B4), 5049. https://doi.org/10.1029/JB095iB04p05049

Dixon, E. T., Honda, M., McDougall, I., Campbell, I. H., & Sigurdsson, I. (2000). Preservation of near-solar neon isotopic ratios in Icelandic basalts. *Earth and Planetary Science Letters*, *180*(3–4), 309–324. https://doi.org/10.1016/S0012-821X(00)00164-3

Dixon, J. E., Bindeman, I. N., Kingsley, R. H., Simons, K. K., Le Roux, P. J., Hajewski, T. R., Swart, P., Langmuir, C. H., Ryan, J. G., Walowski, K. J., Wada, I., & Wallace, P. J. (2017). Light Stable Isotopic Compositions of Enriched Mantle Sources: Resolving the Dehydration Paradox. *Geochemistry, Geophysics, Geosystems*, *18*(11), 3801–3839. https://doi.org/10.1002/2016GC006743

Dixon, J. E., Leist, L., Langmuir, C., & Schilling, J.-G. (2002). Recycled dehydrated lithosphere observed in plume-influenced mid-ocean-ridge basalt. *Nature*, *420*(6914), 385–389. https://doi.org/10.1038/nature01215

Dmitriev, L., Heirtzler, J., & et al. (1979). *Initial Reports of the Deep Sea Drilling Project, 46* (Vol. 46). U.S. Government Printing Office. https://doi.org/10.2973/dsdp.proc.46.1979

Don Hermes, O., & Schilling, J.-G. (1976). Olivine from Reykjanes ridge and Iceland tholeiites, and its significance to the two-mantle source model. *Earth and Planetary Science Letters*, *28*(3), 345–355. https://doi.org/10.1016/0012-821X(76)90196-5

Donnelly, K. E., Goldstein, S. L., Langmuir, C. H., & Spiegelman, M. (2004). Origin of enriched ocean ridge basalts and implications for mantle dynamics. *Earth and Planetary Science Letters*, *226*(3–4), 347–366. https://doi.org/10.1016/j.epsl.2004.07.019

Dosso, L., Bougault, H., & Joron, J.-L. (1993). Geochemical morphology of the North Mid-Atlantic Ridge, 10°–24°N: Trace element-isotope complementarity. *Earth and Planetary Science Letters*, *120*(3–4), 443–462. https://doi.org/10.1016/0012-821X(93)90256-9

Dosso, L., Bougault, H., Langmuir, C., Bollinger, C., Bonnier, O., & Etoubleau, J. (1999). The age and distribution of mantle heterogeneity along the Mid-Atlantic Ridge (31–41°N). *Earth and Planetary Science Letters*, *170*(3), 269–286. https://doi.org/10.1016/S0012-821X(99)00109-0

Dosso, L., Hanan, B. B., Bougault, H., Schilling, J.-G., & Joron, J.-L. (1991). SrNdPb geochemical morphology between 10° and 17°N on the Mid-Atlantic Ridge: A new MORB isotope signature. *Earth and Planetary Science Letters*, *106*(1–4), 29–43. https://doi.org/10.1016/0012-821X(91)90061-L

Draut, A. E., Clift, P. D., Amato, J. M., Blusztajn, J., & Schouten, H. (2009). Arc–continent collision and the formation of continental crust: A new geochemical and isotopic record from the Ordovician Tyrone Igneous Complex, Ireland. *Journal of the Geological Society*, *166*(3), 485–500. https://doi.org/10.1144/0016-76492008-102

Duncan, R. A., Hooper, P. R., Rehacek, J., Marsh, J. S., & Duncan, A. R. (1997). The timing and duration of the Karoo igneous event, southern Gondwana. *Journal of Geophysical Research: Solid Earth*, *102*(B8), 18127–18138. https://doi.org/10.1029/97JB00972

Dungan, M. A., & Rhodes, J. M. (1978). Residual glasses and melt inclusions in basalts from DSDP Legs 45 and 46: Evidence for magma mixing. *Contributions to Mineralogy and Petrology*, *67*(4), 417–431. https://doi.org/10.1007/BF00383301

Dymond, J., & Hogan, L. (1973). Noble gas abundance patterns in deep-sea basalts—Primordial gases from the mantle. *Earth and Planetary Science Letters*, *20*(1), 131–139. https://doi.org/10.1016/0012-821X(73)90150-7

Eason, D. E., Sinton, J. M., Grönvold, K., & Kurz, M. D. (2015). Effects of deglaciation on the petrology and eruptive history of the Western Volcanic Zone, Iceland. *Bulletin of Volcanology*, *77*(6), 47. https://doi.org/10.1007/s00445-015-0916-0

Eiler, J. M., Farley, K. A., Valley, J. W., Hofmann, A. W., & Stolper, E. M. (1996). Oxygen isotope constraints on the sources of Hawaiian volcanism. *Earth and Planetary Science Letters*, *144*(3–4), 453–467. https://doi.org/10.1016/S0012-821X(96)00170-7

Eiler, J. M., Schiano, P., Kitchen, N., & Stolper, E. M. (2000). Oxygen-isotope evidence for recycled crust in the sources of mid-ocean-ridge basalts. *Nature*, *403*(6769), 530–534. https://doi.org/10.1038/35000553

Eissen, J.-P., Juteau, T., Joron, J.-L., Dupre, B., Humler, E., & Al'Mukhamedov, A. (1989). Petrology and Geochemistry of Basalts from the Red Sea Axial Rift at 18 North. *Journal of Petrology*, *30*(4), 791–839. https://doi.org/10.1093/petrology/30.4.791

Elkins, L. J., Hamelin, C., Blichert-Toft, J., Scott, S. R., Sims, K. W. W., Yeo, I. A., Devey, C. W., & Pedersen, R. B. (2016). North Atlantic hotspot-ridge interaction near Jan Mayen Island. *Geochemical Perspectives Letters*, *2*(1), 55–67. https://doi.org/10.7185/geochemlet.1606

Elkins, L. J., Sims, K. W. W., Prytulak, J., Elliott, T., Mattielli, N., Blichert-Toft, J., Blusztajn, J., Dunbar, N., Devey, C., Mertz, D. F., Schilling, J.-G., & Murrell, M. (2011). Understanding melt generation beneath the slow-spreading Kolbeinsey Ridge using 238U, 230Th, and 231Pa excesses. *Geochimica et Cosmochimica Acta*, *75*(21), 6300–6329. https://doi.org/10.1016/j.gca.2011.08.020

Ferguson, D. J., Barnie, T. D., Pyle, D. M., Oppenheimer, C., Yirgu, G., Lewi, E., Kidane, T., Carn, S., & Hamling, I. (2010). Recent rift-related volcanism in Afar, Ethiopia. *Earth and Planetary Science Letters*, *292*(3–4), 409–418. https://doi.org/10.1016/j.epsl.2010.02.010

Field, L., Barnie, T., Blundy, J., Brooker, R. A., Keir, D., Lewi, E., & Saunders, K. (2012). Integrated field, satellite and petrological observations of the November 2010 eruption of Erta Ale. *Bulletin of Volcanology*, *74*(10), 2251–2271. https://doi.org/10.1007/s00445-012-0660-7

Field, L., Blundy, J., Calvert, A., & Yirgu, G. (2013). Magmatic history of Dabbahu, a composite volcano in the Afar Rift, Ethiopia. *Geological Society of America Bulletin*, *125*(1–2), 128–147. https://doi.org/10.1130/B30560.1

Fine, G., & Stolper, E. (1986). Dissolved carbon dioxide in basaltic glasses: Concentrations and speciation. *Earth and Planetary Science Letters*, *76*(3–4), 263–278. https://doi.org/10.1016/0012-821X(86)90078-6

Fino, M., Volpe, L., & Lirer, L. (1973). Volcanology and petrology of the Assab Range (Ethiopia). *Bulletin Volcanologique*, *37*(1), 95–110. https://doi.org/10.1007/BF02596882

Fino, M., Volpe, L., & Lirer, L. (1978). Geology and volcanology of the Edd-Bahar Assoli area (Ethiopia). *Bulletin Volcanologique*, *41*(1), 32–42. https://doi.org/10.1007/BF02597681

Flude, S., McGarvie, D. W., Burgess, R., & Tindle, A. G. (2010). Rhyolites at Kerlingarfjöll, Iceland: The evolution and lifespan of silicic central volcanoes. *Bulletin of Volcanology*, *72*(5), 523–538. https://doi.org/10.1007/s00445-010-0344-0

Frey, F. A., Dickey, J. S., Thompson, G., & Bryan, W. B. (1977). Eastern Indian Ocean DSDP sites: Correlations between petrography, geochemistry and tectonic setting. In J. R. Heirtzler, H. M. Bolli, T. A. Davies, J. B. Saunders, & J. G. Sclater (Eds.), *Indian Ocean Geology and Biostratigraphy: Studies Following Deep-Sea Drilling Legs* (pp. 189–257). American Geophysical Union. https://doi.org/10.1029/SP009p0189

Frey, F. A., Walker, N., Stakes, D., Hart, S. R., & Nielsen, R. (1993). Geochemical characteristics of basaltic glasses from theamar and famous axial valleys, Mid-Atlantic Ridge (36°–37°N): Petrogenetic implications. *Earth and Planetary Science Letters*, *115*(1–4), 117–136. https://doi.org/10.1016/0012-821X(93)90217-W

Fryer, P., Pearce, J. A., Stokking, L. B., & et al. (Eds.). (1992). *Proceedings of the Ocean Drilling Program, 125 Scientific Results* (Vol. 125). Ocean Drilling Program. https://doi.org/10.2973/odp.proc.sr.125.1992

Füri, E., Hilton, D. R., Halldórsson, S. A., Barry, P. H., Hahm, D., Fischer, T. P., & Grönvold, K. (2010). Apparent decoupling of the He and Ne isotope systematics of the Icelandic mantle: The role of He depletion, melt mixing, degassing fractionation and air interaction. *Geochimica et Cosmochimica Acta*, *74*(11), 3307–3332. https://doi.org/10.1016/j.gca.2010.03.023

Furman, T., Bryce, J., Rooney, T., Hanan, B., Yirgu, G., & Ayalew, D. (2006). Heads and tails: 30 million years of the Afar plume. *Geological Society, London, Special Publications*, *259*(1), 95–119. https://doi.org/10.1144/GSL.SP.2006.259.01.09

Gale, A., Escrig, S., Gier, E. J., Langmuir, C. H., & Goldstein, S. L. (2011). Enriched basalts at segment centers: The Lucky Strike (37°17′N) and Menez Gwen (37°50′N) segments of the Mid-Atlantic Ridge: ENRICHED BASALTS AT SEGMENT CENTERS. *Geochemistry, Geophysics, Geosystems*, *12*(6), n/a-n/a. https://doi.org/10.1029/2010GC003446

Gale, A., Laubier, M., Escrig, S., & Langmuir, C. H. (2013). Constraints on melting processes and plume-ridge interaction from comprehensive study of the FAMOUS and North Famous segments, Mid-Atlantic Ridge. *Earth and Planetary Science Letters*, *365*, 209–220. https://doi.org/10.1016/j.epsl.2013.01.022

Gamble, J. A., Smith, I. E. M., McCulloch, M. T., Graham, I. J., & Kokelaar, B. P. (1993). The geochemistry and petrogenesis of basalts from the Taupo Volcanic Zone and Kermadec Island Arc, S.W. Pacific. *Journal of Volcanology and Geothermal Research*, *54*(3–4), 265–290. https://doi.org/10.1016/0377-0273(93)90067-2

Gannoun, A., Burton, K. W., Parkinson, I. J., Alard, O., Schiano, P., & Thomas, L. E. (2007). The scale and origin of the osmium isotope variations in mid-ocean ridge basalts. *Earth and Planetary Science Letters*, *259*(3–4), 541–556. https://doi.org/10.1016/j.epsl.2007.05.014

Gannoun, A., Burton, K. W., Thomas, L. E., Parkinson, I. J., van Calsteren, P., & Schiano, P. (2004). Osmium Isotope Heterogeneity in the Constituent Phases of Mid-Ocean Ridge Basalts. *Science*, *303*(5654), 70–72. https://doi.org/10.1126/science.1090266

Gass, I. G., Mallick, D. I. J., & Cox, K. G. (1973). Volcanic islands of the Red Sea. *Journal of the Geological Society*, *129*(3), 275–309. https://doi.org/10.1144/gsjgs.129.3.0275

Gibson, S. A., Thompson, R. N., Leonardos, O. H., Dickin, A. P., & Mitchell, J. G. (1995). The Late Cretaceous Impact of the Trindade Mantle Plume: Evidence from Large-volume, Mafic, Potassic Magmatism in SE Brazil. *Journal of Petrology*, *36*(1), 189–229. https://doi.org/10.1093/petrology/36.1.189

Giordano, F., D'Antonio, M., Civetta, L., Tonarini, S., Orsi, G., Ayalew, D., Yirgu, G., Dell'Erba, F., Di Vito, M. A., & Isaia, R. (2014). Genesis and evolution of mafic and felsic magmas at Quaternary volcanoes within the Main Ethiopian Rift: Insights from Gedemsa and Fanta 'Ale complexes. *Lithos*, *188*, 130–144. https://doi.org/10.1016/j.lithos.2013.08.008

Gurenko, A. A., & Chaussidon, M. (1995). Enriched and depleted primitive melts included in olivine from Icelandic tholeiites: Origin by continuous melting of a single mantle column. *Geochimica et Cosmochimica Acta*, *59*(14), 2905–2917. https://doi.org/10.1016/0016-7037(95)00184-0

Gurenko, A. A., & Chaussidon, M. (1997). Boron concentrations and isotopic composition of the Icelandic mantle: Evidence from glass inclusions in olivine. *Chemical Geology*, *135*(1–2), 21–34. https://doi.org/10.1016/S0009-2541(96)00102-7

Gurenko, A. A., & Chaussidon, M. (2002). Oxygen isotope variations in primitive tholeiites of Iceland: Evidence from a SIMS study of glass inclusions, olivine phenocrysts and pillow rim glasses. *Earth and Planetary Science Letters*, *205*(1–2), 63–79. https://doi.org/10.1016/S0012-821X(02)01005-1

Gurenko, A. A., & Sobolev, A. V. (2006). Crust–primitive magma interaction beneath neovolcanic rift zone of Iceland recorded in gabbro xenoliths from Midfell, SW Iceland. *Contributions to Mineralogy and Petrology*, *151*(5), 495–520. https://doi.org/10.1007/s00410-006-0079-2

Gysi, A. P., Jagoutz, O., Schmidt, M. W., & Targuisti, K. (2011). Petrogenesis of Pyroxenites and Melt Infiltrations in the Ultramafic Complex of Beni Bousera, Northern Morocco. *Journal of Petrology*, *52*(9), 1679–1735. https://doi.org/10.1093/petrology/egr026

Haase, K. M., Beier, C., Fretzdorff, S., Smellie, J. L., & Garbe-Schönberg, D. (2012). Magmatic evolution of the South Shetland Islands, Antarctica, and implications for continental crust formation. *Contributions to Mineralogy and Petrology*, *163*(6), 1103–1119. https://doi.org/10.1007/s00410-012-0719-7

Haase, K. M., Devey, C. W., & Wieneke, M. (2003). Magmatic processes and mantle heterogeneity beneath the slow-spreading northern Kolbeinsey Ridge segment, North Atlantic. *Contributions to Mineralogy and Petrology*, *144*(4), 428–448. https://doi.org/10.1007/s00410-002-0408-z

Haase, K. M., Mühe, R., & Stoffers, P. (2000). Magmatism during extension of the lithosphere: Geochemical constraints from lavas of the Shaban Deep, northern Red Sea. *Chemical Geology*, *166*(3–4), 225–239. https://doi.org/10.1016/S0009-2541(99)00221-1

Hagos, M., Koeberl, C., & van Wyk de Vries, B. (2016). The Quaternary volcanic rocks of the northern Afar Depression (northern Ethiopia): Perspectives on petrology, geochemistry, and tectonics. *Journal of African Earth Sciences*, *117*, 29–47. https://doi.org/10.1016/j.jafrearsci.2015.11.022

Hall, C. M., Walter, R. C., Westgate, J. A., & York, D. (1984). Geochronology, stratigraphy and geochemistry of Cindery Tuff in Pliocene hominid-bearing sediments of the Middle Awash, Ethiopia. *Nature*, *308*(5954), 26–31. https://doi.org/10.1038/308026a0

Halldórsson, S. A., Barnes, J. D., Stefánsson, A., Hilton, D. R., Hauri, E. H., & Marshall, E. W. (2016). Subducted lithosphere controls halogen enrichments in the Iceland mantle plume source. *Geology*, *44*(8), 679–682. https://doi.org/10.1130/G37924.1

Halldórsson, S. A., Hilton, D. R., Barry, P. H., Füri, E., & Grönvold, K. (2016). Recycling of crustal material by the Iceland mantle plume: New evidence from nitrogen elemental and isotope systematics of subglacial basalts. *Geochimica et Cosmochimica Acta*, *176*, 206–226. https://doi.org/10.1016/j.gca.2015.12.021

Halogens in the mantle beneath the North Atlantic. (1980). *Philosophical Transactions of the Royal Society of London. Series A, Mathematical and Physical Sciences*, *297*(1431), 147–178. https://doi.org/10.1098/rsta.1980.0208

Hamelin, B., & Allègre, C. J. (1985). Large-scale regional units in the depleted upper mantle revealed by an isotope study of the South-West Indian Ridge. *Nature*, *315*(6016), 196–199. https://doi.org/10.1038/315196a0

Hamelin, B., Dupré, B., & Allègre, C. J. (1984). Lead-strontium isotopic variations along the East Pacific Rise and the Mid-Atlantic Ridge: A comparative study. *Earth and Planetary Science Letters*, *67*(3), 340–350. https://doi.org/10.1016/0012-821X(84)90173-0

Hanan, B. B., Blichert-Toft, J., Kingsley, R., & Schilling, J.-G. (2000). Depleted Iceland mantle plume geochemical signature: Artifact of multicomponent mixing?: ICELAND PLUME GEOCHEMICAL SIGNATURE. *Geochemistry, Geophysics, Geosystems*, *1*(4), n/a-n/a. https://doi.org/10.1029/1999GC000009

Hanyu, T., Tatsumi, Y., Senda, R., Miyazaki, T., Chang, Q., Hirahara, Y., Takahashi, T., Kawabata, H., Suzuki, K., Kimura, J.-I., & Nakai, S. (2011). Geochemical characteristics and origin of the HIMU reservoir: A possible mantle plume source in the lower mantle: ORIGIN OF THE HIMU RESERVOIR. *Geochemistry, Geophysics, Geosystems*, *12*(2), n/a-n/a. https://doi.org/10.1029/2010GC003252

Hart, R., Dymond, J., Hogan, L., & Schilling, J. G. (1983). Mantle plume noble gas component in glassy basalts from Reykjanes Ridge. *Nature*, *305*(5933), 403–407. https://doi.org/10.1038/305403a0

Hart, S. R., & Ravizza, G. E. (2013). Os Partitioning Between Phases in Lherzolite and Basalt. In A. Basu & S. Hart (Eds.), *Geophysical Monograph Series* (pp. 123–134). American Geophysical Union. https://doi.org/10.1029/GM095p0123

Hekinian, R., Moore, J. G., & Bryan, W. B. (1976). Volcanic rocks and processes of the Mid-Atlantic Ridge rift valley near 36 � 49? N. *Contributions to Mineralogy and Petrology*, *58*(1), 83–110. https://doi.org/10.1007/BF00384746

Hekinian, R., Pineau, F., Shilobreeva, S., Bideau, D., Gracia, E., & Javoy, M. (2000). Deep sea explosive activity on the Mid-Atlantic Ridge near 34°50′N: Magma composition, vesicularity and volatile content. *Journal of Volcanology and Geothermal Research*, *98*(1–4), 49–77. https://doi.org/10.1016/S0377-0273(99)00190-0

Helgason, J. (1989). The Fjallgardar volcanic ridge in NE Iceland: An aborted early stage plate boundary or a volcanically dormant zone? *Geological Society, London, Special Publications*, *42*(1), 201–213. https://doi.org/10.1144/GSL.SP.1989.042.01.13

Hémond, C., Hofmann, A. W., Vlastélic, I., & Nauret, F. (2006). Origin of MORB enrichment and relative trace element compatibilities along the Mid-Atlantic Ridge between 10° and 24°N: ORIGIN OF MORB ENRICHMENT. *Geochemistry, Geophysics, Geosystems*, *7*(12), n/a-n/a. https://doi.org/10.1029/2006GC001317

Hertogen, J., Janssens, M.-J., & Palme, H. (1980). Trace elements in ocean ridge basalt glasses: Implications for fractionations during mantle evolution and petrogenesis. *Geochimica et Cosmochimica Acta*, *44*(12), 2125–2143. https://doi.org/10.1016/0016-7037(80)90209-4

Hildenbrand, A., Madureira, P., Marques, F. O., Cruz, I., Henry, B., & Silva, P. (2008). Multi-stage evolution of a sub-aerial volcanic ridge over the last 1.3 Myr: S. Jorge Island, Azores Triple Junction. *Earth and Planetary Science Letters*, *273*(3–4), 289–298. https://doi.org/10.1016/j.epsl.2008.06.041

Hildenbrand, A., Marques, F. O., Costa, A. C. G., Sibrant, A. L. R., Silva, P. F., Henry, B., Miranda, J. M., & Madureira, P. (2012). Reconstructing the architectural evolution of volcanic islands from combined K/Ar, morphologic, tectonic, and magnetic data: The Faial Island example (Azores). *Journal of Volcanology and Geothermal Research*, *241–242*, 39–48. https://doi.org/10.1016/j.jvolgeores.2012.06.019

Hildenbrand, A., Weis, D., Madureira, P., & Marques, F. O. (2014). Recent plate re-organization at the Azores Triple Junction: Evidence from combined geochemical and geochronological data on Faial, S. Jorge and Terceira volcanic islands. *Lithos*, *210–211*, 27–39. https://doi.org/10.1016/j.lithos.2014.09.009

Hilton, D. R., Thirlwall, M. F., Taylor, R. N., Murton, B. J., & Nichols, A. (2000). Controls on magmatic degassing along the Reykjanes Ridge with implications for the helium paradox. *Earth and Planetary Science Letters*, *183*(1–2), 43–50. https://doi.org/10.1016/S0012-821X(00)00253-3

Hiyagon, H., Ozima, M., Marty, B., Zashu, S., & Sakai, H. (1992). Noble gases in submarine glasses from mid-oceanic ridges and Loihi seamount: Constraints on the early history of the Earth. *Geochimica et Cosmochimica Acta*, *56*(3), 1301–1316. https://doi.org/10.1016/0016-7037(92)90063-O

Hofmann, A. W., Jochum, K. P., Seufert, M., & White, W. M. (1986). Nb and Pb in oceanic basalts: New constraints on mantle evolution. *Earth and Planetary Science Letters*, *79*(1–2), 33–45. https://doi.org/10.1016/0012-821X(86)90038-5

Ito, E., White, W. M., & Göpel, C. (1987). The O, Sr, Nd and Pb isotope geochemistry of MORB. *Chemical Geology*, *62*(3–4), 157–176. https://doi.org/10.1016/0009-2541(87)90083-0

Jambon, A., Déruelle, B., Dreibus, G., & Pineau, F. (1995). Chlorine and bromine abundance in MORB: The contrasting behaviour of the Mid-Atlantic Ridge and East Pacific Rise and implications for chlorine geodynamic cycle. *Chemical Geology*, *126*(2), 101–117. https://doi.org/10.1016/0009-2541(95)00112-4

Jambon, A., & Zimmermann, J. L. (1987). Major volatiles from a North Atlantic MORB glass and calibration to He: A size fraction analysis. *Chemical Geology*, *62*(3–4), 177–189. https://doi.org/10.1016/0009-2541(87)90084-2

Jambon, A., & Zimmermann, J. L. (1990). Water in oceanic basalts: Evidence for dehydration of recycled crust. *Earth and Planetary Science Letters*, *101*(2–4), 323–331. https://doi.org/10.1016/0012-821X(90)90163-R

Jancin, M., Young, K. D., Voight, B., Aronson, J. L., & Saemundsson, K. (1985). Stratigraphy and K/AR ages across the west flank of the northeast Iceland Axial Rift Zone, in relation to the 7 MA volcano-tectonic reorganization of Iceland. *Journal of Geophysical Research*, *90*(B12), 9961. https://doi.org/10.1029/JB090iB12p09961

Jaques, A. L., & Chappell, B. W. (1980). Petrology and trace element geochemistry of the Papuan Ultramafic Belt. *Contributions to Mineralogy and Petrology*, *75*(1), 55–70. https://doi.org/10.1007/BF00371889

Jeffery, A. J., Gertisser, R., O'Driscoll, B., Pacheco, J. M., Whitley, S., Pimentel, A., & Self, S. (2016). Temporal evolution of a post-caldera, mildly peralkaline magmatic system: Furnas volcano, São Miguel, Azores. *Contributions to Mineralogy and Petrology*, *171*(5), 42. https://doi.org/10.1007/s00410-016-1235-y

Jeffries, T. E., Perkins, W. T., & Pearce, N. J. G. (1995). Measurements of trace elements in basalts and their phenocrysts by laser probe microanalysis inductively coupled plasma mass spectrometry (LPMA-ICP-MS). *Chemical Geology*, *121*(1–4), 131–144. https://doi.org/10.1016/0009-2541(94)00121-N

Jenner, F. E., & O'Neill, H. St. C. (2012). Analysis of 60 elements in 616 ocean floor basaltic glasses: TECHNICAL BRIEF. *Geochemistry, Geophysics, Geosystems*, *13*(2), n/a-n/a. https://doi.org/10.1029/2011GC004009

Jenner, F. E., O'Neill, H. ST. C., Arculus, R. J., & Mavrogenes, J. A. (2010). The Magnetite Crisis in the Evolution of Arc-related Magmas and the Initial Concentration of Au, Ag and Cu. *Journal of Petrology*, *51*(12), 2445–2464. https://doi.org/10.1093/petrology/egq063

Jochum, K. P., & Hofmann, A. W. (1997). Constraints on earth evolution from antimony in mantle-derived rocks. *Chemical Geology*, *139*(1–4), 39–49. https://doi.org/10.1016/S0009-2541(97)00032-6

Jochum, K. P., Hofmann, A. W., Ito, E., Seufert, H. M., & White, W. M. (1983). K, U and Th in mid-ocean ridge basalt glasses and heat production, K/U and K/Rb in the mantle. *Nature*, *306*(5942), 431–436. https://doi.org/10.1038/306431a0

Kamenetsky, V. (1996). Methodology for the study of melt inclusions in Cr-spinel, and implications for parental melts of MORB from FAMOUS area. *Earth and Planetary Science Letters*, *142*(3–4), 479–486. https://doi.org/10.1016/0012-821X(96)00117-3

Kamenetsky, V., & Crawford, A. J. (1998). Melt–peridotite reaction recorded in the chemistry of spinel and melt inclusions in basalt from 43°N, Mid-Atlantic Ridge. *Earth and Planetary Science Letters*, *164*(1–2), 345–352. https://doi.org/10.1016/S0012-821X(98)00226-X

Kamenetsky, V. S., Eggins, S. M., Crawford, A. J., Green, D. H., Gasparon, M., & Falloon, T. J. (1998). Calcic melt inclusions in primitive olivine at 43°N MAR: Evidence for melt–rock reaction/melting involving clinopyroxene-rich lithologies during MORB generation. *Earth and Planetary Science Letters*, *160*(1–2), 115–132. https://doi.org/10.1016/S0012-821X(98)00090-9

Kelley, K. A., Kingsley, R., & Schilling, J.-G. (2013). Composition of plume-influenced mid-ocean ridge lavas and glasses from the Mid-Atlantic Ridge, East Pacific Rise, Galápagos Spreading Center, and

Gulf of Aden: PLUME-INFLUENCED MORB. *Geochemistry, Geophysics, Geosystems*, *14*(1), 223–242. https://doi.org/10.1002/ggge.20049

Kendrick, M. A., Hémond, C., Kamenetsky, V. S., Danyushevsky, L., Devey, C. W., Rodemann, T., Jackson, M. G., & Perfit, M. R. (2017). Seawater cycled throughout Earth's mantle in partially serpentinized lithosphere. *Nature Geoscience*, *10*(3), 222–228. https://doi.org/10.1038/ngeo2902

Kent, R. W., & Fitton, J. G. (2000). Mantle Sources and Melting Dynamics in the British Palaeogene Igneous Province. *Journal of Petrology*, *41*(7), 1023–1040. https://doi.org/10.1093/petrology/41.7.1023

Khalaf, E. E. D. A. H. (2010). Stratigraphy, facies architecture, and palaeoenvironment of Neoproterozoic volcanics and volcaniclastic deposits in Fatira area, Central Eastern Desert, Egypt. *Journal of African Earth Sciences*, *58*(3), 405–426. https://doi.org/10.1016/j.jafrearsci.2010.04.005

Kingsley, R. H., & Schilling, J.-G. (1995). Carbon in Mid-Atlantic Ridge basalt glasses from 28°N to 63°N: Evidence for a carbon-enriched Azores mantle plume. *Earth and Planetary Science Letters*, *129*(1–4), 31–53. https://doi.org/10.1016/0012-821X(94)00241-P

Kobussen, A. F., Griffin, W. L., O'Reilly, S. Y., & Shee, S. R. (2008). Ghosts of lithospheres past: Imaging an evolving lithospheric mantle in southern Africa. *Geology*, *36*(7), 515. https://doi.org/10.1130/G24868A.1

Kurz, M. D., Jenkins, W. J., Schilling, J. G., & Hart, S. R. (1982). Helium isotopic variations in the mantle beneath the central North Atlantic Ocean. *Earth and Planetary Science Letters*, *58*(1), 1–14. https://doi.org/10.1016/0012-821X(82)90099-1

Kurz, M. D., Meyer, P. S., & Sigurdsson, H. (1985). Helium isotopic systematics within the neovolcanic zones of Iceland. *Earth and Planetary Science Letters*, *74*(4), 291–305. https://doi.org/10.1016/S0012-821X(85)80001-7

Kyser, T. K., & O'Neil, J. R. (1984). Hydrogen isotope systematics of submarine basalts. *Geochimica et Cosmochimica Acta*, *48*(10), 2123–2133. https://doi.org/10.1016/0016-7037(84)90392-2

Kyser, T. K., & Rison, W. (1982). Systematics of rare gas isotopes in basic lavas and ultramafic xenoliths. *Journal of Geophysical Research: Solid Earth*, *87*(B7), 5611–5630. https://doi.org/10.1029/JB087iB07p05611

Labidi, J., Cartigny, P., Birck, J. L., Assayag, N., & Bourrand, J. J. (2012). Determination of multiple sulfur isotopes in glasses: A reappraisal of the MORB δ34S. *Chemical Geology*, *334*, 189–198. https://doi.org/10.1016/j.chemgeo.2012.10.028

Langmuir, C. H., Bender, J. F., Bence, A. E., Hanson, G. N., & Taylor, S. R. (1977). Petrogenesis of basalts from the FAMOUS area: Mid-Atlantic Ridge. *Earth and Planetary Science Letters*, *36*(1), 133–156. https://doi.org/10.1016/0012-821X(77)90194-7

Lucic, G., Berg, A.-S., & Stix, J. (2016). Water-rich and volatile-undersaturated magmas at Hekla volcano, Iceland: VOLATILES AT HEKLA VOLCANO, ICELAND. *Geochemistry, Geophysics, Geosystems*, *17*(8), 3111–3130. https://doi.org/10.1002/2016GC006336

Lukács, R., Harangi, S., Bachmann, O., Guillong, M., Danišík, M., Buret, Y., von Quadt, A., Dunkl, I., Fodor, L., Sliwinski, J., Soós, I., & Szepesi, J. (2015). Zircon geochronology and geochemistry to constrain the youngest eruption events and magma evolution of the Mid-Miocene ignimbrite flare-up in the Pannonian Basin, eastern central Europe. *Contributions to Mineralogy and Petrology*, *170*(5–6), 52. https://doi.org/10.1007/s00410-015-1206-8

Luyendyk, B. P., Cann, J. R., & et al. (1979). *Initial Reports of the Deep Sea Drilling Project, 49* (Vol. 49). U.S. Government Printing Office. https://doi.org/10.2973/dsdp.proc.49.1979

Machado, N., Ludden, J. N., Brooks, C., & Thompson, G. (1982). Fine-scale isotopic heterogeneity in the sub-Atlantic mantle. *Nature*, *295*(5846), 226–228. https://doi.org/10.1038/295226a0

Maclennan, J. (2008a). Lead isotope variability in olivine-hosted melt inclusions from Iceland. *Geochimica et Cosmochimica Acta*, *72*(16), 4159–4176. https://doi.org/10.1016/j.gca.2008.05.034

Maclennan, J. (2008b). Concurrent Mixing and Cooling of Melts under Iceland. *Journal of Petrology*, *49*(11), 1931–1953. https://doi.org/10.1093/petrology/egn052

Madureira, P., Moreira, M., Mata, J., Nunes, J. C., Gautheron, C., Lourenço, N., Carvalho, R., & de Abreu, M. P. (2014). Helium isotope systematics in the vicinity of the Azores triple junction: Constraints on the Azores geodynamics. *Chemical Geology*, *372*, 62–71. https://doi.org/10.1016/j.chemgeo.2014.02.015

Maeno, F., & Taniguchi, H. (2007). Spatiotemporal evolution of a marine caldera-forming eruption, generating a low-aspect ratio pyroclastic flow, 7.3 ka, Kikai caldera, Japan: Implication from near-vent eruptive deposits. *Journal of Volcanology and Geothermal Research*, *167*(1–4), 212–238. https://doi.org/10.1016/j.jvolgeores.2007.05.003

Marschall, H. R., Wanless, V. D., Shimizu, N., Pogge von Strandmann, P. A. E., Elliott, T., & Monteleone, B. D. (2017). The boron and lithium isotopic composition of mid-ocean ridge basalts and the mantle. *Geochimica et Cosmochimica Acta*, *207*, 102–138. https://doi.org/10.1016/j.gca.2017.03.028

Marty, B., & Humbert, F. (1997). Nitrogen and argon isotopes in oceanic basalts. *Earth and Planetary Science Letters*, *152*(1–4), 101–112. https://doi.org/10.1016/S0012-821X(97)00153-2

Marty, B., & Jambon, A. (1987). C3He in volatile fluxes from the solid Earth: Implications for carbon geodynamics. *Earth and Planetary Science Letters*, *83*(1–4), 16–26. https://doi.org/10.1016/0012-821X(87)90047-1

Marty, B., & Ozima, M. (1986). Noble gas distribution in oceanic basalt glasses. *Geochimica et Cosmochimica Acta*, *50*(6), 1093–1097. https://doi.org/10.1016/0016-7037(86)90390-X

Marty, B., & Tolstikhin, I. N. (1998). CO_2 fluxes from mid-ocean ridges, arcs and plumes. *Chemical Geology*, *145*(3–4), 233–248. https://doi.org/10.1016/S0009-2541(97)00145-9

Marty, B., Zashu, S., & Ozima, M. (1983). Two noble gas components in a Mid-Atlantic Ridge basalt. *Nature*, *302*(5905), 238–240. https://doi.org/10.1038/302238a0

Mathez, E. A. (1976). Sulfur solubility and magmatic sulfides in submarine basalt glass. *Journal of Geophysical Research*, *81*(23), 4269–4276. https://doi.org/10.1029/JB081i023p04269

Mattey, D. P., Carr, R. H., Wright, I. P., & Pillinger, C. T. (1984). Carbon isotopes in submarine basalts. *Earth and Planetary Science Letters*, *70*(2), 196–206. https://doi.org/10.1016/0012-821X(84)90005-0

McGarvie, D. W., Stevenson, J. A., Burgess, R., Tuffen, H., & Tindle, A. G. (2007). Volcano–ice interactions at Prestahnúkur, Iceland: Rhyolite eruption during the last interglacial–glacial transition. *Annals of Glaciology*, *45*, 38–47. https://doi.org/10.3189/172756407782282453

Melson, W. G., Rabinowitz, P. D., & et al. (1979). *Initial Reports of the Deep Sea Drilling Project, 45* (Vol. 45). U.S. Government Printing Office. https://doi.org/10.2973/dsdp.proc.45.1979

Mercer, C. N., Hofstra, A. H., Todorov, T. I., Roberge, J., Burgisser, A., Adams, D. T., & Cosca, M. (2015). Pre-Eruptive Conditions of the Hideaway Park Topaz Rhyolite: Insights into Metal Source and Evolution of Magma Parental to the Henderson Porphyry Molybdenum Deposit, Colorado. *Journal of Petrology*, *56*(4), 645–679. https://doi.org/10.1093/petrology/egv010

Mertz, D. F., Devey, C. W., Todt, W., Stoffers, P., & Hofmann, A. W. (1991). Sr-Nd-Pb isotope evidence against plume-asthenosphere mixing north of Iceland. *Earth and Planetary Science Letters*, *107*(2), 243–255. https://doi.org/10.1016/0012-821X(91)90074-R

Mertz, D. F., & Haase, K. M. (1997). The radiogenic isotope composition of the high-latitude North Atlantic mantle. *Geology*, *25*(5), 411. https://doi.org/10.1130/0091-7613(1997)025<0411:TRICOT>2.3.CO;2

Meurer, W. P., Sturm, M. A., Klein, E. M., & Karson, J. A. (2001). Basalt compositions from the Mid-Atlantic Ridge at the SMARK area (22°30′N to 22°50′N) – implications for parental liquid variability at isotopically homogeneous spreading centers. *Earth and Planetary Science Letters*, *186*(3–4), 451–469. https://doi.org/10.1016/S0012-821X(01)00260-6

Meyer, P. S., & Bryan, W. B. (1996). Petrology of basaltic glasses from the TAG Segment: Implications for a deep hydrothermal heat source. *Geophysical Research Letters*, *23*(23), 3435–3438. https://doi.org/10.1029/96GL01033

Meyer, P. S., Sigurdsson, H., & Schilling, J. (1985). Petrological and geochemical variations along Iceland's Neovolcanic Zones. *Journal of Geophysical Research*, *90*(B12), 10043. https://doi.org/10.1029/JB090iB12p10043

Michael, P. (1995). Regionally distinctive sources of depleted MORB: Evidence from trace elements and H_2O. *Earth and Planetary Science Letters*, *131*(3–4), 301–320. https://doi.org/10.1016/0012-821X(95)00023-6

Michael, P. J., & Cornell, W. C. (1998). Influence of spreading rate and magma supply on crystallization and assimilation beneath mid-ocean ridges: Evidence from chlorine and major element chemistry of mid-ocean ridge basalts. *Journal of Geophysical Research: Solid Earth*, *103*(B8), 18325–18356. https://doi.org/10.1029/98JB00791

Michael, P. J., & Graham, D. W. (2015). The behavior and concentration of CO_2 in the suboceanic mantle: Inferences from undegassed ocean ridge and ocean island basalts. *Lithos*, *236–237*, 338–351. https://doi.org/10.1016/j.lithos.2015.08.020

Michael, P. J., & Schilling, J.-G. (1989). Chlorine in mid-ocean ridge magmas: Evidence for assimilation of seawater-influenced components. *Geochimica et Cosmochimica Acta*, *53*(12), 3131–3143. https://doi.org/10.1016/0016-7037(89)90094-X

Miyashiro, A., Shido, F., & Ewing, M. (1969). Diversity and origin of abyssal tholeiite from the Mid-Atlantic Ridge near 24� and 30� North latitude. *Contributions to Mineralogy and Petrology*, *23*(1), 38–52. https://doi.org/10.1007/BF00371331

Moorbath, S., & Walker, G. P. L. (1965). Strontium Isotope Investigation of Igneous Rocks From Iceland. *Nature*, *207*(4999), 837–840. https://doi.org/10.1038/207837a0

Moreira, M., & Allègre, C.-J. (2002). Rare gas systematics on Mid Atlantic Ridge (37–40°N). *Earth and Planetary Science Letters*, *198*(3–4), 401–416. https://doi.org/10.1016/S0012-821X(02)00519-8

Moreira, M., Breddam, K., Curtice, J., & Kurz, M. D. (2001). Solar neon in the Icelandic mantle: New evidence for an undegassed lower mantle. *Earth and Planetary Science Letters*, *185*(1–2), 15–23. https://doi.org/10.1016/S0012-821X(00)00351-4

Moreira, M., Escartin, J., Gayer, E., Hamelin, C., Bezos, A., Guillon, F., & Cannat, M. (2011). Rare gas systematics on Lucky Strike basalts (37°N, North Atlantic): Evidence for efficient homogenization in a long-lived magma chamber system?: RARE GAS ON LUCKY STRIKE BASALTS. *Geophysical Research Letters*, *38*(8), n/a-n/a. https://doi.org/10.1029/2011GL046794

Mungall, J. E., & Martin, R. F. (1994). Severe leaching of trachytic glass without devitrification, Terceira, Azores. *Geochimica et Cosmochimica Acta*, *58*(1), 75–83. https://doi.org/10.1016/0016-7037(94)90447-2

Murton, B. J. (2002). Plume-Ridge Interaction: A Geochemical Perspective from the Reykjanes Ridge. *Journal of Petrology*, *43*(11), 1987–2012. https://doi.org/10.1093/petrology/43.11.1987

Neave, D. A., Maclennan, J., Thordarson, T., & Hartley, M. E. (2015). The evolution and storage of primitive melts in the Eastern Volcanic Zone of Iceland: The 10 ka Grímsvötn tephra series (i.e. the Saksunarvatn ash). *Contributions to Mineralogy and Petrology*, *170*(2), 21. https://doi.org/10.1007/s00410-015-1170-3

Nichols, A. R. L., Carroll, M. R., & Höskuldsson, Á. (2002). Is the Iceland hot spot also wet? Evidence from the water contents of undegassed submarine and subglacial pillow basalts. *Earth and Planetary Science Letters*, *202*(1), 77–87. https://doi.org/10.1016/S0012-821X(02)00758-6

Nichols, A. R. L., & Wysoczanski, R. J. (2007). Using micro-FTIR spectroscopy to measure volatile contents in small and unexposed inclusions hosted in olivine crystals. *Chemical Geology*, *242*(3–4), 371–384. https://doi.org/10.1016/j.chemgeo.2007.04.007

Nielsen, R. L., Ustunisik, G., Lange, A. E., Tepley, F. J., & Kent, A. J. R. (2020). Trace Element and Isotopic Characteristics of Plagioclase Megacrysts in Plagioclase Ultraphyric Basalts (PUB). *Geochemistry, Geophysics, Geosystems*, *21*(2). https://doi.org/10.1029/2019GC008638

Nielsen, S. G., Shimizu, N., Lee, C.-T. A., & Behn, M. D. (2014). Chalcophile behavior of thallium during MORB melting and implications for the sulfur content of the mantle. *Geochemistry, Geophysics, Geosystems*, *15*(12), 4905–4919. https://doi.org/10.1002/2014GC005536

Nishio, Y., Ishii, T., Gamo, T., & Sano, Y. (1999). Volatile element isotopic systematics of the Rodrigues Triple Junction Indian Ocean MORB: Implications for mantle heterogeneity. *Earth and Planetary Science Letters*, *170*(3), 241–253. https://doi.org/10.1016/S0012-821X(99)00113-2

Nishio, Y., Nakai, S., Ishii, T., & Sano, Y. (2007). Isotope systematics of Li, Sr, Nd, and volatiles in Indian Ocean MORBs of the Rodrigues Triple Junction: Constraints on the origin of the DUPAL anomaly. *Geochimica et Cosmochimica Acta*, *71*(3), 745–759. https://doi.org/10.1016/j.gca.2006.10.004

Nishio, Y., Sasaki, S., Gamo, T., Hiyagon, H., & Sano, Y. (1998). Carbon and helium isotope systematics of North Fiji Basin basalt glasses: Carbon geochemical cycle in the subduction zone. *Earth and Planetary Science Letters*, *154*(1–4), 127–138. https://doi.org/10.1016/S0012-821X(97)00187-8

Niu, Y., Bideau, D., Hékinian, R., & Batiza, R. (2001). Mantle compositional control on the extent of mantle melting, crust production, gravity anomaly, ridge morphology, and ridge segmentation: A case study at the Mid-Atlantic Ridge 33–35°N. *Earth and Planetary Science Letters*, *186*(3–4), 383–399. https://doi.org/10.1016/S0012-821X(01)00255-2

Nohara, M., Hirose, K., Eissen, J.-P., Urabe, T., & Joshima, M. (1994). The North Fiji Basin basalts and their magma sources: Part II. Sr-Nd isotopic and trace element constraints. *Marine Geology*, *116*(1–2), 179–195. https://doi.org/10.1016/0025-3227(94)90175-9

Ohba, T., Matsuoka, K., Kimura, Y., Ishikawa, H., & Fujimaki, H. (2009). Deep Crystallization Differentiation of Arc Tholeiite Basalt Magmas from Northern Honshu Arc, Japan. *Journal of Petrology*, *50*(6), 1025–1046. https://doi.org/10.1093/petrology/egp030

O'Reilly, W., Brown, K., Styles, P., & Bloxam, T. W. (1993). A detailed geochemical and rock magnetic study of dredged basalt from the Sheba Ridge, Gulf of Aden. *Marine Geophysical Researches*, *15*(2), 101–119. https://doi.org/10.1007/BF01204131

Ottonello, G., Piccardo, G. B., Joron, J. L., & Treuil, M. (1978). Evolution of the upper mantle under the Assab Region (Ethiopia): Suggestions from petrology and geochemistry of tectonitic ultramafic xenoliths and host basaltic lavas. *Geologische Rundschau*, *67*(2), 547–575. https://doi.org/10.1007/BF01802804

Peate, D. W., Baker, J. A., Jakobsson, S. P., Waight, T. E., Kent, A. J. R., Grassineau, N. V., & Skovgaard, A. C. (2009). Historic magmatism on the Reykjanes Peninsula, Iceland: A snap-shot of melt generation at a ridge segment. *Contributions to Mineralogy and Petrology*, *157*(3), 359–382. https://doi.org/10.1007/s00410-008-0339-4

Peate, D. W., Hawkesworth, C. J., van Calsteren, P. W., Taylor, R. N., & Murton, B. J. (2001). 238U–230Th constraints on mantle upwelling and plume–ridge interaction along the Reykjanes Ridge. *Earth and Planetary Science Letters*, *187*(3–4), 259–272. https://doi.org/10.1016/S0012-821X(01)00266-7

Perkins, M. E., & Nash, B. P. (2002). Explosive silicic volcanism of the Yellowstone hotspot: The ash fall tuff record. *Geological Society of America Bulletin*, *114*(3), 367–381. https://doi.org/10.1130/0016-7606(2002)114<0367:ESVOTY>2.0.CO;2

Pik, R., Deniel, C., Coulon, C., Yirgu, G., Hofmann, C., & Ayalew, D. (1998). The northwestern Ethiopian Plateau flood basalts: Classification and spatial distribution of magma types. *Journal of Volcanology and Geothermal Research*, *81*(1–2), 91–111. https://doi.org/10.1016/S0377-0273(97)00073-5

Pimentel, A., Zanon, V., de Groot, L. V., Hipólito, A., Di Chiara, A., & Self, S. (2016). Stress-induced comenditic trachyte effusion triggered by trachybasalt intrusion: Multidisciplinary study of the AD 1761 eruption at Terceira Island (Azores). *Bulletin of Volcanology*, *78*(3), 22. https://doi.org/10.1007/s00445-016-1015-6

Pineau, F., Shilobreeva, S., Hekinian, R., Bideau, D., & Javoy, M. (2004). Deep-sea explosive activity on the Mid-Atlantic Ridge near 34°50′N: A stable isotope (C, H, O) study. *Chemical Geology*, *211*(1–2), 159–175. https://doi.org/10.1016/j.chemgeo.2004.06.029

Poreda, R., & Brozolo, F. R. di. (1984). Neon isotope variations in Mid-Atlantic Ridge basalts. *Earth and Planetary Science Letters*, *69*(2), 277–289. https://doi.org/10.1016/0012-821X(84)90187-0

Poreda, R., Schilling, J.-G., & Craig, H. (1986). Helium and hydrogen isotopes in ocean-ridge basalts north and south of Iceland. *Earth and Planetary Science Letters*, *78*(1), 1–17. https://doi.org/10.1016/0012-821X(86)90168-8

Pracht, M., & Kinnaird, J. A. (1997). Carboniferous subvolcanic activity on the Beara Peninsula, SW Ireland. *Geological Journal*, *32*(4), 297–312. https://doi.org/10.1002/(SICI)1099-1034(199712)32:4<297::AID-GJ736>3.0.CO;2-X

Ragnarsdóttir, K. V., Walther, J. V., & Arnórsson, S. (1984). Description and interpretation of the composition of fluid and alteration mineralogy in the geothermal system, at Svartsengi, Iceland. *Geochimica et Cosmochimica Acta*, *48*(7), 1535–1553. https://doi.org/10.1016/0016-7037(84)90409-5

Raquin, A., & Moreira, M. (2009). Atmospheric 38Ar/36Ar in the mantle: Implications for the nature of the terrestrial parent bodies. *Earth and Planetary Science Letters*, *287*(3–4), 551–558. https://doi.org/10.1016/j.epsl.2009.09.003

Rea, D. K., Basov, La., Scholl, D. W., & Allan, J. F. (Eds.). (1995). *Proceedings of the Ocean Drilling Program, 145 Scientific Results* (Vol. 145). Ocean Drilling Program. https://doi.org/10.2973/odp.proc.sr.145.1995

Reekie, C. D. J., Jenner, F. E., Smythe, D. J., Hauri, E. H., Bullock, E. S., & Williams, H. M. (2019). Sulfide resorption during crustal ascent and degassing of oceanic plateau basalts. *Nature Communications*, *10*(1), 82. https://doi.org/10.1038/s41467-018-08001-3

Révillon, S. (1999). Petrogenesis of picrites from the Caribbean Plateau and the North Atlantic magmatic province. *Lithos*, *49*(1–4), 1–21. https://doi.org/10.1016/S0024-4937(99)00038-9

Reynolds, J. R., & Langmuir, C. H. (1997). Petrological systematics of the Mid-Atlantic Ridge south of Kane: Implications for ocean crust formation. *Journal of Geophysical Research: Solid Earth*, *102*(B7), 14915–14946. https://doi.org/10.1029/97JB00391

Ripley, E. M., & Al-Jassar, T. J. (1987). Sulfur and oxygen isotope studies of melt-country rock interaction, Babbitt Cu-Ni deposit, Duluth Complex, Minnesota. *Economic Geology*, *82*(1), 87–107. https://doi.org/10.2113/gsecongeo.82.1.87

Roeder, P., Gofton, E., & Thornber, C. (2006). Cotectic Proportions of Olivine and Spinel in Olivine-Tholeiitic Basalt and Evaluation of Pre-Eruptive Processes. *Journal of Petrology*, *47*(5), 883–900. https://doi.org/10.1093/petrology/egi099

Rogers, N. W. (1993). The isotope and trace element geochemistry of basalts from the volcanic islands of the southern Red Sea. *Geological Society, London, Special Publications*, *76*(1), 455–467. https://doi.org/10.1144/GSL.SP.1993.076.01.24

Rooney, T., Furman, T., Bastow, I., Ayalew, D., & Yirgu, G. (2007). Lithospheric modification during crustal extension in the Main Ethiopian Rift. *Journal of Geophysical Research*, *112*(B10), B10201. https://doi.org/10.1029/2006JB004916

Rooney, T. O., Hanan, B. B., Graham, D. W., Furman, T., Blichert-Toft, J., & Schilling, J.-G. (2012). Upper Mantle Pollution during Afar Plume–Continental Rift Interaction. *Journal of Petrology*, *53*(2), 365–389. https://doi.org/10.1093/petrology/egr065

Rowe, E. C., & Schilling, J.-G. (1979). Fluorine in Iceland and Reykjanes Ridge basalts. *Nature*, *279*(5708), 33–37. https://doi.org/10.1038/279033a0

Roy-Barman, M., & Allègre, C. J. (1994). Ratios of mid-ocean ridge basalts and abyssal peridotites. *Geochimica et Cosmochimica Acta*, *58*(22), 5043–5054. https://doi.org/10.1016/0016-7037(94)90230-5

Roy-Barman, M., Wasserburg, G. J., Papanastassiou, D. A., & Chaussidon, M. (1998). Osmium isotopic compositions and Re–Os concentrations in sulfide globules from basaltic glasses. *Earth and Planetary Science Letters*, *154*(1–4), 331–347. https://doi.org/10.1016/S0012-821X(97)00180-5

Ryan, J. G., & Langmuir, C. H. (1987). The systematics of lithium abundances in young volcanic rocks. *Geochimica et Cosmochimica Acta*, *51*(6), 1727–1741. https://doi.org/10.1016/0016-7037(87)90351-6

Ryan, J. G., & Langmuir, C. H. (1993). The systematics of boron abundances in young volcanic rocks. *Geochimica et Cosmochimica Acta*, *57*(7), 1489–1498. https://doi.org/10.1016/0016-7037(93)90008-K

Sakai, H., Marais, D. J. D., Ueda, A., & Moore, J. G. (1984). Concentrations and isotope ratios of carbon, nitrogen and sulfur in ocean-floor basalts. *Geochimica et Cosmochimica Acta*, *48*(12), 2433–2441. https://doi.org/10.1016/0016-7037(84)90295-3

Salters, V. J. M. (1996). The generation of mid-ocean ridge basalts from the Hf and Nd isotope perspective. *Earth and Planetary Science Letters*, *141*(1–4), 109–123. https://doi.org/10.1016/0012-821X(96)00070-2

Sarda, P., Staudacher, T., & Allegre, C. (1988). Neon isotopes in submarine basalts. *Earth and Planetary Science Letters*, *91*(1–2), 73–88. https://doi.org/10.1016/0012-821X(88)90152-5

Sarda, P., Staudacher, T., & Allègre, C. J. (1985). 40Ar36Ar in MORB glasses: Constraints on atmosphere and mantle evolution. *Earth and Planetary Science Letters*, *72*(4), 357–375. https://doi.org/10.1016/0012-821X(85)90058-5

Schiano, P., Birck, J.-L., & Allègre, C. J. (1997). Osmium-strontium-neodymium-lead isotopic covariations in mid-ocean ridge basalt glasses and the heterogeneity of the upper mantle. *Earth and Planetary Science Letters*, *150*(3–4), 363–379. https://doi.org/10.1016/S0012-821X(97)00098-8

Schiano, P., & Bourdon, B. (1999). On the preservation of mantle information in ultramafic nodules: Glass inclusions within minerals versus interstitial glasses. *Earth and Planetary Science Letters*, *169*(1–2), 173–188. https://doi.org/10.1016/S0012-821X(99)00074-6

Schiellerup, H. (1995). Generation and equilibration of olivine tholeiites in the northern rift zone of Iceland. A petrogenetic study of the Bláfjall table mountain. *Journal of Volcanology and Geothermal Research*, *65*(3–4), 161–179. https://doi.org/10.1016/0377-0273(94)00116-X

Schilling, J.-G. (1973). Iceland Mantle Plume: Geochemical Study of Reykjanes Ridge. *Nature*, *242*(5400), 565–571. https://doi.org/10.1038/242565a0

Schilling, J.-G., & Kingsley, R. (2017). *Platinum-group elements (PGE), Re, Ni, Cu, Ag and Cd variations along the Reykjanes Ridge and Iceland South-West Neovolcanic Rift Zone, from 50°N to 65°N: Implications on sulfide bearing PGE mantle source heterogeneities and partial melting effects*

(1.0) [Application/pdf,application/vnd.ms-excel]. Interdisciplinary Earth Data Alliance (IEDA). https://doi.org/10.1594/IEDA/100712

Schilling, J.-G., Kingsley, R., Fontignie, D., Poreda, R., & Xue, S. (1999). Dispersion of the Jan Mayen and Iceland mantle plumes in the Arctic: A He-Pb-Nd-Sr isotope tracer study of basalts from the Kolbeinsey, Mohns, and Knipovich Ridges. *Journal of Geophysical Research: Solid Earth*, *104*(B5), 10543–10569. https://doi.org/10.1029/1999JB900057

Schlanger, S. O., Jackson, E. D., & et al. (1976). *Initial Reports of the Deep Sea Drilling Project, 33* (Vol. 33). U.S. Government Printing Office. https://doi.org/10.2973/dsdp.proc.33.1976

Schneider, W., & Wachendorf, H. (1973). Vulkanismus und Graben-Bildung im Roten Meer. *Geologische Rundschau*, *62*(3), 754–773. https://doi.org/10.1007/BF01820959

Shibata, T., Thompson, G., & Frey, F. A. (1979). Tholeiitic and alkali basalts from the Mid-Atlantic Ridge at 43 ° N. *Contributions to Mineralogy and Petrology*, *70*(2), 127–141. https://doi.org/10.1007/BF00374441

Shido, F., Miyashiro, A., & Ewing, M. (1974). Compositional variation in pillow lavas from the Mid-Atlantic Ridge. *Marine Geology*, *16*(4), 177–190. https://doi.org/10.1016/0025-3227(74)90083-8

Shirey, S. B., Bender, J. F., & Langmuir, C. H. (1987). Three-component isotopic heterogeneity near the Oceanographer transform, Mid-Atlantic Ridge. *Nature*, *325*(6101), 217–223. https://doi.org/10.1038/325217a0

Shorttle, O., Moussallam, Y., Hartley, M. E., Maclennan, J., Edmonds, M., & Murton, B. J. (2015). Fe-XANES analyses of Reykjanes Ridge basalts: Implications for oceanic crust's role in the solid Earth oxygen cycle. *Earth and Planetary Science Letters*, *427*, 272–285. https://doi.org/10.1016/j.epsl.2015.07.017

Sigurdsson, H. (1981). First-order major element variation in basalt glasses from the Mid-Atlantic Ridge: 29°N to 73°N. *Journal of Geophysical Research: Solid Earth*, *86*(B10), 9483–9502. https://doi.org/10.1029/JB086iB10p09483

Smith, I. E. M., Blake, S., Wilson, C. J. N., & Houghton, B. F. (2008). Deep-seated fractionation during the rise of a small-volume basalt magma batch: Crater Hill, Auckland, New Zealand. *Contributions to Mineralogy and Petrology*, *155*(4), 511–527. https://doi.org/10.1007/s00410-007-0255-z

Smith, S. E., Casey, J. R., Bryan, W. B., Dmitriev, L., Silantyev, S., & Magakyan, R. (1998). Geochemistry of basalts from the Hayes Transform region of the Mid-Atlantic Ridge. *Journal of Geophysical Research: Solid Earth*, *103*(B3), 5305–5329. https://doi.org/10.1029/97JB03208

Snyder, D. C. (2004). The Role of Open-System Processes in the Development of Silicic Magma Chambers: A Chemical and Isotopic Investigation of the Fogo A Trachyte Deposit, Sao Miguel, Azores. *Journal of Petrology*, *45*(4), 723–738. https://doi.org/10.1093/petrology/egg104

Snyder, D. C., Widom, E., Pietruszka, A. J., Carlson, R. W., & Schmincke, H.-U. (2007). Time scales of formation of zoned magma chambers: U-series disequilibria in the Fogo A and 1563 A.D. trachyte deposits, São Miguel, Azores. *Chemical Geology*, *239*(1–2), 138–155. https://doi.org/10.1016/j.chemgeo.2007.01.002

Stakes, D. S., Shervais, J. W., & Hopson, C. A. (1984). The volcanic-tectonic cycle of the FAMOUS and AMAR Valleys, Mid-Atlantic Ridge (36°47′N): Evidence from basalt glass and phenocryst compositional variations for a steady state magma chamber beneath the valley midsections, AMAR 3. *Journal of Geophysical Research: Solid Earth*, *89*(B8), 6995–7028. https://doi.org/10.1029/JB089iB08p06995

Staudacher, Th., Sarda, Ph., Richardson, S. H., Allègre, C. J., Sagna, I., & Dmitriev, L. V. (1989). Noble gases in basalt glasses from a Mid-Atlantic Ridge topographic high at 14°N: Geodynamic consequences. *Earth and Planetary Science Letters*, *96*(1–2), 119–133. https://doi.org/10.1016/0012-821X(89)90127-1

Stolper, E., Sherman, S., Garcia, M., Baker, M., & Seaman, C. (2004). Glass in the submarine section of the HSDP2 drill core, Hilo, Hawaii: HSDP2 DRILL CORE, HAWAII. *Geochemistry, Geophysics, Geosystems*, *5*(7). https://doi.org/10.1029/2003GC000553

Sturm, M. E., Goldstein, S. J., Klein, E. M., Karson, J. A., & Murrell, M. T. (2000). Uranium-series age constraints on lavas from the axial valley of the Mid-Atlantic Ridge, MARK area. *Earth and Planetary Science Letters*, *181*(1–2), 61–70. https://doi.org/10.1016/S0012-821X(00)00177-1

Sun, W., Bennett, V. C., Eggins, S. M., Arculus, R. J., & Perfit, M. R. (2003). Rhenium systematics in submarine MORB and back-arc basin glasses: Laser ablation ICP-MS results. *Chemical Geology*, *196*(1–4), 259–281. https://doi.org/10.1016/S0009-2541(02)00416-3

Tang, M., McDonough, W. F., & Ash, R. D. (2017). Europium and strontium anomalies in the MORB source mantle. *Geochimica et Cosmochimica Acta*, *197*, 132–141. https://doi.org/10.1016/j.gca.2016.10.025

Teklay, M., Scherer, E. E., Mezger, K., & Danyushevsky, L. (2010). Geochemical characteristics and Sr–Nd–Hf isotope compositions of mantle xenoliths and host basalts from Assab, Eritrea: Implications for the composition and thermal structure of the lithosphere beneath the Afar Depression. *Contributions to Mineralogy and Petrology*, *159*(5), 731–751. https://doi.org/10.1007/s00410-009-0451-0

Thomson, A., & Maclennan, J. (2013). The Distribution of Olivine Compositions in Icelandic Basalts and Picrites. *Journal of Petrology*, *54*(4), 745–768. https://doi.org/10.1093/petrology/egs083

Thorarinsson, S. B., & Tegner, C. (2009). Magma chamber processes in central volcanic systems of Iceland: Constraints from layered gabbro of the Austurhorn intrusive complex. *Contributions to Mineralogy and Petrology*, *158*(2), 223–244. https://doi.org/10.1007/s00410-009-0379-4

Thordarson, T., Self, S., Óskarsson, N., & Hulsebosch, T. (1996). Sulfur, chlorine, and fluorine degassing and atmospheric loading by the 1783–1784 AD Laki (Skaftár Fires) eruption in Iceland. *Bulletin of Volcanology*, *58*(2–3), 205–225. https://doi.org/10.1007/s004450050136

Thorseth, I. H., Furnes, H., & Tumyr, O. (1991). A textural and chemical study of Icelandic palagonite of varied composition and its bearing on the mechanism of the glass-palagonite transformation. *Geochimica et Cosmochimica Acta*, *55*(3), 731–749. https://doi.org/10.1016/0016-7037(91)90337-5

Thy, P. (1983). Phase relations in transitional and alkali basaltic glasses from Iceland. *Contributions to Mineralogy and Petrology*, *82*(2–3), 232–251. https://doi.org/10.1007/BF01166618

Timm, C., Hoernle, K., Werner, R., Hauff, F., den Bogaard, P. van, White, J., Mortimer, N., & Garbe-Schönberg, D. (2010). Temporal and geochemical evolution of the Cenozoic intraplate volcanism of Zealandia. *Earth-Science Reviews*, *98*(1–2), 38–64. https://doi.org/10.1016/j.earscirev.2009.10.002

Tomlinson, E. L., Thordarson, T., Lane, C. S., Smith, V. C., Manning, C. J., Müller, W., & Menzies, M. A. (2012). Petrogenesis of the Sólheimar ignimbrite (Katla, Iceland): Implications for tephrostratigraphy. *Geochimica et Cosmochimica Acta*, *86*, 318–337. https://doi.org/10.1016/j.gca.2012.03.012

Trønnes, R. G. (1990). Basaltic melt evolution of the Hengill Volcanic System, SW Iceland, and evidence for clinopyroxene assimilation in primitive tholeiitic magmas. *Journal of Geophysical Research*, *95*(B10), 15893. https://doi.org/10.1029/JB095iB10p15893

Tuller-Ross, B., Marty, B., Chen, H., Kelley, K. A., Lee, H., & Wang, K. (2019). Potassium isotope systematics of oceanic basalts. *Geochimica et Cosmochimica Acta*, *259*, 144–154. https://doi.org/10.1016/j.gca.2019.06.001

Ulrich, M., Hémond, C., Nonnotte, P., & Jochum, K. P. (2012). OIB/seamount recycling as a possible process for E-MORB genesis: OIB/SEAMOUNT RECYCLING = E-MORB? *Geochemistry, Geophysics, Geosystems*, *13*(6), n/a-n/a. https://doi.org/10.1029/2012GC004078

Uto, K., Hoang, N., & Matsui, K. (2004). Cenozoic lithospheric extension induced magmatism in Southwest Japan. *Tectonophysics*, *393*(1–4), 281–299. https://doi.org/10.1016/j.tecto.2004.07.039

Vigier, N., Bourdon, B., Joron, J. L., & Allègre, C. J. (1999). U-decay series and trace element systematics in the 1978 eruption of Ardoukoba, Asal rift: Timescale of magma crystallization. *Earth and Planetary Science Letters*, *174*(1–2), 81–98. https://doi.org/10.1016/S0012-821X(99)00256-3

Volker, F., Altherr, R., Jochum, K.-P., & McCulloch, M. T. (1997). Quaternary volcanic activity of the southern Red Sea: New data and assessment of models on magma sources and Afar plume-lithosphere interaction. *Tectonophysics*, *278*(1–4), 15–29. https://doi.org/10.1016/S0040-1951(97)00092-9

Wallace, P., & Carmichael, I. S. E. (1992). Sulfur in basaltic magmas. *Geochimica et Cosmochimica Acta*, *56*(5), 1863–1874. https://doi.org/10.1016/0016-7037(92)90316-B

Walraven, F., Frick, C., & Lubala, R. T. (1992). Pb-isotope geochronology of the Schiel complex, Northern Transvaal, South Africa. *Journal of African Earth Sciences (and the Middle East)*, *15*(1), 103–110. https://doi.org/10.1016/0899-5362(92)90011-Z

Welke, H., Moorbath, S., Cumming, G. L., & Sigurdsson, H. (1968). Lead isotope studies on igneous rocks from Iceland. *Earth and Planetary Science Letters*, *4*(3), 221–231. https://doi.org/10.1016/0012-821X(68)90039-3

White, W. M. (1993). 238U/204Pb in MORB and open system evolution of the depleted mantle. *Earth and Planetary Science Letters*, *115*(1–4), 211–226. https://doi.org/10.1016/0012-821X(93)90223-V

Yalçın, H., Gündoğdu, M. N., Gourgaud, A., Vidal, P., & Uçurum, A. (1998). Geochemical characteristics of Yamadağı volcanics in central east Anatolia: An example from collision-zone volcanism. *Journal of Volcanology and Geothermal Research*, *85*(1–4), 303–326. https://doi.org/10.1016/S0377-0273(98)00061-4

Yang, A. Y., Zhao, T.-P., Qi, L., Yang, S.-H., & Zhou, M.-F. (2011). Chalcophile elemental constraints on sulfide-saturated fractionation of Cenozoic basalts and andesites in SE China. *Lithos*, *127*(1–2), 323–335. https://doi.org/10.1016/j.lithos.2011.08.016

Yang, S., Humayun, M., & Salters, V. J. M. (2018). Elemental Systematics in MORB Glasses From the Mid-Atlantic Ridge. *Geochemistry, Geophysics, Geosystems*, *19*(11), 4236–4259. https://doi.org/10.1029/2018GC007593

Yi, W., Halliday, A. N., Alt, J. C., Lee, D.-C., Rehkämper, M., Garcia, M. O., Langmuir, C. H., & Su, Y. (2000). Cadmium, indium, tin, tellurium, and sulfur in oceanic basalts: Implications for chalcophile element fractionation in the Earth. *Journal of Geophysical Research: Solid Earth*, *105*(B8), 18927–18948. https://doi.org/10.1029/2000JB900152

Zanon, V., & Pimentel, A. (2015). Spatio-temporal constraints on magma storage and ascent conditions in a transtensional tectonic setting: The case of the Terceira Island (Azores). *American Mineralogist*, *100*(4), 795–805. https://doi.org/10.2138/am-2015-4936

Appendix 2: Additional Background and Geochemical Data for Chapter 4

A2.1: Grain Size from Thin Section

To constrain grain size, we characterize the 3D shapes and crystal size distribution from thin section images (e.g., Antonelli et al., 2019, Monteiro et al., 2021) we apply a scale to three high resolution thin section images (Figures A2.8-A2.10) of samples in the field area. The thin section image was converted to an 8-bit grayscale image in Fiji (Schindelin et al., 2012). The contrast was increased, and brightness decreased to isolate the brightest grains of quartz and feldspar. The Weka segmentation plugin for ImageJ (Arganda-Carreras et al., 2017) was used to segment the image into individual grains. Lastly, we converted the segmented image into a binary file and used the Analyze Selection tool in ImageJ to quantify an elliptical fit to each grain.

To accurately assess the grain size distribution, we correct the grain size measurements from the 2D thin section images using a combination of ShapeCalc (Mangler et al., 2022) and CSDCorrections (Higgins, 2000). ShapeCalc takes the size of the major and minor ellipse axes from the selection analysis in ImageJ as input and estimates the 3D crystal shape. The 2D data along with the crystal shape from ShapeCalc are then input into CSDCorrections to correct to the 3D grain size distribution. With this method, we find the median grain size to be between 0.33-0.57 mm among the three thin sections (Figure A2.8-A2.10).

A2.2: Size and Spacing of Melt Patches

Figures A2.5 and A2.6 present outcrop measurements for the size of the Type (I) and Type (II) melt patches and Figure A2.7 shows the distribution of the spacing of Type (II) patches. The spacing of Type (I) melt patches can be found in Figure 2 of the main text. Spacing and size measurements were obtained from multiple outcrop surfaces of different orientations to control for the 3D structure.

A2.3: Petrographic Descriptions

The schist in the field area belongs to the upper member of the Littleton Formation. The schist is composed of qtz+bt+ms+sil+plag+/-gt. The assemblage bt+gt+sil is in equilibrium with *in situ* granitic melt (Type (II) melt patches, Figure A2.10). A pervasive foliation, S1, is defined by the micas and elongate quartz and feldspar. A second foliation, S2, is present as asymmetric cleavage or simple shear of the S1 foliation. The lineation in the field area is defined by sillimanite and ms-aggregates, which are contemporaneous to post-dating the S2 foliation, and are folded by the F2/F3 generation of regional folding (Figure 4.1 and A2.10). Qtz exhibits undulose extinction and grain boundary migration with subsequent grain boundary area reduction in qtz+fsp-rich layers. This observation suggests high temperature deformation followed by post-kinematic recrystallization. The timing of post-kinematic recrystallization must post-date the development of the S2 foliation and mineral aggregate lineation.

Both Type (I) and Type (II) melt patches are post-kinematic relative to the S2 foliation and mineral aggregate lineation. Additionally, the melt patches post-date F3 regional folding as the orientation of the melt patches is unaffected by a 100 m-scale, F3 fold about the Main Cliff climbing wall in the field area. Discrete shear zones which are found at the outcrop scale in the field area are contemporaneous to post-kinematic relative to foliation boudinage and the emplacement of Type (I) melt patches. These shear zones are classified as the S3 foliation and are generally subhorizontal to shallowly-ESE-dipping and anastomosing. Most of the shear zones display top-to-the-northwest simple shear based on the offset of relict bedding planes, and the deflection and folding of dikes and foliations.

A2.4: Zircon Concordia of Littleton Schist and Granite Leucosomes

Zircons were separated by first crushing the sample with a hammer followed by shatterboxing. Fine particles were removed by washing the grains with water and decanting. Strongly magnetic grains were separated from the washed grains using a Frantz magnetic separator. Finally, the densest grains, including zircon, were separated from low-density minerals in Methylene Iodide (MEI). From the dense mineral fraction, we manually picked zircons and mounted them in epoxy. The epoxy mounts were polished to expose the centers of the zircon grains. Zircon mounts were analyzed for U-Pb isotopes at the Arizona LaserChron Center using Laser Ablation-Inductively Coupled Plasma–Mass Spectrometry (LA-ICP-MS). Analytical and data processing methodology follows that of Pullen et al. (2018).

Sample RY219 is characterized by a detrital age population with a distribution of zircon ages from ~380-2500 Ma (Figures A2.13 and A2.14). The most prominent peak is the result of Ordovician-Devonian plutonism during the Taconic and Acadian orogenies (Bradley and Sullivan, 2017). Zircons with ages between 550-700 Ma are likely the product of erosion from Avalonia during deposition of the Central Maine Terrane. Ages older than ~1 Ga are likely sourced from cratonic regions on both Laurentia (Grenville Orogen) and Gondwana (Pan-African orogen).

In contrast, sample RY2142 is characterized by a singular peak at 361.85 ±.71 Ma (Figures A2.11 and A2.12). All zircons were subhedral to euhedral, commonly with well-developed zoning. There is no discernable contrast between the U-Pb ages of zircon rims and cores, within the measurement error. It is clear that the melt patches do not contain detrital grains considering that the age of emplacement is younger than the depositional age of the Littleton Fm (Bradley and Sullivan, 2017).

A2.5: Microprobe Methodology

The major element compositions of Biotite, Garnet, Muscovite, and Plagioclase were analyzed by wavelength dispersive spectrometry on the 5-spectrometer JEOL 8200 electron microprobe (EMP) at the Massachusetts Institute of Technology. All analyses of minerals were conducted with a 15 kV accelerating voltage, a 10 nA beam current and a 1 µm spot size. Online data reduction utilized the CITZAF correction package (Armstrong, 1995) and the atomic number correction, the absorption coefficients, and the fluorescence correction available in CITZAF.

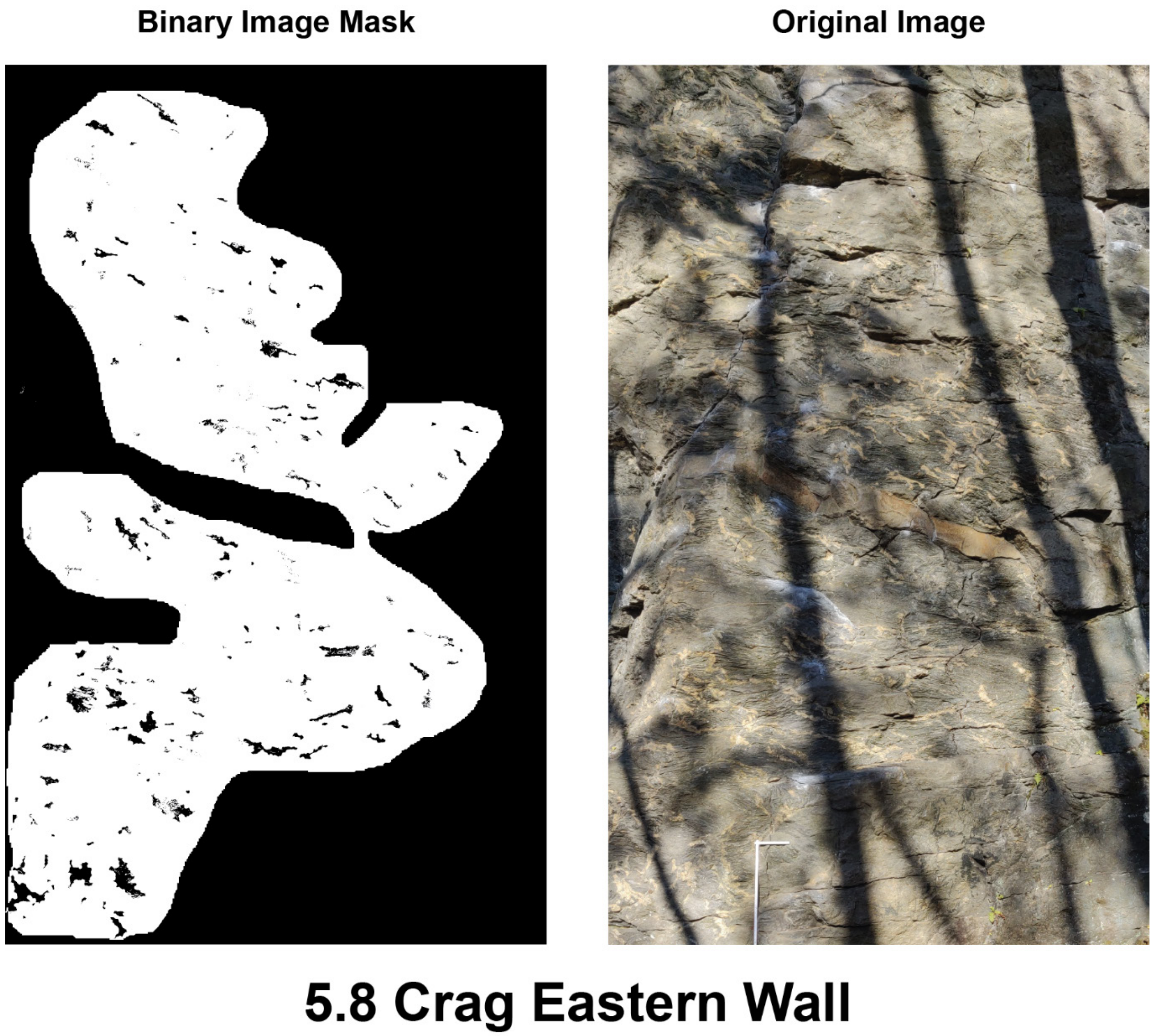

Figure A2.1: Outcrop image of 5.8 Crag climbing wall in the field area (right). Binary image of Type (I) melt patches segmented from the image (left). Calculation of melt fraction utilizes the total area of the white region. Blacked out regions have poor resolution or are exposures of a quartz-rich bedding face. The outcrop is located at 43.8011 N, 71.8381 W.

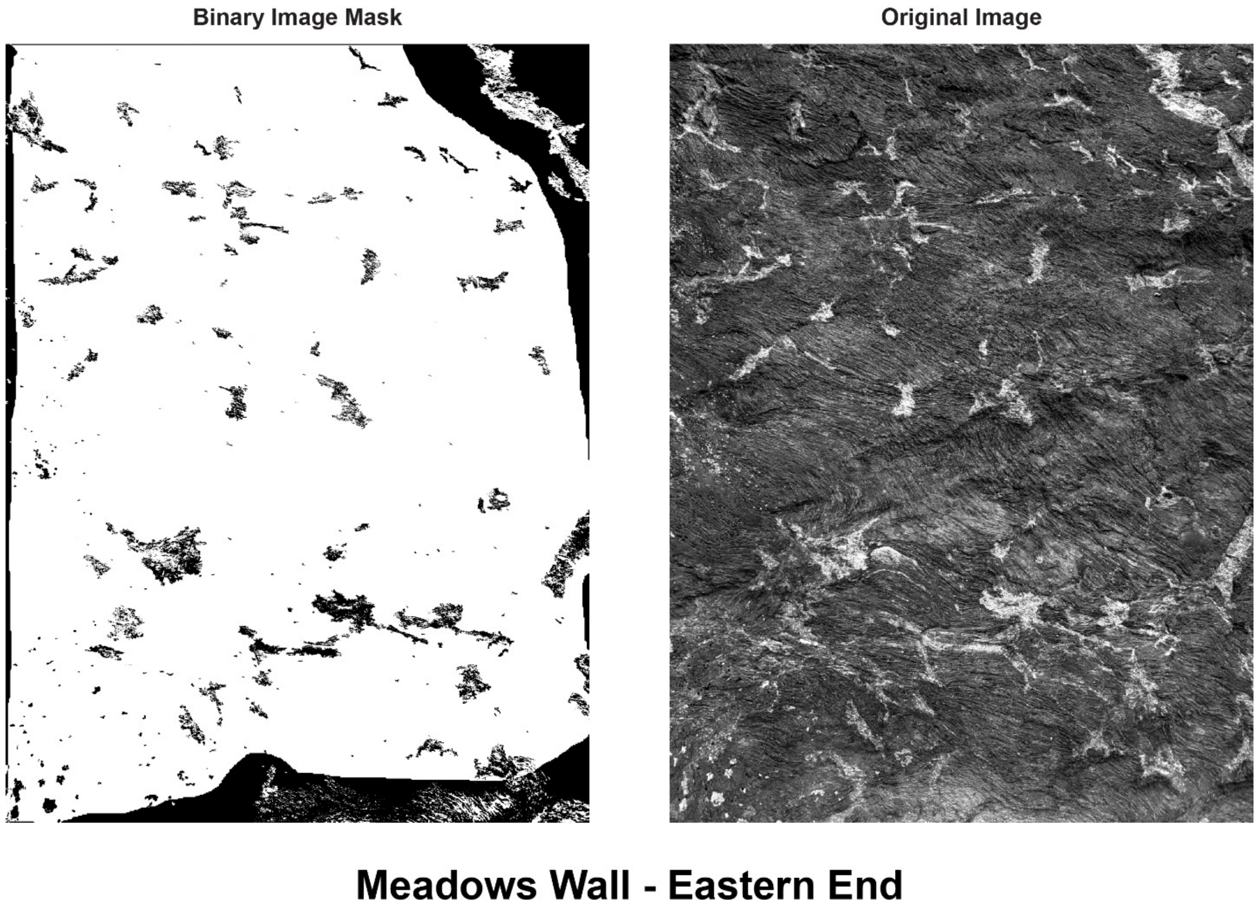

Figure A2.2: Outcrop image of the far east end of Meadows Wall in the field area (right). Binary image mask with the large dike (upper right) and poorly lit bottom edge removed from the considered area (left). The outcrop is located at 43.8025 N, 71.8312 W.

Figure A2.3: Outcrop image of a well exposed foliation parallel and lineation perpendicular face on the NW end of the Orange Crush climbing wall in the field area (right). Binary image with dark regions removed (left). The outcrop is located at 43.8031 N, 71.8357 W.

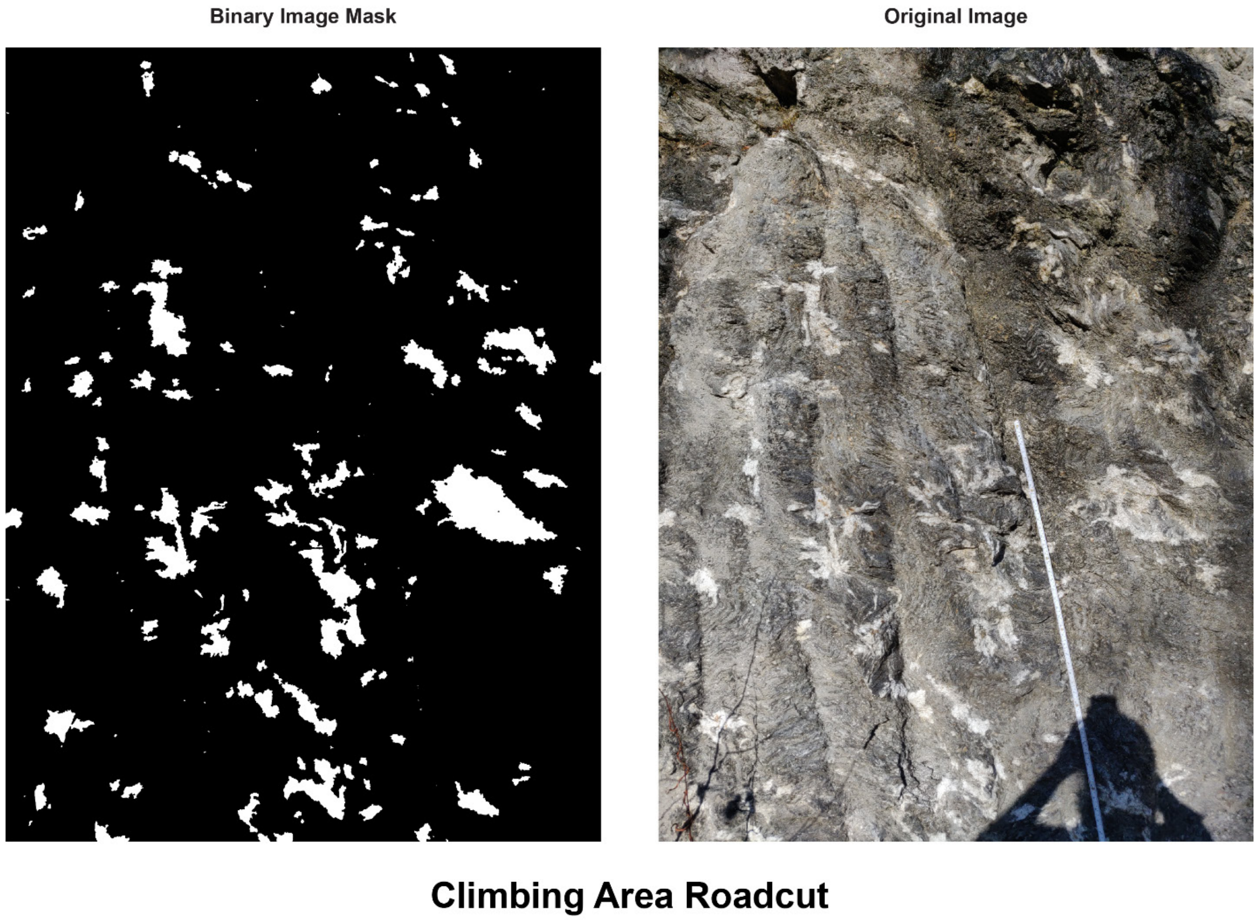

Figure A2.4: Image of the west end of a roadcut in the field area (right). Binary image of melt patches (left). The entire image was used to calculate a melt fraction of ~7%. The outcrop is located at 43.8020 N, 71.8332 W.

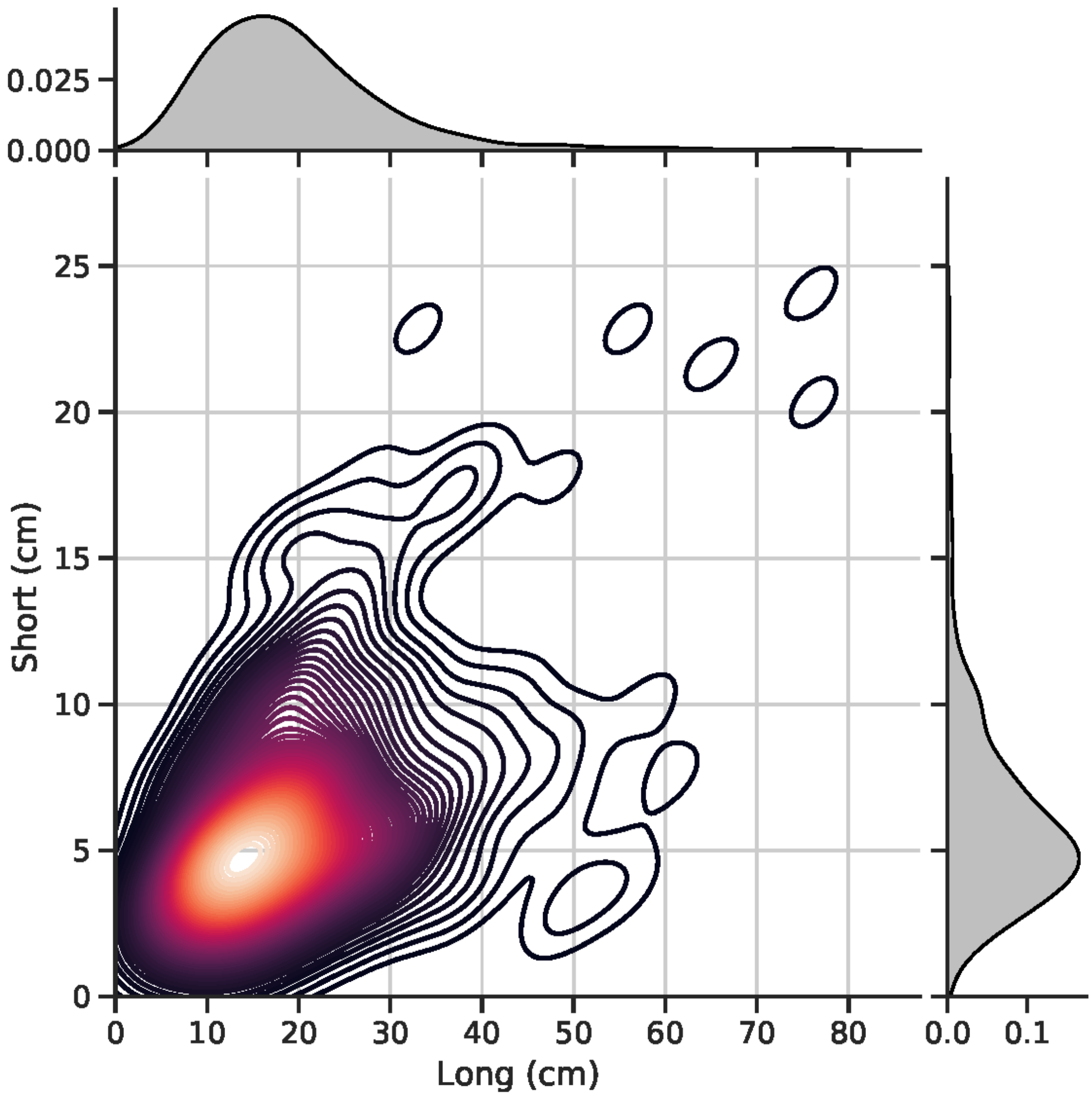

Figure A2.5: Size of discordant, Type (I) granite melt patches in the field area. Melt Patches are subelliptical on the outcrop face, and therefore we represent the shape with two measurements: the length of the long and short axes.

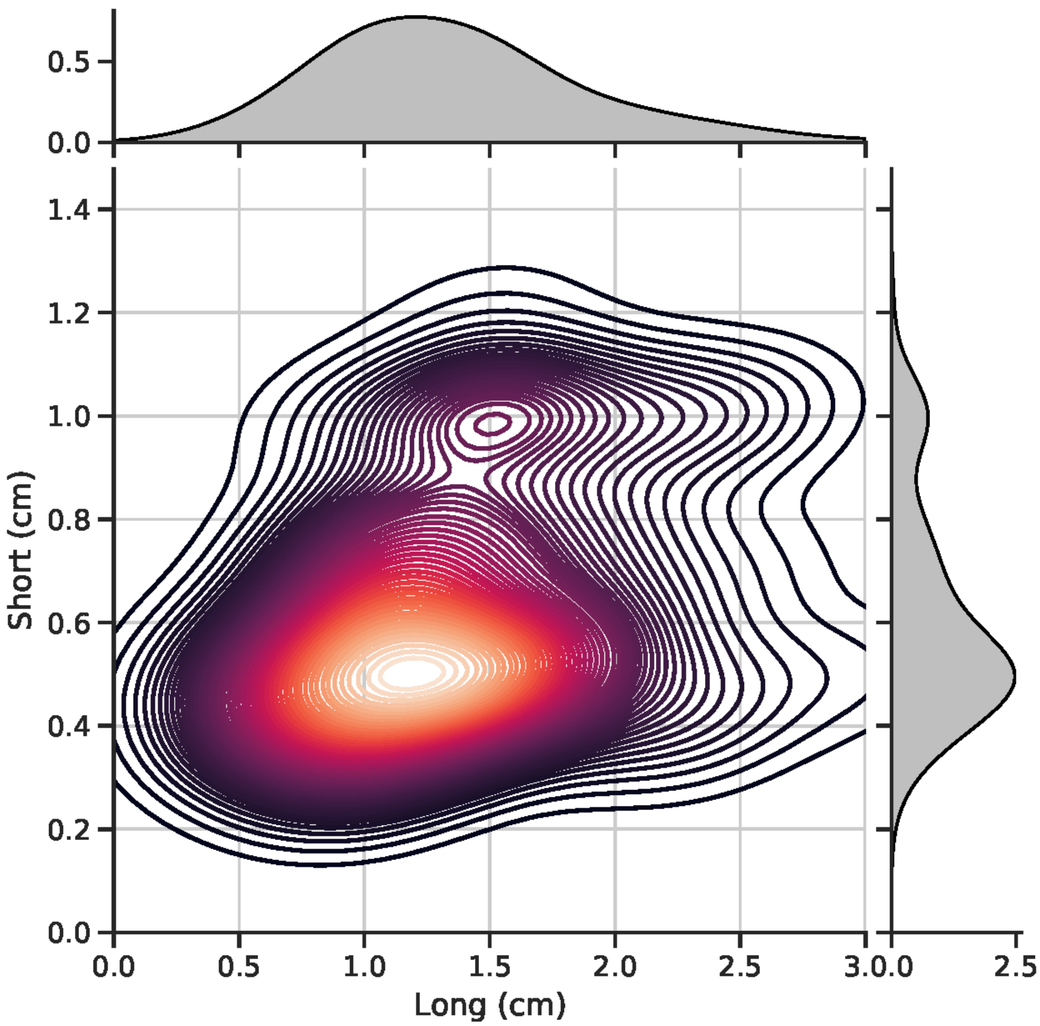

Figure A2.6: Size of Type (II) melt patches in the field area. Small melt patches are measured in the same manner as large melt patches.

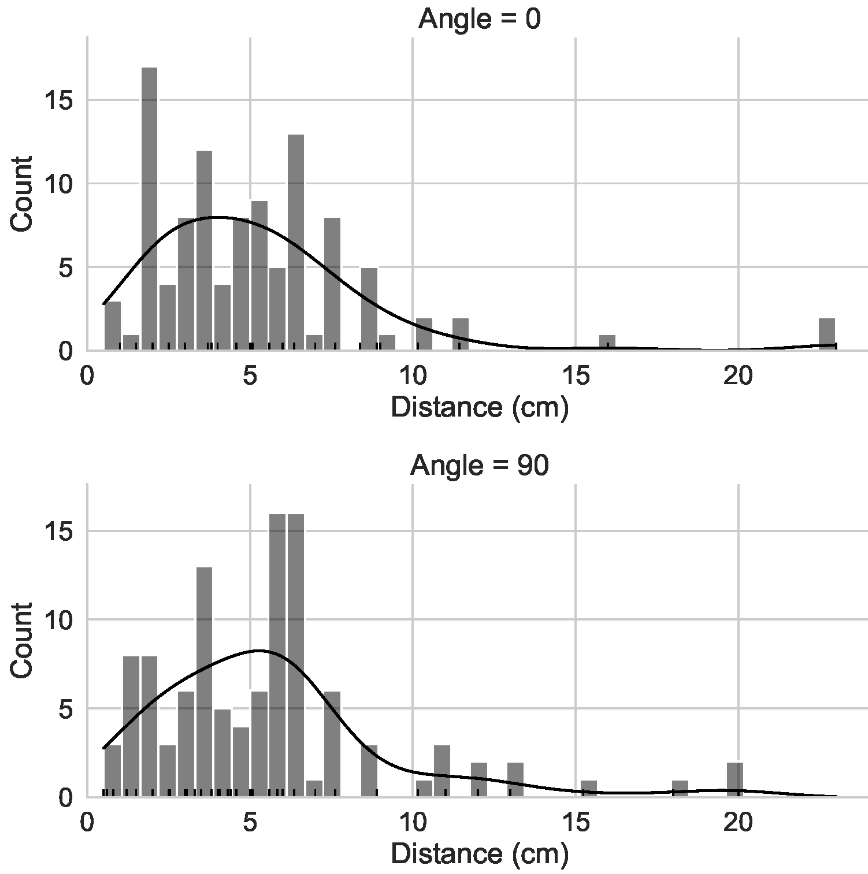

Figure A2.7: Spacing of small granite melt patches parallel to the long (0°) and short (90°) axes of each melt patch. This is generally no greater than 10 cm and no less than 1 cm.

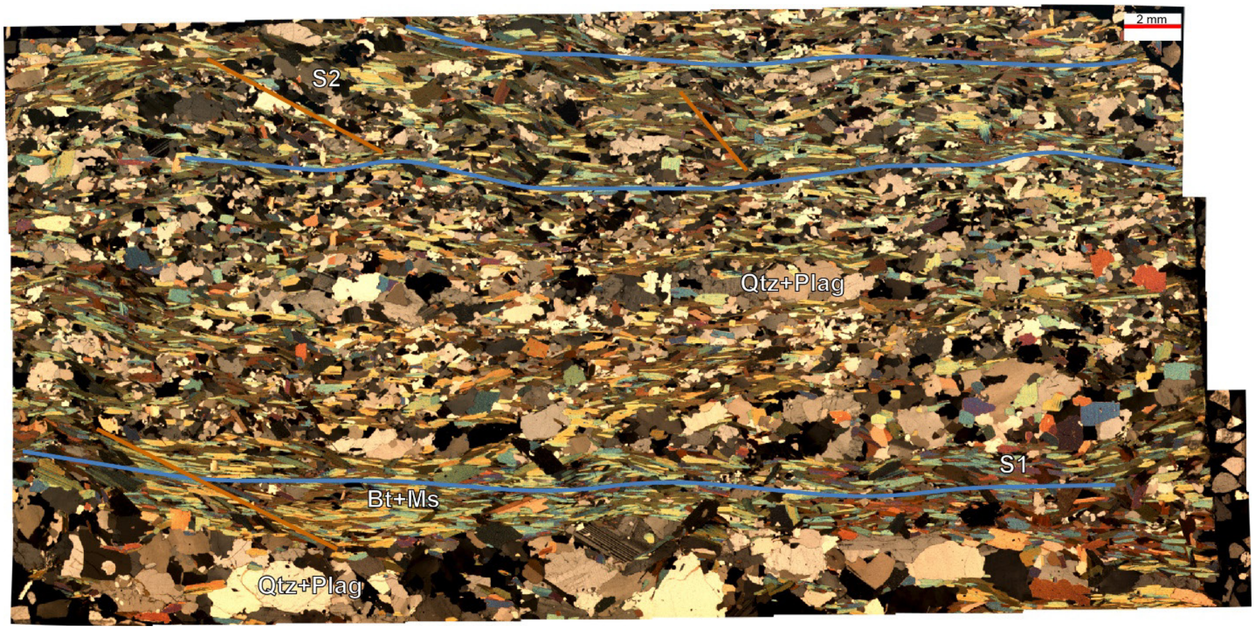

Figure A2.8: Plane polarized light thin section image of sample RY200. Sample location is 43.8029 N, 71.8393 W.

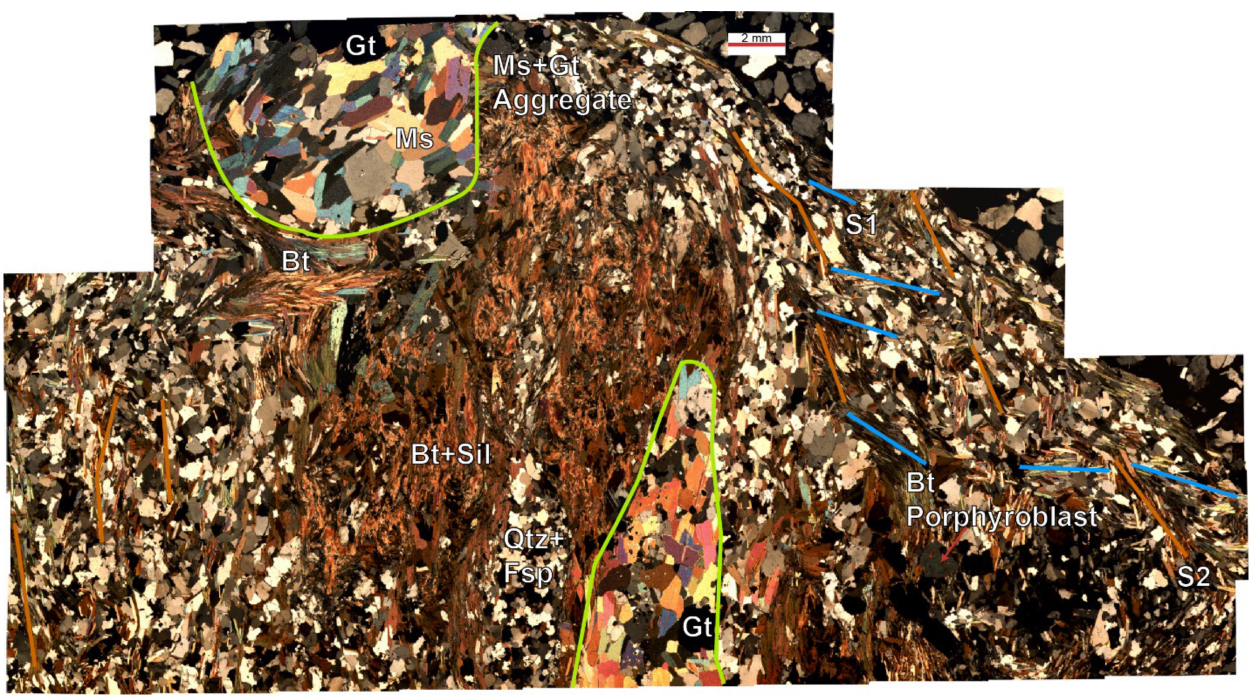

Figure A2.9: Plane polarized light thin section image of sample RY202. Sample location is 43.8020 N, 71.8332 W.

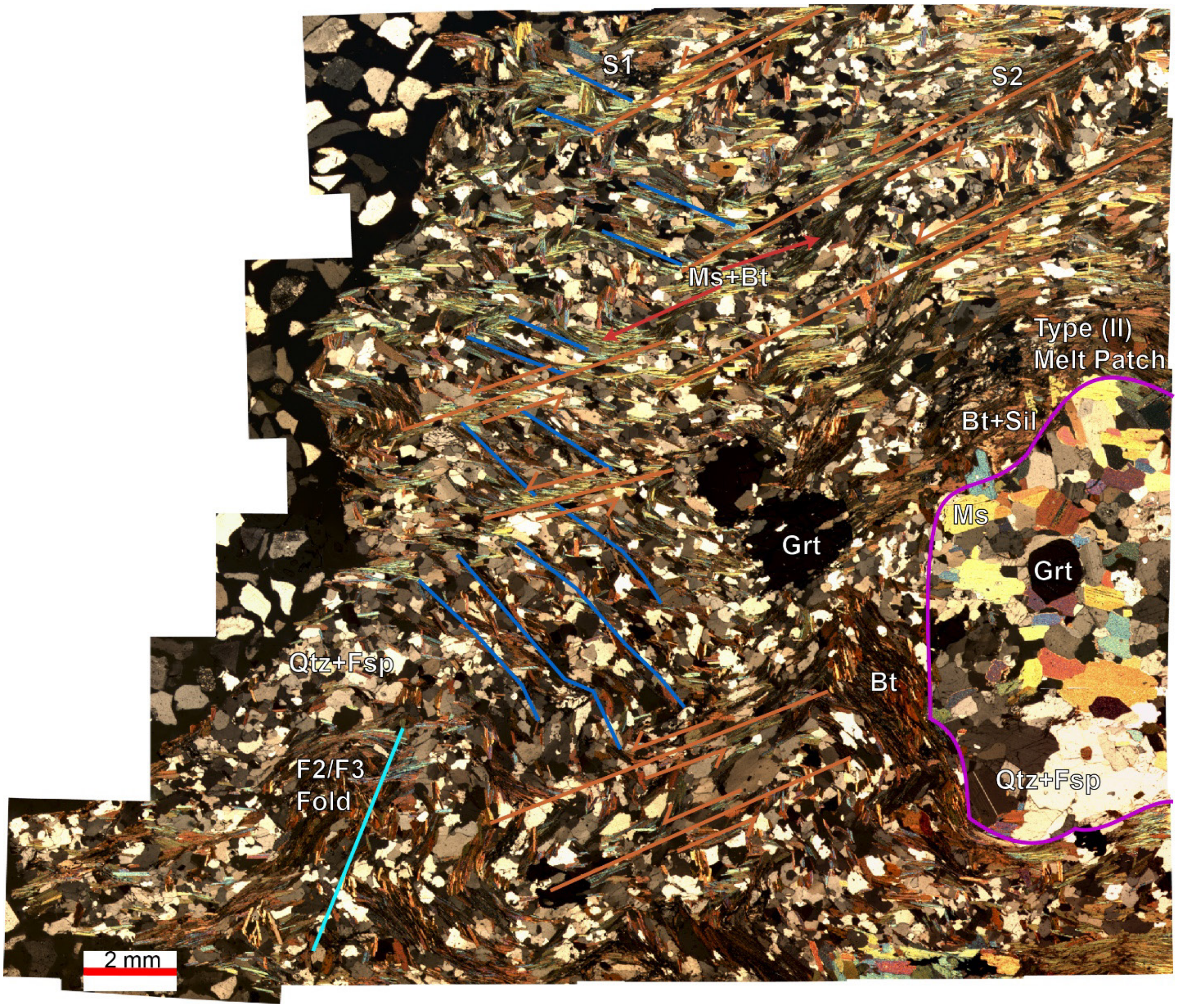

Figure A2.10: Plane polarized light thin section image of sample RY202A. Sample location is 43.8020 N, 71.8332 W. Type (II) granitic melt patch is visible on the right-hand side of the section, and is mantled by a melanocratic assemblage of Bt+Sil+Gt.

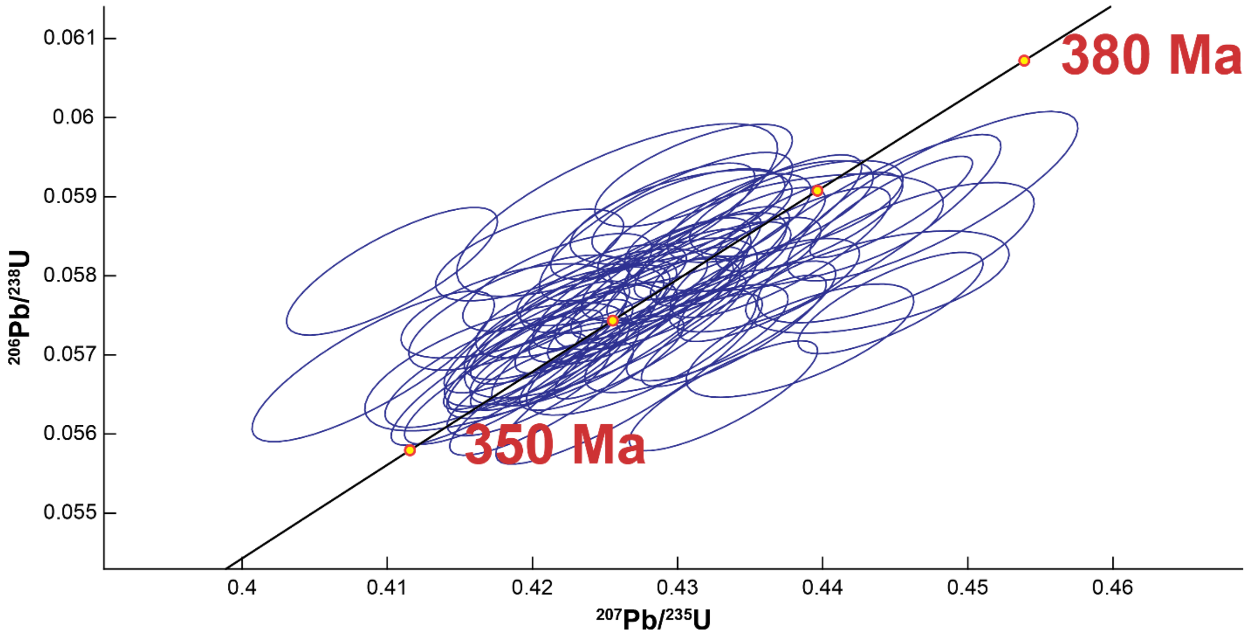

Figure A2.11: Zircon U-Pb concordia diagram for sample RY-21-42. Sample from 43.8020 N, 71.8332 W.

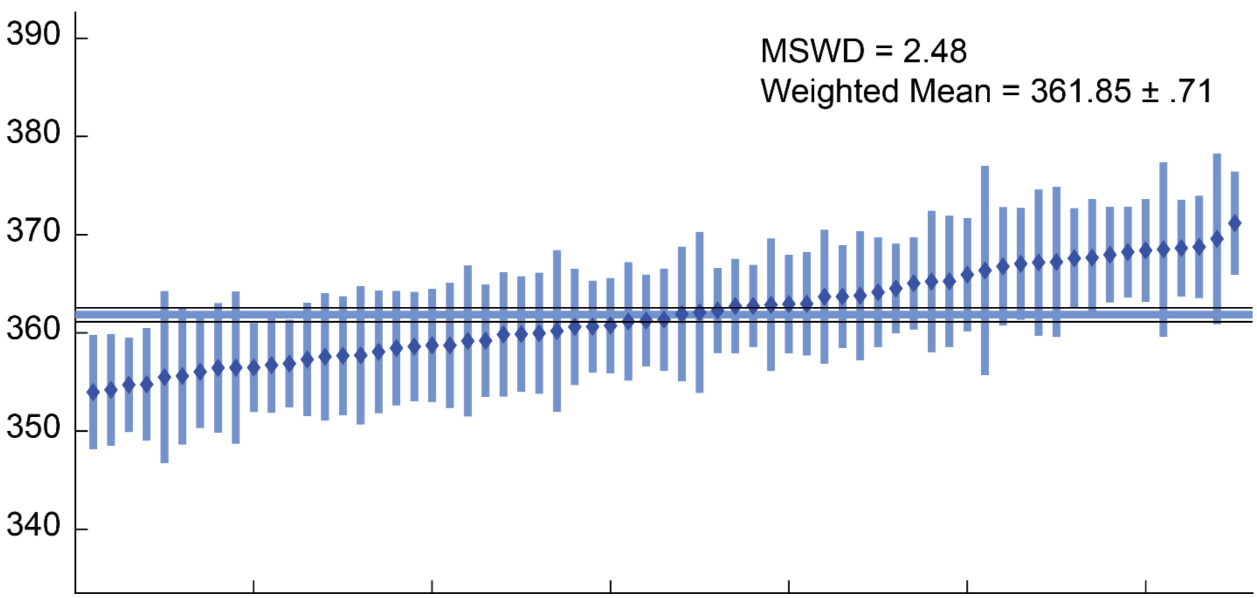

Figure A2.12: Mean age of accepted zircon measurements. Some outliers were manually removed to further constrain the mean age. The removal of outliers does not significantly change the weighted mean age (less than .5 Myr change).

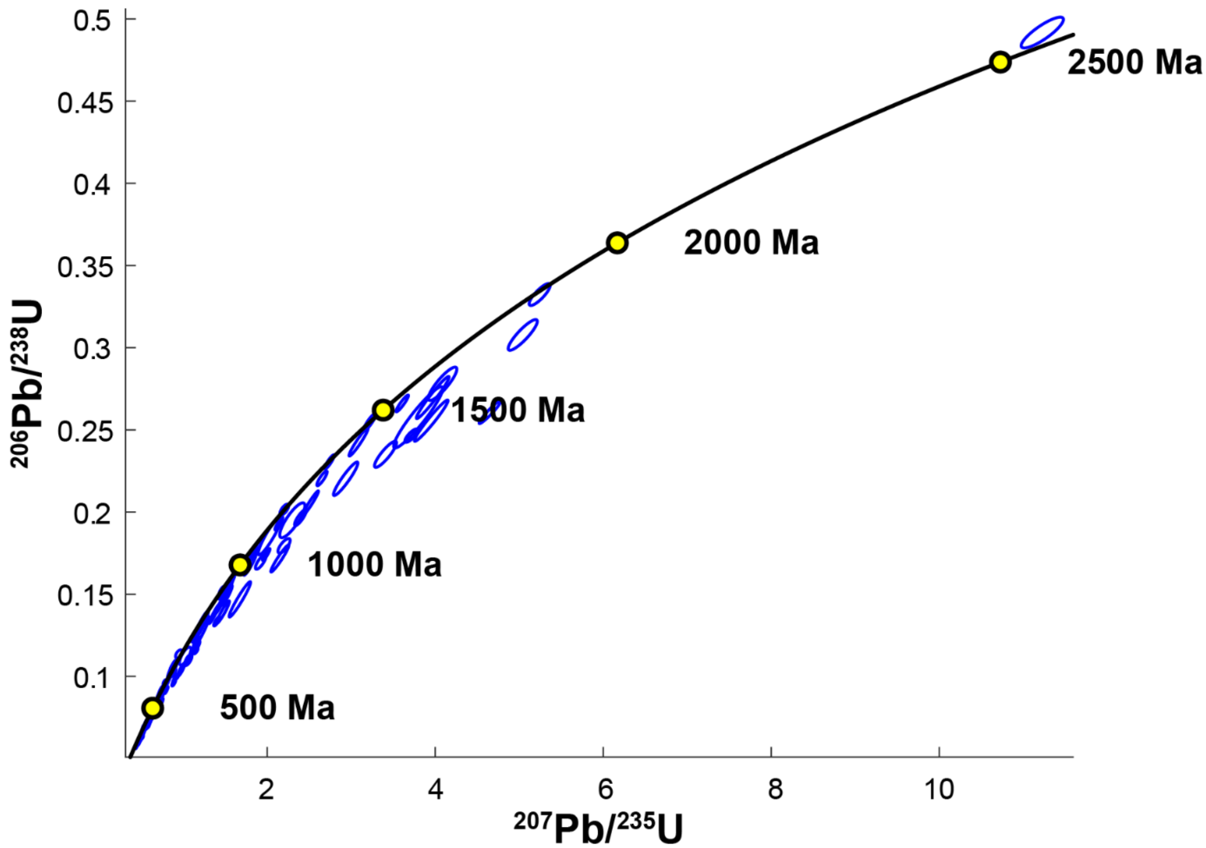

Figure A2.13: Concordant zircon U-Pb measurements for sample RY219. Sample from 43.8020 N, 71.8332 W. Grains with discordance greater than 30% were removed.

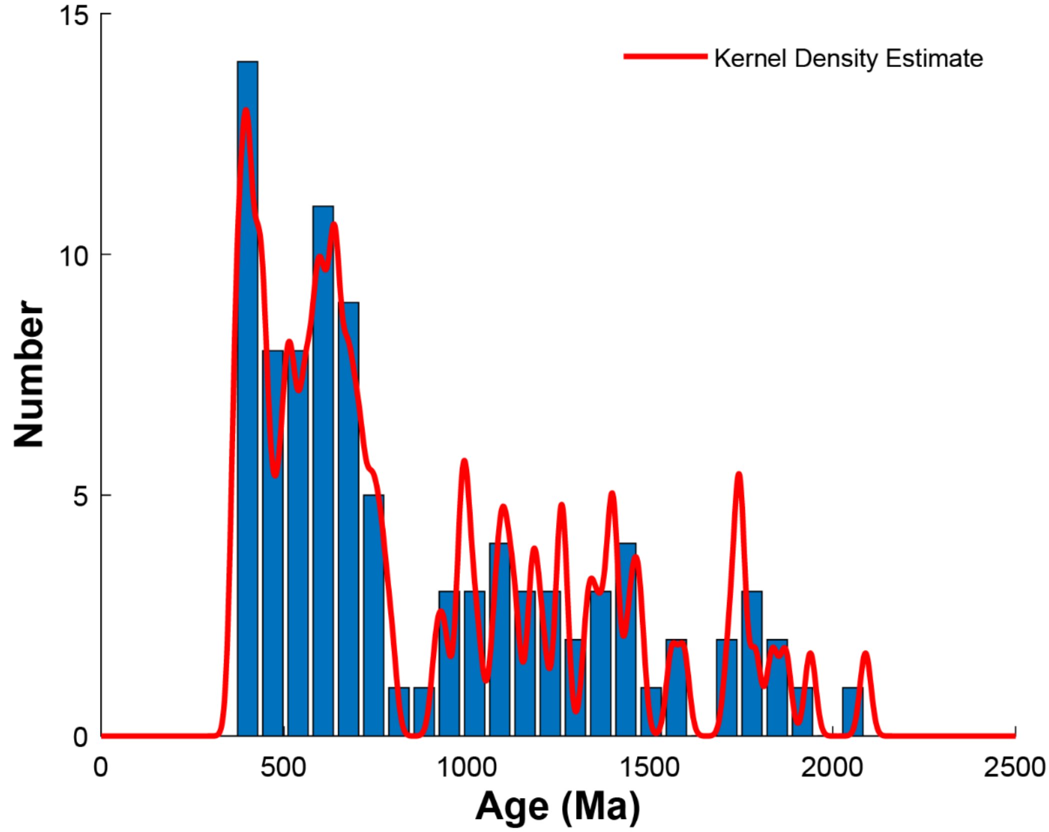

Figure S14: Distribution of concordant ages for a sample of Littleton schist (RY219) with the Kernel Density profile overlain in red. Zircons are primarily detrital and likely sourced from Laurentian, Taconic, and Avalonian lithologies.

Table A2.1: Mineral compositions for sample RY202A (43.8020 N, 71.8332 W) and RY2130A (43.7849 N, 71.7938 W). Provided as separate excel file.

Sample	*RY2130A*	*RY2130A*	*RY2130A*	*RY2130A*	*RY2130A*	*RY2130A*	*RY2130A*	*RY2130A*
Mineral	Gt	Gt	Gt	Gt	Gt	Gt	Gt	Gt
SiO_2	36.32	36.51	36.41	36.57	36.39	36.2	36.5	36.36
TiO_2	0.0204	0.0661	0	0	0	0	0	0
Al_2O_3	21.71	21.86	21.6	21.82	21.84	21.59	21.78	21.63
FeO	37.05	36.94	36.46	37.13	37.11	36.22	36.53	36.3
MnO	2.53	2.64	3.1	3.32	2.6	2.83	3.07	3.11
MgO	2.2	2.03	1.88	1.8	2.15	2.14	2.09	2.12
CaO	0.5359	0.539	0.5602	0.535	0.5917	0.5916	0.5555	0.5811
Na_2O	0.0031	0	0	0	0.0246	0.0061	0	0
K_2O	0	0	0	0	0	0	0	0
Total	100.3903	100.6376	100.0276	101.2379	100.7517	99.6023	100.5429	100.1642

Sample	*RY2130A*	*RY2130A*	*RY2130A*	*RY2130A*	*RY2130A*	*RY2130A*	*RY2130A*	*RY2130A*
Mineral	Gt	Gt	Gt	Gt	Gt	Gt	Gt	Gt
SiO2	36.39	36.48	36.52	36.49	36.64	36.74	36.4	36.29
TiO2	0.0254	0	0	0.0152	0	0	0.0102	0
Al2O3	21.73	21.85	21.91	21.74	21.57	21.61	21.78	21.58
FeO	36.34	36.39	36.29	36.11	35.88	35.98	36.22	36.62
MnO	3.15	3.09	3.09	3.22	3.27	3.66	3.63	3.55
MgO	2.09	2	1.99	1.93	1.89	1.86	1.84	1.76
CaO	0.5778	0.5908	0.5908	0.5875	0.6321	0.4576	0.3962	0.4148
Na2O	0	0.0307	0	0	0.0184	0	0.0246	0.0401
K2O	0	0	0.0135	0.0082	0.0046	0.0016	0.003	0.0036
Total	100.3522	100.477	100.4392	100.1114	99.9051	100.3267	100.3039	100.2899

Sample	*RY2130A*	*RY2130A*	*RY2130A*	*RY2130A*	*RY2130A*	*RY2130A*	*RY2130A*	*RY2130A*
Mineral	Gt	Gt	Gt	Gt	Gt	Gt	Gt	Gt
SiO_2	36.63	36.5	36.27	36.42	36.58	36.52	36.41	36.77
TiO_2	0.0152	0.0152	0.1416	0.1012	0.0405	0.0707	0	0.0505
Al_2O_3	21.71	21.73	21.68	21.74	21.61	21.51	21.66	21.77
FeO	36.45	36.35	36.56	36.59	37.18	37.92	37.21	36.97
MnO	3.34	3.3	3.35	3.46	3.34	2.94	3.39	3.45
MgO	1.85	1.91	1.85	1.84	1.69	1.6103	1.69	1.7
CaO	0.4164	0.4258	0.4028	0.4084	0.4632	0.5247	0.4217	0.3986
Na_2O	0.0614	0.0061	0.0308	0.0277	0	0	0	0.0862
K_2O	0.0069	0.0036	0	0.0062	0.0147	0.0003	0	0
Total	100.4833	100.2407	100.2851	100.6283	100.9184	101.0959	100.7886	101.1987

Table DR2 cont'd

Sample	*RY2130A*	*RY2130A*	*RY2130A*	*RY2130A*	*RY2130A*	*RY2130A*	*RY2130A*	*RY2130A*
Mineral	Gt	Gt	Gt	Gt	Gt	Gt	Gt	Bt
SiO_2	36.42	36.43	36.7	36.52	36.69	36.92	36.5	34.79
TiO_2	0.0202	0.0303	0.0555	0.0303	0	0.0353	0.0101	2.82
Al_2O_3	21.62	21.72	21.83	21.65	21.78	21.61	21.54	19.6
FeO	37.45	36.92	37.13	37.32	36.83	37.32	38.13	24.72
MnO	3.54	3.52	3.5	3.36	3.53	3.2	2.98	0.036
MgO	1.71	1.72	1.67	1.73	1.67	1.5799	1.3489	5.79
CaO	0.4279	0.4182	0.4048	0.4182	0.4421	0.4271	0.4936	0
Na_2O	0	0	0	0	0	0	0.0496	0.3157
K_2O	0	0.0036	0	0.0095	0	0	0.0062	8.74
Total	101.2263	100.762	101.2902	101.0379	100.942	101.0922	101.0966	96.8633

Sample	*RY2130A*	*RY2130A*	*RY2130A*	*RY2130A*	*RY2130A*	*RY2130A*	*RY2130A*	*RY2130A*
Mineral	Bt	Bt	Bt	Bt	Bt	Bt	Plag	Plag
SiO_2	34.7	34.29	34.55	34.36	34.31	33.82	65.82	64.82
TiO_2	2.7	3.48	2.95	3.1	3.34	3.13	-	-
Al_2O_3	19.6	19.22	19.45	19.17	19.13	18.86	21.89	21.51
FeO	24.46	24.46	24.72	24.97	24.77	24.91	0.0336	0.0054
MnO	0.0542	0.0561	0.0685	0.0822	0.069	0.0714	-	-
MgO	5.94	5.88	5.71	5.73	5.52	5.72	-	-
CaO	0	0	0	0	0.0018	0.0051	2.16	2.2
Na_2O	0.3311	0.3623	0.2809	0.3283	0.3474	0.3455	10.4	10.72
K_2O	8.68	8.79	8.72	8.73	8.74	8.9	0.0869	0.0825
Total	96.5023	96.5385	96.5085	96.5294	96.2282	95.8025	100.3904	99.338

Sample	*RY2130A*	*RY2130A*	*RY2130A*	*RY2130A*	*RY2130A*	*RY2130A*	*RY2130A*	*RY2130A*
Mineral	Plag	Plag	Plag	Plag	Plag	Ms	Ms	Ms
SiO_2	65.5	64.97	64.79	65.26	65.33	47.83	46.17	46.08
TiO_2	-	-	-	-	-	0.9877	0.8015	0.8614
Al_2O_3	21.24	21.66	21.65	22.1	21.59	38.52	36.73	36.6
FeO	0.031	0.0074	0.0143	0.0103	0.0482	1.2356	1.1591	1.2302
MnO	-	-	-	-	-	0	0	0.0051

MgO	-	-	-	0.0079	-	0.4125	0.3955	0.4237
CaO	1.87	2.23	2.14	2.3	2.14	0	0	0
Na_2O	10.94	11.05	10.75	10.55	10.72	1.0738	1.2127	1.1153
K_2O	0.085	0.0747	0.0784	0.0904	0.0658	7.08	8.74	8.49
Total	99.6661	99.9922	99.4228	100.3186	99.8941	97.1397	95.2088	94.8058

Table DR2 cont'd

Sample	*RY2130A*	*RY2130A*	*RY2130A*	*RY2130A*	*RY2130A*	*RY2130A*	*RY2130A*	*RY202A*
Mineral	Ms	Ms	Ms	Ms	Ms	Ms	Ms	Gt
SiO_2	45.91	45.93	46.88	46.03	45.96	46.05	46.01	36.29
TiO_2	0.7352	0.8347	0.8117	0.905	0.845	0.9926	0.7957	0.0911
Al_2O_3	36.88	37.01	37.3	37.06	37.36	36.92	37.03	21.58
FeO	1.2565	1.0397	1.1831	1.1823	1.1801	1.1806	1.1117	35.98
MnO	0.0117	0.0046	0	0.002	0.0005	0.001	0	3.77
MgO	0.3948	0.34	0.4435	0.4393	0.4212	0.4072	0.4157	1.67
CaO	0	0	0	0	0	0	0	0.7243
Na_2O	1.1497	1.0761	1.0886	1.0641	1.166	1.1459	1.1667	0
K_2O	8.53	8.6	7.03	8.74	8.93	8.75	8.92	0.003
Total	94.868	94.8351	94.7369	95.5106	95.9069	95.4793	95.4699	100.1678

Sample	*RY202A*	*RY202A*	*RY202A*	*RY202A*	*RY202A*	*RY202A*	*RY202A*	*RY202A*
Mineral	Gt	Gt	Gt	Gt	Gt	Gt	Gt	Gt
SiO_2	36.11	35.73	36.25	36.37	36.2	36.07	35.96	36.11
TiO_2	0	0.0303	0	0	0	0.0303	0.0907	0
Al_2O_3	21.5	21.49	21.64	21.58	21.45	21.55	21.37	21.47
FeO	34.25	33.84	33.77	34.2	34.84	35.96	35.42	34.17
MnO	5.79	5.85	6.03	5.7	5.12	4.15	4.73	5.94
MgO	2.01	2.01	2.01	1.99	1.95	1.6402	1.73	1.92
CaO	0.3512	0.3652	0.3087	0.4185	0.4453	0.6436	0.4664	0.3636
Na_2O	0.0337	0.0061	0.0183	0	0.0521	0	0	0
K_2O	0	0.0052	0.0151	0.0065	0.0072	0.002	0.0105	0.0013

Total	100.0834	99.3269	100.042	100.2649	100.1031	100.0984	99.7952	100.0133

Sample	*RY202A*	*RY202A*	*RY202A*	*RY202A*	*RY202A*	*RY202A*	*RY202A*	*RY202A*
Mineral	Gt	Gt	Gt	Gt	Gt	Gt	Gt	Gt
SiO_2	36.26	36.21	36.25	36.27	36.11	35.77	36.02	36.08
TiO_2	0	0.0454	0.0655	0	0	0	0	0
Al_2O_3	21.54	21.45	21.57	21.41	21.27	21.44	21.51	21.42
FeO	33.42	33.5	33.65	33.99	34.44	34.62	35.52	34.53
MnO	5.98	5.88	5.93	5.55	5.14	4.97	4.1	4.85
MgO	1.98	2.01	2.03	1.97	1.93	1.87	1.92	1.96
CaO	0.395	0.3902	0.3784	0.4832	0.5035	0.4904	0.4974	0.4751
Na_2O	0.061	0.0274	0	0.0031	0.0703	0.0275	0.0337	0
K_2O	0	0.0062	0	0	0	0	0	0
Total	99.6817	99.6281	99.9196	99.6764	99.4989	99.2404	99.6012	99.3362

Table DR2 cont'd

Sample	*RY202A*	*RY202A*	*RY202A*	*RY202A*	*RY202A*	*RY202A*	*RY202A*	*RY202A*
Mineral	Gt	Gt	Gt	Gt	Gt	Gt	Gt	Gt
SiO_2	36.31	36.1	36.48	36.23	36.49	36.24	36.32	36
TiO_2	0.0151	0.0099	0	0	0	0	0	0
Al_2O_3	21.52	21.9	21.4	21.53	21.47	21.61	21.57	21.39
FeO	34.11	34.22	34.44	35.29	35.66	35	33.4	33.3
MnO	5.18	5.29	5.38	4.76	4.2	4.64	6.11	6.05
MgO	1.96	2.05	2.06	1.93	1.87	1.92	2.17	2.14
CaO	0.4281	0.4137	0.4155	0.4696	0.5292	0.4637	0.3478	0.4043
Na_2O	0.0518	0.0097	0.1129	0.1622	0.052	0.0672	0.0698	0.1582
K_2O	0	0	0	0	0	0	0	0.002
Total	99.6732	99.9934	100.2883	100.3718	100.2711	99.941	99.9912	99.4762

Sample	*RY202A*	*RY202A*	*RY202A*	*RY202A*	*RY202A*	*RY202A*	*RY202A*	*RY202A*
Mineral	Gt	Gt	Gt	Gt	Bt	Bt	Bt	Bt
SiO_2	36.02	36.3	36.32	36.4	34.2	34.45	34.76	35.07
TiO_2	0	0	0	0	2.41	2.27	2.8	2.7
Al_2O_3	21.14	21.55	21.7	21.42	19.26	19.2	19.39	19.62
FeO	33.35	33.52	34.1	34.78	22	22.36	22.42	21.77

MnO	6.15	6.16	5.96	4.91	0.1111	0.1214	0.075	0.0864
MgO	2.17	2.07	2.08	1.96	7.69	7.67	7.37	7.07
CaO	0.3938	0.3763	0.3807	0.4322	0.0364	0.0328	0	0.0029
Na_2O	0.0884	0.1126	0.0641	0.0823	0.3418	0.3717	0.2498	0.2774
K_2O	0	0	0	0	8.25	8.19	8.37	8.37
Total	99.3123	100.0889	100.6607	99.9846	94.3809	94.7104	95.4349	95.0039

Sample	*RY202A*	*RY202A*	*RY202A*	*RY202A*	*RY202A*	*RY202A*	*RY202A*	*RY202A*
Mineral	Bt	Bt	Bt	Bt	Bt	Bt	Plag	Plag
SiO_2	34.67	34.61	34.53	34.45	34.74	34.56	65.03	64.5
TiO_2	2.76	2.87	2.74	2.91	2.79	2.67	-	-
Al_2O_3	19.6	19.28	19.29	19.07	19.34	19.42	21.17	21.55
FeO	22.03	22.25	21.96	22.24	22.32	22.65	0.0418	0.0285
MnO	0.0893	0.076	0.0804	0.0503	0.0631	0.0498	-	-
MgO	7.22	7.33	7.29	7.32	7.43	7.18	0	0
CaO	0.0066	0.0188	0.0154	0	0	0.0301	1.81	1.98
Na_2O	0.3178	0.3265	0.3232	0.2711	0.3104	0.3143	11.31	10.97
K_2O	8.33	8.35	8.33	8.29	8.26	8.15	0.0679	0.0692
Total	95.109	95.1447	94.5591	94.6941	95.298	95.0465	99.4297	99.0978

Table DR2 cont'd

Sample	*RY202A*	*RY202A*	*RY202A*	*RY202A*	*RY202A*	*RY202A*	*RY202A*	*RY202A*
Mineral	Plag	Plag	Plag	Plag	Ms	Ms	Ms	Ms
SiO_2	65.28	65.52	64.3	64.96	47.86	46.96	44.84	43.26
TiO_2	-	-	-	-	0.6087	0.9531	0.9053	0.6582
Al_2O_3	21.54	21.85	21.51	21.33	38.44	38.31	35.86	35.77
FeO	0.0797	0.0113	0.0251	0.0236	1.31	1.2808	1.1515	1.2152
MnO	-	-	-	-	0	0	0	0.0036
MgO	0	0.009	0	0.0137	0.4289	0.4715	0.4103	0.474
CaO	1.87	1.87	1.9	1.92	0	0.0369	0.0126	0
Na_2O	10.51	10.72	10.7	11.02	1.1252	1.0273	1.0967	1.28
K_2O	0.0641	0.0613	0.0812	0.0593	7.25	6.66	8.66	8.55
Total	99.3439	100.0415	98.5164	99.3267	97.0229	95.6997	92.9365	91.2111

Sample	*RY202A*	*RY202A*	*RY202A*	*RY202A*
Mineral	Ms	Ms	Ms	Ms

SiO_2	44.35	45.45	44.03	45.01
TiO_2	0.7791	0.6747	0.7131	0.8502
Al_2O_3	36.22	36.17	36.01	35.79
FeO	1.1143	1.2125	1.0566	1.1579
MnO	0.0036	0.0025	0.0203	0.0071
MgO	0.4591	0.4808	0.4666	0.3971
CaO	0	0	0.0034	0.024
Na_2O	1.1461	1.2596	1.1243	1.0756
K_2O	8.69	8.67	8.52	8.32
Total	92.7623	93.9402	91.9444	92.632

5633

References for Supplementary Materials

Arganda-Carreras, I., Kaynig, V., Rueden, C., Eliceiri, K. W., Schindelin, J., Cardona, A., & Sebastian Seung, H. (2017). Trainable Weka Segmentation: A machine learning tool for microscopy pixel classification. *Bioinformatics*, *33*(15), 2424–2426. https://doi.org/10.1093/bioinformatics/btx180

Bradley, D. C., & O'Sullivan, P. (2017). Detrital zircon geochronology of pre- and syncollisional strata, Acadian orogen, Maine Appalachians. *Basin Research*, *29*(5), 571–590. https://doi.org/10.1111/bre.12188

Giordano, D., Russell, J. K., & Dingwell, D. B. (2008). Viscosity of magmatic liquids: A model. *Earth and Planetary Science Letters*, *271*(1–4), 123–134. https://doi.org/10.1016/j.epsl.2008.03.038

Higgins, M. D. (2000). Measurement of crystal size distributions. *American Mineralogist*, *85*(9), 1105–1116. https://doi.org/10.2138/am-2000-8-901

Holtzman, B. K., Groebner, N. J., Zimmerman, M. E., Ginsberg, S. B., & Kohlstedt, D. L. (2003). Stress-driven melt segregation in partially molten rocks: MELT SEGREGATION IN MOLTEN ROCKS. *Geochemistry, Geophysics, Geosystems*, *4*(5), n/a-n/a. https://doi.org/10.1029/2001GC000258

Ji, S. (2004). A generalized mixture rule for estimating the viscosity of solid-liquid suspensions and mechanical properties of polyphase rocks and composite materials: A GENERALIZED MIXTURE RULE. *Journal of Geophysical Research: Solid Earth*, *109*(B10). https://doi.org/10.1029/2004JB003124

Kohlstedt, D. L., Zimmerman, M. E., & Mackwell, S. J. (2010). Stress-driven Melt Segregation in Partially Molten Feldspathic Rocks. *Journal of Petrology*, *51*(1–2), 9–19. https://doi.org/10.1093/petrology/egp043

Mangler, M. F., Humphreys, M. C. S., Wadsworth, F. B., Iveson, A. A., & Higgins, M. D. (2022). Variation of plagioclase shape with size in intermediate magmas: A window into incipient plagioclase crystallisation. *Contributions to Mineralogy and Petrology*, *177*(6), 64. https://doi.org/10.1007/s00410-022-01922-9

McKenzie, D. (1984). The Generation and Compaction of Partially Molten Rock. *Journal of Petrology*, *25*(3), 713–765. https://doi.org/10.1093/petrology/25.3.713

McKenzie, D., & Holness, M. (2000). Local deformation in compacting flows: Development of pressure shadows. *Earth and Planetary Science Letters*, *180*(1–2), 169–184. https://doi.org/10.1016/S0012-821X(00)00152-7

Newman, S., & Lowenstern, J. B. (2002). VolatileCalc: A silicate melt–H2O–CO2 solution model written in Visual Basic for excel. *Computers & Geosciences*, *28*(5), 597–604. https://doi.org/10.1016/S0098-3004(01)00081-4

Pullen, A., Ibáñez-Mejia, M., Gehrels, G. E., Giesler, D., & Pecha, M. (2018). Optimization of a Laser Ablation-Single Collector-Inductively Coupled Plasma-Mass Spectrometer (Thermo Element 2) for Accurate, Precise, and Efficient Zircon U-Th-Pb Geochronology. *Geochemistry, Geophysics, Geosystems*, *19*(10), 3689–3705. https://doi.org/10.1029/2018GC007889

Rosenberg, C. L., & Handy, M. R. (2005). Experimental deformation of partially melted granite revisited: Implications for the continental crust. *Journal of Metamorphic Geology*, *23*(1), 19–28. https://doi.org/10.1111/j.1525-1314.2005.00555.x

Schindelin, J., Arganda-Carreras, I., Frise, E., Kaynig, V., Longair, M., Pietzsch, T., Preibisch, S., Rueden, C., Saalfeld, S., Schmid, B., Tinevez, J.-Y., White, D. J., Hartenstein, V., Eliceiri, K., Tomancak, P., & Cardona, A. (2012). Fiji: An open-source platform for biological-image analysis. *Nature Methods*, *9*(7), 676–682. https://doi.org/10.1038/nmeth.2019

Wark, D. A., & Watson, E. B. (1998). Grain-scale permeabilities of texturally equilibrated, monomineralic rocks. *Earth and Planetary Science Letters*, *164*(3–4), 591–605. https://doi.org/10.1016/S0012-821X(98)00252-0

Weinberg, R. F., Veveakis, E., & Regenauer-Lieb, K. (2015). Compaction-driven melt segregation in migmatites. *Geology*, *43*(6), 471–474. https://doi.org/10.1130/G36562.1